MODELLING MULTIDRUG RESISTANCE DRIVEN BY EFFLUX PUMP EXPRESSION IN GRAM-NEGATIVE BACTERIA

by

GEORGE HENRY YOULDEN

A thesis submitted to
The University of Birmingham
for the degree of
DOCTOR OF PHILOSOPHY

School Of Mathematics
College Of Engineering And Physical Sciences
University Of Birmingham & University Of Nottingham
August 2020

Abstract

Efflux pumps are an essential mechanism for bacteria that can account for antibiotic resistance. If an efflux pump can expel an antibiotic so that its concentration within the cell is below a killing threshold the bacteria can become resistant to the antibiotic. Efflux pumps may be specific or they may pump various different substances and compounds. The latter is one main reason that many efflux pumps are linked with multi drug resistance (MDR). In particular overexpression of the AcrAB−TolC efflux pump system is commonly linked with MDR in both *Escherichia coli* (*E. coli*) and *Salmonella*. We look at the complex gene regulation network (GRN) central to controlling the efflux pump genes *acrAB* and *acrEF* in *Salmonella* and their resulting effect on intracellular antibiotic concentration. By using mathematical modelling, we first represent the gene regulatory network solely, we present a model in the form of a system of ordinary differential equations (ODEs). Using time dependent asymptotic analysis, we can examine in detail the behaviour of the efflux system on various different timescales before analysing asymptotically approximated steady states. In our second model, we produce a spatial model governing the diffusion and efflux of antibiotic in *Salmonella*, via the efflux pumps AcrAB, AcrEF, MdsAB and MdtAB. Using parameter fitting techniques on experimental data, we are able to establish the behaviour of multiple *Salmonella* strains, which enables us to produce efflux profiles for each individual efflux pump system. In our final model, by using insights from our asymptotic analysis we produce a multiscale model, combining our ODE and PDE models. This model implements a feedback mechanism between the intracellular antibiotic concentration and components of the GRN, enabling us to model the behaviour of the bacteria in response to antibiotic. By performing parameter sensitivity analysis, we are then able to look into various different methods to inhibit efflux pumps, preventing expulsion of antibiotic to counter MDR.

ACKNOWLEDGEMENTS

Firstly, I would like to thank my University of Birmingham supervisor Dr Sara Jabbari. Your support and guidance throughout my research have gone beyond all measure and I have the utmost admiration and respect for you. I would also like to thank my University of Nottingham supervisor Professor John King. I am so appreciative to have had the opportunity to work with someone so incredibly knowledgeable. I am very grateful to the collaboration of the University of Birmingham and the University of Nottingham to provide me with a joint scholarship and thank EPSRC for funding my research. I would like to thank my experimental collaborators, of special note Dr Jessica Blair, it has been an absolute pleasure working with you. I would like to thank all of my friends, many from the University of Birmingham Swimming Club, for supporting me through this journey. Finally, I would like to thank my parents Sharon and Lawrence, sister Sophie and partner Joel. I am sure you will all be ecstatic that I am one step closer to getting a "job"!!

CONTENTS

LIST OF FIGURES

LIST OF TABLES

LIST OF ABBREVIATIONS

AMR Antimicrobial resistance

AUC Area under curve

DNA Deoxyribonucleic acid

EPI Efflux pump inhibitor

FTCS Forward time centered space

GRN Gene regulatory network

H-NS Histone-like nucleoid-structuring protein

MDR Multiple drug resistance

mRNA Messenger ribonucleic acid

ODE Ordinary differential equation

PDE Partial differential equation

QSS Quasi steady state

RND Resistance nodulation division

TA Transcriptional Activator

CHAPTER 1

INTRODUCTION

1.1 Antibiotic resistance

Antibiotics are a type of drug that are used to treat bacterial infections, by interfering with the growth or an essential mechanism for survival of the bacteria. These essential mechanisms can include maintaining the structure of the cell envelope, protein production and DNA replication [86]. The World Health Organisation (WHO) has declared antibiotic resistance a crisis that must be dealt with the utmost urgency. Antibiotic resistance is reaching alarming levels, with treatment options for various infections becoming ineffective [64, 65]. The use of antibiotics has been prevalent since the discovery of penicillin by Alexander Fleming in the early twentieth century [23]. However, the widespread use of antibiotics has exerted selection pressures on bacteria, causing mutant strains that are antibiotic resistant. There are currently 17 classes of antibiotics, but for each of these a mechanism for resistance has emerged [23]. Whilst the development of new antibiotics is a possibility for treating these resistant bacteria, the discovery of new antibiotics has massively slowed within the twenty first century, with the possibility of a post antibiotic era in the coming years [2]. Thus, there is massive importance to look into alternative and novel treatments for fighting bacterial infections. In February 2017, the WHO released a priority list of antibiotic resistant bacteria in need of new antibiotics. *Enterobacteriaceae*, which is a large family of Gram-Negative bacteria including *Salmonella* and *Escherichia*

coli (*E. coli*) were marked in the first priority group, labelling their carbapenem and cephalosporin resistant strains as a critical priority for new antibiotics to be sought. *Salmonella* resistant to fluoroquinolone was marked as a high priority in the second group [100].

1.2 Gram-Negative bacteria including *Salmonella*

Gram-negative bacteria are a group of bacteria that are defined by the Gram staining method of differentiating bacteria. The Gram staining method determines whether a bacteria is Gram-positive or Gram-negative by detecting peptidoglycan in the bacteria's cell wall. Gram-negative bacteria's cell walls are much thinner meaning they contain much less peptidoglycan [7]. This is not the only difference, as Gram-positive and Gram-negative bacteria vary in many of their structures between the plasma membrane and the capsule as shown in Figure 1.1. The main noticeable difference is the inclusion of the outer membrane in Gram-negative bacteria.

Salmonella is a genus of rod shaped pathogenic bacteria that is Gram-negative. There are two species in this genus, *Salmonella enterica* and *Salmonella bongori* [1]. This type of bacteria is one of the main causes of intestinal infections from food, most commonly from poultry products. In most cases of infection, antibiotics are not needed, however for *Salmonella typhi* which causes Typhoid fever, antibiotics are necessary [80]. *Salmonella typhi* can transmit from human to human by the fecal to oral route, and hence bad sanitation is a leading cause of transmission [81]. *Salmonella typhi* not only infects the intestines, but has developed to grow in tissues of other organs. Due to overuse of many different types of antibiotics, multi drug resistant (MDR) strains have developed, most prominently in South Asia and Africa. Large mortality rates are highly prominent in developing countries in these regions, due to poor sanitation and the high prevelance of immunodeficiency diseases [80].

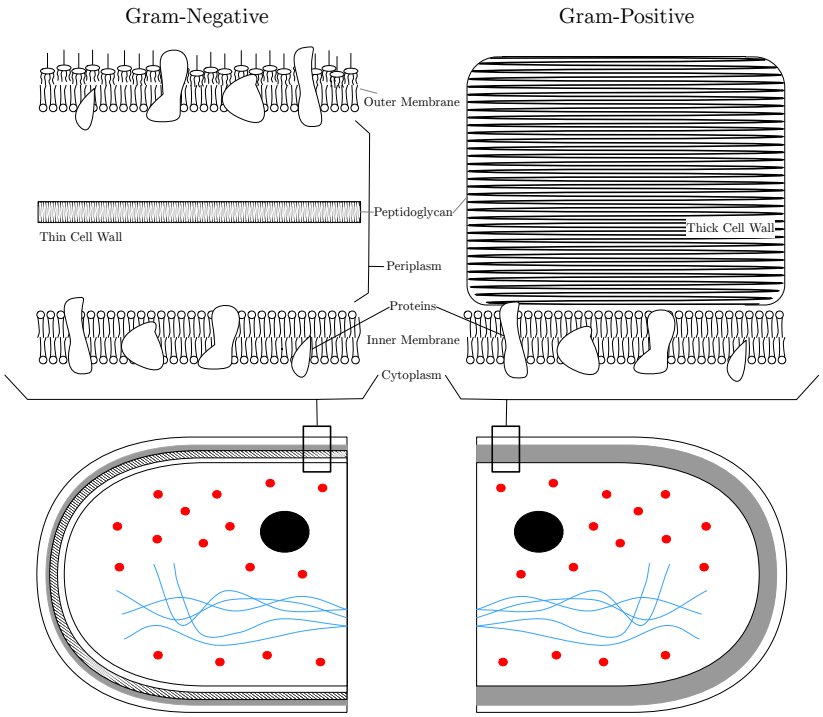

Figure 1.1: The differences in structure between Gram-negative and Gram-positive bacteria between the plasma membrane and the capsule. On the left we exhibit Gram-Negative with its double membrane structure, whereas on the right we have the Gram-Positive singular membrane structure. Recreated from [7].

1.3 Efflux pumps

Efflux pumps are an essential mechanism for bacteria that can account for antibiotic resistance. However, they are not exclusive to bacteria as they are found in all three domains of life: Eukaryota, Bacteria and Archaea [82]. Efflux pumps are transport proteins found on the cell membrane that expel substances into the external surrounding environment. If an efflux pump can expel an antibiotic so that its concentration within the cell is below a killing threshold the bacteria can become resistant to the antibiotic. Efflux pumps may be specific or they may pump various different substances and compounds. The latter is one main reason that many efflux pumps are linked with MDR. Many bacteria that confer MDR exhibit overexpression of efflux pumps. Overexpression is often caused by mutations of local gene repressors or changes to transcriptional regulators that affect the production of proteins associated with efflux [97].

Many efflux pumps that exhibit MDR are part of the resistance nodulation division (RND) family [32]. This family of efflux pumps found in Gram-Negative bacteria, span both membranes meaning they can expel a substance straight from the cell's cytoplasm to the outside of the cell. In particular, a member of this family is the AcrAB-TolC system which is common between both *E. coli* and *Salmonella*. We exhibit this system in Figure 1.2. The AcrAB-TolC system is tripartite, composed of the transporter protein AcrB, the accessory protein AcrA and an outer membrane protein TolC [26]. The efflux of drugs and other substances through the AcrAB-TolC system is induced by proton motive force. Proton motive force is caused by hydrogen ions moving from the bacteria's periplasm to the cytoplasm, this movement causes an electrochemical gradient that drives transport of the drug through the efflux pump, expelling the drug or other undesired substances from the bacteria [68]. From genomic analysis, it has been shown that *Salmonella* strains contain five RND efflux pump systems, AcrAB, AcrAD, AcrEF, MdsAB and MdtAB [41]. Of special note is the efflux pump system AcrEF-TolC, which is highly homologous to the AcrAB-TolC system. Various studies have shown that strains deficient in AcrAB commonly exhibit upregulation of AcrEF [12, 104].

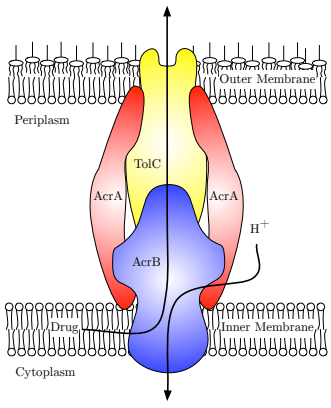

Figure 1.2: The AcrAB-TolC system common in *E. coli* and *Salmonella*, exhibiting proton motive force. Reproduced from [70].

1.4 Gene regulatory networks

In response to environmental stimuli, bacteria are able to control expression of certain genes via gene regulatory networks (GRNs) [34]. This includes altering the expression of efflux pump genes in response to a certain antibiotic. In order for a gene to be expressed, it must undergo the processes of transcription (messenger ribonucleic acid [mRNA] synthesis from a deoxyribonucleic acid [DNA] template) and translation (protein synthesis from mRNA by ribosomes). In bacteria, translation in most cases takes place as soon as transcription of mRNA occurs. This is due to the lack of a nuclear membrane and the high instability and degradation of mRNA molecules. In addition, one strand of mRNA can be translated multiple times before it is degraded. For these reasons it means that bacteria can quickly adapt to changes in environmental stimuli [71]. Certain genes however cannot simply be expressed as they may be part of a regulatory network, where they need to be activated by another gene's activator protein or repression by a repressor protein must be removed for transcription to occur. Repressor proteins bind to an operator site of a certain gene, which blocks transcription, whereas activator proteins bind to the promoter site of a certain gene, which promotes the initiation of gene transcription. We exhibit these processes in Figure 1.3. All bacteria have complicated networks of genes controlling gene expression, which enable the bacteria to change their behaviour depending on which genes are expressed [101].

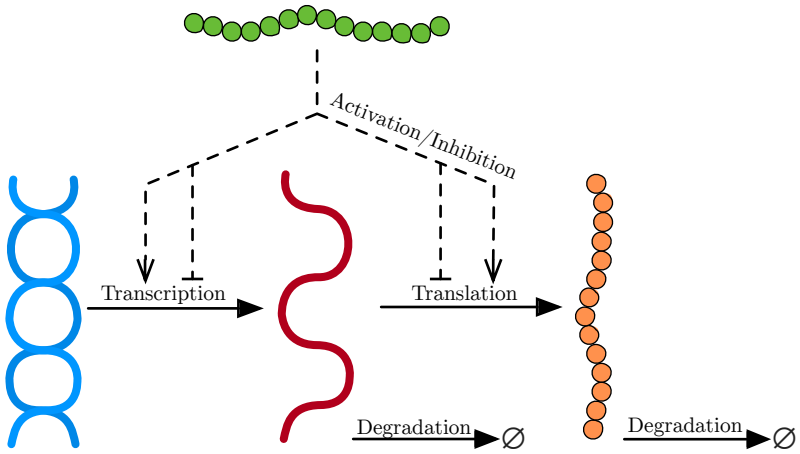

Figure 1.3: Processes of gene regulation and protein synthesis. We exhibit here a gene in the DNA (blue helix) being transcribed to mRNA (red strand), the mRNA is then translated to create a protein (orange chain). Here both mRNA and protein undergo degradation. We also exhibit by the dashed lines the potential activation or inhibition from a protein within the system upon the transcription and translation processes.

Gram-negative bacteria express a significant number of efflux pumps on their cell membranes. This causes them to be naturally resistant to various antibiotics. Overexpression of these efflux pumps often confers MDR. However, regulation of efflux pump expression is complicated and it is therefore important to understand the processes governing it. In Figure 1.4, we look at the regulation of AcrAB, these are two of the proteins that form the AcrAB-TolC system. In our first chapter, we use mathematical modelling techniques to represent this GRN with a system of ordinary differential equations (ODEs). This will further our understanding of the regulation of these genes and hence the AcrAB-TolC system, enabling us to look into inhibition to counter MDR.

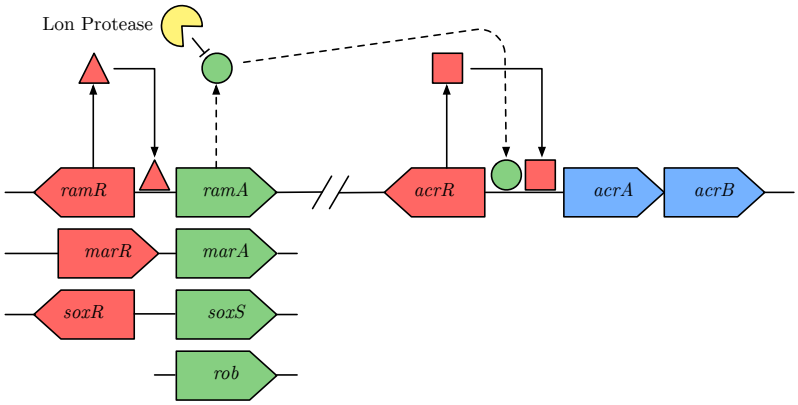

Figure 1.4: The GRN governing the expression of *acrAB* in Salmonella. We represent activator genes in green, repressor genes are coloured red and the efflux genes in blue. The shapes along the lines with text in italics are the genes themselves, with shapes under the top line being lesser underlying regulators. The other shapes without text are the proteins produced by the genes. If a protein is on the same line before a gene, it is either activating or repressing the gene's transcription. We note the yellow enzyme Lon Protease, this enzyme degrades RamA protein. Finally, the dashed lines show the processes that are limited when the triangular protein RamR is bound. This network has been reproduced from [10].

1.5 Antibiotic adjuvants

Due to the emergence of MDR pathogens and lack of new antibiotic discovery, novel treatment methods have been sought. Antibiotic adjuvants are molecular compounds that are used in combination with antibiotics, to enhance the activity of the antibiotic against the pathogen [102]. There are many forms of adjuvants that include anti-virulence and anti-resistance drugs. Anti-virulence drugs operate by disarming certain mechanisms of the bacteria, rather than killing them [6]. In addition, anti-virulence drugs do not directly prevent bacterial growth. These factors are thought to put less evolutionary pressure on the bacteria and thus have a low chance of contributing to the emergence of new resistant strains [72]. There are various different anti-virulence drug strategies, including reducing bacterial adhesion to host cells, inhibiting toxins, and disrupting gene regulation conferring determinants of virulence [73]. Virulence is defined as the ability of

a pathogen to infect and cause damage to its host [16]. There are many determinants of virulence in bacteria including: quantity of bacteria, entry route to the host, virulence factors (gene products that enhance virulence potential) and host defence mechanisms [67]. Notably, it has been shown that AcrB defective mutant *Salmonella* showed reduced virulence as a result of the lack of efflux pump activity [95]. For a comprehensive study linking various efflux pumps and virulence see [3, 68].

Anti-resistance drugs are also used to enhance the activity of an antibiotic against the pathogen, however, they operate by targeting the pathogen's mechanisms of resistance [102]. Examples of anti-resistance drugs include β-lactamase inhibitors, drugs that affect membrane permeability and efflux pump inhibitors (EPIs) [53]. Notably, EPIs inhibit the action of efflux pumps, they can target efflux pumps directly (efflux inhibitors), or can be used indirectly to target gene expression (efflux modulators) [35]. Their main purpose is to increase the intracellular concentration of antibiotic, such that the bacteria is unable to survive [84]. The development of novel EPIs is considered a promising strategy with the ability to make a bacterium more sensitive to antibiotics and reverse MDR [87], particularly the development of EPIs to treat Gram-negative infections [13].

1.6 Previous mathematical models of efflux pumps and gene regulatory networks

Firstly, it must be noted that there are no known mathematical models that consider wider GRNs that control efflux pump expression. Current models only consider the efflux pump gene with a maximum of two regulatory genes. Thus, in this section we will look to models of GRNs that control expression of different mechanisms, as well as looking into models of efflux pump function. We begin by discussing general efflux pump models, moving onto larger scale models that include efflux and finally, discussing various different methods of modelling GRNs.

Michelson and Slate [57] present a model of the p-glycoprotein pump, associated with

MDR in cancer patients. This pump is energy dependent, meaning it relies on the process of dephosphorylation of adenosine triphosphate (ATP) to adenosine diphosphate (ADP) to function. This is different to the proton motive force driving the AcrAB efflux pump. They formulate a combined partial differential equation (PDE) and ODE model for the concentration of drug within the system, relating it to the concentrations of ATP and ADP using Michaelis-Menten Kinetics. They run simulations of the model, with different initial conditions of ATP and ADP. Their findings show that the pump is much more effective at pumping the drug out of the system from an initial state that contains ATP and ADP than an initial state of ATP depletion. However, they also showed that depleting a cell completely of ATP would not be enough to be an effective method for blocking drug efflux.

Michelson and Slate [58] also expand on their previous model of the p-glycoprotein pump, in this case including the presence of an inhibitor that prevents the drug from binding to the pump. Three situations, competitive inhibition (multiple molecules are able to bind to the efflux pump binding site), non-competitive inhibition (only the inhibitor is able to bind to the efflux pump binding site) with inhibitor efflux and non-competitive inhibition without inhibitor efflux were modelled. In the competitive case it was shown that by decreasing the size of the dissociation constant of this inhibitor binding to the pump, there was increased overall drug exposure. There were larger differences in drug exposure with a larger initial concentration of drug, with little differences in drug exposure for smaller initial concentration of drug. For the non-competitive cases, firstly with efflux of the inhibitor, the drug exposure is slightly more than the competitive case. For the case with no efflux of the inhibitor the drug exposure is further increased for inhibitors that have a high affinity to bind. Thus, this shows that a non competitive inhibitor that cannot be effluxed itself would be the most effective treatment method for blocking drug efflux.

Yi *et al.* [103] develop a single cell model that encompasses drug delivery and efflux simultaneously to look into MDR of cancer cells. In this model a cell is impaled with

a diffusional microburet which can deliver a drug into the cell by controlled diffusion. Efflux is modelled through active transport using Michaelis-Menten equations, building from Michelson and Slate [57, 58]. Efflux is also modelled through passive transport, simulations of this model show that passive transport can have a large effect on the cells' intracellular concentration of the drug at steady state.

Perez *et al.* [66] use an ODE model efflux in *E. coli* by TetB, a member of the major facilitator superfamily of efflux pumps. This type of efflux pump spans one membrane and is responsible for resistance to tetracycline antibiotics. In this model, we have diffusion through two membranes of the antibiotic into the cytoplasm, with efflux from the cytoplasm to the periplasm. By finding the steady states of the model, binding constants for the pump were found as well constants relating to the pump efficiency.

Diao *et al.* [25] produce an ODE model of a yeast efflux pump found in *Saccharomyces cerevisiae*. They model the negative feedback loop of a regulator, efflux pump and inducer (a substrate of the efflux pump). Charlebois *et al.* [18] also produce an ODE model of the efflux pump in *Saccharomyces cerevisiae*. Here a more complex model is produced, consisting of three genes that are part of a drug resistance network involved with efflux pump expression.

Nagano and Nikaido [60] present an ODE model of antibiotic efflux in *E. coli*, from the AcrAB-TolC efflux pump system. This model includes the enzyme β-lactamase located in the periplasm, which breaks down the antibiotic. They assume efflux transport undergoes Michaelis-Menten kinetics, with diffusion into the cell given by Fick's law. By using parameter fitting techniques, they are able to find various binding coefficients for various antibiotics with AcrB. Lim and Nikaido [51] continue this work, extending the study to find binding coefficients for various different penicillins.

The AcrAB-TolC efflux pump system and genes that govern the system's expression have been the topic of other mathematical models. Rossi *et al.* [79] experimentally manipulated the degradation of MarA (a known activator of *acrAB* expression) in *E. coli*, to see the resulting effects on downstream genes. A generic mathematical model was formu-

lated consisting of three genes: an activator and two downstream genes. This ODE model showed that activators with a long half life had an advantage by increasing the coordination of the downstream genes. The analytical results were replicated experimentally with *marA* and downstream genes *inaA* and *acrAB*.

Langevin and Dunlop [48] exhibit an ODE population model of *E. coli* undergoing stress from two diverse chemicals, the antibiotic chloramphenicol and the jet biofuel precursor pinene. Both of these chemicals can be effluxed by the AcrAB-TolC system. Experiments are taken on different strains of bacteria (wild-type and *acrAB* knock outs), introducing chemical stressors as step functions at different rates. The experiments look into the cost of efflux pumps, and show that at certain low levels of antibiotic the bacteria without efflux pumps is more likely to survive. The mathematical model created has two species competing against each other consuming a substrate. By parameter fitting techniques the model is able to show agreement to the experimental data. Conclusions were then able to be made to find the conditions where expressing the AcrAB-TolC efflux pump would be more beneficial. It is shown that the benefit of efflux pumps is highly dependent on the rate of stress introduction.

None of the above models, take into account the wider system of genes governing the regulation of the proteins that make up these efflux pumps. Thus, they do not have the potential to ascertain the complete switch dynamics of the cell in response to the antibiotic. To fully model this behaviour, we would need to include the wider GRN governing these pumps. We now look into various methods of modelling GRNs. We include a selection to showcase a variety of techniques but our review is by no means exhaustive. See also [44], for example, for a more complete overview and review of some of these methods.

Glass and Kauffman [36] were the first to present a Boolean model of GRNs. Here, they propose modelling genes as switches of expression where they can be active (1) or inactive (0). All genes in the network undergo regulation functions which change their value depending on whether a gene is an activator or repressor and the current state of

expression. Although this type of modelling is limited due to the level of the detail, it was found useful for proving the existence of steady states. If a steady state is found for a discrete model, then a corresponding steady state should be approached by a homologous continuous model. In addition, oscillatory behaviour in a homologous continuous model, will have a closed cyclic path in the discrete model.

Shmulevich *et al.* [85] expand on the work of Glauss and Kauffman to produce a probabilistic Boolean model of GRNs. In this model, genes can have multiple regulation functions, with the choice of regulation function being probabilistic. This type of model has been proven useful when not enough is biologically known about the GRN and how certain genes interact with each other. One of the downsides of these Boolean models is that experiments on GRNs do not produce discrete valued measurements and do not have discontinuous jumps between states at certain time steps. Thus discrete models lose detail and accuracy when data is discretised to fit them. An alternative is to model these networks continuously.

Weaver *et al.* [96] present a linear model of GRNs. In this model, each gene's expression level depends on a summation of the levels of its regulators. In this model this summation is scaled in order to limit the concentration to be between 0 and 1. This squashed function is then multiplied by maximal expression levels from data to provide a realistic fit. One of the issues of this model is the low level of detail and little information that can be extracted from it, including analysis of the processes in the network.

Nachman *et al.* [59] increase the level of detail in their model of GRNs by delving deeper into transcription, including transcriptional factors that can bind to the promoter site of a gene. They start by modelling one singular gene, deriving equations that model the effects of having one or multiple regulators. They construct a differential equation governing mRNA concentration, including transcriptional and degradation terms. By applying and fitting this to data, they show that transcriptional rate parameters can be gained. One issue with this model is transcriptional factors are likely to be proteins also in the system, and equations governing their behaviour have not been defined.

Li *et al.* [50] model the GRN governing the cell division cycle in the bacterium *Caulobacter crescentus*. This bacterium can be divided into types, a mobile swarmer cell or an immobile stalked cell. The stalked cell is able to replicate the division cycle and it is on this that the model focuses. The process is centred around the expression of three proteins CtrA, GcrA, and DnaA. To model this process, a system of 16 ODEs were derived to model a simplified version of the cycle. These ODEs contain 44 parameters, however in this model the size of these were determined by trial and error. Despite this, the model has proved to be very accurate, matching up to experimental data of the wild-type strain and 16 mutant strains.

Tian and Burrage [89] develop a general technique for producing stochastic models of GRNs. This technique involves introducing Poisson random variables into ODE models. Their method showed that they are able to include stochastic elements into robust ODE models, without deriving equations from first principles. They applied this technique to various existing ODE models of GRNs and ran simulations of the models. From this, they were able to demonstrate the effect of noise on these networks.

Davidson *et al.* [22] model the regulatory network governing extra-cellular protease (exoprotease) production in the Gram-positive bacterium *Bacillus subtilis*. They investigate the role of the two regulators DegU and Spo0A, however the model itself is centered on the auto-regulation of DegU, which includes phosphorylation processes. An ODE system consisting of 6 differential equations and 14 parameters is produced to determine the dynamics of exoprotease expression. Steady state analysis was implemented on the model which revealed three different zones of responses from the system.

Finally, Jabbari *et al.* [42] produce a model of the *agr* operon that governs quorum sensing in *Staphylococcus aureus*. They produce a system of 12 ODEs with 17 parameters. However as data upon these parameter sizes were not yet available at the time, they nondimensionalised their model. This took away the dependence on specific parameter values, resulting in 11 parameter groupings where approximate sizes could be given dependent on the size of certain reactions in relation to each other. They perform a series

of time dependent asymptotic analyses upon the nondimensionalised system. Doing this provided insights to the behaviour of the system on various different timescales. This enabled them to produce a step by step breakdown of the dominant processes that govern the GRN that control the quorum sensing process.

These GRN models are only a small sample of possible GRN models in bacteria, there are even more GRN models that we have not considered in Eukaryota. Here, we have covered a large range of mathematical models from literature and we will use ideas from these papers in our methodology. In Chapter 2, we formulate a mathematical model of the GRN governing the AcrAB-TolC system, using ODEs to provide a sufficient amount of detail and insights into the network. We could have instead opted for a PDE model, however as there is little data on the spatial dynamics of the gene products within the GRN, we use ODEs to reduce the number of unknown parameters in the model. We ran simulations of the ODE model, using parameters from the biology of the network and consultations with the Piddock Laboratory (University Of Birmingham) to produce realistic results. In Chapter 3, we nondimensionalise our model to reduce the dependency on specific parameter values. We are then able to complete a set of time dependent asymptotic analyses to simplify our model into a step by step breakdown of the GRN. In chapters 4 and 5, we formulate a PDE model to model the effect of various efflux pumps in *Salmonella* (including AcrAB-TolC) on expelling a substrate ethidium bromide. We implement parameter fitting techniques on the model using experimental data in order to ascertain efflux profiles of each efflux pump system. Finally in Chapter 6, we produce a multiscale model by combining our GRN and substrate models. This enables us to make predictions on manipulating the GRN, displaying the resulting effects on the spatial dynamics of the substrate. By producing this final model, we are able to target and highlight areas of the GRN that the intracellular substrate concentration is most sensitive. We are then able to hypothesise new treatment methods that keep the intracellular concentration above a killing threshold to combat MDR.

CHAPTER 2

MODEL FORMULATION

2.1 Model schematic & reactions

To formulate our model of the GRN governing *acrAB* expression, we must first delve into the processes governing the GRN. We exhibit a detailed schematic of the GRN in Figure 2.1. We note that in this network, we also include the homologue of *acrAB*, *acrEF*. Experimentally, this efflux pump gene expression has been shown to become more prevalent when there is less production of AcrAB or the *acrAB* genes are deleted, inactivated, or when the protein is produced, but non-functional [95].

We will consider two strains of *Salmonella Typhimurium* (S. Typhimurium) in this model. Firstly a wild-type strain, this is a typical strain of S. Typhimurium that we would expect to encounter in a natural population. Secondly, we consider the strain S. Typhimurium (SL1344), this strain displays MDR as a consequence of a *ramR::aph* mutation in the *ramR* gene, resulting in production of a non-functional RamR protein [77]. For simplicity, we will refer to this strain as the RamR variant or mutant strain. To consider as much of the GRN around efflux as possible, we assume that the strains are subject to stress, e.g. antibiotic or oxidative stress. We detail the steps involved in *acrAB* and *acrEF* regulation shown in Figure 2.1 below, exhibiting the processes involved in the wild-type case before explaining the differences in processes of the MDR-associated RamR variant [10, 98].

Wild-type strain:

- Expression of *ramR* results in the production of the RamR protein, which can bind to the *ramA* operator site, the network's main transcriptional activator [77].
- Expression of the *ramA* gene is repressed by bound RamR protein, less RamA is produced compared to the variant below.
- We assume that the cell is stressed and thus secondary transcriptional activators *soxS*, *marA* and *rob* are expressed constitutively resulting in production of SoxS, MarA and Rob protein [63].
- We assume that the gene *envR/acrS* (which for simplicity, we will refer to as *envR* for the rest of this thesis) is expressed constitutively, resulting in production of EnvR.
- EnvR protein binds to the operator region of *acrEF* inhibiting its expression [38].
- The *acrR* gene is expressed resulting in production of AcrR protein which shares the same site as EnvR protein in binding to the inhibitor region of the *acrAB* gene, both inhibiting its expression [52].
- RamA protein shares the same site with SoxS to bind to the *acrAB* promoter region, activating its expression.
- Post transcription of *acrAB*, the RNA protein CsrA acts as a stabiliser of translation of *acrAB* mRNA into AcrAB protein [75].

RamR variant (mutant) strain:

- Mutations in *ramR* cause a conformational change to RamR protein meaning it is unable to bind to the *ramA* operator site. Therefore inhibition of *ramA* expression is lost in this mutant.
- The *ramA* gene is expressed more highly than in the wild-type resulting in higher concentrations of RamA protein.
- RamA is regulated post-translationally through degradation by the enzyme Lon Protease [76].
- RamA binds to its own promoter site and activates its transcription.
- A high concentration of RamA protein (compared to the wild-type) shares the same site with SoxS to bind to the *acrAB* promoter region, activating its expression.
- Transcription of the *acrAB* gene occurs at a high rate compared to the wild-type case, due to the high RamA protein concentration compared to the wild-type.

We note that whilst the processes upon *ramA* regulation are only listed in the RamR mutant strain, they may still occur in the wild-type strain. However we expect the effect from these processes to be minimal due to the lower concentration of RamA in the strain. Furthermore, mathematically each of the secondary transcriptional activators (secondary TAs) *soxS*, *marA* and *rob* would have equivalent representations. Thus for simplicity, we group these activators together and refer to them as *soxS* or secondary TAs for the remainder of the work.

It has been shown experimentally that with decreased *acrAB* expression, greater expression of the homologue efflux pump gene *acrEF* occurs (which operates similarly to *acrAB*) [12]. This may be through known mechanisms in the network, for example through the repressor *envR*. However, since these mechanisms have not yet been fully elucidated, we capture this behaviour in the model by a simple direct link between AcrAB

levels and expression of *acrEF*, noting that this is an area where extra detail can be incorporated in future work. Finally, we note that RamA protein is believed to be capable of binding at the *acrR* gene, however no effect on *acrR* transcription has yet been demonstrated. We nevertheless include this in our model under the assumption that RamA inhibits *acrR* transcription to explore the potential effects upon efflux pump expression.

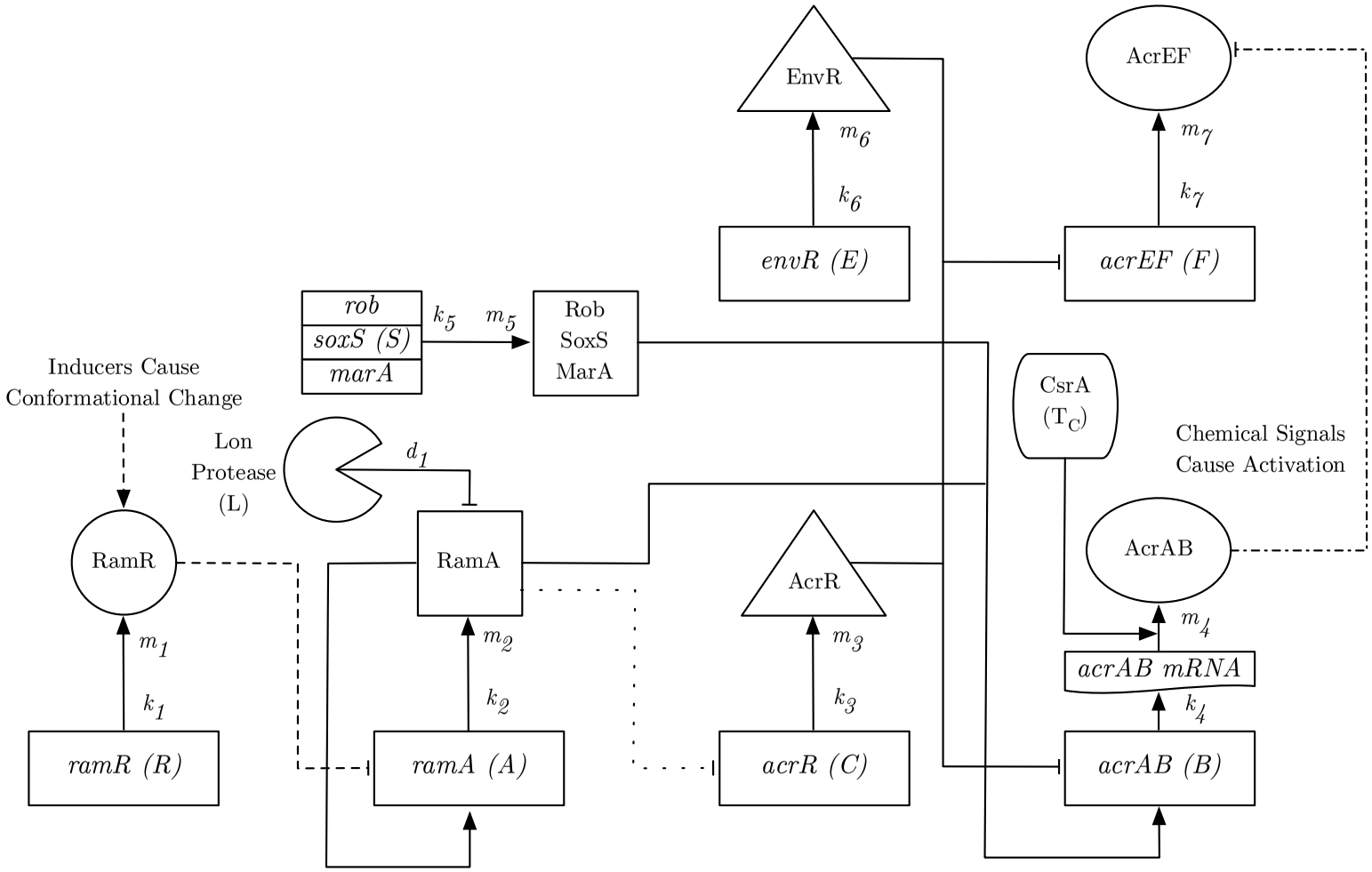

Figure 2.1: A schematic diagram exhibiting the regulation of *acrAB* expression. In the rectangles we have the genes involved in this network, the shapes first linked out from these genes are the proteins produced by them (we omit most mRNA stages for simplicity). The two shapes not linked to the genes are the enzyme Lon Protease and the translation activator CsrA. Solid lines capture the behaviour of both the wild-type and RamR variant, while the dashed line is relevant only for the wild-type. The dotted line shows potential inhibition of *acrR* expression whilst finally the dashed dotted line represents our link between expression of both efflux pumps. Here the rates k_i for $i = 1, ..., 7$ are rates of transcription, whereas m_i are rates of translation.

2.2 Modelling activation and inhibition of gene transcription

In order to model our biological system mathematically, we must look into the kinetics of how activator proteins activate or repressor proteins inhibit a gene by binding to an operator site. In the following subsections, we model all situations that are present in our GRN.

2.2.1 One protein and one binding site

The first situation that we model is one protein and one binding site that the protein can reversibly bind to. We show this in Figure 2.2. In order to model this and further situations, we look into the proportion of time that a protein is bound or unbound to a binding site. Our aim is to obtain equations for these time proportions in terms of the protein concentrations and their binding and unbinding rates. To be able to do this, we introduce the following notation:

Φ: Proportion of time that the binding site is empty (all proteins are unbound),

Φ_X: Proportion of time that the binding site is occupied by protein X (protein X is bound).

We could also alternatively consider these proportions of time as probabilities. Since we are dealing with proportions, it follows that all proportions of time must add up to unity

$$\Phi_X(t) + \Phi(t) = 1. \tag{2.1}$$

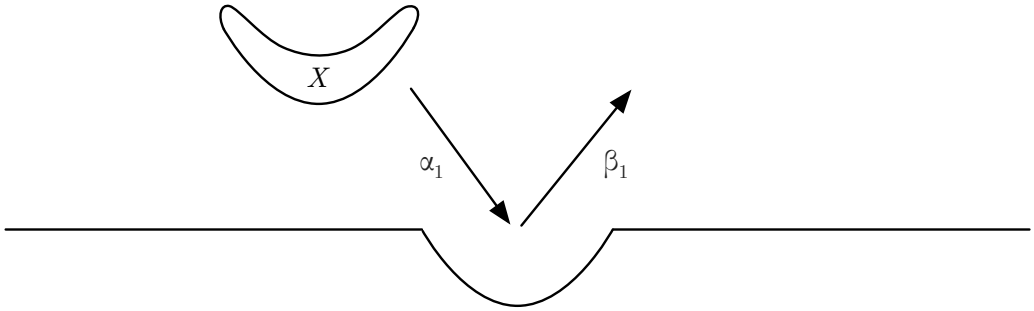

Figure 2.2: One protein with one binding site. Here we exhibit the protein X binding to the site at rate α_1 and unbinding from the site at rate β_1.

Using the law of mass action which states that "The rate of a chemical reaction is directly proportional to the product of the concentration or active masses of the reacting substances" [83], we can construct ordinary differential equations (ODEs) for each proportion of time. In this case we are interested in the change of the proportion of time that protein X is bound:

$$\frac{d\Phi_X}{dt} = \alpha_1 X\Phi - \beta_1\Phi_X. \tag{2.2}$$

By assuming that there is enough protein in the system that all proportions of time are at quasi-steady state (QSS) [14], and by using equation (2.1) we obtain

$$0 = \alpha_1 X(1-\Phi_X) - \beta_1\Phi_X. \tag{2.3}$$

Rearranging, we can find our desired equation for Φ_X and also for Φ by using (2.1)

$$\Phi_X = \frac{X}{X+K_X}, \qquad\qquad \Phi = \frac{K_X}{X+K_X}, \tag{2.4}$$

where $K_X = \dfrac{\beta_1}{\alpha_1}$ is the dissociation constant for protein X. We comment that the behaviour of these constants are such that as $K_X \to 0$, $\Phi \to 0$ and $\Phi_X \to 1$, conversely as $K_X \to \infty$, $\Phi \to 1$ and $\Phi_X \to 0$. We must now apply these equations to an ODE for the rate of change of an arbitrary gene's mRNA, which we denote as G_m. Note that mRNA will undergo degradation at some rate, which we include in the following equations as δ_m.

Protein X is an activator protein binding to a promoter site.

In this case, we assume that there is a high level of transcription of the gene's mRNA when the activator protein is bound. It is often the case that there is a small basal transcription rate (k_b) regardless of whether protein X is bound. It is particularly useful to include this basal rate when a gene is self activating: by including this rate we reduce the risk that the gene quickly reaches steady state at zero. Thus the equation we achieve is as follows

$$\frac{dG_m}{dt} = k_1\Phi_X + k_b - \delta_m G_m, \tag{2.5}$$

$$= k_1\frac{X}{X + K_X} + k_b - \delta_m G_m. \tag{2.6}$$

Protein X is a repressor protein binding to an operator site.

In this case, we assume that if a repressor is bound, there will be no transcription. This means we must look at when there is no protein bound for transcription to occur. Thus in this case the equation we achieve is as follows

$$\frac{dG_m}{dt} = k_1\Phi - \delta_m G_m, \tag{2.7}$$

$$= k_1\frac{K_X}{X + K_X} - \delta_m G_m. \tag{2.8}$$

2.2.2 Two proteins with one binding site each

In this situation, we model two proteins with one binding site each that the protein can reversibly bind to, we show this in Figure 2.3. As there is an extra protein and an extra binding site in this case, we must introduce some new notation:

Φ_X**:** Proportion of time that the binding site is occupied by protein X (protein X is bound),

Φ_Y**:** Proportion of time that the binding site is occupied by protein Y (protein Y is bound),

Φ_{XY}**:** Proportion of time that the binding sites are both occupied (proteins X and Y are bound).

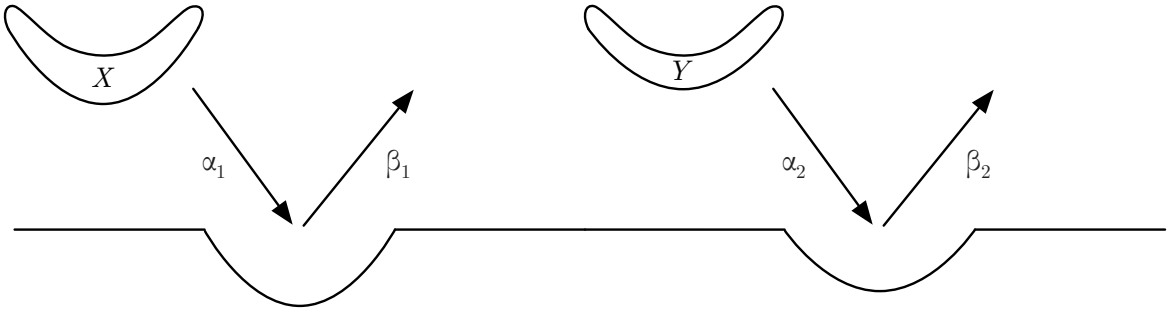

Figure 2.3: Two proteins with two distinct binding sites. Here we exhibit the protein X binding to a site at rate α_1 and unbinding from the site at rate β_1. We also have a different shape protein Y binding to a different binding site at rate α_2 and unbinding from the site at rate β_2.

Using the the law of mass action, we can find equations for the rate of change of all proportions of time that proteins are bound to any of the binding sites

$$\frac{d\Phi_X}{dt} = \alpha_1 X\Phi + \beta_2\Phi_{XY} - \beta_1\Phi_X - \alpha_2 Y\Phi_X, \tag{2.9}$$

$$\frac{d\Phi_Y}{dt} = \alpha_2 Y\Phi + \beta_1\Phi_{XY} - \beta_2\Phi_Y - \alpha_1 X\Phi_Y, \tag{2.10}$$

$$\frac{d\Phi_{XY}}{dt} = \alpha_1 X\Phi_Y + \alpha_2 Y\Phi_X - \beta_1\Phi_{XY} - \beta_2\Phi_{XY}. \tag{2.11}$$

By assuming that there is enough protein in the system that all proportions of time are at quasi-steady state ($\frac{d\Phi_X}{dt} = 0$, $\frac{d\Phi_Y}{dt} = 0$ and $\frac{d\Phi_{XY}}{dt} = 0$), and by using a similar equation to (2.1) that all time proportions must add to unity, we obtain:

$$0 = \alpha_1 X(1 - \Phi_X - \Phi_Y - \Phi_{XY}) + \beta_2\Phi_{XY} - \beta_1\Phi_X - \alpha_2 Y\Phi_X, \tag{2.12}$$

$$0 = \alpha_2 Y(1 - \Phi_X - \Phi_Y - \Phi_{XY}) + \beta_1\Phi_{XY} - \beta_2\Phi_Y - \alpha_1 X\Phi_Y, \tag{2.13}$$

$$0 = \alpha_1 X\Phi_Y + \alpha_2 Y\Phi_X - \beta_1\Phi_{XY} - \beta_2\Phi_{XY}. \tag{2.14}$$

We now have a simultaneous system of equations which we can solve for to achieve

$$\Phi = \frac{K_X K_Y}{K_X K_Y + K_Y X + K_X Y + XY}, \tag{2.15}$$

$$\Phi_X = \frac{K_Y X}{K_X K_Y + K_Y X + K_X Y + XY}, \tag{2.16}$$

$$\Phi_Y = \frac{K_X Y}{K_X K_Y + K_Y X + K_X Y + XY}, \tag{2.17}$$

$$\Phi_{XY} = \frac{XY}{K_X K_Y + K_Y X + K_X Y + XY}, \tag{2.18}$$

where $K_X = \frac{\beta_1}{\alpha_1}$ and $K_Y = \frac{\beta_2}{\alpha_2}$ are dissociation constants for proteins X and Y respectively.

Protein X is an activator protein binding to a promoter site and protein Y is a repressor protein binding to an operator site.

In this case, we assume that there is no transcription if the repressor protein Y is bound to the site. We also have a higher transcription rate when only protein X is bound. In addition we could include a basal transcription rate that is active regardless of whether protein X is bound. Thus the equation we achieve is as follows

$$\frac{dG_m}{dt} = k_1 \Phi_X + k_b - \delta_m G_m, \tag{2.19}$$

$$= k_1 \frac{K_Y X}{(K_X + X)(K_Y + Y)} + G_C - \delta_m G_m. \tag{2.20}$$

2.2.3 Two sets of two proteins binding to one binding site for each set

In this situation, we model two sets each consisting of two proteins and one binding site. Within each set, the proteins share the same binding site that they can reversibly bind. We display this in Figure 2.4. As there are two extra proteins in this case, we introduce some new notation:

Φ_W**:** Proportion of time that the binding site is occupied by protein W (protein W is bound),

Φ_X: Proportion of time that the binding site is occupied by protein X (protein X is bound),

Φ_Y: Proportion of time that the binding site is occupied by protein Y (protein Y is bound),

Φ_Z: Proportion of time that the binding site is occupied by protein Z (protein Z is bound),

Φ_{WY}: Proportion of time that the binding sites are both occupied (proteins W and Y are bound),

Φ_{WZ}: Proportion of time that the binding sites are both occupied (proteins W and Z are bound).

Φ_{XY}: Proportion of time that the binding sites are both occupied (proteins X and Y are bound).

Φ_{XZ}: Proportion of time that the binding sites are both occupied (proteins X and Z are bound).

Using the the law of mass action, we can find equations for the rate of change of all proportions of time that proteins are bound to any of the binding sites

$$\frac{d\Phi_W}{dt} = \alpha_1 W\Phi + \beta_3\Phi_{WY} + \beta_4\Phi_{WZ} - \beta_1\Phi_W - \alpha_3 Y\Phi_W - \alpha_4 Z\Phi_W, \tag{2.21}$$

$$\frac{d\Phi_X}{dt} = \alpha_2 X\Phi + \beta_3\Phi_{XY} + \beta_4\Phi_{WZ} - \beta_2\Phi_X - \alpha_3 Y\Phi_X - \alpha_4 Z\Phi_X, \tag{2.22}$$

$$\frac{d\Phi_Y}{dt} = \alpha_1 Y\Phi + \beta_1\Phi_{WY} + \beta_2\Phi_{XY} - \beta_3\Phi_Y - \alpha_1 W\Phi_Y - \alpha_2 X\Phi_Y, \tag{2.23}$$

$$\frac{d\Phi_Z}{dt} = \alpha_2 Z\Phi + \beta_1\Phi_{WZ} + \beta_2\Phi_{XZ} - \beta_4\Phi_Z - \alpha_1 W\Phi_Z - \alpha_2 X\Phi_Z, \tag{2.24}$$

$$\frac{d\Phi_{WY}}{dt} = \alpha_1 W\Phi_Y + \alpha_3 Y\Phi_W - \beta_1\Phi_{WY} - \beta_3\Phi_{WY}, \tag{2.25}$$

$$\frac{d\Phi_{WZ}}{dt} = \alpha_1 W\Phi_Z + \alpha_4 Z\Phi_W - \beta_1\Phi_{WZ} - \beta_4\Phi_{WZ}, \tag{2.26}$$

$$\frac{d\Phi_{XY}}{dt} = \alpha_2 X\Phi_Y + \alpha_3 Y\Phi_X - \beta_2\Phi_{XY} - \beta_3\Phi_{XY}, \tag{2.27}$$

$$\frac{d\Phi_{XZ}}{dt} = \alpha_2 X\Phi_Z + \alpha_4 Z\Phi_X - \beta_2\Phi_{XZ} - \beta_4\Phi_{XZ}. \tag{2.28}$$

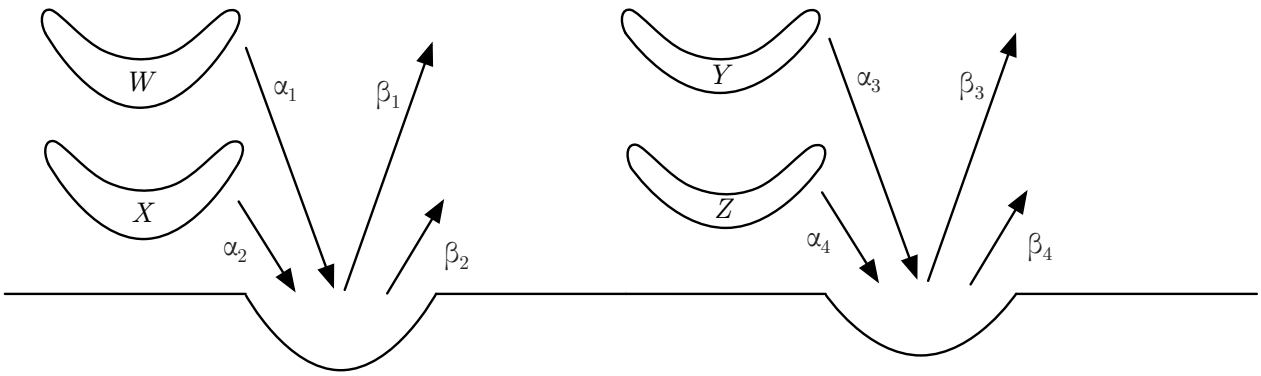

Figure 2.4: Two sets of two proteins binding to one binding site for each set. Here we exhibit the protein W binding to a site at rate α_1 and unbinding from the site at rate β_1. This protein is in competition to bind for the same site as protein X which binds to the site at rate α_2 and unbinds from the site at rate β_2. We also have a different shape protein Y binding to a different binding site at rate α_3 and unbinding from the site at rate β_3. This protein is in competition to bind for the same site as protein Z which binds to the site at rate α_4 and unbinds from the site at rate β_4.

By assuming that there is enough protein in the system that all proportions of time are at quasi-steady state and by using a similar equation to (2.1) (now $\Phi = 1 - \Phi_W - \Phi_X - \Phi_Y - \Phi_Z - \Phi_{WY} - \Phi_{WZ} - \Phi_{XY} - \Phi_{XZ}$) we have a simultaneous system of equations that can be solved to obtain

$$\Phi = \frac{K_W K_X K_Y K_Z}{(K_X W + K_W X + K_X K_W)(Y K_Z + Z K_Y + K_Z K_Y)}, \tag{2.29}$$

$$\Phi_W = \frac{W K_X K_Y K_Z}{(K_X W + K_W X + K_X K_W)(Y K_Z + Z K_Y + K_Z K_Y)}, \tag{2.30}$$

$$\Phi_X = \frac{X K_W K_Y K_Z}{(K_X W + K_W X + K_X K_W)(Y K_Z + Z K_Y + K_Z K_Y)}, \tag{2.31}$$

$$\Phi_Y = \frac{Y K_X K_W K_Z}{(K_X W + K_W X + K_X K_W)(Y K_Z + Z K_Y + K_Z K_Y)}, \tag{2.32}$$

$$\Phi_Z = \frac{Z K_X K_W K_Y}{(K_X W + K_W X + K_X K_W)(Y K_Z + Z K_Y + K_Z K_Y)}, \tag{2.33}$$

$$\Phi_{WY} = \frac{WY K_X K_Z}{(K_X W + K_W X + K_X K_W)(Y K_Z + Z K_Y + K_Z K_Y)}, \tag{2.34}$$

$$\Phi_{WZ} = \frac{WZK_XK_Y}{(K_XW + K_WX + K_XK_W)(YK_Z + ZK_Y + K_ZK_Y)}, \tag{2.35}$$

$$\Phi_{XY} = \frac{XYK_WK_Z}{(K_XW + K_WX + K_XK_W)(YK_Z + ZK_Y + K_ZK_Y)}, \tag{2.36}$$

$$\Phi_{XZ} = \frac{XZK_WK_Y}{(K_XW + K_WX + K_XK_W)(YK_Z + ZK_Y + K_ZK_Y)}, \tag{2.37}$$

where $K_W = \frac{\beta_1}{\alpha_1}$, $K_X = \frac{\beta_2}{\alpha_2}$, $K_Y = \frac{\beta_3}{\alpha_3}$ and $K_Z = \frac{\beta_4}{\alpha_4}$ are dissociation constants for proteins W, X, Y and Z respectively.

Protein W and X are activator proteins binding to a promoter site and proteins Y and Z are repressor proteins binding to an operator site.

In this case, we assume that there is no transcription if either of the repressor proteins Y or Z is bound to the site. We also have a higher transcription rate when either W or X is bound. In addition we could include a basal transcription rate that is active regardless of whether protein W or X is bound. Thus the equation we achieve is as follows

$$\frac{dG_m}{dt} = k_1(\Phi_W + \Phi_X) + k_b - \delta_m G_m, \tag{2.38}$$

$$= k_1 \frac{K_YK_Z(XK_W + WK_X)}{(K_XW + K_WX + K_XK_W)(YK_Z + ZK_Y + K_ZK_Y)} + k_b - \delta_m G_m. \tag{2.39}$$

2.3 Ordinary differential equation models

In this section we produce a model of the GRN in Figure 2.1. In section 1.6 we compared various different modelling techniques for GRNs. We choose to use a system of ordinary differential equations (ODEs) to provide a sufficient level of detail and insights into the network. For GRNs, the principal processes affecting mRNA and proteins are transcription, translation and degradation. We exhibit this in equation (2.40). Here G_m and G represent mRNA and protein respectively associated with an arbitrary gene. We note that transcription and translation terms may be affected by the concentrations of other proteins, with translation terms always being reliant on the same gene's mRNA [24].

$$\underbrace{\frac{dG_m}{dt}}_{\substack{\text{Rate of change}\\ \text{of mRNA}\\ \text{concentration}}} = \underbrace{k}_{\text{Transcription}} - \underbrace{\delta G_m}_{\text{Degradation}} . \qquad \underbrace{\frac{dG}{dt}}_{\substack{\text{Rate of change}\\ \text{of protein}\\ \text{concentration}}} = \underbrace{mG_m}_{\text{Translation}} - \underbrace{\delta G}_{\text{Degradation}} . \tag{2.40}$$

The equations for the GRN model are as follows:

$$\frac{dR_m}{dt} = k_1 - \delta_m R_m, \tag{2.41}$$

$$\frac{dA_m}{dt} = k_2 \frac{K_R A}{(A + K_{A_1})(R + K_R)} + k_2' - \delta_m A_m, \tag{2.42}$$

$$\frac{dC_m}{dt} = k_3 \frac{K_{A_2}}{A + K_{A_2}} - \delta_m C_m, \tag{2.43}$$

$$\frac{dB_m}{dt} = k_4 \frac{K_{E_2} K_C (K_S A + K_{A_1} S)}{(K_C E + K_{E_2} K_C + K_{E_2} C)(K_{A_1} K_S + K_{A_1} S + K_S A)} - \delta_m B_m, \tag{2.44}$$

$$\frac{dS_m}{dt} = k_5 - \delta_m S_m, \tag{2.45}$$

$$\frac{dE_m}{dt} = k_6 - \delta_m E_m, \tag{2.46}$$

$$\frac{dF_m}{dt} = k_7 \frac{K_{E_1}}{K_{E_1} + E} - \delta_m F_m, \tag{2.47}$$

$$\frac{dR}{dt} = \mu(m_1 R_m - \delta_p R), \tag{2.48}$$

$$\frac{dA}{dt} = m_2 A_m - \delta_p A - d_1 L A, \tag{2.49}$$

$$\frac{dC}{dt} = m_3 C_m - \delta_p C, \tag{2.50}$$

$$\frac{dB}{dt} = \frac{T_C}{T_C + K_{T_C}} m_4 B_m - \delta_p B, \tag{2.51}$$

$$\frac{dS}{dt} = m_5 S_m - \delta_p S, \tag{2.52}$$

$$\frac{dE}{dt} = m_6 E_m - \delta_p E, \tag{2.53}$$

$$\frac{dF}{dt} = m_7 \frac{K_B F_m}{B + K_B} - \delta_p F. \tag{2.54}$$

We note that all of the differential equations have linear terms regarding degradation, which we group as the same rate for mRNAs and proteins respectively (δ_m and δ_p). RamA, SoxS and MarA are the only proteins that we know of that undergo enzyme degradation in the GRN, all degraded by Lon Protease. The secondary TA Rob however does not experience this degradation [30]. Since we have grouped together SoxS, MarA and Rob together, we opt not to include this additional enzyme degradation, instead only including enzyme degradation for RamA in equation (2.49).

In the case of transcription and translation, the terms are not so straightforward. In equation (2.42), we exhibit the activation of *ramA* transcription by its own protein, whilst being repressed by RamR protein at the *ramA* operator site, derived from (2.20). In equation (2.43), we have the potential repression of transcription of *acrR* mRNA transcription by RamR protein, derived from (2.8). In equation (2.44), we see the effect of the activator protein RamA and the underlying activators Rob, SoxS and MarA (which we group as one variable S) binding to a promoter site to activate transcription of *acrAB* mRNA, whilst the proteins AcrR and EnvR bind to an operator site to repress *acrAB* mRNA transcription, derived from (2.20). In equation (2.47), we have the repression of transcription of *acrEF* mRNA transcription by EnvR protein, derived from (2.8). In equation (2.51), we see the activation effect from CsrA in the translation terms for AcrAB, derived from (2.6). Furthermore in equation (2.54), by including AcrAB in the translation term, we are able to include the link between AcrAB and AcrEF concentrations, derived from (2.8). Finally, we incorporate the RamR variant via a mutant coefficient (μ) in equation (2.48). By setting this value to zero, we can replicate the case of mutated RamR as this

results in no translation of *ramR* mRNA. Conversely by setting this value to one we have full translation, but also degradation of RamR protein.

We denote all of the variables and parameters used to run simulations of our GRN model in Table 2.1 and Table 2.2. We note that our model does not contain a signal (such as an antibiotic or toxic substrate) that activates the GRN. Instead, we have chosen our model to focus solely on the GRN to first greater understand the processes within the network, leaving the introduction of an explicit signal for later work in Chapters 4-6. For our simulations, we have chosen initial conditions of all mRNA and protein variables to be very small (0.01nM), such that the system starts from a down-regulated state. Here, we are making the assumption that there is at least a low concentration of mRNA and protein of all genes at all times in the system. Whilst a down-regulated initial state may not be the case in all scenarios (genes also involved with other cellular processes may already be up regulated), we have chosen these initial conditions in order to show a greater potential of processes within the GRN. We exhibit the notation for these conditions in (2.55) for the mRNA and protein of an arbitrary gene:

$$G_m(0) = G_{m0}, \qquad G(0) = G_0. \tag{2.55}$$

2.3.1 Simulations

By using estimated parameter values shown in Table 2.2, we produce numerical simulations of the GRN model for both wild-type and RamR mutant strains using ode45 in MATLAB, exhibited in Figure 2.5. Where possible we have been guided by data in the experimental literature for parameter values. Remaining parameters are chosen to give biologically plausible results. We note that between strains, we have identical simulations of both mRNA and protein for *soxS* and *envR*. This is expected as the expression of these genes are constitutive in both strains. We see sizeable differences in the concentrations of RamR (Figure 2.5(h)) between both strains due to the mutation of this protein in the RamR mutant strain. We see resulting increased expression of *ramA*, producing larger

Variables	Description	Units
R_m	Concentration of *ramR* mRNA	nM
R	Concentration of RamR	nM
A_m	Concentration of *ramA* mRNA	nM
A	Concentration of RamA	nM
C_m	Concentration of *acrR* mRNA	nM
C	Concentration of AcrR	nM
B_m	Concentration of *acrAB* mRNA	nM
B	Concentration of AcrAB	nM
S_m	Concentration of *rob*, *soxS* and *marA* mRNA	nM
S	Concentration of Rob, SoxS and MarA	nM
E_m	Concentration of *envR* mRNA	nM
E	Concentration of EnvR	nM
F_m	Concentration of *acrEF* mRNA	nM
F	Concentration of AcrEF	nM

Table 2.1: Variables used in our GRN model along with their respective units.

Parameter	Description	Estimate	Units	Reference
k_1	Transcription Rate of *ramR* mRNA	30	nM min^{-1}	
m_1	Translation Rate of RamR	1	min^{-1}	[93]
k_2	Transcription Rate of *ramA* mRNA	1	nM min^{-1}	
m_2	Translation Rate of RamA	1	min^{-1}	[93]
k_3	Transcription Rate of *acrR* mRNA	10	nM min^{-1}	
m_3	Translation Rate of AcrR	1	min^{-1}	[93]
k_4	Transcription Rate of *acrAB* mRNA	1	nM min^{-1}	
m_4	Translation Rate of AcrAB	1	min^{-1}	[93]
k_5	Transcription Rate of *rob*, *soxS* and *marA* mRNA	1	nM min^{-1}	
m_5	Translation Rate of Rob, SoxS and MarA	1	min^{-1}	[93]
k_6	Transcription Rate of *envR* mRNA	10	nM min^{-1}	
m_6	Translation Rate of EnvR	1	min^{-1}	[93]
k_7	Transcription Rate of *acrEF* mRNA	0.1	nM min^{-1}	
m_7	Translation Rate of AcrEF	1	min^{-1}	[93]
k_2'	Lower Transcriptional Rate of RamA	0.01	nM min^{-1}	
δ_m	Degradation Rate of mRNA	1	min^{-1}	[74]
δ_p	Degradation Rate of proteins	0.02	min^{-1}	[40]
$d_1 L$	Degradation caused by Lon Protease	0.37	min^{-1}	[76]
K_R	Dissociation Constant of RamR	65.8	nM	[8]
K_{A_1}	Dissociation Constant of RamA with *ramA* and *acrAB*	2	nM	
K_{A_2}	Dissociation Constant of RamA with *acrR*	2	nM	
K_C	Dissociation Constant of AcrR	20.2	nM	[8]
K_{E_1}	Dissociation Constant of EnvR with *acrEF*	20.2	nM	
K_{E_2}	Dissociation Constant of EnvR with *acrAB*	20.2	nM	
K_S	Dissociation Constant of *rob*, *soxS* and *marA*	200	nM	
K_{T_C}	Dissociation Constant of CsrA	0.02	nM	
K_B	Chemical Signals Constant of AcrAB	1	nM	
T_C	Concentration of CsrA	1	nM	
μ	Mutation Coefficient	0 or 1	N/A	

Table 2.2: A table of parameters used in our GRN model and their estimated values. Those with estimates gained from references are noted in the reference column. The remainder have been chosen through investigation and discussion with the Piddock laboratory (University Of Birmingham) to give biologically plausible results.

concentrations of mRNA and protein (Figures 2.5(b) and (i)) in the RamR mutant strain. Since we have a higher concentration of RamA in the RamR variant, we see inhibition of *acrR* expression, resulting in lower concentrations of mRNA and protein (Figures 2.5(c) and (j)) in the RamR variant strain. We see a resulting larger concentration of *acrAB* mRNA and protein (Figures 2.5(d) and (k)) in the RamR variant strain with a lower concentration of the homologue efflux pump protein AcrEF (Figure 2.5(n)) compared to the wild-type. These simulations clearly exhibit the potential of the RamR mutant strain to display MDR, with the steady state concentration for AcrAB (Figure 2.5(k)), the main efflux pump in the GRN, being over four times larger in the mutant strain than the wild-type. This results in the combined efflux of both AcrAB and AcrEF concentrations being much larger in the RamR mutant strain, even with the increased concentration of AcrEF in the wild-type strain.

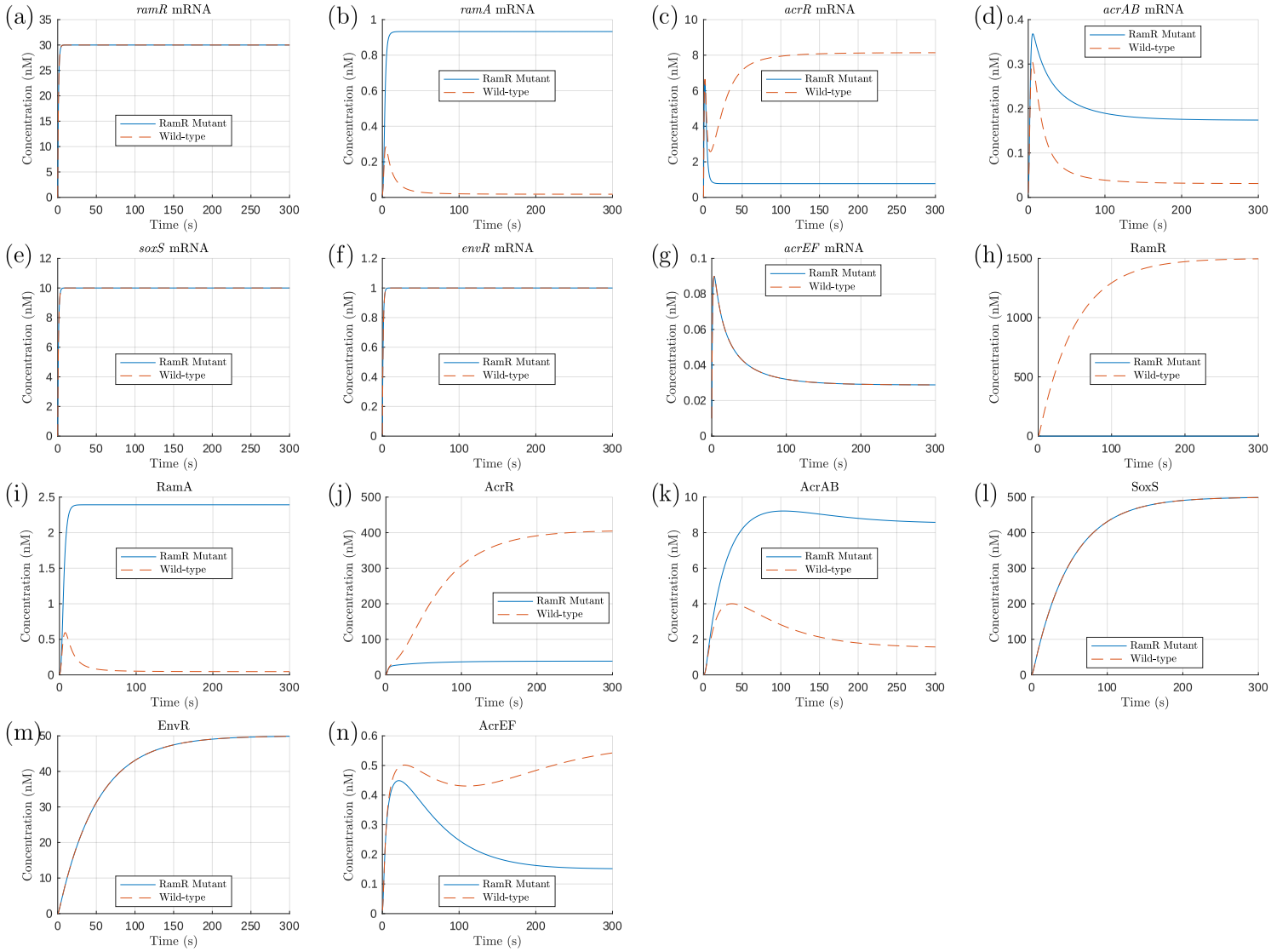

Figure 2.5: Plots of numerical simulations of the GRN model (2.41)-(2.54) using ode45 in MATLAB. For each mRNA and protein, we exhibit the differences between the wild-type and the RamR mutant strains. We limit the time of the simulations to 300 minutes.

2.4 Discussion

In this chapter, we have formulated an ODE model of the GRN. We started our model formulation by listing the processes governing the expression of the efflux pump genes *acrAB* and *acrEF*. In order to assist detailing the processes within the network, we introduced two strains of *Salmonella*, namely a wild-type and a RamR variant. By first listing the processes of the wild-type strain, we displayed the differences in the RamR variant, highlighting areas of the network that causes the RamR variant strain to confer MDR.

We have then exhibited our method for deriving our ODEs. By modelling the proportion of time that a protein is bound to a gene binding site, we can formulate equations of gene expression based on whether the binding protein is an activator or repressor. We have detailed our derivations for all binding processes that feature within the GRN. By using these derivations, we have then detailed our ODE model for the GRN, consisting of fourteen differential equations and twenty nine parameters.

Finally, we have run numerical simulations of our model, using a combination of parameter values from data as well as estimates drawn from investigation and discussion with the Piddock laboratory (University Of Birmingham). This has enabled us to view the behaviour of the network and an overview of how the genes within the network interact, starting from basal initial conditions of concentration.

This model does however have limitations. One downside of the model is that it is too complex to yield analytically tractable solutions. In addition, results are dependent on parameter values, making it difficult to draw strong conclusions from the model. In the next chapter, we will use asymptotic techniques to break the full solution into separate timescales. This analysis should reduce the dependency on precise parameter values and give us analytical solutions for various different timescales, enabling us to draw stronger conclusions from further analysis into the network.

CHAPTER 3

TIME-DEPENDENT ASYMPTOTIC ANALYSIS

3.1 Motivation

As shown in the previous chapter, the GRN we are modelling is complex and thus in order to look into effective inhibition techniques to combat efflux pump expression, the processes within the system need to be fully analysed. With our previous model, we do not have a full set of analytically solvable solutions or steady states. Thus we are limited in the analysis we can conduct on the model without using numerical simulations.

In this chapter, we will use a series of asymptotic analyses to approximate these steady state values and gain analytical solutions for the variables on intermediate timescales. This analysis will enable us to show the effect upon variables at different timescales by varying parameters in the GRN. We will conduct two full asymptotic analyses for the wild-type and mutant strains, separate analysis for each strain is needed as the steps involved to reach each timescale will differ. By discovering the behaviour on each timescale, we are able to see the dominant processes involved in the GRN between both strains. By deriving the asymptotically approximated steady states, we will also be able to compare different strategies to inhibit efflux expression that will be most effective for individual strains.

3.2 Nondimensional model

We nondimensionalise the model from Chapter 2 by using the following variable scalings:

$$\begin{aligned}
R_m &= \frac{k_1}{\delta_m} R_m^*, & S_m &= \frac{k_5}{\delta_m} S_m^*, & A &= K_A A^*, & E &= K_{E_2} E^*, \\
A_m &= \frac{k_2}{\delta_m} A_m^*, & E_m &= \frac{k_6}{\delta_m} E_m^*, & C &= K_C C^*, & F &= \frac{k_7 m_7}{\delta_m^2} F^*, \\
C_m &= \frac{k_3}{\delta_m} C_m^*, & F_m &= \frac{k_7}{\delta_m} F_m^*, & B &= \frac{k_4}{\delta_m} B^*, & t &= \frac{1}{\delta_m} T, \\
B_m &= \frac{k_4}{\delta_m} B_m^*, & R &= K_R R^*, & S &= K_S S^*.
\end{aligned} \tag{3.1}$$

here the asterisks denote nondimensional variables. We have chosen these scalings in order to simplify our system of equations and create nondimensional parameters over which we have insight into their relative sizes. We note that these have the added effect of simplifying the somewhat complex transcription and translation terms. Substituting these scalings (dropping the asterisks) reduces the model to the following system of equations,

$$\frac{dR_m}{dT} = 1 - R_m, \tag{3.2}$$

$$\frac{dA_m}{dT} = \frac{A}{(A+1)(R+1)} + \alpha - A_m, \tag{3.3}$$

$$\frac{dC_m}{dT} = \frac{\lambda}{A+\lambda} - C_m, \tag{3.4}$$

$$\frac{dB_m}{dT} = \frac{A+S}{(1+S+A)(1+E+C)} - B_m, \tag{3.5}$$

$$\frac{dS_m}{dT} = 1 - S_m, \tag{3.6}$$

$$\frac{dE_m}{dT} = 1 - E_m, \tag{3.7}$$

$$\frac{dF_m}{dT} = \frac{\eta}{\eta+E} - F_m \tag{3.8}$$

$$\frac{dR}{dT} = \mu\rho\, R_m - \mu\Delta\, R \tag{3.9}$$

$$\frac{dA}{dT} = \theta\, A_m - \Delta\, A - \upsilon\, A, \tag{3.10}$$

$$\frac{dC}{dT} = \gamma\, C_m - \Delta\, C, \tag{3.11}$$

$$\frac{dB}{dT} = \beta\, B_m - \Delta\, B, \tag{3.12}$$

$$\frac{dS}{dT} = \sigma\, S_m - \Delta\, S, \tag{3.13}$$

$$\frac{dE}{dT} = \xi\, E_m - \Delta\, E, \tag{3.14}$$

$$\frac{dF}{dT} = \frac{F_m}{\omega B + 1} - \Delta\, F. \tag{3.15}$$

The nondimensionalised parameter groupings that have emerged are as follows

$$\Delta = \frac{\delta_p}{\delta_m}, \qquad \theta = \frac{k_2 m_2}{\delta_m^2 K_A}, \qquad \sigma = \frac{k_5 m_5}{\delta_m^2 K_S}, \qquad \beta = \frac{m_4 T_C}{\delta_m (T_C + K_{T_C})},$$
$$\rho = \frac{k_1 m_1}{\delta_m^2 K_R}, \qquad \upsilon = \frac{d_1 L}{\delta_m}, \qquad \eta = \frac{K_{E_1}}{K_{E_2}}, \qquad \xi = \frac{k_6 m_6}{\delta_m^2 K_{E_2}},$$
$$\alpha = \frac{k_2'}{k_2}, \qquad \gamma = \frac{k_3 m_3}{\delta_m^2 K_C}, \qquad \lambda = \frac{K_{A_1}}{K_{A_2}}, \qquad \omega = \frac{k_4}{\delta_m K_B}.$$

We assume that all mRNAs and proteins are initially present at a low concentration to monitor how the system upregulates. Thus, we choose low value generic dimensionless initial conditions as follows

$$R_m(0) = A_m(0) = C_m(0) = B_m(0) = S_m(0) = E_m(0) = F_m(0) = 0.01,$$
$$R(0) = A(0) = C(0) = B(0) = S(0) = E(0) = F(0) = 0.01. \tag{3.16}$$

From here on we will refer to these initial conditions with the following notation (similar to the previous chapter). For any gene G, we will refer to the mRNA initial condition as G_{m0} and the protein initial condition as G_0.

3.3 Parameter grouping sizes

By using information about the size of certain parameters compared to others, we can estimate relative parameter sizes within the nondimensional groupings. We start by choosing a parameter grouping that we know to be small (and denote it having the value ϵ):

$$\alpha = \frac{k_2'}{k_2} = \epsilon. \tag{3.17}$$

The grouping α is the ratio of a low basal rate of transcription to the higher transcription rate of *ramA* mRNA. We now assign the remaining parameter groupings an order of

magnitude relative to (3.17). We assume that

$$\Delta = \frac{\delta_p}{\delta_m} = O(\epsilon), \tag{3.18}$$

i.e. mRNA degradation occurs at a much faster rate than the degradation of proteins. We do not know all of the exact degradation rates for the mRNAs and proteins of genes within the network. However, in a similar Gram-negative bacteria *E. coli* it was observed that 80% of 4,288 mRNAs had half-lives between 3 and 8 minutes [9], whereas for proteins, the vast majority have half-lives of between 5 and 20 hours [54]. In *Salmonella*, on a study of 870 proteins, the calculated median half-life was 99.30 minutes [94]. For individual proteins within the GRN, it has been shown for RamA in a mutant strain with no Lon Protease, there was very little observable degradation within 10 minutes, indicating that the protein is highly stable [76]. Finally, in *E. coli* it has also been observed that AcrA and AcrB lasted for approximately six days [17].

At $O(\epsilon^{\frac{1}{2}})$ we have the following parameter groupings

$$\upsilon = \frac{d_1 L}{\delta_m}, \qquad \sigma = \frac{k_5 m_5}{\delta_m^2 K_S}, \qquad \xi = \frac{k_6 m_6}{\delta_m^2 K_{E_2}}. \tag{3.19}$$

Having $\upsilon = O(\epsilon^{\frac{1}{2}})$ follows from (3.18), as the rate of degradation of RamA by Lon protease ($d_1 L$) is larger than the natural rate of protein degradation (δ_p) [76]. Thus, we expect this grouping to be a larger order of magnitude than Δ. For σ, as the secondary TAs are all underlying activators, we expect that the dissociation constant is relatively large, (furthermore by setting this grouping to this size we obtain the most realistic behaviour). Finally, for ξ the transcription and translation rates for EnvR should be small as this is a repressor of the homologue efflux pump system AcrEF, and thus we expect this grouping to be the same size as σ which governs similar underlying genes.

Finally, we have the parameter groupings that we choose to be $O(1)$. Firstly,

$$\lambda = \frac{K_{A_1}}{K_{A_2}}, \qquad \eta = \frac{K_{E_1}}{K_{E_2}}, \qquad \omega = \frac{k_4}{\delta_m K_B}. \tag{3.20}$$

For λ, the dissociation constants that make up this grouping correspond to the same proteins, but binding to different binding sites. With no evidence to the contrary, we make the assumption that the constants are roughly equal. For η, there is contradictory evidence in the literature over whether EnvR preferentially binds *acrAB*, *acrEF* or both equally [38, 37]. As a result, we also assume these dissociation constants are roughly equal and explore variations to this choice in the parameter sensitivity section. As for ω, we know very little about the chemical signals that cause activation of AcrEF, and hence we keep this as $O(1)$ for simplicity. The rest of the $O(1)$ parameter groupings are as follows

$$\theta = \frac{k_2 m_2}{\delta_m^2 K_A}, \qquad \rho = \frac{k_1 m_1}{\delta_m^2 K_R}, \qquad \gamma = \frac{k_3 m_3}{\delta_m^2 K_C}, \qquad \beta = \frac{m_4 T_C}{\delta_m \left(T_C + K_{T_C}\right)}. \tag{3.21}$$

The groupings in (3.21) correspond to the expression of RamA, RamR, AcrR and AcrAB respectively. These four proteins constitute the primary TAs and the central pathway for the GRN, and thus it is not unreasonable to assume that expression of their genes is relatively high and the respective dissociation constants are likely to be smaller. It has also been shown experimentally in a wild-type *Salmonella* strain, that expression of *ramA* and *acrAB* was higher than *soxS, marA* and *acrEF* [99]. Therefore, we expect these groupings to be the largest in order. Testing more subtle differences in size did not bring significant variations to the behaviour of the model. In Table 3.1, we summarise all of the above parameter grouping sizes, chosen for definiteness. We could alternatively choose another size for the intermediate scaling between $O(\epsilon)$ and $O(1)$, however in the following analysis *soxS* (σ) and *envR* (ξ) translation appear together independently on the same timescale. Therefore, whilst the time scaling to reach this timescale may change, we do not expect change in the order of the following processes in the analysis. In addition, the remaining parameter refers to RamA degradation (υ) which will primarily affect the

steady states of variables, the dependence on this parameter scaling is therefore covered in the sensitivity analysis in Section 3.8. The parameters below are therefore scaled as follows

$$\begin{aligned}
\Delta &= \epsilon\Delta', & \theta &= \theta', & \sigma &= \epsilon^{\frac{1}{2}}\sigma', \\
\rho &= \rho', & \upsilon &= \epsilon^{\frac{1}{2}}\upsilon', & \eta &= \eta', \\
\alpha &= \epsilon\alpha', & \gamma &= \gamma', & \lambda &= \lambda', \\
\beta &= \beta', & \xi &= \epsilon^{1/2}\xi', & \omega &= \omega',
\end{aligned} \tag{3.22}$$

where the parameters with primes are taken to be $O(1)$. By substituting these into our nondimensional model and dropping primes, we obtain the following system of equations, where all parameters are $O(1)$:

$$\frac{dR_m}{dT} = 1 - R_m, \tag{3.23}$$

$$\frac{dA_m}{dT} = \frac{A}{(A+1)(R+1)} + \epsilon\alpha - A_m, \tag{3.24}$$

$$\frac{dC_m}{dT} = \frac{\lambda}{A+\lambda} - C_m, \tag{3.25}$$

$$\frac{dB_m}{dT} = \frac{A+S}{(1+S+A)(1+E+C)} - B_m, \tag{3.26}$$

$$\frac{dS_m}{dT} = 1 - S_m, \tag{3.27}$$

$$\frac{dE_m}{dT} = 1 - E_m, \tag{3.28}$$

$$\frac{dF_m}{dT} = \frac{\eta}{\eta+E} - F_m, \tag{3.29}$$

$$\frac{dR}{dT} = \mu\rho\, R_m - \mu\epsilon\Delta\, R, \tag{3.30}$$

$$\frac{dA}{dT} = \theta\, A_m - \epsilon\Delta\, A - \epsilon^{1/2}\upsilon\, A, \tag{3.31}$$

$$\frac{dC}{dT} = \gamma\, C_m - \epsilon\Delta\, C, \tag{3.32}$$

$$\frac{dB}{dT} = \beta\, B_m - \epsilon\Delta\, B, \tag{3.33}$$

$$\frac{dS}{dT} = \epsilon^{1/2}\sigma\, S_m - \epsilon\Delta\, S, \tag{3.34}$$

$$\frac{dE}{dT} = \epsilon^{1/2}\xi\, E_m - \epsilon\Delta\, E, \tag{3.35}$$

$$\frac{dF}{dT} = \frac{F_m}{\omega B + 1} - \epsilon\Delta\, F, \tag{3.36}$$

with initial conditions (3.16). We will follow some numerical simulations of the model with a time-dependent asymptotic analysis in order to extract the dominant behaviours over time. Throughout our simulations, we take $\epsilon = 0.01$, and all other parameters as unity.

Nondimensional Parameter	Size
α, δ	$O(\epsilon)$
υ, σ, ξ	$O(\epsilon^{\frac{1}{2}})$
ρ, θ, γ, β, η, λ, ω	$O(1)$

Table 3.1: Nondimensionalised parameter groupings and their orders of magnitude.

3.4 Numerical simulation

We exhibit a numerical simulation of (3.16) and (3.23)-(3.36) in Figure 3.1 showing both the wild-type and RamR variant cases. For both cases, we see the rapid production of mRNA (a)-(g), reaching steady state very quickly for most variables. The efflux genes' mRNAs (d) and (g) reach steady state more slowly due to being affected by regulatory protein concentrations. All proteins (h)-(n) reach steady state at a later timescale than the mRNA. These simulations enable us to exhibit the differences between mutant and wild-type strains, caused by the mutation to RamR protein (h). This mutation causes overexpression of *ramA* mRNA (b) and protein (i) which in turn causes lower concentrations of *acrR* mRNA (c) and protein (j). These concentrations combined result in a higher concentration of *acrAB* mRNA (d) and protein (k), which itself causes lower expression of AcrEF (n). We note that the steady state concentration of AcrAB is significantly higher in the mutant case than the wild-type case. Unless otherwise stated, these are the numerical simulations that we match our asymptotic approximations to in the following sections.

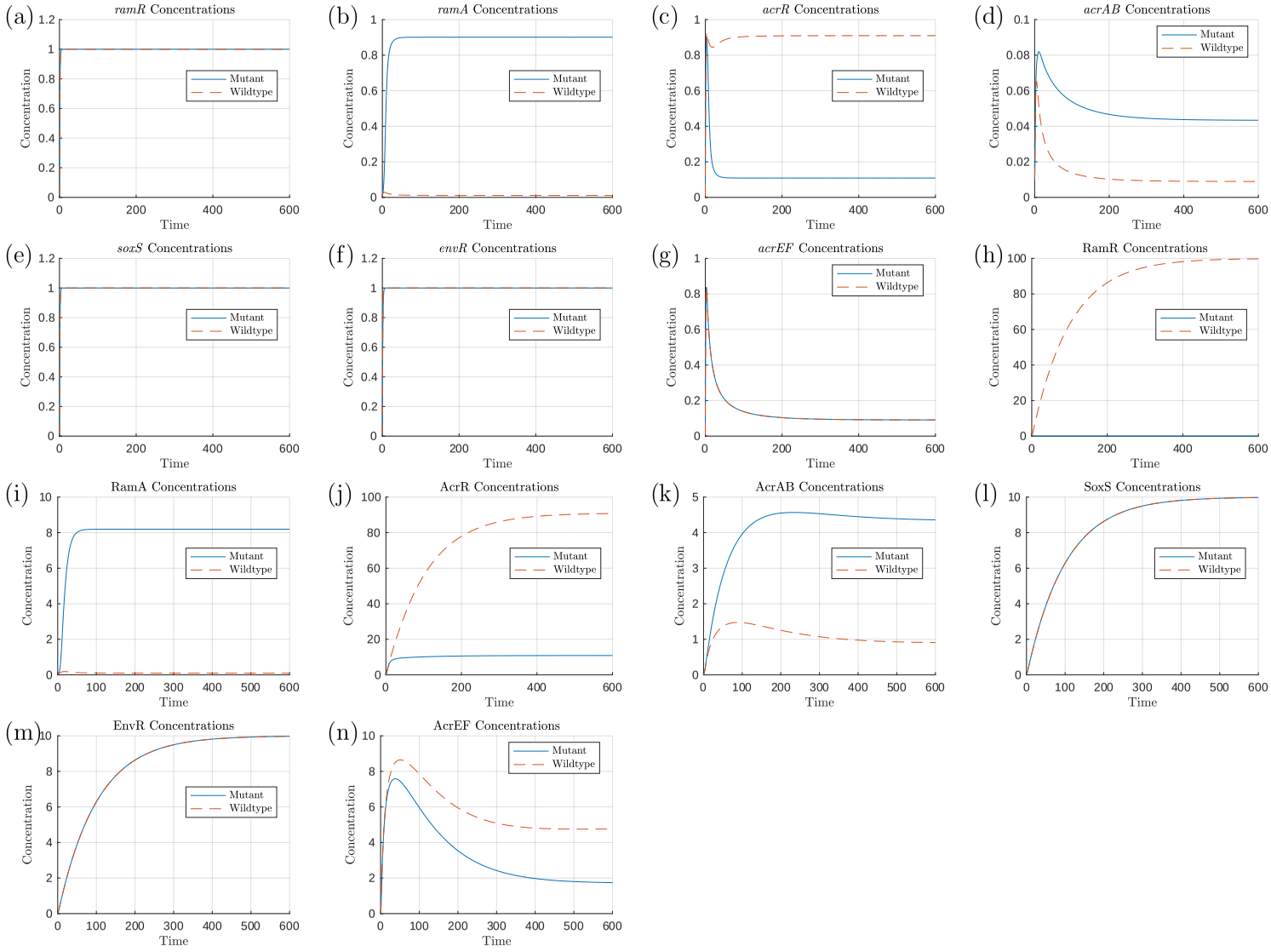

Figure 3.1: Numerical simulations of the nondimensionalised model (3.23)-(3.36) with down regulated initial conditions of 0.01 for all variables. We use $\epsilon = 0.01$ and all other parameters are unity.

3.5 Asymptotic analysis for $\epsilon \to 0$

We now exploit asymptotic analyses to break down the full solution into smaller timescales to investigate how the system evolves over time. For an insight into various asymptotic techniques and methods, some used in this section, see [45]. Variable scalings on each timescale are obtained by first finding the long-term behaviour of each variable on the previous timescale. Once this long-term or near blow up behaviour is found, we can identify the scalings based on how each variable behaves compared to our time variable T. For example if a nondimensionalised variable G behaves on the previous timescale as follows

$$G \sim T \text{ as } T \to \infty,$$

then to move to the next timescale we must scale G in the same way that we do for T. The scalings to reach each timescale mathematically appear in a set sequence, where new behaviour entering the leading order balance determines the scaling for T. These scalings could also be revealed by analysing the correction terms for the asymptotic approximations on each timescale. In Section 3.6.1, we exhibit both methods of revealing the scalings to reach the next timescale. Throughout the next sections, we will draw comparisons between the numerical solutions and asymptotic approximations. In all figures asymptotic approximations will be shown in circles, whereas the numerical simulations will be shown as solid lines. We take $\epsilon = 0.01$ unless otherwise stated.

3.6 Asymptotic analysis of the wild-type dynamics

We begin with the wild-type case where RamR protein is not mutated (i.e $\mu = 1$). We denote the variable scalings for each timescale in Table 3.2. Here the scalings are given in relation to the original nondimensionalised variables in (3.1).

Timescale	Variable														
	T	R_m	R	A_m	A	C_m	C	B_m	B	S_m	S	E_m	E	F_m	F
1	$\epsilon\hat{T}$	$\epsilon\hat{R}_m$	$\epsilon\hat{R}$	$\epsilon\hat{A}_m$	$\epsilon\hat{A}$	$\epsilon\hat{C}_m$	$\epsilon\hat{C}$	$\epsilon\hat{B}_m$	$\epsilon\hat{B}$	$\epsilon\hat{S}_m$	$\epsilon\hat{S}$	$\epsilon\hat{E}_m$	$\epsilon\hat{E}$	$\epsilon\hat{F}_m$	$\epsilon\hat{F}$
2	$\epsilon^{\frac{1}{2}}\tilde{T}$	$\epsilon^{\frac{1}{2}}\tilde{R}_m$	$\epsilon\hat{R}$	$\epsilon\hat{A}_m$	$\epsilon\hat{A}$	$\epsilon^{\frac{1}{2}}\tilde{C}_m$	$\epsilon\hat{C}$	$\epsilon\hat{B}_m$	$\epsilon\hat{B}$	$\epsilon^{\frac{1}{2}}\tilde{S}_m$	$\epsilon\hat{S}$	$\epsilon^{\frac{1}{2}}\tilde{E}_m$	$\epsilon\hat{E}$	$\epsilon^{\frac{1}{2}}\tilde{F}_m$	$\epsilon\hat{F}$
3	$\epsilon^{\frac{1}{4}}\bar{T}$	$\epsilon^{\frac{1}{4}}\bar{R}_m$	$\epsilon^{\frac{1}{2}}\bar{R}$	$\epsilon\hat{A}_m$	$\epsilon\hat{A}$	$\epsilon^{\frac{1}{4}}\bar{C}_m$	$\epsilon^{\frac{1}{2}}\bar{C}$	$\epsilon\hat{B}_m$	$\epsilon\hat{B}$	$\epsilon^{\frac{1}{4}}\bar{S}_m$	$\epsilon\hat{S}$	$\epsilon^{\frac{1}{4}}\bar{E}_m$	$\epsilon\hat{E}$	$\epsilon^{\frac{1}{4}}\bar{F}_m$	$\epsilon^{\frac{1}{2}}\bar{F}$
4	$\epsilon^{\frac{1}{6}}\tilde{T}$	$\epsilon^{\frac{1}{6}}\tilde{R}_m$	$\epsilon^{\frac{1}{3}}\tilde{R}$	$\epsilon\hat{A}_m$	$\epsilon\hat{A}$	$\epsilon^{\frac{1}{6}}\tilde{C}_m$	$\epsilon^{\frac{1}{3}}\tilde{C}$	$\epsilon\hat{B}_m$	$\epsilon\hat{B}$	$\epsilon^{\frac{1}{6}}\tilde{S}_m$	$\epsilon^{\frac{5}{6}}\tilde{S}$	$\epsilon^{\frac{1}{6}}\tilde{E}_m$	$\epsilon^{\frac{5}{6}}\tilde{E}$	$\epsilon^{\frac{1}{6}}\tilde{F}_m$	$\epsilon^{\frac{1}{3}}\tilde{F}$
5	$\epsilon^{\frac{1}{8}}T'$	$\epsilon^{\frac{1}{8}}R'_m$	$\epsilon^{\frac{1}{4}}R'$	$\epsilon\hat{A}_m$	$\epsilon\hat{A}$	$\epsilon^{\frac{1}{8}}C'_m$	$\epsilon^{\frac{1}{4}}C'$	$\epsilon^{\frac{7}{8}}B'_m$	$\epsilon\hat{B}$	$\epsilon^{\frac{1}{8}}S'_m$	$\epsilon^{\frac{3}{4}}S'$	$\epsilon^{\frac{1}{8}}E'_m$	$\epsilon^{\frac{3}{4}}E'$	$\epsilon^{\frac{1}{8}}F'_m$	$\epsilon^{\frac{1}{4}}F'$
6	$T^\dagger$	$R_m^\dagger$	$R^\dagger$	$\epsilon\hat{A}_m$	$\epsilon\hat{A}$	$C_m^\dagger$	$C^\dagger$	$\epsilon^{\frac{1}{2}}B_m^\dagger$	$\epsilon^{\frac{1}{2}}B^\dagger$	$S_m^\dagger$	$\epsilon^{\frac{1}{2}}S^\dagger$	$E_m^\dagger$	$\epsilon^{\frac{1}{2}}E^\dagger$	$F_m^\dagger$	$F^\dagger$
7	$\epsilon^{-\frac{1}{2}}T^\ddagger$	$R_m^\dagger$	$\epsilon^{-\frac{1}{2}}R^\ddagger$	$\epsilon\hat{A}_m$	$\epsilon^{\frac{1}{2}}A^\ddagger$	$C_m^\dagger$	$\epsilon^{-\frac{1}{2}}C^\ddagger$	$\epsilon^{\frac{1}{2}}B_m^\dagger$	$B^\ddagger$	$S_m^\dagger$	$S^\ddagger$	$E_m^\dagger$	$E^\ddagger$	$F_m^\dagger$	$\epsilon^{-\frac{1}{2}}F^\ddagger$
8	$\epsilon^{-1}\phi^{-1}\delta^{-1}T^\diamond$	$R_m^\dagger$	$\epsilon^{-1}\phi^{-1}\delta^{-1}R^\diamond$	$\epsilon\hat{A}_m$	$\epsilon^{\frac{1}{2}}A^\ddagger$	$C_m^\dagger$	$\epsilon^{-1}\phi^{-1}\delta^{-1}C^\diamond$	$\epsilon\phi\delta B_m^\diamond$	$\phi B^\diamond$	$S_m^\dagger$	$\epsilon^{-\frac{1}{2}}\phi^{-1}\delta^{-1}S^\diamond$	$E_m^\dagger$	$\epsilon^{-\frac{1}{2}}\phi^{-1}\delta^{-1}E^\diamond$	$\epsilon^{-\frac{1}{2}}\phi\delta F_m^\diamond$	$\epsilon^{-\frac{1}{2}}\delta F^\diamond$
9	$\epsilon^{-1}T^+$	$R_m^\dagger$	$\epsilon^{-1}R^+$	$\epsilon\hat{A}_m$	$\epsilon^{\frac{1}{2}}A^\ddagger$	$C_m^\dagger$	$\epsilon^{-1}C^+$	ϵB_m^+	$\phi B^\diamond$	$S_m^\dagger$	$\epsilon^{-\frac{1}{2}}S^+$	$E_m^\dagger$	$\epsilon^{-\frac{1}{2}}E^+$	$\epsilon^{-\frac{1}{2}}F_m^+$	$\epsilon^{-\frac{1}{2}}\delta F^\diamond$

Table 3.2: The scalings for each variable required on each timescale for the wild-type asymptotic analysis. These scalings are in relation to our nondimensionalised variables in (3.2)-(3.15). We have $\phi = \ln(1/\epsilon)^{-1}$ and $\delta = \ln(\ln(1/\epsilon))^{-1}$ which are explained in the timescales in which they feature. We note that production of most mRNAs dominates on the earlier timescales with protein production dominating the later timescales.

3.6.1 Timescale 1: mRNA transcription

On this initial timescale all variables must be scaled to $O(\epsilon)$ to reflect their initial conditions. We thus take the following scalings

$$\begin{aligned} T &= \epsilon\hat{T}, & R_m &= \epsilon\hat{R}_m, & A_m &= \epsilon\hat{A}_m, & C_m &= \epsilon\hat{C}_m, & B_m &= \epsilon\hat{B}_m, \\ S_m &= \epsilon\hat{S}_m, & E_m &= \epsilon\hat{E}_m, & F_m &= \epsilon\hat{F}_m, & R &= \epsilon\hat{R}, & A &= \epsilon\hat{A}, \\ C &= \epsilon\hat{C}, & B &= \epsilon\hat{B}, & S &= \epsilon\hat{S}, & E &= \epsilon\hat{E}, & F &= \epsilon\hat{F}. \end{aligned} \tag{3.37}$$

Using these scalings, the system of equations rescaled for the first timescale is

$$\begin{aligned} \frac{d\hat{R}_m}{d\hat{T}} &= 1 - \epsilon\hat{R}_m, & \frac{d\hat{R}}{d\hat{T}} &= \mu\rho\,\epsilon\hat{R}_m - \epsilon^2\mu\Delta\hat{R}, \\ \frac{d\hat{A}_m}{d\hat{T}} &= \frac{\epsilon\hat{A}}{(\epsilon\hat{A}+1)(\epsilon\hat{R}+1)} + \epsilon\alpha - \epsilon\hat{A}_m, & \frac{d\hat{A}}{d\hat{T}} &= \theta\,\epsilon\hat{A}_m - \epsilon^{\frac{3}{2}}\upsilon\hat{A} - \epsilon^2\Delta\hat{A}, \\ \frac{d\hat{C}_m}{d\hat{T}} &= \frac{\lambda}{\epsilon\hat{A}+\lambda} - \epsilon\hat{C}_m, & \frac{d\hat{C}}{d\hat{T}} &= \gamma\,\epsilon\hat{C}_m - \epsilon^2\Delta\hat{C}, \\ \frac{d\hat{B}_m}{d\hat{T}} &= \frac{\epsilon\hat{A}+\epsilon\hat{S}}{(1+\epsilon\hat{S}+\epsilon\hat{A})(1+\epsilon\hat{E}+\epsilon\hat{C})} - \epsilon\hat{B}_m, & \frac{d\hat{B}}{d\hat{T}} &= \beta\,\epsilon\hat{B}_m - \epsilon^2\Delta\hat{B}, \\ \frac{d\hat{S}_m}{d\hat{T}} &= 1 - \epsilon\hat{S}_m, & \frac{d\hat{S}}{d\hat{T}} &= \epsilon^{3/2}\sigma\,\hat{S}_m - \epsilon^2\Delta\hat{S}, \\ \frac{d\hat{E}_m}{d\hat{T}} &= 1 - \epsilon\hat{E}_m, & \frac{d\hat{E}}{d\hat{T}} &= \epsilon^{3/2}\xi\,\hat{E}_m - \epsilon^2\Delta\hat{E}, \\ \frac{d\hat{F}_m}{d\hat{T}} &= \frac{\eta}{\eta+\epsilon\hat{E}} - \epsilon\hat{F}_m, & \frac{d\hat{F}}{d\hat{T}} &= \frac{\epsilon\hat{F}_m}{\epsilon\omega\hat{B}+1} - \epsilon^2\Delta\hat{F}. \end{aligned} \tag{3.38}$$

At leading order, we have the following system of equations

$$\begin{aligned} \frac{d\hat{R}_m}{d\hat{T}} &= 1, & \frac{d\hat{R}}{d\hat{T}} &= 0, \\ \frac{d\hat{A}_m}{d\hat{T}} &= 0, & \frac{d\hat{A}}{d\hat{T}} &= 0, \\ \frac{d\hat{C}_m}{d\hat{T}} &= 1, & \frac{d\hat{C}}{d\hat{T}} &= 0, \\ \frac{d\hat{B}_m}{d\hat{T}} &= 0, & \frac{d\hat{B}}{d\hat{T}} &= 0, \end{aligned}$$

$$\begin{aligned}
\frac{d\hat{S}_m}{d\hat{T}} &= 1, & \frac{d\hat{S}}{d\hat{T}} &= 0,\\
\frac{d\hat{E}_m}{d\hat{T}} &= 1, & \frac{d\hat{E}}{d\hat{T}} &= 0,\\
\frac{d\hat{F}_m}{d\hat{T}} &= 1, & \frac{d\hat{F}}{d\hat{T}} &= 0.
\end{aligned} \tag{3.39}$$

The ODE system has now been reduced and we can extract the dominant behaviour on this timescale. Solving the reduced model subject to the initial conditions gives the following asymptotic approximations on this timescale:

$$\begin{aligned}
&\hat{R}_m = \hat{T} + R_{m0}, && \hat{R} = R_0, && \hat{A}_m = A_{m0}, && \hat{A} = A_0,\\
&\hat{C}_m = \hat{T} + C_{m0}, && \hat{C} = C_0, && \hat{B}_m = B_{m0}, && \hat{B} = B_0,\\
&\hat{S}_m = \hat{T} + S_{m0}, && \hat{S} = S_0, && \hat{E}_m = \hat{T} + E_{m0}, && \hat{E} = E_0,\\
&\hat{F}_m = \hat{T} + F_{m0}, && \hat{F} = F_0.
\end{aligned} \tag{3.40}$$

We plot the asymptotic approximations of all variables on this timescale against the numerical solutions in Figure 3.2. As expected, we see the transcription of various gene's mRNA occurring first with protein levels remaining at their initial value. The transcription of *ramA* and *acrAB* mRNA are currently not active due to there being insufficient levels of activator protein bound to their promoter sites to achieve any level of transcription at leading order. We have now analysed this first timescale and must determine the scalings necessary to reach the next timescale. We now demonstrate two possible methods for revealing these scalings.

Method 1: Analysing the leading order balance

In this method, we determine the scalings for each variable by first analysing their long term behaviour on the current timescale. We can then look at which new terms will first enter the leading order balance on the next timescale to reveal the exact scaling. For this

timescale, as $\hat{T} \to \infty$ we have

$$\hat{R}_m, \hat{C}_m, \hat{S}_m, \hat{E}_m, \hat{F}_m \sim \hat{T}, \tag{3.41}$$

with every other variable still constant at their initial condition. We now propose a new time scaling to reach the next timescale:

$$\hat{T} = \delta(\epsilon)\check{T}, \tag{3.42}$$

where $\delta(\epsilon)$ is a function of ϵ. Since we are scaling forwards in time, we must have that $\delta(\epsilon) > 1$. Substituting this scaling (3.42) into the solutions (3.40) for our variables that evolve on this timescale . We have

$$\begin{aligned} &\hat{R}_m = \delta(\epsilon)\check{T} + R_{m0}, \qquad &&\hat{C}_m = \delta(\epsilon)\check{T} + C_{m0}, \qquad &&\hat{S}_m = \delta(\epsilon)\check{T} + S_{m0}, \\ &\hat{E}_m = \delta(\epsilon)\check{T} + E_{m0}, \qquad &&\hat{F}_m = \delta(\epsilon)\check{T} + F_{m0}. \end{aligned} \tag{3.43}$$

Notably, we have terms of $O(\delta(\epsilon)) > O(1)$, in order for these terms to be $O(1)$ on the subsequent timescale, we must then take the following variable scalings

$$\hat{R}_m = \delta(\epsilon)\check{R}_m, \quad \hat{C}_m = \delta(\epsilon)\check{C}_m, \quad \hat{S}_m = \delta(\epsilon)\check{S}_m, \quad \hat{E}_m = \delta(\epsilon)\check{E}_m, \quad \hat{F}_m = \delta(\epsilon)\check{F}_m. \tag{3.44}$$

Using the combination of scalings (3.42)-(3.44), our system of equations (3.38) become

$$\begin{aligned} \frac{d\check{R}_m}{d\check{T}} &= 1 - \epsilon\delta(\epsilon)\check{R}_m, & \frac{1}{\delta(\epsilon)}\frac{d\hat{R}}{d\check{T}} &= \epsilon\delta(\epsilon)\mu\rho\,\check{R}_m - \epsilon^2\mu\Delta\hat{R}, \\ \frac{1}{\delta(\epsilon)}\frac{d\hat{A}_m}{d\check{T}} &= \frac{\epsilon\hat{A}}{(\epsilon\hat{A}+1)(\epsilon\hat{R}+1)} + \epsilon\alpha - \epsilon\hat{A}_m, & \frac{1}{\delta(\epsilon)}\frac{d\hat{A}}{d\check{T}} &= \epsilon\theta\,\hat{A}_m - \epsilon^{\frac{3}{2}}\upsilon\,\hat{A} - \epsilon^2\Delta\hat{A}, \end{aligned} \tag{3.45}$$

$$\begin{aligned} \frac{d\check{C}_m}{d\check{T}} &= \frac{\lambda}{\epsilon\hat{A}+\lambda} - \epsilon\delta(\epsilon)\check{C}_m, & \frac{1}{\delta(\epsilon)}\frac{d\hat{C}}{d\check{T}} &= \epsilon\delta(\epsilon)\gamma\,\check{C}_m - \epsilon^2\Delta\hat{C}, \\ \frac{1}{\delta(\epsilon)}\frac{d\hat{B}_m}{d\check{T}} &= \frac{\epsilon\hat{A}+\epsilon\hat{S}}{(1+\epsilon\hat{S}+\epsilon\hat{A})(1+\epsilon\hat{E}+\epsilon\hat{C})} - \epsilon\hat{B}_m, & \frac{1}{\delta(\epsilon)}\frac{d\hat{B}}{d\check{T}} &= \epsilon\beta\,\hat{B}_m - \epsilon^2\Delta\hat{B}, \end{aligned} \tag{3.46}$$

$$
\begin{aligned}
\frac{d\check{S}_m}{d\check{T}} &= 1 - \epsilon\delta(\epsilon)\check{S}_m, & \frac{1}{\delta(\epsilon)}\frac{d\hat{S}}{d\check{T}} &= \epsilon^{\frac{3}{2}}\delta(\epsilon)\sigma\,\check{S}_m - \epsilon^2\Delta\hat{S},\\
\frac{d\check{E}_m}{d\check{T}} &= 1 - \epsilon\delta(\epsilon)\check{E}_m, & \frac{1}{\delta(\epsilon)}\frac{d\hat{E}}{d\check{T}} &= \epsilon^{\frac{3}{2}}\xi\,\check{E}_m - \epsilon^2\Delta\hat{E},\\
\frac{d\check{F}_m}{d\check{T}} &= \frac{\eta}{\eta + \epsilon\hat{E}} - \epsilon\delta(\epsilon)\check{F}_m, & \frac{1}{\delta(\epsilon)}\frac{d\hat{F}}{d\check{T}} &= \frac{\epsilon\delta(\epsilon)\check{F}_m}{\epsilon\omega\hat{B}+1} - \epsilon^2\Delta\hat{F}.
\end{aligned}
\tag{3.47}
$$

We can see from this system of equations that the smallest scaling $\delta(\epsilon)$ that brings in a new term to the leading order balance is $\delta(\epsilon) = \epsilon^{-\frac{1}{2}}$. This scaling brings in RamR, AcrR and AcrEF translation in equations (3.45), (3.46) and (3.47) respectively.

Method 2: Analysing the correction term

In this method, we look at the behaviour of the correction terms on the current timescale to determine the time scaling to reach the subsequent timescale. For all 14 of our variables we take the following asymptotic expansions, with notation for a gene mRNA G_m and protein G.

$$
G_m = g_{m0} + \epsilon^{\frac{1}{2}} g_{m1} + \epsilon g_{m2} + ..., \qquad G = g_0 + \epsilon^{\frac{1}{2}} g_1 + \epsilon g_2 + \dots . \tag{3.48}
$$

In addition to the leading order system of equations (3.39) and solutions (3.40), the first non trivial correction terms are defined by the following system of equations

$$
\begin{aligned}
\frac{d\hat{r}_{m2}}{d\hat{T}} &= -r_{m0}, & \frac{d\hat{r}_0}{d\hat{T}} &= \mu\rho r_{m0},\\
\frac{d\hat{a}_{m2}}{d\hat{T}} &= a_0 + \alpha - a_{m0}, & \frac{d\hat{a}_0}{d\hat{T}} &= \theta a_{m0},\\
\frac{d\hat{c}_{m2}}{d\hat{T}} &= -\frac{a_0}{\lambda} - c_{m0}, & \frac{d\hat{c}_0}{d\hat{T}} &= \gamma c_{m0},\\
\frac{d\hat{b}_{m2}}{d\hat{T}} &= a_0 + s_0 - b_{m0}, & \frac{d\hat{b}_0}{d\hat{T}} &= \beta b_{m0},\\
\frac{d\hat{s}_{m2}}{d\hat{T}} &= -s_{m0}, & \frac{d\hat{s}_0}{d\hat{T}} &= \sigma s_{m0},\\
\frac{d\hat{e}_{m2}}{d\hat{T}} &= -e_{m0}, & \frac{d\hat{e}_0}{d\hat{T}} &= \xi e_{m0},\\
\frac{d\hat{f}_{m2}}{d\hat{T}} &= -\frac{e_0}{\eta} - f_{m0}, & \frac{d\hat{f}_0}{d\hat{T}} &= f_{m0}.
\end{aligned}
\tag{3.49}
$$

Solving this system of equations we have:

$$\begin{aligned}
\hat{R}_m &\sim \hat{T} + R_{m0} + \epsilon\left(-\frac{1}{2}\hat{T}^2 - R_{m0}\hat{T}\right), & \hat{R} &\sim R_0 + \epsilon\left(\frac{1}{2}\mu\rho\hat{T}^2 + \mu\rho R_{m0}\hat{T}\right),\\
\hat{A}_m &\sim A_{m0} + \epsilon\left((A_0 + \alpha - A_{m0})\hat{T}\right), & \hat{A} &\sim A_0 + \epsilon\left(\theta A_{m0}\hat{T}\right),\\
\hat{C}_m &\sim \hat{T} + C_{m0} + \epsilon\left(-\frac{1}{2}\hat{T}^2 - \left(\frac{A_0}{\lambda} + C_{m0}\right)\hat{T}\right), & \hat{C} &\sim C_0 + \epsilon\left(\frac{1}{2}\gamma\hat{T}^2 + \gamma C_{m0}\hat{T}\right),\\
\hat{B}_m &\sim B_{m0} + \epsilon\left((A_0 + S_0 - B_{m0})\hat{T}\right), & \hat{B} &\sim B_0 + \epsilon\left(\beta B_{m0}\hat{T}\right),\\
\hat{S}_m &\sim \hat{T} + S_{m0} + \epsilon\left(-\frac{1}{2}\hat{T}^2 - S_{m0}\hat{T}\right), & \hat{S} &\sim S_0 + \epsilon^{\frac{3}{2}}\left(\frac{1}{2}\sigma\hat{T}^2 + \sigma S_{m0}\hat{T}\right),\\
\hat{E}_m &\sim \hat{T} + E_{m0} + \epsilon\left(-\frac{1}{2}\hat{T}^2 - E_{m0}\hat{T}\right), & \hat{E} &\sim E_0 + \epsilon^{\frac{3}{2}}\left(\frac{1}{2}\xi\hat{T}^2 + \xi E_{m0}\hat{T}\right),\\
\hat{F}_m &\sim \hat{T} + F_{m0} + \epsilon\left(-\frac{1}{2}\hat{T}^2 - \left(\frac{E_0}{\eta} + F_{m0}\right)\hat{T}\right), & \hat{F} &\sim F_0 + \epsilon\left(\frac{1}{2}\hat{T}^2 + F_{m0}\hat{T}\right). \quad (3.50)
\end{aligned}$$

For the variables that have not evolved at leading order, we can see that the correction terms for $\hat{R}, \hat{C}$ and $\hat{F}$ become $O(1)$ when $\hat{T} = O(\epsilon^{-\frac{1}{2}})$. Since this is the smallest possible time scaling to bring in correction terms, this gives us our time scaling $\hat{T} = \epsilon^{-\frac{1}{2}}\check{T}$ to reach the next timescale. The variables $\hat{S}$ and $\hat{E}$ become leading order at $\hat{T} = O(\epsilon^{-\frac{3}{4}})$ whilst the variables $\hat{A}_m, \hat{A}, \hat{B}_m$ and $\hat{B}$ become leading order at $\hat{T} = O(\epsilon^{-1})$, which gives us insight into potential scalings for future timescales past the subsequent timescale. For the variables that have evolved at leading order, applying the scaling $\hat{T} = \epsilon^{-\frac{1}{2}}\check{T}$, the leading order terms become $O(\epsilon^{-\frac{1}{2}})$. For these terms to be $O(1)$ on the subsequent timescale we must also apply the following variable scalings

$$\hat{R}_m = \epsilon^{-\frac{1}{2}}\check{R}_m, \quad \hat{C}_m = \epsilon^{-\frac{1}{2}}\check{C}_m, \quad \hat{S}_m = \epsilon^{-\frac{1}{2}}\check{S}_m, \quad \hat{E}_m = \epsilon^{-\frac{1}{2}}\check{E}_m, \quad \hat{F}_m = \epsilon^{-\frac{1}{2}}\check{F}_m. \quad (3.51)$$

Notably, both methods return the same scalings as they are mathematically set in sequence and cannot be chosen. For brevity, we omit the steps involved in these methods for the subsequent timescales.

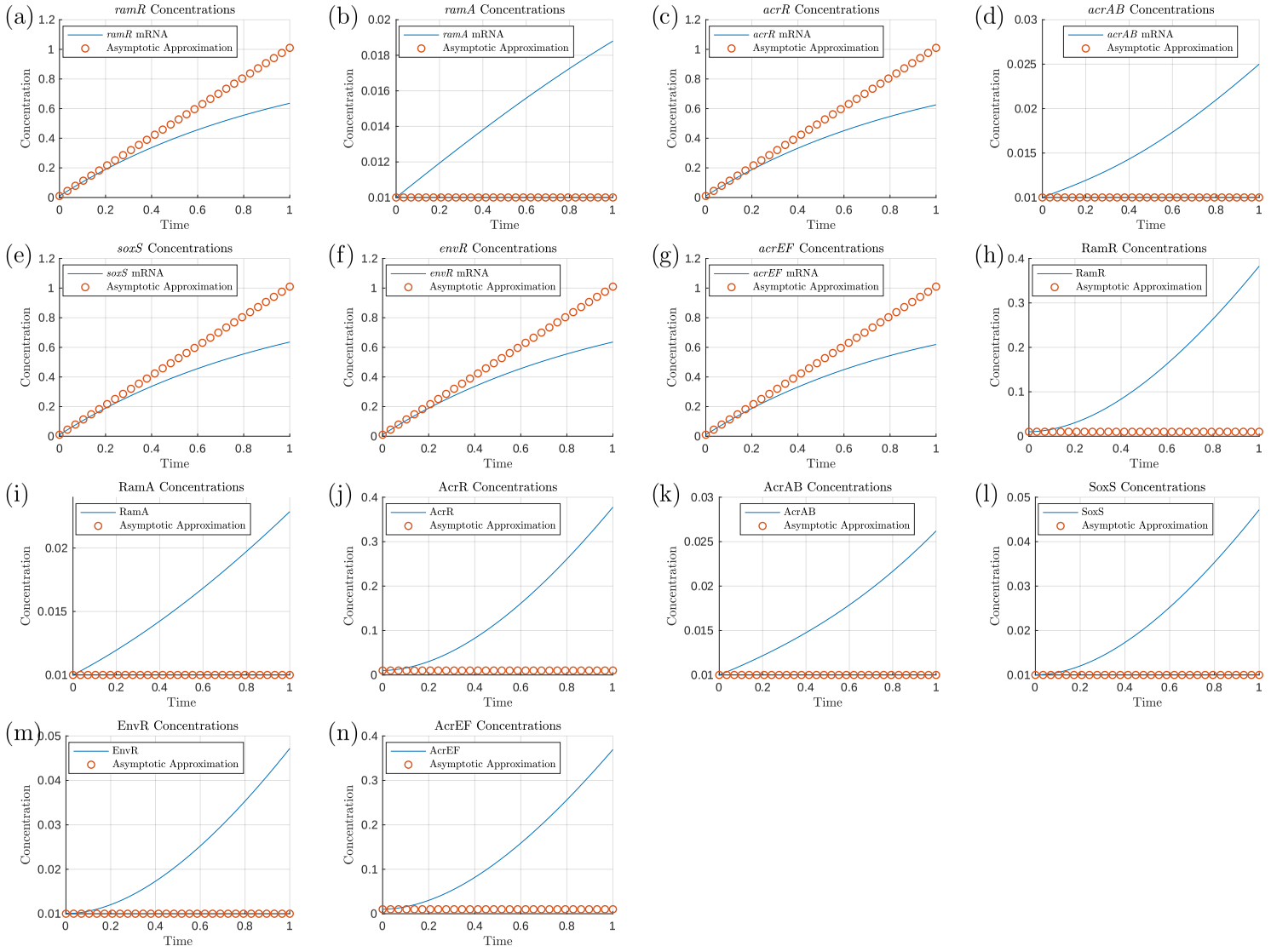

Figure 3.2: Asymptotic approximations on timescale 1 for the wild-type dynamics ($\epsilon = 0.01$). On this timescale, time is $O(\epsilon)$, so we expect the asymptotics to be accurate around $T = \epsilon = 0.01$. For reference, the subsequent timescale has time at $O(\epsilon^{\frac{1}{2}})$. Most figures are still at initial condition, as no reaction terms have come into their equations at leading order.

3.6.2 Timescale 2: Protein translation

We move onto the second timescale, here protein translation occurs for RamR, AcrR and AcrEF in equations (3.53)-(3.55). We take the following scalings based on the variables on the previous timescale's long-term behaviour

$$\begin{aligned} \hat{T} &= \epsilon^{-\frac{1}{2}}\check{T}, & \hat{R}_m &= \epsilon^{-\frac{1}{2}}\check{R}_m, & \hat{C}_m &= \epsilon^{-\frac{1}{2}}\check{C}_m, \\ \hat{S}_m &= \epsilon^{-\frac{1}{2}}\check{S}_m, & \hat{E}_m &= \epsilon^{-\frac{1}{2}}\check{E}_m, & \hat{F}_m &= \epsilon^{-\frac{1}{2}}\check{F}_m. \end{aligned} \tag{3.52}$$

After rescaling, the system of equations for the second timescale is

$$\begin{aligned} \frac{d\check{R}_m}{d\check{T}} &= 1 - \epsilon^{\frac{1}{2}}\check{R}_m, & \frac{d\hat{R}}{d\check{T}} &= \mu\rho\,\check{R}_m - \epsilon^{\frac{3}{2}}\mu\Delta\hat{R}, \\ \frac{d\hat{A}_m}{d\check{T}} &= \frac{\epsilon^{\frac{1}{2}}\hat{A}}{(\epsilon\hat{A}+1)(\epsilon\hat{R}+1)} + \epsilon^{\frac{1}{2}}\alpha - \epsilon^{\frac{1}{2}}\hat{A}_m, & \frac{d\hat{A}}{d\check{T}} &= \epsilon^{\frac{1}{2}}\theta\,\hat{A}_m - \epsilon\upsilon\,\hat{A} - \epsilon^{\frac{3}{2}}\Delta\hat{A}, \\ \frac{d\check{C}_m}{d\check{T}} &= \frac{\lambda}{\epsilon\hat{A}+\lambda} - \epsilon^{\frac{1}{2}}\check{C}_m, & \frac{d\hat{C}}{d\check{T}} &= \gamma\,\check{C}_m - \epsilon^{\frac{3}{2}}\Delta\hat{C}, \\ \frac{d\hat{B}_m}{d\check{T}} &= \frac{\epsilon^{\frac{1}{2}}\hat{A} + \epsilon^{\frac{1}{2}}\hat{S}}{(1+\epsilon\hat{S}+\epsilon\hat{A})(1+\epsilon\hat{E}+\epsilon\hat{C})} - \epsilon^{\frac{1}{2}}\hat{B}_m, & \frac{d\hat{B}}{d\check{T}} &= \epsilon^{\frac{1}{2}}\beta\,\hat{B}_m - \epsilon^{\frac{3}{2}}\Delta\hat{B}, \\ \frac{d\check{S}_m}{d\check{T}} &= 1 - \epsilon^{\frac{1}{2}}\check{S}_m, & \frac{d\hat{S}}{d\check{T}} &= \epsilon^{\frac{1}{2}}\sigma\,\check{S}_m - \epsilon^{\frac{3}{2}}\Delta\hat{S}, \\ \frac{d\check{E}_m}{d\check{T}} &= 1 - \epsilon^{\frac{1}{2}}\check{E}_m, & \frac{d\hat{E}}{d\check{T}} &= \epsilon^{\frac{1}{2}}\xi\,\check{E}_m - \epsilon^{\frac{3}{2}}\Delta\hat{E}, \\ \frac{d\check{F}_m}{d\check{T}} &= \frac{\eta}{\eta+\epsilon\hat{E}} - \epsilon^{\frac{1}{2}}\check{F}_m, & \frac{d\hat{F}}{d\check{T}} &= \frac{\check{F}_m}{\epsilon\omega\hat{B}+1} - \epsilon^{\frac{3}{2}}\Delta\hat{F}. \end{aligned} \tag{3.53, 3.54, 3.55}$$

At leading order, we have the following system of equations

$$\begin{aligned} \frac{d\check{R}_m}{d\check{T}} &= 1, & \frac{d\hat{R}}{d\check{T}} &= \mu\rho\,\check{R}_m, \\ \frac{d\hat{A}_m}{d\check{T}} &= 0, & \frac{d\hat{A}}{d\check{T}} &= 0, \\ \frac{d\check{C}_m}{d\check{T}} &= 1, & \frac{d\hat{C}}{d\check{T}} &= \gamma\,\check{C}_m, \end{aligned}$$

$$\frac{d\hat{B}_m}{d\check{T}} = 0, \qquad \frac{d\hat{B}}{d\check{T}} = 0,$$
$$\frac{d\check{S}_m}{d\check{T}} = 1, \qquad \frac{d\hat{S}}{d\check{T}} = 0,$$
$$\frac{d\check{E}_m}{d\check{T}} = 1, \qquad \frac{d\hat{E}}{d\check{T}} = 0,$$
$$\frac{d\check{F}_m}{d\check{T}} = 1, \qquad \frac{d\hat{F}}{d\check{T}} = \check{F}_m. \tag{3.56}$$

Solving this reduced system of ODEs and matching to the long-term dominant behaviour on the previous timescale using Van Dyke's rule [91], gives the following asymptotic approximations

$$\check{R}_m = \check{T}, \qquad \hat{R} = \frac{\mu\rho}{2}\check{T}^2 + R_0 \qquad \hat{A}_m = A_{m0}, \qquad \hat{A} = A_0,$$
$$\check{C}_m = \check{T}, \qquad \hat{C} = \frac{\gamma}{2}\check{T}^2 + C_0, \qquad \hat{B}_m = B_{m0}, \qquad \hat{B} = B_0,$$
$$\check{S}_m = \check{T}, \qquad \hat{S} = S_0, \qquad \check{E}_m = \check{T}, \qquad \hat{E} = E_0,$$
$$\check{F}_m = \check{T}, \qquad \hat{F} = \frac{1}{2}\check{T}^2 + F_0. \tag{3.57}$$

We plot these asymptotic approximations against the numerical solutions in Figure 3.3. We see the translation of some of the genes transcribed on the previous timescale appearing at leading order on this timescale. This is expected as bacteria have fast translation processes, such that translation occurs as soon as the gene is transcribed. The translation is not present for EnvR and the underlying activators which agrees with what we might expect from biological intuition as these are a homologue gene and secondary TAs respectively, thus we expect lower expression of these genes.

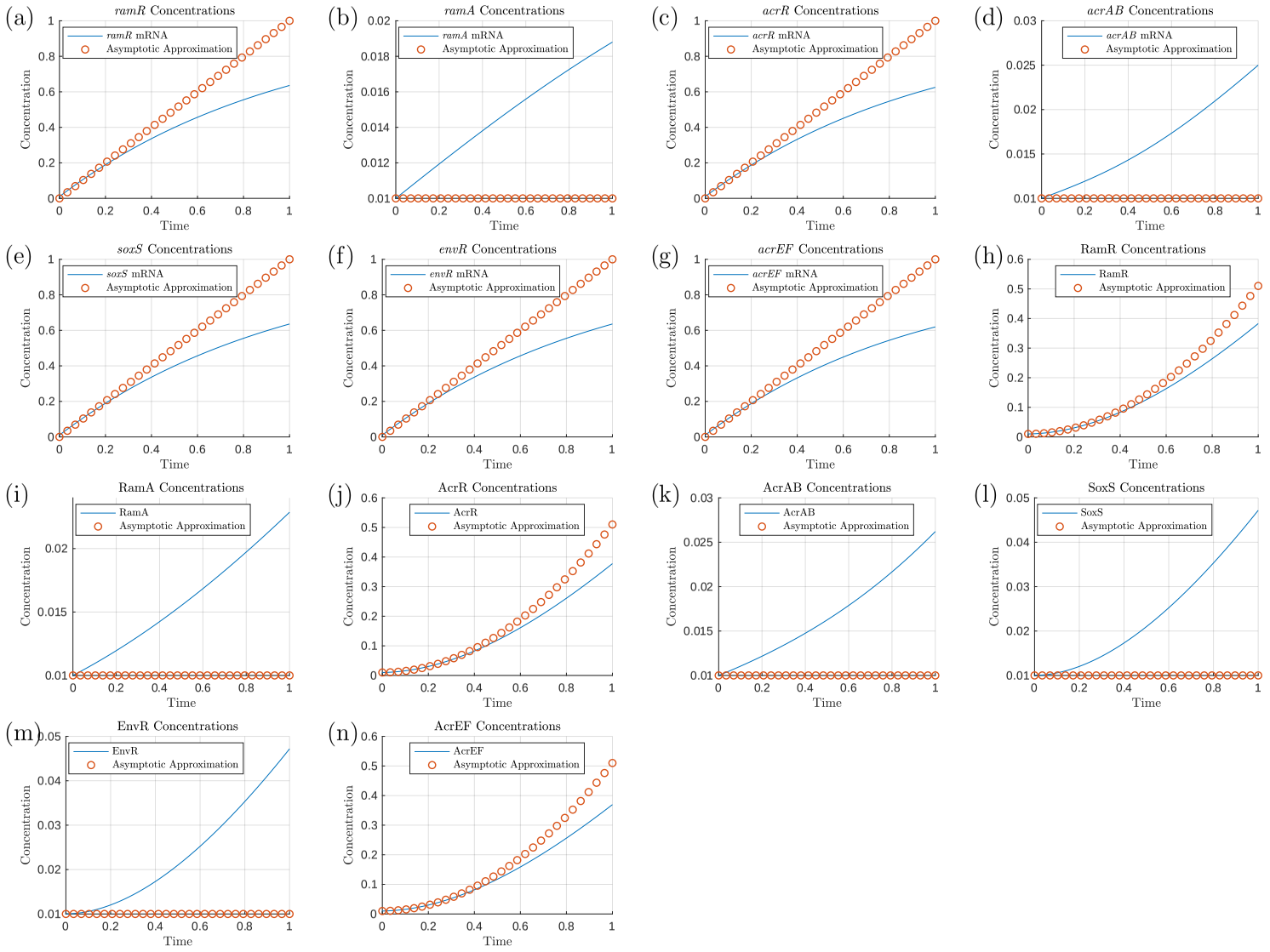

Figure 3.3: Asymptotic approximations on timescale 2 for the wild-type dynamics ($\epsilon = 0.01$). On this timescale, time is $O(\epsilon^{\frac{1}{2}})$, so we expect the asymptotics to be accurate around $T = \epsilon^{\frac{1}{2}} = 0.1$. For reference, the previous and subsequent timescales have time at $O(\epsilon)$ and $O(\epsilon^{\frac{1}{4}})$ respectively.

3.6.3 Timescale 3: SoxS and EnvR translation

On this third timescale protein translation occurs at leading order for the rest of the proteins for which transcription of their corresponding mRNA occurred on timescale 1 in equations (3.59)-(3.60). We take the following scalings:

$$\begin{aligned}
\check{T} &= \epsilon^{-\frac{1}{4}}\bar{T}, & \check{R}_m &= \epsilon^{-\frac{1}{4}}\bar{R}_m, & \check{C}_m &= \epsilon^{-\frac{1}{4}}\bar{C}_m,\\
\check{S}_m &= \epsilon^{-\frac{1}{4}}\bar{S}_m, & \check{E}_m &= \epsilon^{-\frac{1}{4}}\bar{E}_m, & \check{F}_m &= \epsilon^{-\frac{1}{4}}\bar{F}_m,\\
\hat{R} &= \epsilon^{-\frac{1}{2}}\bar{R}, & \hat{C} &= \epsilon^{-\frac{1}{2}}\bar{C}, & \hat{F} &= \epsilon^{-\frac{1}{2}}\bar{F}.
\end{aligned} \tag{3.58}$$

The system of equations rescaled for the third timescale is

$$\begin{aligned}
\frac{d\bar{R}_m}{d\bar{T}} &= 1-\epsilon^{\frac{1}{4}}\bar{R}_m, & \frac{d\bar{R}}{d\bar{T}} &= \mu\rho\,\bar{R}_m-\epsilon^{\frac{5}{4}}\mu\Delta\bar{R},\\
\frac{d\hat{A}_m}{d\bar{T}} &= \frac{\epsilon^{\frac{1}{4}}\hat{A}}{(\epsilon\hat{A}+1)(\epsilon^{\frac{1}{2}}\bar{R}+1)}+\epsilon^{\frac{1}{4}}\alpha-\epsilon^{\frac{1}{4}}\hat{A}_m, & \frac{d\hat{A}}{d\bar{T}} &= \epsilon^{\frac{1}{4}}\theta\,\hat{A}_m-\epsilon^{\frac{3}{4}}\upsilon\,\hat{A}-\epsilon^{\frac{5}{4}}\Delta\hat{A},\\
\frac{d\bar{C}_m}{d\bar{T}} &= \frac{\lambda}{\epsilon\hat{A}+\lambda}-\epsilon^{\frac{1}{4}}\bar{C}_m, & \frac{d\bar{C}}{d\bar{T}} &= \gamma\,\bar{C}_m-\epsilon^{\frac{5}{4}}\Delta\bar{C},\\
\frac{d\hat{B}_m}{d\bar{T}} &= \frac{\epsilon^{\frac{1}{4}}\hat{A}+\epsilon^{\frac{1}{4}}\hat{S}}{(1+\epsilon\hat{S}+\epsilon\hat{A})(1+\epsilon\hat{E}+\epsilon^{\frac{1}{2}}\bar{C})}-\epsilon^{\frac{1}{4}}\hat{B}_m, & \frac{d\hat{B}}{d\bar{T}} &= \epsilon^{\frac{1}{4}}\beta\,\hat{B}_m-\epsilon^{\frac{5}{4}}\Delta\hat{B},\\
\frac{d\bar{S}_m}{d\bar{T}} &= 1-\epsilon^{\frac{1}{4}}\bar{S}_m, & \frac{d\hat{S}}{d\bar{T}} &= \sigma\,\bar{S}_m-\epsilon^{\frac{5}{4}}\Delta\hat{S}, \qquad (3.59)\\
\frac{d\bar{E}_m}{d\bar{T}} &= 1-\epsilon^{\frac{1}{4}}\bar{E}_m, & \frac{d\hat{E}}{d\bar{T}} &= \xi\,\bar{E}_m-\epsilon^{\frac{5}{4}}\Delta\hat{E}, \qquad (3.60)\\
\frac{d\bar{F}_m}{d\bar{T}} &= \frac{\eta}{\eta+\epsilon\hat{E}}-\epsilon^{\frac{1}{4}}\bar{F}_m, & \frac{d\bar{F}}{d\bar{T}} &= \frac{\bar{F}_m}{\epsilon\omega\hat{B}+1}-\epsilon^{\frac{5}{4}}\Delta\bar{F}.
\end{aligned}$$

At leading order, we have the following system of equations

$$\begin{aligned}
\frac{d\bar{R}_m}{d\bar{T}} &= 1, & \frac{d\bar{R}}{d\bar{T}} &= \mu\rho\,\bar{R}_m,\\
\frac{d\hat{A}_m}{d\bar{T}} &= 0, & \frac{d\hat{A}}{d\bar{T}} &= 0,\\
\frac{d\bar{C}_m}{d\bar{T}} &= 1, & \frac{d\bar{C}}{d\bar{T}} &= \gamma\,\bar{C}_m,
\end{aligned}$$

$$\begin{aligned}
\frac{d\hat{B}_m}{d\bar{T}} &= 0, & \frac{d\hat{B}}{d\bar{T}} &= 0,\\
\frac{d\bar{S}_m}{d\bar{T}} &= 1, & \frac{d\hat{S}}{d\bar{T}} &= \sigma\bar{S}_m,\\
\frac{d\bar{E}_m}{d\bar{T}} &= 1, & \frac{d\hat{E}}{d\bar{T}} &= \xi\bar{E}_m,\\
\frac{d\bar{F}_m}{d\bar{T}} &= 1, & \frac{d\bar{F}}{d\bar{T}} &= \bar{F}_m.
\end{aligned} \tag{3.61}$$

Taking this leading order balance, solving and matching to the long-term dominant behaviour on the previous timescale gives the following asymptotic approximations

$$\begin{aligned}
&\bar{R}_m = \bar{T}, && \bar{R} = \frac{\mu\rho}{2}\bar{T}^2, && \hat{A}_m = A_{m0}, && \hat{A} = A_0,\\
&\bar{C}_m = \bar{T}, && \bar{C} = \frac{\gamma}{2}\bar{T}^2, && \hat{B}_m = B_{m0}, && \hat{B} = B_0,\\
&\bar{S}_m = \bar{T}, && \hat{S} = \frac{\sigma}{2}\bar{T}^2 + S_0, && \bar{E}_m = \bar{T}, && \hat{E} = \frac{\xi}{2}\bar{T}^2 + E_0,\\
&\bar{F}_m = \bar{T}, && \bar{F} = \frac{1}{2}\bar{T}^2. &&&&
\end{aligned} \tag{3.62}$$

We plot these asymptotic approximations against the numerical solutions in Figure 3.4. On this timescale, we see the translation of all mRNAs that were previously transcribed on the earlier timescales. This makes logical sense as we expect rapid translation in response to changes at the transcriptional level.

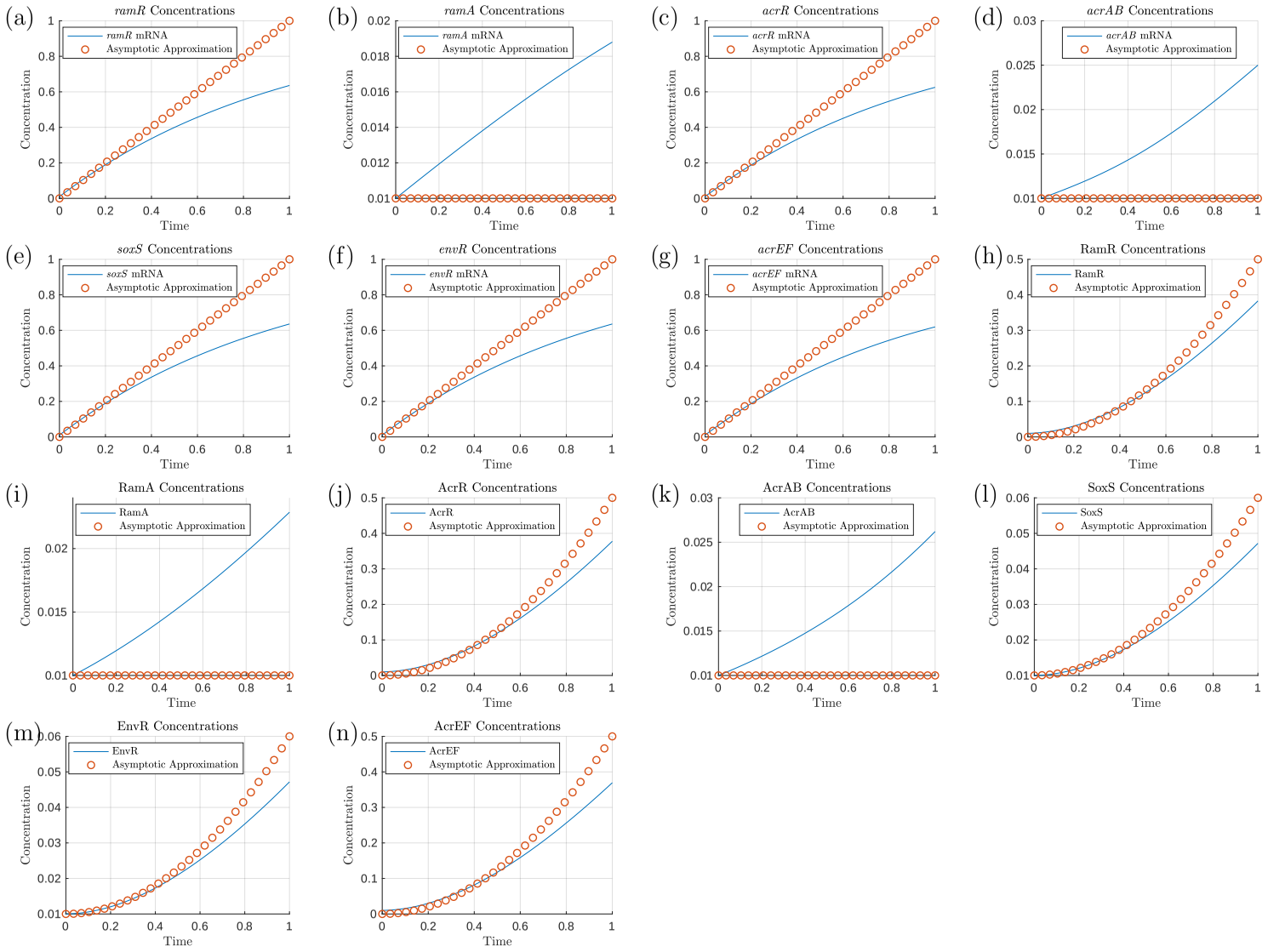

Figure 3.4: Asymptotic approximations on timescale 3 for the wild-type dynamics ($\epsilon = 0.01$). On this timescale, time is $O(\epsilon^{\frac{1}{4}}) \approx 0.3162$, so we expect the asymptotics to be accurate around $T = \epsilon^{\frac{1}{4}}$. For reference, the previous and subsequent timescales have time at $O(\epsilon^{\frac{1}{2}})$ and $O(\epsilon^{\frac{1}{6}})$ respectively.

3.6.4 Timescale 4: *acrAB* mRNA transcription

For this timescale, transcription of the efflux pump gene *acrAB* emerges in equation (3.64). We take the following scalings:

$$\begin{aligned}
\bar{T} &= \epsilon^{-\frac{1}{12}}\tilde{T}, & \bar{R}_m &= \epsilon^{-\frac{1}{12}}\tilde{R}_m, & \bar{C}_m &= \epsilon^{-\frac{1}{12}}\tilde{C}_m, & \bar{S}_m &= \epsilon^{-\frac{1}{12}}\tilde{S}_m,\\
\bar{E}_m &= \epsilon^{-\frac{1}{12}}\tilde{E}_m, & \bar{F}_m &= \epsilon^{-\frac{1}{12}}\tilde{F}_m, & \bar{R} &= \epsilon^{-\frac{1}{6}}\tilde{R}, & \bar{C} &= \epsilon^{-\frac{1}{6}}\tilde{C},\\
\hat{S} &= \epsilon^{-\frac{1}{6}}\tilde{S}, & \hat{E} &= \epsilon^{-\frac{1}{6}}\tilde{E}, & \bar{F} &= \epsilon^{-\frac{1}{6}}\tilde{F}. & &
\end{aligned} \tag{3.63}$$

After rescaling, the system of equations for the fourth timescale is

$$\begin{aligned}
\frac{d\tilde{R}_m}{d\tilde{T}} &= 1-\epsilon^{\frac{1}{6}}\tilde{R}_m, & \frac{d\tilde{R}}{d\tilde{T}} &= \mu\rho\,\tilde{R}_m-\epsilon^{\frac{7}{6}}\mu\Delta\tilde{R},\\
\frac{d\hat{A}_m}{d\tilde{T}} &= \frac{\epsilon^{\frac{1}{6}}\hat{A}}{(\epsilon\hat{A}+1)(\epsilon^{\frac{1}{3}}\tilde{R}+1)}+\epsilon^{\frac{1}{6}}\alpha-\epsilon^{\frac{1}{6}}\hat{A}_m, & \frac{d\hat{A}}{d\tilde{T}} &= \epsilon^{\frac{1}{6}}\theta\,\hat{A}_m-\epsilon^{\frac{2}{3}}\upsilon\,\hat{A}-\epsilon^{\frac{7}{6}}\Delta\hat{A},\\
\frac{d\tilde{C}_m}{d\tilde{T}} &= \frac{\lambda}{\epsilon\hat{A}+\lambda}-\epsilon^{\frac{1}{6}}\tilde{C}_m, & \frac{d\tilde{C}}{d\tilde{T}} &= \gamma\,\tilde{C}_m-\epsilon^{\frac{7}{6}}\Delta\tilde{C},\\
\frac{d\hat{B}_m}{d\tilde{T}} &= \frac{\epsilon^{\frac{1}{6}}\hat{A}+\tilde{S}}{(1+\epsilon^{\frac{5}{6}}\tilde{S}+\epsilon\hat{A})(1+\epsilon^{\frac{5}{6}}\tilde{E}+\epsilon^{\frac{1}{3}}\tilde{C})}-\epsilon^{\frac{1}{6}}\hat{B}_m, & \frac{d\hat{B}}{d\tilde{T}} &= \epsilon^{\frac{1}{6}}\beta\,\hat{B}_m-\epsilon^{\frac{7}{6}}\Delta\hat{B},\\
\frac{d\tilde{S}_m}{d\tilde{T}} &= 1-\epsilon^{\frac{1}{6}}\tilde{S}_m, & \frac{d\tilde{S}}{d\tilde{T}} &= \sigma\,\tilde{S}_m-\epsilon^{\frac{7}{6}}\Delta\tilde{S},\\
\frac{d\tilde{E}_m}{d\tilde{T}} &= 1-\epsilon^{\frac{1}{6}}\tilde{E}_m, & \frac{d\tilde{E}}{d\tilde{T}} &= \xi\,\tilde{E}_m-\epsilon^{\frac{7}{6}}\Delta\,\tilde{E},\\
\frac{d\tilde{F}_m}{d\tilde{T}} &= \frac{\eta}{\eta+\epsilon^{\frac{5}{6}}\tilde{E}}-\epsilon^{\frac{1}{6}}\tilde{F}_m, & \frac{d\tilde{F}}{d\tilde{T}} &= \frac{\tilde{F}_m}{\epsilon\omega\hat{B}+1}-\epsilon^{\frac{7}{6}}\Delta\tilde{F}.
\end{aligned} \tag{3.64}$$

At leading order, we have the following system of equations

$$\begin{aligned}
\frac{d\tilde{R}_m}{d\tilde{T}} &= 1, & \frac{d\tilde{R}}{d\tilde{T}} &= \mu\rho\,\tilde{R}_m,\\
\frac{d\hat{A}_m}{d\tilde{T}} &= 0, & \frac{d\hat{A}}{d\tilde{T}} &= 0,\\
\frac{d\tilde{C}_m}{d\tilde{T}} &= 1, & \frac{d\tilde{C}}{d\tilde{T}} &= \gamma\,\tilde{C}_m,
\end{aligned}$$

$$\begin{aligned}
\frac{d\hat{B}_m}{d\tilde{T}} &= \tilde{S}, & \frac{d\hat{B}}{d\tilde{T}} &= 0,\\
\frac{d\tilde{S}_m}{d\tilde{T}} &= 1, & \frac{d\tilde{S}}{d\tilde{T}} &= \sigma\tilde{S}_m,\\
\frac{d\tilde{E}_m}{d\tilde{T}} &= 1, & \frac{d\tilde{E}}{d\tilde{T}} &= \xi\tilde{E}_m,\\
\frac{d\tilde{F}_m}{d\tilde{T}} &= 1, & \frac{d\tilde{F}}{d\tilde{T}} &= \tilde{F}_m.
\end{aligned} \tag{3.65}$$

Solving this leading order system of ODEs and matching to the dominant behaviour on the previous timescale gives us

$$\begin{aligned}
\tilde{R}_m &= \tilde{T}, & \tilde{R} &= \frac{\mu\rho}{2}\tilde{T}^2, & \hat{A}_m &= A_{m0}, & \hat{A} &= A_0,\\
\tilde{C}_m &= \tilde{T}, & \tilde{C} &= \frac{\gamma}{2}\tilde{T}^2, & \hat{B}_m &= \frac{\sigma}{6}\tilde{T}^3 + B_{m0}, & \hat{B} &= B_0,\\
\tilde{S}_m &= \tilde{T}, & \tilde{S} &= \frac{\sigma}{2}\tilde{T}^2, & \tilde{E}_m &= \tilde{T}, & \tilde{E} &= \frac{\xi}{2}\tilde{T}^2,\\
\tilde{F}_m &= \tilde{T}, & \tilde{F} &= \frac{1}{2}\tilde{T}^2. & & & &
\end{aligned} \tag{3.66}$$

We plot these asymptotic approximations against the full solution in Figure 3.5. This is the first timescale on which the efflux gene *acrAB* is transcribed. We notice that this is being driven by the secondary TAs binding to the promoter site of *acrAB*.

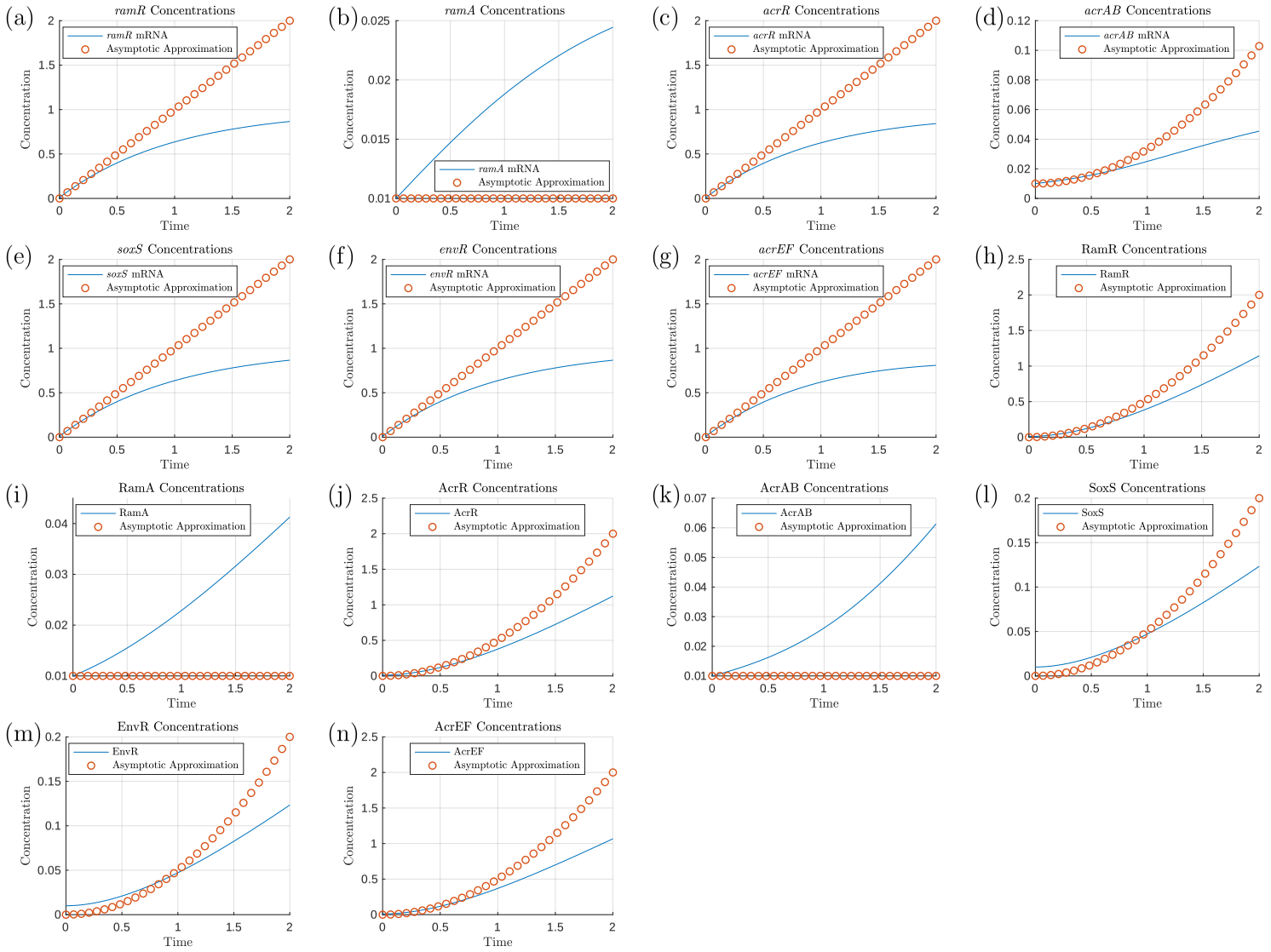

Figure 3.5: Asymptotic approximations on timescale 4 for the wild-type dynamics ($\epsilon = 0.01$). On this timescale, time is $O(\epsilon^{\frac{1}{6}})$, so we expect the asymptotics to be accurate around $T = \epsilon^{\frac{1}{6}} \approx 0.4642$. For reference, the previous and subsequent timescales have time at $O(\epsilon^{\frac{1}{4}})$ and $O(\epsilon^{\frac{1}{8}})$ respectively. Note we depict the simulations over a longer period of time than earlier timescales.

3.6.5 Timescale 5: AcrAB translation

We move onto the fifth timescale, here the translation term for AcrAB appears in the leading order balance in equation (3.68). We take the following scalings based on the variables on the previous timescale's long-term behaviour

$$\begin{aligned}
\bar{T} &= \epsilon^{-\frac{1}{24}} T', & \bar{R}_m &= \epsilon^{-\frac{1}{24}} R'_m, & \bar{C}_m &= \epsilon^{-\frac{1}{24}} C'_m, & \bar{S}_m &= \epsilon^{-\frac{1}{24}} S'_m, \\
\bar{E}_m &= \epsilon^{-\frac{1}{24}} E'_m, & \bar{F}_m &= \epsilon^{-\frac{1}{24}} F'_m, & \bar{R} &= \epsilon^{-\frac{1}{12}} R', & \bar{C} &= \epsilon^{-\frac{1}{12}} C', \\
\hat{S} &= \epsilon^{-\frac{1}{12}} S', & \hat{E} &= \epsilon^{-\frac{1}{12}} E', & \bar{F} &= \epsilon^{-\frac{1}{12}} F', & \hat{B}_m &= \epsilon^{-\frac{1}{8}} B'_m.
\end{aligned} \tag{3.67}$$

The system of equations rescaled for the fifth timescale is

$$\begin{aligned}
\frac{dR'_m}{dT'} &= 1 - \epsilon^{\frac{1}{8}} R'_m, & \frac{dR'}{dT'} &= \mu\rho\, R'_m - \epsilon^{\frac{9}{8}} \mu\Delta\, R', \\
\frac{d\hat{A}_m}{dT'} &= \frac{\epsilon^{\frac{1}{8}} \hat{A}}{(\epsilon\hat{A}+1)(\epsilon^{\frac{1}{4}} R'+1)} + \epsilon^{\frac{1}{8}}\alpha - \epsilon^{\frac{1}{8}} \hat{A}_m, & \frac{d\hat{A}}{dT'} &= \epsilon^{\frac{1}{8}}\theta\, \hat{A}_m - \epsilon^{\frac{5}{8}}\upsilon\, \hat{A} - \epsilon^{\frac{9}{8}}\Delta\hat{A}, \\
\frac{dC'_m}{dT'} &= \frac{\lambda}{\epsilon\hat{A}+\lambda} - \epsilon^{\frac{1}{8}} C'_m, & \frac{dC'}{dT'} &= \gamma\, C'_m - \epsilon^{\frac{9}{8}}\Delta C', \\
\frac{dB'_m}{dT'} &= \frac{\epsilon^{\frac{1}{4}}\hat{A} + S'}{(1+\epsilon^{\frac{3}{4}} S' + \epsilon\hat{A})(1+\epsilon^{\frac{3}{4}} E' + \epsilon^{\frac{1}{4}} C')} - \epsilon^{\frac{1}{8}} B'_m, & \frac{d\hat{B}}{dT'} &= \beta\, B'_m - \epsilon^{\frac{9}{8}}\Delta\, \hat{B}, \\
\frac{dS'_m}{dT'} &= 1 - \epsilon^{\frac{1}{8}} S'_m, & \frac{dS'}{dT'} &= \sigma\, S'_m - \epsilon^{\frac{9}{8}}\Delta\, S', \\
\frac{dE'_m}{dT'} &= 1 - \epsilon^{\frac{1}{8}} E'_m, & \frac{dE'}{dT'} &= \xi\, E'_m - \epsilon^{\frac{9}{8}}\Delta\, E', \\
\frac{dF'_m}{dT'} &= \frac{\eta}{\eta + \epsilon^{\frac{3}{4}} E'} - \epsilon^{\frac{1}{8}} F'_m, & \frac{dF'}{dT'} &= \frac{F'_m}{\epsilon\omega\hat{B}+1} - \epsilon^{\frac{9}{8}}\Delta F'.
\end{aligned} \tag{3.68}$$

At leading order, we have the following system of equations

$$\begin{aligned}
\frac{dR'_m}{dT'} &= 1, & \frac{dR'}{dT'} &= \mu\rho\, R'_m, \\
\frac{d\hat{A}_m}{dT'} &= 0, & \frac{d\hat{A}}{dT'} &= 0, \\
\frac{dC'_m}{dT'} &= 1, & \frac{dC'}{dT'} &= \gamma\, C'_m,
\end{aligned}$$

$$\begin{aligned}
\frac{dB'_m}{dT'} &= S', & \frac{d\hat{B}}{dT'} &= \beta B'_m,\\
\frac{dS'_m}{dT'} &= 1, & \frac{dS'}{dT'} &= \sigma S'_m,\\
\frac{dE'_m}{dT'} &= 1, & \frac{dE'}{dT'} &= \xi E'_m,\\
\frac{dF'_m}{dT'} &= 1, & \frac{dF'}{dT'} &= F'_m.
\end{aligned} \tag{3.69}$$

Solving this leading order system and matching to the long-term dominant behaviour on the previous timescale gives the following asymptotic approximations

$$\begin{aligned}
R'_m &= T', & R' &= \frac{\mu\rho}{2}T'^2, & \hat{A}_m &= A_{m0}, & \hat{A} &= A_0,\\
C'_m &= T', & C' &= \frac{\gamma}{2}T'^2, & B'_m &= \frac{\sigma}{6}T'^3, & \hat{B} &= \frac{\beta\sigma}{24}T'^4 + B_0,\\
S'_m &= T', & S' &= \frac{\sigma}{2}T'^2, & E'_m &= T', & E' &= \frac{\xi}{2}T'^2,\\
F'_m &= T', & F' &= \frac{1}{2}T'^2.
\end{aligned} \tag{3.70}$$

The above asymptotic approximations are plotted against the full solution in Figure 3.6. In this timescale, we have translation of AcrAB at the leading order, we note that this is being driven here by the secondary TA. We note there is disparity between the approximations and numerics. We could eliminate this by matching to additional orders of behaviour on the previous timescale, however for simplicity in solutions for the latter timescales, we have opted not to do so. We also note that these discrepancies decrease when $\epsilon \to 0$.

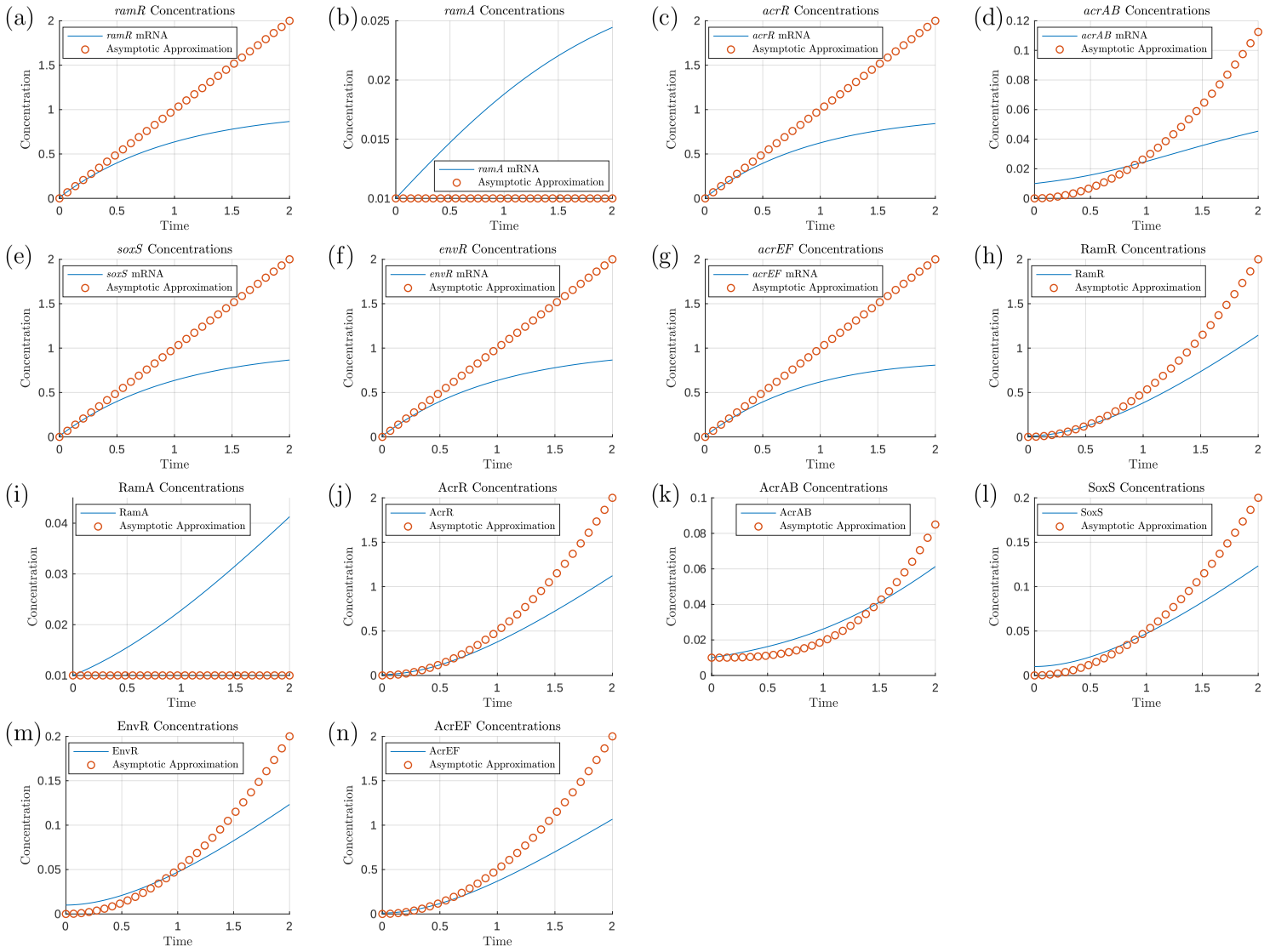

Figure 3.6: Asymptotic approximations on timescale 5 for the wild-type dynamics ($\epsilon = 0.01$). On this timescale, time is $O(\epsilon^{\frac{1}{8}})$, so we expect the asymptotics to be accurate around $T = \epsilon^{\frac{1}{8}} \approx 0.5623$. For reference, the previous and subsequent timescales have time at $O(\epsilon^{\frac{1}{6}})$ and $O(1)$ respectively.

3.6.6 Timescale 6: mRNA degradation and full protein translation

For this timescale, mRNA degradation and expression of *ramA* enters the leading order balance in all mRNA equations and (3.72). We take the following variable scalings

$$\begin{aligned}
&T' = \epsilon^{-\frac{1}{8}} T^\dagger, \quad R'_m = \epsilon^{-\frac{1}{8}} R^\dagger_m, \quad C'_m = \epsilon^{-\frac{1}{8}} C^\dagger_m, \quad S'_m = \epsilon^{-\frac{1}{8}} S^\dagger_m, \quad E'_m = \epsilon^{-\frac{1}{8}} E^\dagger_m, \\
&F'_m = \epsilon^{-\frac{1}{8}} F^\dagger_m, \quad R' = \epsilon^{-\frac{1}{4}} R^\dagger, \quad C' = \epsilon^{-\frac{1}{4}} C^\dagger, \quad S' = \epsilon^{-\frac{1}{4}} S^\dagger, \quad E' = \epsilon^{-\frac{1}{4}} E^\dagger, \\
&F' = \epsilon^{-\frac{1}{4}} F^\dagger, \quad B'_m = \epsilon^{-\frac{3}{8}} B^\dagger_m, \quad \hat{B} = \epsilon^{-\frac{1}{2}} B^\dagger.
\end{aligned} \tag{3.71}$$

After rescaling, the system of equations for the sixth timescale is

$$\begin{aligned}
\frac{dR^\dagger_m}{dT^\dagger} &= 1 - R^\dagger_m, & \frac{dR^\dagger}{dT^\dagger} &= \mu\rho\, R^\dagger_m - \epsilon\mu\Delta\, R^\dagger, \\
\frac{d\hat{A}_m}{dT^\dagger} &= \frac{\hat{A}}{(\epsilon\hat{A}+1)(R^\dagger+1)} + \alpha - \hat{A}_m, & \frac{d\hat{A}}{dT^\dagger} &= \theta\, \hat{A}_m - \epsilon^{\frac{1}{2}} \upsilon\, \hat{A} - \epsilon\Delta\hat{A}, \\
\frac{dC^\dagger_m}{dT^\dagger} &= \frac{\lambda}{\epsilon\hat{A}+\lambda} - C^\dagger_m, & \frac{dC^\dagger}{dT^\dagger} &= \gamma\, C^\dagger_m - \epsilon\Delta C^\dagger, \\
\frac{dB^\dagger_m}{dT^\dagger} &= \frac{\epsilon^{\frac{1}{2}}\hat{A} + S^\dagger}{(1+\epsilon^{\frac{1}{2}}S^\dagger + \epsilon\hat{A})(1+\epsilon^{\frac{1}{2}}E^\dagger + C^\dagger)} - B^\dagger_m, & \frac{dB^\dagger}{dT^\dagger} &= \beta\, B^\dagger_m - \epsilon\Delta\, B^\dagger, \\
\frac{dS^\dagger_m}{dT^\dagger} &= 1 - S^\dagger_m, & \frac{dS^\dagger}{dT^\dagger} &= \sigma\, S^\dagger_m - \epsilon\Delta\, S^\dagger, \\
\frac{dE^\dagger_m}{dT^\dagger} &= 1 - E^\dagger_m, & \frac{dE^\dagger}{dT^\dagger} &= \xi\, E^\dagger_m - \epsilon\Delta\, E^\dagger, \\
\frac{dF^\dagger_m}{dT^\dagger} &= \frac{\eta}{\eta + \epsilon^{\frac{1}{2}}E^\dagger} - F^\dagger_m, & \frac{dF^\dagger}{dT^\dagger} &= \frac{F^\dagger_m}{\epsilon^{\frac{1}{2}}\omega B^\dagger + 1} - \epsilon\Delta F^\dagger.
\end{aligned} \tag{3.72}$$

At leading order, we have the following system of equations

$$\begin{aligned}
\frac{dR^\dagger{}_m}{dT^\dagger} &= 1 - R^\dagger_m, & \frac{dR^\dagger}{dT^\dagger} &= \mu\rho\, R^\dagger_m, \\
\frac{d\hat{A}_m}{dT^\dagger} &= \frac{\hat{A}}{R^\dagger+1} + \alpha - \hat{A}_m, & \frac{d\hat{A}}{dT^\dagger} &= \theta\hat{A}_m, \\
\frac{dC^\dagger_m}{dT^\dagger} &= 1 - C^\dagger_m, & \frac{dC^\dagger}{dT^\dagger} &= \gamma\, C^\dagger_m,
\end{aligned}$$

$$\begin{aligned}
\frac{dB^\dagger{}_m}{dT^\dagger} &= \frac{S^\dagger}{1+C^\dagger} - B^\dagger_m, & \frac{dB^\dagger}{dT^\dagger} &= \beta B^\dagger_m,\\
\frac{dS^\dagger_m}{dT^\dagger} &= 1 - S^\dagger_m, & \frac{dS^\dagger}{dT^\dagger} &= \sigma S^\dagger_m,\\
\frac{dE^\dagger_m}{dT^\dagger} &= 1 - E^\dagger_m, & \frac{dE^\dagger}{dT^\dagger} &= \xi E^\dagger_m,\\
\frac{dF^\dagger_m}{dT^\dagger} &= 1 - F^\dagger_m, & \frac{dF^\dagger}{dT^\dagger} &= F^\dagger_m.
\end{aligned} \tag{3.73}$$

Solving and matching to the long-term dominant behaviour on the previous timescale gives the following asymptotic approximations

$$\begin{aligned}
&R^\dagger_m = 1 - e^{-T^\dagger}, \quad R^\dagger = \mu\rho(T^\dagger - e^{-T^\dagger} - 1), && C^\dagger_m = 1 - e^{-T^\dagger}, \quad C^\dagger = \gamma(T^\dagger - e^{-T^\dagger} - 1),\\
&B^\dagger_m = \frac{\sigma T^\dagger}{\gamma T^\dagger + 1}, \quad B^\dagger = \frac{\beta\sigma}{\gamma}\left(T^\dagger - \frac{\ln(T^\dagger\gamma + 1)}{\gamma}\right), && S^\dagger_m = 1 - e^{-T^\dagger}, \quad S^\dagger = \sigma(T^\dagger - e^{-T^\dagger} - 1),\\
&E^\dagger_m = 1 - e^{-T^\dagger}, \quad E^\dagger = \xi(T^\dagger - e^{-T^\dagger} - 1), && F^\dagger_m = 1 - e^{-T^\dagger}, \quad F^\dagger = T^\dagger - e^{-T^\dagger} - 1,
\end{aligned} \tag{3.74}$$

while the behaviour for both *ramA* mRNA ($\hat{A}_m$) and RamA protein ($\hat{A}$) depends on the relationship between the parameters μ,θ and ρ. If $\dfrac{\theta}{\mu\rho} \neq 1$ we have

$$\begin{aligned}
\hat{A}_m &= \frac{(\mu\rho A_0 - \theta\,(\alpha + A_0))\left(T^\dagger\mu\rho + 1\right)^{\frac{\theta}{\mu\rho}} + \left(T^\dagger\mu\rho + 1\right)\theta\,\alpha}{(\mu\rho - \theta)(\mu\rho T^\dagger + 1)},\\
\hat{A} &= \frac{(\mu\rho A_0 - \theta\,(\alpha + A_0))\left(T^\dagger\mu\rho + 1\right)^{\frac{\theta}{\mu\rho}} + \left(T^\dagger\mu\rho + 1\right)\theta\,\alpha}{\mu\rho - \theta}.
\end{aligned} \tag{3.75}$$

In this case we have different long term blow up behaviour depending on whether $\dfrac{\theta}{\mu\rho} < 1$ or $\dfrac{\theta}{\mu\rho} > 1$, detailed below. For the case where $\dfrac{\theta}{\mu\rho} = 1$ we have

$$\hat{A}_m = \alpha\,\ln\left(T^\dagger + 1\right) + A_0 + \alpha, \qquad \hat{A} = \left(\alpha\,\ln\left(T^\dagger + 1\right) + A_0\right)\left(T^\dagger + 1\right). \tag{3.76}$$

Here we have taken the case where $\theta = 1, \mu = 1, \rho = 1$ for simplicity of displaying the solutions.

We can see that we have three cases of long-term behaviour for both *ramA* mRNA ($\hat{A}_m$) and RamA protein ($\hat{A}$). We exhibit the relation between this long-term behaviour and our parameter groupings as follows

$$\hat{A}_m \sim \begin{cases} C_A & \text{for } \frac{\theta}{\mu\rho} < 1, \\ \ln(T^\dagger) & \text{for } \frac{\theta}{\mu\rho} = 1, \\ T^{\dagger\,\frac{\theta}{\mu\rho}-1} & \text{for } \frac{\theta}{\mu\rho} > 1, \end{cases} \tag{3.77}$$

$$\hat{A} \sim \begin{cases} T^\dagger, & \text{for } \frac{\theta}{\mu\rho} < 1, \\ T^\dagger \ln(T^\dagger) & \text{for } \frac{\theta}{\mu\rho} = 1, \\ T^{\dagger\,\frac{\theta}{\mu\rho}} & \text{for } \frac{\theta}{\mu\rho} > 1, \end{cases} \tag{3.78}$$

where here C_A is a constant. We note that the parameter θ relates to RamA production, whilst ρ relates to RamR production. Since RamR is a repressor of *ramA* expression, we might expect its rate of production to dominate, thus we note that the case $\dfrac{\theta}{\mu\rho} < 1$ is the most biologically plausible and use the resulting behaviour to move to the next timescale. For all future numerical simulations, we set $\theta = 0.5$ to satisfy this inequality.

We plot these asymptotic approximations against the full solution in Figure 3.7. This is the first timescale where the *ramA* gene is expressed at leading order, this is due to there being little RamA protein in the system to activate its own expression. We note we have transcription of *ramA* mRNA and translation of RamR coming into this timescale. In addition to this we have degradation terms for all mRNAs, this is causing the mRNAs to level off and reach steady state. In addition to this, the local repressor of *acrAB* (AcrR) is bound to the operator site of *acrAB* which is in effect limiting the transcription of this gene. For *acrAB* mRNA we have a slight mismatch of the approximation to the solution, we could prevent this by matching to lower orders of behaviour on the previous timescale (or reduce the discrepancy with a smaller value of ϵ). However, we have chosen not to do this for simplicity of solutions on this and further timescales.

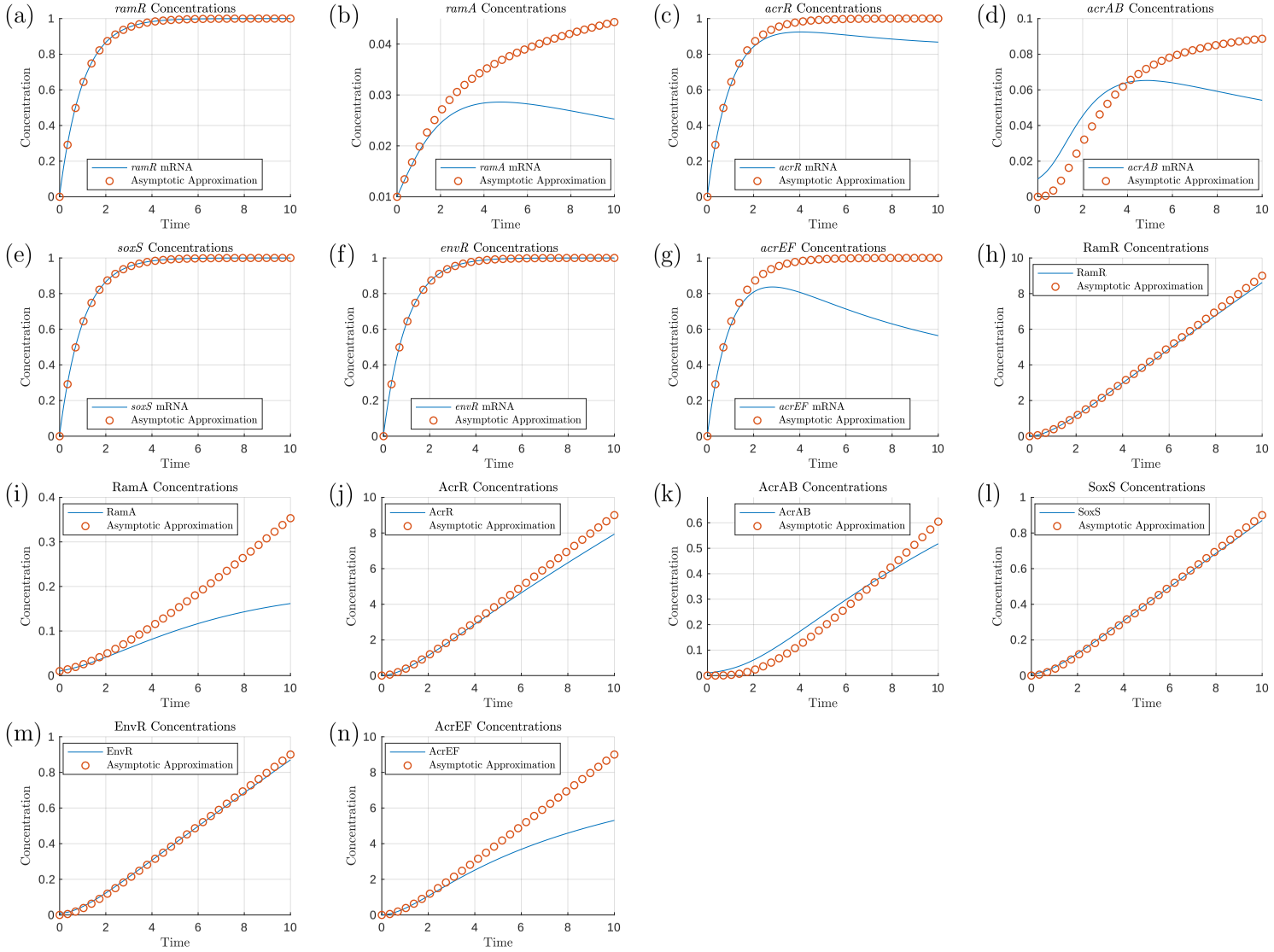

Figure 3.7: Asymptotic approximations on timescale 6 for the wild-type dynamics ($\epsilon = 0.01$). On this timescale, time is $O(1)$, so we expect the asymptotics to be accurate around $T = 1$. For reference, the previous and subsequent timescales have time at $O(\epsilon^{\frac{1}{8}})$ and $O(\epsilon^{-\frac{1}{2}})$ respectively. Note we depict the simulations over a longer period of time than earlier timescales.

3.6.7 Timescale 7: Degradation of RamA, inhibition of *acrAB* and *acrEF*

For this timescale, we have a change of the terms involved in transcription of *acrAB* and *acrEF*, with new terms emerging at leading order in equations (3.80) and (3.81). We also have RamA degradation entering the leading order balance in equation (3.82). We take the following variable scalings:

$$T^\dagger = \epsilon^{-\frac{1}{2}} T^\ddagger, \qquad R^\dagger = \epsilon^{-\frac{1}{2}} R^\ddagger, \qquad C^\dagger = \epsilon^{-\frac{1}{2}} C^\ddagger, \qquad B^\dagger = \epsilon^{-\frac{1}{2}} B^\ddagger,$$
$$S^\dagger = \epsilon^{-\frac{1}{2}} S^\ddagger, \qquad E^\dagger = \epsilon^{-\frac{1}{2}} E^\ddagger, \qquad F^\dagger = \epsilon^{-\frac{1}{2}} F^\ddagger, \qquad \hat{A} = \epsilon^{-\frac{1}{2}} A^\ddagger. \tag{3.79}$$

The system of equations rescaled for the seventh timescale is

$$\begin{aligned}
\epsilon^{\frac{1}{2}} \frac{dR_m^\dagger}{dT^\ddagger} &= 1 - R_m^\dagger, \\
\epsilon \frac{d\hat{A}_m}{dT^\ddagger} &= \frac{A^\ddagger}{(\epsilon^{\frac{1}{2}} A^\ddagger + 1)(\epsilon^{-\frac{1}{2}} R^\ddagger + 1)} + \epsilon^{\frac{1}{2}} \alpha - \epsilon^{\frac{1}{2}} \hat{A}_m, \\
\epsilon^{\frac{1}{2}} \frac{dC_m^\dagger}{dT^\ddagger} &= \frac{\lambda}{\epsilon^{\frac{1}{2}} A^\ddagger + \lambda} - C_m^\dagger, \\
\epsilon \frac{dB_m^\dagger}{dT^\ddagger} &= \frac{\epsilon^{\frac{1}{2}} A^\ddagger + S^\ddagger}{(1 + S^\ddagger + \epsilon^{\frac{1}{2}} A^\ddagger)(1 + E^\ddagger + \epsilon^{-\frac{1}{2}} C^\ddagger)} - \epsilon^{\frac{1}{2}} B_m^\dagger,
\end{aligned} \tag{3.80}$$

$$\begin{aligned}
\epsilon^{\frac{1}{2}} \frac{dS_m^\dagger}{dT^\ddagger} &= 1 - S_m^\dagger, \\
\epsilon^{\frac{1}{2}} \frac{dE_m^\dagger}{dT^\ddagger} &= 1 - E_m^\dagger, \\
\epsilon^{\frac{1}{2}} \frac{dF_m^\dagger}{dT^\ddagger} &= \frac{\eta}{\eta + E^\ddagger} - F_m^\dagger,
\end{aligned} \tag{3.81}$$

$$\begin{aligned}
\frac{dR^\ddagger}{dT^\ddagger} &= \mu\rho\, R_m^\dagger - \epsilon^{\frac{1}{2}} \mu\Delta\, R^\ddagger, \\
\frac{dA^\ddagger}{dT^\ddagger} &= \theta\, \hat{A}_m - \upsilon\, A^\ddagger - \epsilon^{\frac{1}{2}} \Delta A^\ddagger, \\
\frac{dC^\ddagger}{dT^\ddagger} &= \gamma\, C_m^\dagger - \epsilon^{\frac{1}{2}} \Delta C^\ddagger, \\
\frac{dB^\ddagger}{dT^\ddagger} &= \beta\, B_m^\ddagger - \epsilon^{\frac{1}{2}} \Delta\, B^\ddagger, \\
\frac{dS^\ddagger}{dT^\ddagger} &= \sigma\, S_m^\dagger - \epsilon^{\frac{1}{2}} \Delta\, S^\ddagger, \\
\frac{dE^\ddagger}{dT^\ddagger} &= \xi\, E_m^\dagger - \epsilon^{\frac{1}{2}} \Delta\, E^\ddagger, \\
\frac{dF^\ddagger}{dT^\ddagger} &= \frac{F_m^\dagger}{\omega B^\ddagger + 1} - \epsilon^{\frac{1}{2}} \Delta F^\ddagger.
\end{aligned} \tag{3.82}$$

At leading order, we have the following system of equations

$$\begin{aligned}
R_m^\dagger &= 1, \\
\hat{A}_m &= \frac{A^\ddagger}{R^\ddagger} + \alpha, \\
C_m^\dagger &= 1,
\end{aligned}$$

$$\begin{aligned}
\frac{dR^\ddagger}{dT^\ddagger} &= \mu\rho\, R_m^\dagger, \\
\frac{dA^\ddagger}{dT^\ddagger} &= \theta \hat{A}_m - \upsilon\, A^\ddagger, \\
\frac{dC^\ddagger}{dT^\ddagger} &= \gamma\, C_m^\dagger,
\end{aligned}$$

$$
\begin{aligned}
B_m^\dagger &= \frac{S^\ddagger}{(1+S^\ddagger)C^\ddagger}, & \frac{dB^\ddagger}{dT^\ddagger} &= \beta B_m^\dagger,\\
S_m^\dagger &= 1, & \frac{dS^\ddagger}{dT^\ddagger} &= \sigma S_m^\dagger,\\
E_m^\dagger &= 1, & \frac{dE^\ddagger}{dT^\ddagger} &= \xi E_m^\dagger,\\
F_m^\dagger &= \frac{\eta}{\eta+E^\ddagger}, & \frac{dF^\ddagger}{dT^\ddagger} &= \frac{F_m^\dagger}{\omega B^\ddagger+1}.
\end{aligned} \tag{3.83}
$$

Solving the leading order balance and matching to the long-term dominant behaviour on the previous timescale gives the following asymptotic approximations

$$
\begin{aligned}
&R_m^\dagger = 1, && R^\ddagger = \mu\rho T^\ddagger, && \hat{A}_m = \frac{\alpha\upsilon\mu\rho T^\ddagger}{\upsilon\mu\rho T^\ddagger-\theta}, && A^\ddagger = \frac{\theta\alpha\mu\rho T^\ddagger}{\upsilon\mu\rho T^\ddagger-\theta},\\
&C_m^\dagger = 1, && C^\ddagger = \gamma T^\ddagger, && B_m^\dagger = \frac{\sigma}{\gamma(\sigma T^\ddagger+1)}, && S_m^\dagger = 1,\\
&S^\ddagger = \sigma T^\ddagger, && E_m^\dagger = 1, && E^\ddagger = \xi T^\ddagger, && F_m^\dagger = \frac{\eta}{\eta+\xi T^\ddagger},\\
&B^\ddagger = \frac{\beta}{\gamma}\ln(\sigma T^\ddagger+1), && && F^\ddagger = \frac{\eta\gamma}{\beta\omega\xi}\ln(\beta\omega\ln(\xi T^\ddagger+\eta)+\gamma). &&
\end{aligned} \tag{3.84}
$$

We plot asymptotic approximations of those variables that evolve on this timescale against the numerical solutions in Figure 3.8. On this timescale, we have repressor proteins dominating the transcription terms for *acrAB* and *acrEF*. With lower levels of transcription, degradation dominates and the concentrations of the mRNAs lower. We note that in this wild-type case RamA production occurs late compared to other proteins (starting on the previous timescale) and is quickly degraded to achieve only low levels in comparison to other proteins in the system. On this timescale, all other mRNAs have reached steady state and AcrAB and AcrEF grow logarithmically. With logarithmic behaviour for both $B^\ddagger$ and $F^\ddagger$, we must justify the scalings we take to the next timescale. Suppose we scale

our variable as $T^{\ddagger} = \epsilon^{-\alpha} T^{\diamond}$ then

$$\begin{aligned} B^{\ddagger} &\sim \ln(T^{\ddagger}), \\ &\sim \ln(\epsilon^{-\alpha} T^{\diamond}), \\ &\sim \alpha \ln(1/\epsilon) + \ln(T^{\diamond}), \\ &\sim \ln(1/\epsilon) + \ln(T^{\diamond}). \end{aligned} \tag{3.85}$$

This means that moving to the next timescale, we should scale $B^{\ddagger}$ by $\ln(1/\epsilon)$. We can apply a similar process again supposing we scale our variable as $T^{\ddagger} = \epsilon^{-\alpha} T^{\diamond}$ then

$$\begin{aligned} F^{\ddagger} &\sim \ln(\ln(T^{\ddagger})), \\ &\sim \ln(\ln(\epsilon^{-\alpha} T^{\diamond})), \\ &\sim \ln(\alpha \ln(1/\epsilon) + \ln(T^{\diamond})), \\ &\sim \ln(\alpha \ln(1/\epsilon)(1 + \frac{\ln(T^{\diamond})}{\alpha \ln(1/\epsilon)})), \\ &\sim \ln(\alpha) + \ln(\ln(1/\epsilon)) + \ln(1 + \frac{\ln(T^{\diamond})}{\alpha \ln(1/\epsilon)}), \\ &\sim \ln(\alpha) + \ln(\ln(1/\epsilon)) + \ln(\frac{\ln(T^{\diamond})}{\alpha \ln(1/\epsilon)}), \\ &\sim \ln(\ln(1/\epsilon)) + \ln(\ln(T^{\diamond})). \end{aligned} \tag{3.86}$$

This means that moving to the next timescale, we should scale $F^{\ddagger}$ by $\ln(\ln(1/\epsilon))$.

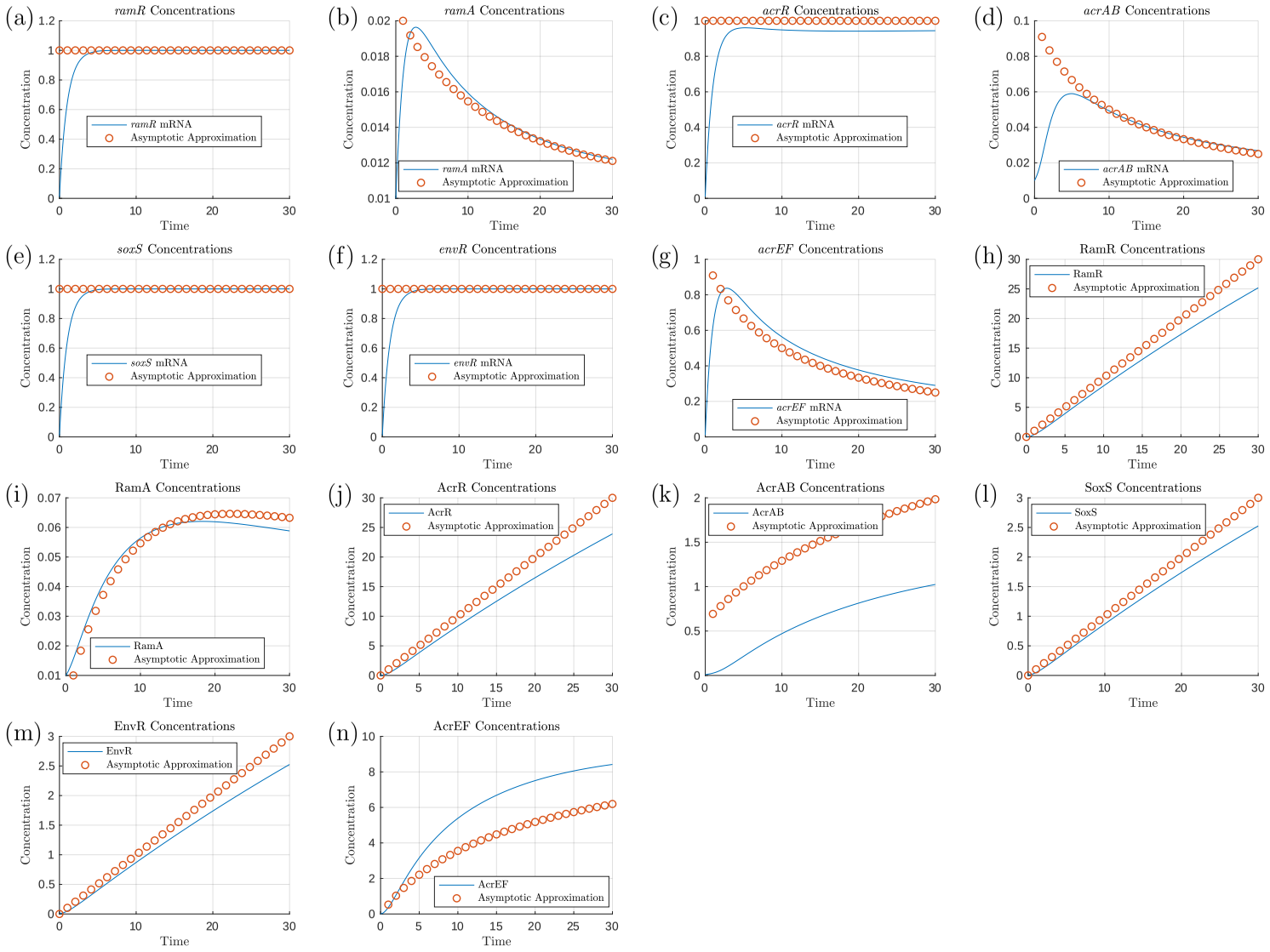

Figure 3.8: Asymptotic approximations on timescale 7 for the wild-type dynamics ($\epsilon = 0.01$). On this timescale, time is $O(\epsilon^{-\frac{1}{2}})$, so we expect the asymptotics to be accurate around $T = \epsilon^{-\frac{1}{2}} = 10$. For reference, the previous and subsequent timescales have time at $O(1)$ and $O(\epsilon^{-1}\phi^{-1}\delta^{-1})$ respectively. Disparities in these simulations can be reduced by reducing the value of ϵ.

3.6.8 Timescale 8: AcrEF degradation

On this timescale, degradation of AcrEF emerges in equation (3.88). We take the following scalings:

$$
\begin{aligned}
T^{\ddagger} &= \epsilon^{-\frac{1}{2}} \ln(1/\epsilon)^{-1} \ln(\ln(1/\epsilon))^{-1} T^{\diamond}, & R^{\ddagger} &= \epsilon^{-\frac{1}{2}} \ln(1/\epsilon)^{-1} \ln(\ln(1/\epsilon))^{-1} R^{\diamond}, \\
C^{\ddagger} &= \epsilon^{-\frac{1}{2}} \ln(1/\epsilon)^{-1} \ln(\ln(1/\epsilon))^{-1} C^{\diamond}, & S^{\ddagger} &= \epsilon^{-\frac{1}{2}} \ln(1/\epsilon)^{-1} \ln(\ln(1/\epsilon))^{-1} S^{\diamond}, \\
E^{\ddagger} &= \epsilon^{-\frac{1}{2}} \ln(1/\epsilon)^{-1} \ln(\ln(1/\epsilon))^{-1} E^{\diamond}, & B_m^{\dagger} &= \epsilon^{\frac{1}{2}} \ln(1/\epsilon) \ln(\ln(1/\epsilon)) B_m^{\diamond}, \\
F_m^{\dagger} &= \epsilon^{\frac{1}{2}} \ln(1/\epsilon) \ln(\ln(1/\epsilon)) F_m^{\diamond}, & B^{\ddagger} &= \ln(1/\epsilon) B^{\diamond}, \\
F^{\ddagger} &= \ln(\ln(1/\epsilon)) F^{\diamond}.
\end{aligned}
\tag{3.87}
$$

For simplicity in presentation, we choose to express the log functions as $\phi = \ln(1/\epsilon)^{-1}$ and $\delta = \ln(\ln(1/\epsilon))^{-1}$. Using these scalings, the system of equations rescaled for the eighth timescale is

$$
\begin{aligned}
\frac{dR^{\diamond}}{dT^{\diamond}} &= \mu\rho R_m^{\dagger} - \phi\delta\mu\Delta R^{\diamond}, \\
\epsilon\phi^{-1}\delta^{-1}\frac{dR_m^{\dagger}}{dT^{\diamond}} &= 1 - R_m^{\dagger}, & \epsilon^{\frac{1}{2}}\phi^{-1}\delta^{-1}\frac{dA^{\ddagger}}{dT^{\diamond}} &= \theta\hat{A}_m - \upsilon\, A^{\ddagger} - \epsilon^{\frac{1}{2}}\Delta A^{\ddagger}, \\
\epsilon^{\frac{3}{2}}\phi^{-1}\delta^{-1}\frac{d\hat{A}_m}{dT^{\diamond}} &= \frac{A^{\ddagger}}{(\epsilon^{\frac{1}{2}}A^{\ddagger}+1)(\epsilon^{-1}\phi\delta R^{\diamond}+1)} + \epsilon^{\frac{1}{2}}\alpha - \epsilon^{\frac{1}{2}}\hat{A}_m, & \frac{dC^{\diamond}}{dT^{\diamond}} &= \gamma\, C_m^{\dagger} - \phi\delta\Delta C^{\diamond}, \\
\epsilon\phi^{-1}\delta^{-1}\frac{dC_m^{\dagger}}{dT^{\diamond}} &= \frac{\lambda}{\epsilon^{\frac{1}{2}}A^{\ddagger}+\lambda} - C_m^{\dagger}, & \phi^{-1}\delta^{-1}\frac{dB^{\diamond}}{dT^{\diamond}} &= \delta^{-1}\beta B_m^{\diamond} - \Delta B^{\diamond}, \\
\epsilon^2\phi^{-2}\delta^{-2}\frac{dB_m^{\diamond}}{dT^{\diamond}} &= \frac{\epsilon^{\frac{1}{2}}A^{\ddagger} + \epsilon^{-\frac{1}{2}}\phi\delta S^{\diamond}}{(1+\epsilon^{-\frac{1}{2}}\phi\delta S^{\diamond} + \epsilon^{\frac{1}{2}}A^{\ddagger})(1+\epsilon^{-\frac{1}{2}}\phi\delta E^{\diamond} + \epsilon^{-1}\phi\delta C^{\diamond})} - \epsilon\phi^{-1}\delta^{-1}B_m^{\diamond}, \\
\epsilon\phi^{-1}\delta^{-1}\frac{dS_m^{\dagger}}{dT^{\diamond}} &= 1 - S_m^{\dagger}, & \frac{dS^{\diamond}}{dT^{\diamond}} &= \sigma S_m^{\dagger} - \phi\delta\Delta S^{\diamond}, \\
\epsilon\phi^{-1}\delta^{-1}\frac{dE_m^{\dagger}}{dT^{\diamond}} &= 1 - E_m^{\dagger}, & \frac{dE^{\diamond}}{dT^{\diamond}} &= \xi E_m^{\dagger} - \phi\delta\Delta E^{\diamond}, \\
\epsilon^{\frac{3}{2}}\phi^{-2}\delta^{-2}\frac{dF_m^{\diamond}}{dT^{\diamond}} &= \frac{\eta}{\eta + \epsilon^{-\frac{1}{2}}\phi\delta E^{\diamond}} - \epsilon^{\frac{1}{2}}\phi^{-1}\delta^{-1}F_m^{\diamond}, & \phi^{-1}\delta^{-1}\frac{dF^{\diamond}}{dT^{\diamond}} &= \frac{F_m^{\diamond}}{\omega B^{\diamond} + \phi} - \Delta F^{\diamond}.
\end{aligned}
\tag{3.88}
$$

At leading order, we have the following system of equations

$$\begin{aligned}
R_m^\dagger &= 1, & \frac{dR^\diamond}{dT^\diamond} &= \mu\rho\, R_m^\dagger,\\
\hat{A}_m &= \alpha, & A^\ddagger &= \frac{\theta}{\upsilon}\hat{A}_m,\\
C_m^\dagger &= 1, & \frac{dC^\diamond}{dT^\diamond} &= \gamma\, C_m^\dagger,\\
B_m^\diamond &= \frac{S^\diamond}{(\epsilon^{\frac{1}{2}}\phi^{-1}\delta^{-1}+S^\diamond)C^\diamond}, & \frac{dB^\diamond}{dT^\diamond} &= 0,\\
S_m^\dagger &= 1, & \frac{dS^\diamond}{dT^\diamond} &= \sigma S_m^\dagger,\\
E_m^\dagger &= 1, & \frac{dE^\diamond}{dT^\diamond} &= \xi E_m^\dagger,\\
F_m^\diamond &= \frac{\eta}{\epsilon^{\frac{1}{2}}\phi^{-1}\delta^{-1}\eta+E^\diamond}, & \frac{dF^\diamond}{dT^\diamond} &= 0.
\end{aligned} \tag{3.89}$$

To be able to match to the logarithmic behaviour on the previous timescale, we must go to second order for B and F. By taking the expansions $B = b_0 + \phi b_1 ...$ and $F = f_0 + \phi\delta f_1 + ...$, we have the following equations

$$\frac{db_1^\diamond}{dT^\diamond} = \beta B_m^\diamond, \tag{3.90}$$

$$\frac{df_1^\diamond}{dT^\diamond} = \frac{F_m^\diamond}{\omega b_0^\diamond} - \Delta f_0^\diamond. \tag{3.91}$$

Solving and matching to the long-term dominant behaviour on the previous timescale gives the following asymptotic approximations

$$\begin{aligned}
&R_m^\dagger = 1, && R^\diamond = \mu\rho T^\diamond, && \hat{A}_m = \alpha,\\
&A^\ddagger = \frac{\theta\alpha}{\upsilon}, && C_m^\dagger = 1, && C^\diamond = \gamma T^\diamond,\\
&S_m^\dagger = 1, && S^\diamond = \sigma T^\diamond, && E_m^\dagger = 1,\\
&E^\diamond = \xi T^\diamond, && B_m^\diamond = \frac{\sigma}{\gamma(\epsilon^{\frac{1}{2}}\phi^{-1}\delta^{-1}+\sigma T^\diamond)}, && F_m^\diamond = \frac{\eta}{\epsilon^{\frac{1}{2}}\phi^{-1}\delta^{-1}\eta+\xi T^\diamond},\\
&B^\diamond = \frac{\beta}{2\gamma} + \phi\frac{\beta}{\gamma}(\ln(\sigma T^\diamond + \epsilon^{\frac{1}{2}}\phi^{-1}\delta^{-1}) + \ln(\phi\delta)),\\
&F^\diamond = \frac{\eta\gamma}{\beta\omega\xi} + \delta\frac{\eta\gamma}{\beta\omega\xi}\ln(\beta\omega) + \phi\delta(\frac{\eta\gamma}{\beta\omega\xi}\ln(\xi T^\diamond + \epsilon^{\frac{1}{2}}\phi^{-1}\delta^{-1}) + \frac{\eta\gamma}{\beta\omega\xi}\ln(\phi\delta) + \gamma).
\end{aligned} \tag{3.92}$$

We plot these asymptotic approximations against the full solution in Figure 3.9. We include the second order terms to show the logarithmic behaviour of AcrAB and AcrEF. We note there is disparity in fit for the plots of AcrAB and AcrEF, therefore we include additional plots (Figure 3.9 (o) and (p)) with a smaller value of ϵ to prove the accuracy of the asymptotic approximations.

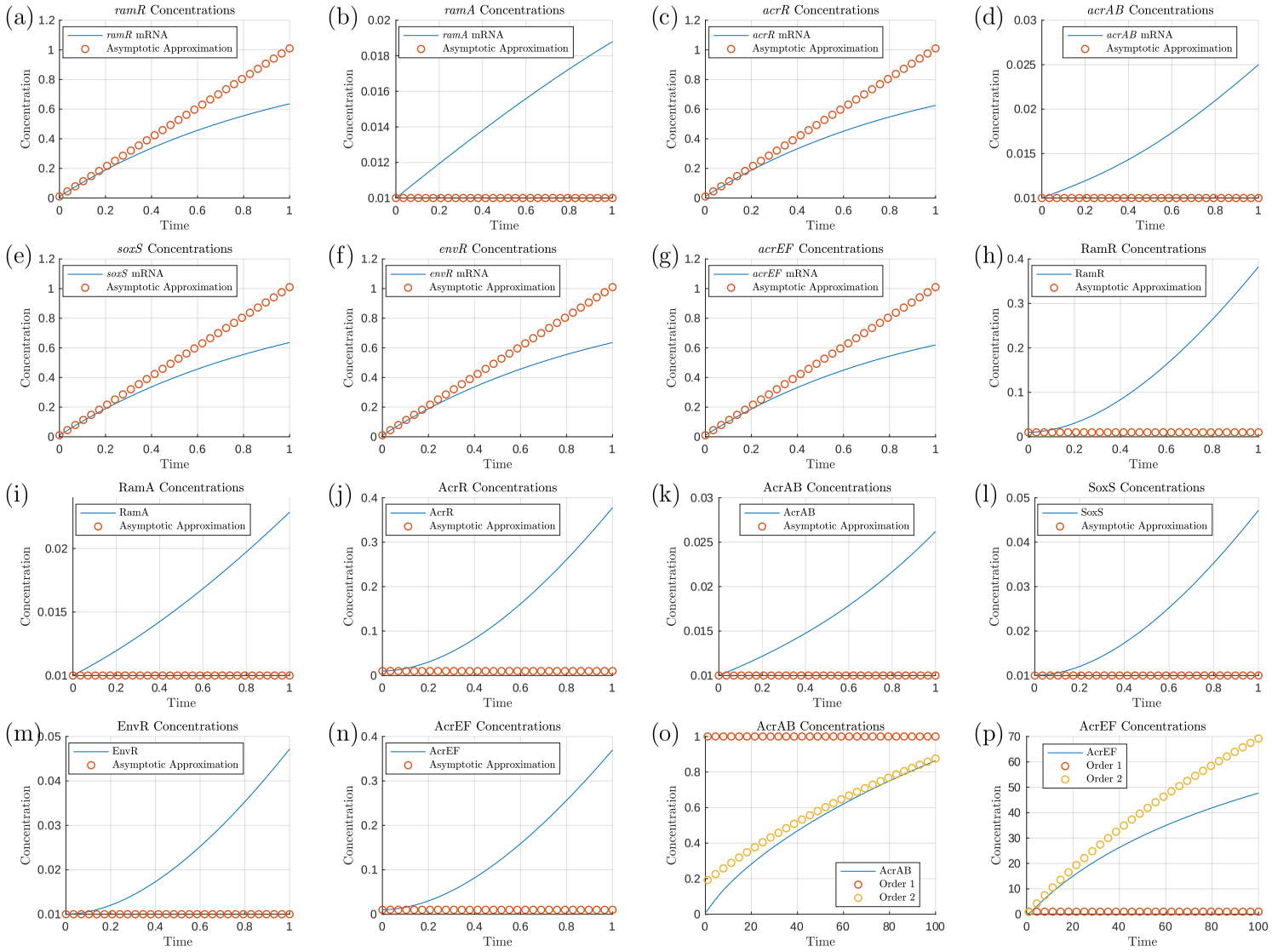

Figure 3.9: Asymptotic approximations on timescale 8 for the wild-type dynamics ($\epsilon = 0.01$). On this timescale, time is $O(\epsilon^{-1}\phi\delta)$, so we expect the asymptotics to be accurate around $T = \epsilon^{-1}\phi\delta \approx 14.2188$. For reference, the previous and subsequent timescales have time at $O(\epsilon^{-\frac{1}{2}})$ and $O(\epsilon^{-1})$ respectively. In (o) and (p), we exhibit the solutions of AcrAB and AcrEF with $\epsilon = 0.0001$ to prove the validity of the asymptotic approximations. Note we depict the simulations over a longer period of time than earlier timescales.

3.6.9 Timescale 9: final timescale, protein degradation

We move onto the final timescale, here degradation for all proteins that were not already at steady state emerge in the leading order balance. We take the following final scalings based on the variables of the previous timescale's long-term behaviour

$$\begin{aligned}
T^{\diamond} &= \ln(1/\epsilon)\ln(\ln(1/\epsilon))T^{+}, & R^{\diamond} &= \ln(1/\epsilon)\ln(\ln(1/\epsilon))R^{+},\\
C^{\diamond} &= \ln(1/\epsilon)\ln(\ln(1/\epsilon))C^{+}, & S^{\diamond} &= \ln(1/\epsilon)\ln(\ln(1/\epsilon))S^{+},\\
E^{\diamond} &= \ln(1/\epsilon)\ln(\ln(1/\epsilon))E^{+}, & B_m^{\diamond} &= \ln(1/\epsilon)^{-1}\ln(\ln(1/\epsilon))^{-1}B_m^{+},\\
F_m^{\diamond} &= \ln(1/\epsilon)^{-1}\ln(\ln(1/\epsilon))^{-1}F_m^{+}. & &
\end{aligned} \tag{3.93}$$

Our system of equations rescaled for the ninth timescale is

$$\begin{aligned}
\epsilon\frac{dR_m^{\dagger}}{dT^{+}} &= 1 - R_m^{\dagger}, & \frac{dR^{+}}{dT^{+}} &= \mu\rho\, R_m^{\dagger} - \mu\Delta\, R^{+},\\
\epsilon^{\frac{3}{2}}\frac{d\hat{A}_m}{dT^{+}} &= \frac{A^{\ddagger}}{(\epsilon^{\frac{1}{2}}A^{\ddagger}+1)(\epsilon^{-1}R^{+}+1)} + \epsilon^{\frac{1}{2}}\alpha - \epsilon^{\frac{1}{2}}\hat{A}_m, & \epsilon^{\frac{1}{2}}\frac{dA^{\ddagger}}{dT^{+}} &= \theta\,\hat{A}_m - \upsilon\, A^{\ddagger} - \epsilon^{\frac{1}{2}}\Delta A^{\ddagger},\\
\epsilon\frac{dC_m^{\dagger}}{dT^{+}} &= \frac{\lambda}{A^{+}+\lambda} - C_m^{\dagger}, & \frac{dC^{+}}{dT^{+}} &= \gamma\, C_m^{\dagger} - \Delta C^{+},\\
\epsilon^{2}\frac{dB_m^{+}}{dT^{+}} &= \frac{A^{+}+\epsilon^{-\frac{1}{2}}S^{+}}{(1+\epsilon^{-\frac{1}{2}}S^{+}+A^{+})(1+\epsilon^{-\frac{1}{2}}E^{+}+\epsilon^{-1}C^{+})} - \epsilon B_m^{+}, & \frac{dB^{\diamond}}{dT^{+}} &= \beta\phi\, B_m^{+} - \Delta\, B^{\diamond},\\
\epsilon\frac{dS_m^{\dagger}}{dT^{+}} &= 1 - S_m^{\dagger}, & \frac{dS^{+}}{dT^{+}} &= \sigma\, S_m^{\dagger} - \Delta\, S^{+},\\
\epsilon\frac{dE_m^{\dagger}}{dT^{+}} &= 1 - E_m^{\dagger}, & \frac{dE^{+}}{dT^{+}} &= \xi\, E_m^{\dagger} - \Delta\, E^{+},\\
\epsilon^{\frac{3}{2}}\frac{dF_m^{+}}{dT^{+}} &= \frac{\eta}{\eta+\epsilon^{-\frac{1}{2}}E^{+}} - \epsilon^{\frac{1}{2}}F_m^{+}, & \frac{dF^{\diamond}}{dT^{+}} &= \frac{\phi\delta F_m^{+}}{(\omega B^{\diamond}+\phi)} - \Delta F^{\diamond}.
\end{aligned} \tag{3.94}$$

Here, the terms $\phi = \ln(1/\epsilon)^{-1}$ and $\delta = \ln(\ln(1/\epsilon))^{-1}$ have emerged from logarithmic behaviour on previous timescales. With the value of $\epsilon = 0.01$, these terms are effectively $O(1)$, so we include them in the leading order balance. Matching to the long-term dominant behaviour on the previous timescale gives the following asymptotic approximations

$$
\begin{aligned}
R_m^\dagger &= 1, & \frac{dR^+}{dT^+} &= \mu\rho\, R_m^\dagger - \mu\Delta R^+,\\
\hat{A}_m &= \alpha, & A^\ddagger &= \frac{\theta}{\upsilon}\hat{A}_m,\\
C_m^\dagger &= 1, & \frac{dC^+}{dT^+} &= \gamma\, C_m^\dagger - \Delta C^+,\\
B_m^+ &= \frac{1}{C^+}, & \frac{dB^\diamond}{dT^+} &= \phi\beta B_m^+ - \Delta B^\diamond,\\
S_m^\dagger &= 1, & \frac{dS^+}{dT^+} &= \sigma S_m^\dagger - \Delta S^+,\\
E_m^\dagger &= 1, & \frac{dE^+}{dT^+} &= \xi E_m^\dagger - \Delta E^+,\\
F_m^+ &= \frac{\eta}{E^+}, & \frac{dF^\diamond}{dT^+} &= \frac{\phi\delta F_m^+}{(\omega B^\diamond + \phi)} - \Delta F^\diamond.
\end{aligned} \tag{3.95}
$$

This system of ODEs can be solved, matching to the long-term dominant behaviour on the previous timescale gives the following asymptotic approximations

$$
\begin{aligned}
&R_m^\dagger = 1, \quad R^+ = \frac{\rho}{\Delta}(1 - e^{-\mu\Delta T^+}), \quad \hat{A}_m = \alpha, && A^\ddagger = \frac{\theta\alpha}{\upsilon},\\
&C_m^\dagger = 1, \quad C^+ = \frac{\gamma}{\Delta}(1 - e^{-\Delta T^+}), \quad S_m^\dagger = 1, && S^+ = \frac{\sigma}{\Delta}(1 - e^{-\Delta T^+}),\\
&E_m^\dagger = 1, \quad E^+ = \frac{\xi}{\Delta}(1 - e^{-\Delta T^+}) \quad B_m^+ = \frac{\Delta}{\gamma(1 - e^{-\Delta T^+})}, && F_m^+ = \frac{\eta\Delta}{\xi(1 - e^{-\Delta T^+})},\\
&B^\diamond = \frac{\phi\beta}{\gamma}(1 + \ln(\gamma(e^{\Delta T^+} - 1))e^{-\Delta T^+}), && F^\diamond = \frac{\delta\eta\gamma}{\xi(\beta\omega + \gamma)}(1 + \frac{\gamma}{\beta\omega}e^{-\Delta T^+}).
\end{aligned} \tag{3.96}
$$

On this final timescale, we see all proteins reaching a steady state as their degradation terms appear at leading order. We note that the approximated steady states match closely to the numerics. Thus we should be able to draw strong conclusions by performing steady state analysis on the approximations.

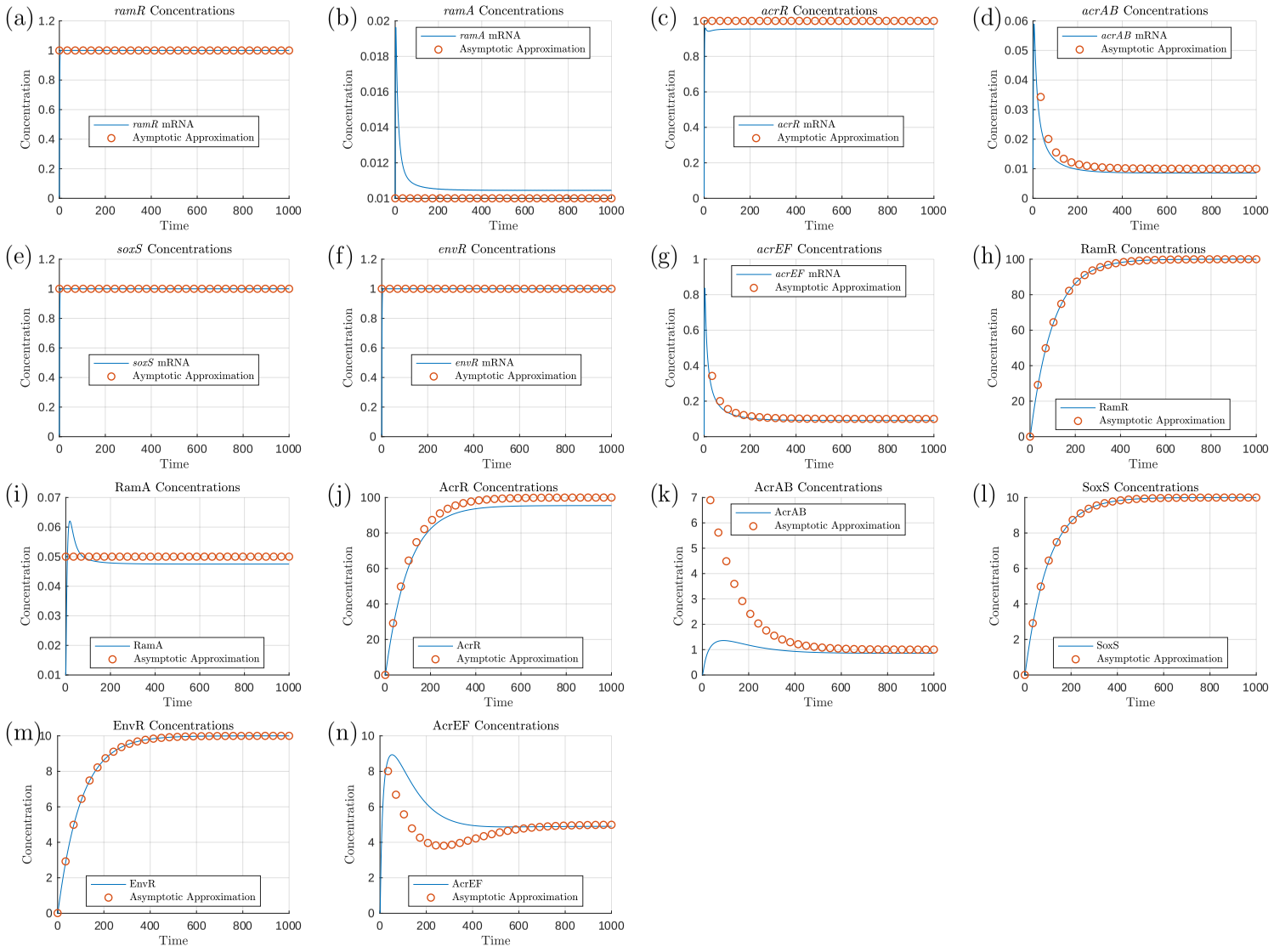

Figure 3.10: Asymptotic approximations on timescale 9 for the wild-type dynamics ($\epsilon = 0.01$). On this timescale, time is $O(\epsilon^{-1})$, so we expect the asymptotics to be accurate around $T = \epsilon^{-1} = 100$. For reference, the previous timescale has time at $O(\epsilon^{-1}\phi^{-1}\delta^{-1})$. Note we depict the simulations over a longer period of time than earlier timescales.

3.6.10 Summary

In Figure 3.11 we exhibit the leading order processes in timescale order from our asymptotic analysis for the wild-type case. We detail the order of dominant processes shown in the schematics. As predicted by the analysis:

- Genes that are not highly regulated by proteins are expressed, resulting in their mRNA transcription and protein translation.
- If produced subject to the relevant stress, SoxS (the secondary TAs) does not significantly increase *acrAB* expression but the asymptotic analysis reveals that it may effect the timescale on which expression of *acrAB* first occurs.
- When produced, RamR inhibits *ramA* expression, preventing RamA from achieving activation of *acrAB* at leading order. AcrR also lowers (but does not shut off entirely) transcription of *acrAB*.
- EnvR binds to the promoter site of *acrEF* repressing its transcription.
- Degradation of all proteins brings the system to a steady state. The system would remain at this state with efflux proteins present until the relevant stress is removed from the cells, at which point the system would revert to a state of basal efflux.

We note that at steady state, the local repressors of the efflux pumps (*acrR* and *envR*) have been expressed to a large enough concentration that they are dominant in the leading order processes and are the only gene products impacting efflux pump expression. We can see at this point the system is reduced to four genes affecting efflux pump expression, and thus at steady state for this case we should focus on these genes as potential inhibition targets. This concludes the wild-type asymptotic analysis. We have broken down the system into nine timescales. For each of these timescales we have obtained full analytical solutions.

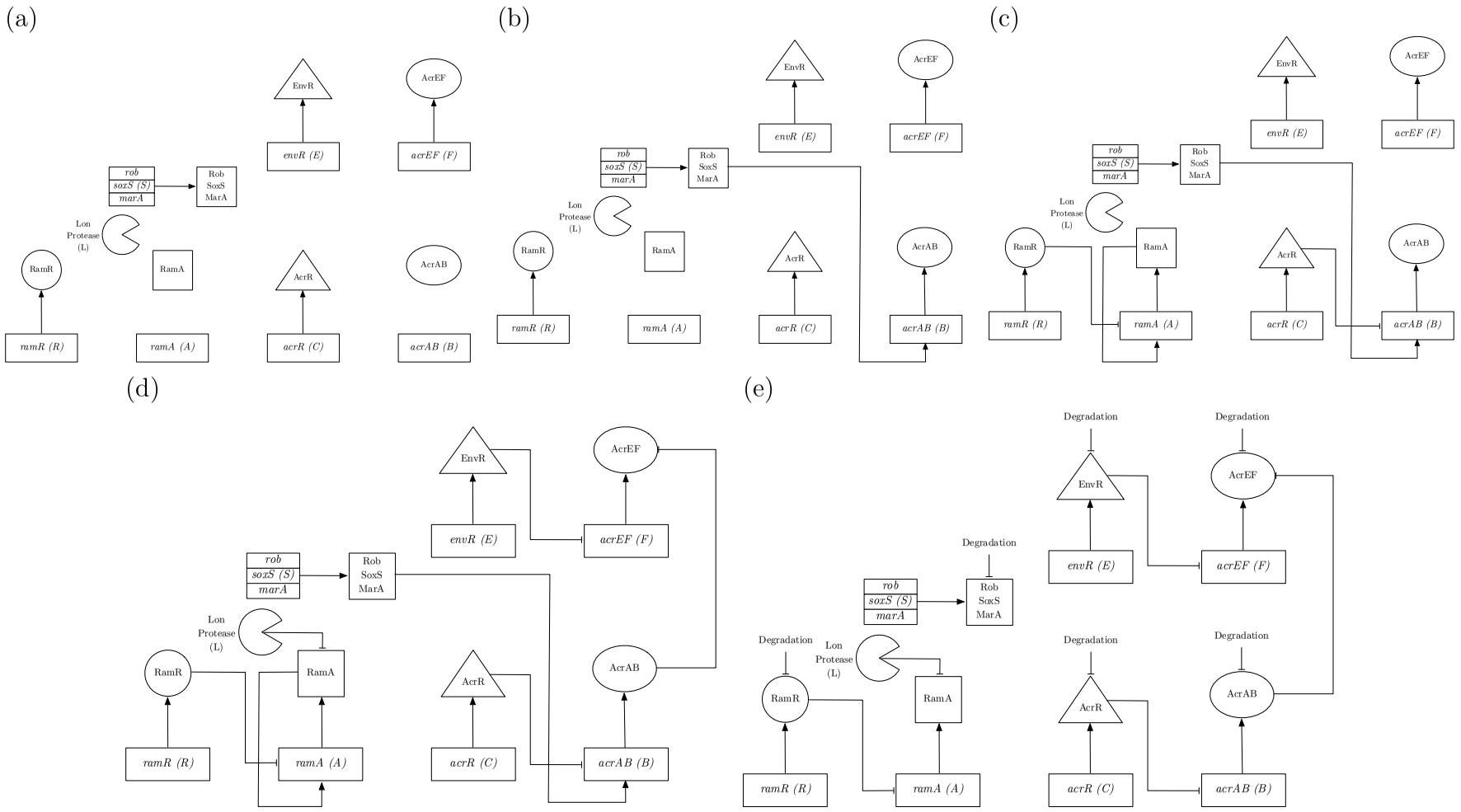

Figure 3.11: Schematic diagrams showing the order in which processes appear at leading order in the asymptotic analysis for the wild-type case. We show these processes in timescale order, starting from initial processes and finishing at steady state in (e). As we evolve the schematic, we insert and remove arrows or lines depending on which terms enter or leave the leading order balance.

Timescale	Variable														
	T	R_m	R	A_m	A	C_m	C	B_m	B	S_m	S	E_m	E	F_m	F
1	$\epsilon\hat{T}$	$\epsilon\hat{R}_m$	$\epsilon\hat{R}$	$\epsilon\hat{A}_m$	$\epsilon\hat{A}$	$\epsilon\hat{C}_m$	$\epsilon\hat{C}$	$\epsilon\hat{B}_m$	$\epsilon\hat{B}$	$\epsilon\hat{S}_m$	$\epsilon\hat{S}$	$\epsilon\hat{E}_m$	$\epsilon\hat{E}$	$\epsilon\hat{F}_m$	$\epsilon\hat{F}$
2	$\epsilon^{\frac{1}{2}}\check{T}$	$\epsilon^{\frac{1}{2}}\check{R}_m$	$\epsilon\hat{R}$	$\epsilon\hat{A}_m$	$\epsilon\hat{A}$	$\epsilon^{\frac{1}{2}}\check{C}_m$	$\epsilon\hat{C}$	$\epsilon\hat{B}_m$	$\epsilon\hat{B}$	$\epsilon^{\frac{1}{2}}\check{S}_m$	$\epsilon\hat{S}$	$\epsilon^{\frac{1}{2}}\check{E}_m$	$\epsilon\hat{E}$	$\epsilon^{\frac{1}{2}}\check{F}_m$	$\epsilon\hat{F}$
3	$\epsilon^{\frac{1}{4}}\bar{T}$	$\epsilon^{\frac{1}{4}}\bar{R}_m$	$\epsilon\hat{R}$	$\epsilon\hat{A}_m$	$\epsilon\hat{A}$	$\epsilon^{\frac{1}{4}}\bar{C}_m$	$\epsilon^{\frac{1}{2}}\bar{C}$	$\epsilon\hat{B}_m$	$\epsilon\hat{B}$	$\epsilon^{\frac{1}{4}}\bar{S}_m$	$\epsilon\hat{S}$	$\epsilon^{\frac{1}{4}}\bar{E}_m$	$\epsilon\hat{E}$	$\epsilon^{\frac{1}{4}}\bar{F}_m$	$\epsilon^{\frac{1}{2}}\bar{F}$
4	$\epsilon^{\frac{1}{6}}\tilde{T}$	$\epsilon^{\frac{1}{6}}\tilde{R}_m$	$\epsilon\hat{R}$	$\epsilon\hat{A}_m$	$\epsilon\hat{A}$	$\epsilon^{\frac{1}{6}}\tilde{C}_m$	$\epsilon^{\frac{1}{3}}\tilde{C}$	$\epsilon\hat{B}_m$	$\epsilon\hat{B}$	$\epsilon^{\frac{1}{6}}\tilde{S}_m$	$\epsilon^{\frac{5}{6}}\tilde{S}$	$\epsilon^{\frac{1}{6}}\tilde{E}_m$	$\epsilon^{\frac{5}{6}}\tilde{E}$	$\epsilon^{\frac{1}{6}}\tilde{F}_m$	$\epsilon^{\frac{1}{3}}\tilde{F}$
5	$\epsilon^{\frac{1}{8}}T'$	$\epsilon^{\frac{1}{8}}R'_m$	$\epsilon\hat{R}$	$\epsilon\hat{A}_m$	$\epsilon\hat{A}$	$\epsilon^{\frac{1}{8}}C'_m$	$\epsilon^{\frac{1}{4}}C'$	$\epsilon^{\frac{7}{8}}B'_m$	$\epsilon\hat{B}$	$\epsilon^{\frac{1}{8}}S'_m$	$\epsilon^{\frac{3}{4}}S'$	$\epsilon^{\frac{1}{8}}E'_m$	$\epsilon^{\frac{3}{4}}E'$	$\epsilon^{\frac{1}{8}}F'_m$	$\epsilon^{\frac{1}{4}}F'$
6	$T^\dagger$	$R^\dagger_m$	$\epsilon\hat{R}$	$\epsilon\hat{A}_m$	$\epsilon\hat{A}$	$C^\dagger_m$	$C^\dagger$	$\epsilon^{\frac{1}{2}}B^\dagger_m$	$\epsilon^{\frac{1}{2}}B^\dagger$	$S^\dagger_m$	$\epsilon^{\frac{1}{2}}S^\dagger$	$E^\dagger_m$	$\epsilon^{\frac{1}{2}}E^\dagger$	$F^\dagger_m$	$F^\dagger$
7	$\frac{1}{2\kappa}\phi^{-1}+T^\ddagger$	$R^\dagger_m$	$\epsilon\hat{R}$	$\epsilon^{\frac{1}{2}}A^\ddagger_m$	$\epsilon^{\frac{1}{2}}A^\ddagger$	$C^\dagger_m$	$\phi^{-1}C^\ddagger$	$\epsilon^{\frac{1}{2}}B^\dagger_m$	$\epsilon^{\frac{1}{2}}\phi^{-1}B^\ddagger$	$S^\dagger_m$	$\epsilon^{\frac{1}{2}}\phi^{-1}S^\ddagger$	$E^\dagger_m$	$\epsilon^{\frac{1}{2}}\phi^{-1}E^\ddagger$	$F^\dagger_m$	$\phi^{-1}F^\ddagger$
8	$\frac{1}{\kappa}\phi^{-1}+T^\diamond$	$R^\dagger_m$	$\epsilon\hat{R}$	$A^\diamond_m$	$A^\diamond$	$C^\dagger_m$	$\phi^{-2}C^\diamond$	$\phi B^\diamond_m$	$B^\diamond$	$S^\dagger_m$	$\epsilon^{\frac{1}{2}}\phi^{-2}S^\diamond$	$E^\dagger_m$	$\epsilon^{\frac{1}{2}}\phi^{-2}E^\diamond$	$\epsilon^{-\frac{1}{2}}\phi F^\diamond_m$	$\phi^{-2}F^\diamond$
9	$\epsilon^{-\frac{1}{2}}\left(\frac{1}{\kappa}\phi^{-1}+T^+\right)$	$R^\dagger_m$	$\epsilon\hat{R}$	$A^\diamond_m$	$\epsilon^{-\frac{1}{2}}A^+$	$\epsilon^{-\frac{1}{2}}C^+_m$	$\phi^{-3}C^+$	$\phi^2B^+_m$	$\epsilon^{-\frac{1}{2}}\phi B^+$	$S^\dagger_m$	$\phi^{-2}S^+$	$E^\dagger_m$	$\phi^{-2}E^+$	$\epsilon^{-\frac{1}{2}}\phi F^\diamond_m$	$\phi^{-4}F^+$
10	$\epsilon^{-1}\left(\frac{1}{\kappa}\phi^{-1}+\check{T}\right)$	$R^\dagger_m$	$\epsilon\hat{R}$	$A^\diamond_m$	$\epsilon^{-\frac{1}{2}}A^+$	$\epsilon^{-\frac{1}{2}}C^+_m$	$\epsilon^{-\frac{1}{2}}\phi^{-3}\check{C}$	$\epsilon^{\frac{1}{2}}\phi^2\check{B}_m$	$\epsilon^{-\frac{1}{2}}\check{B}$	$S^\dagger_m$	$\epsilon^{-\frac{1}{2}}\phi^{-2}\check{S}$	$E^\dagger_m$	$\epsilon^{-\frac{1}{2}}\phi^{-2}\check{E}$	$\phi\check{F}_m$	$\phi^{-4}\delta^{-1}\check{F}$

Table 3.3: The scalings for each variable required on each timescale for the mutant asymptotic analysis. These scalings are in relation to our nondimensionalised variables in (3.2)-(3.15) Here we have $\kappa=\frac{1}{2}(-1+\sqrt{1+4\theta})$, $\phi=\ln(1/\epsilon)^{-1}$ and $\delta=\ln(\ln(1/\epsilon))^{-1}$ as explained in the timescales in which they feature.

3.7 Asymptotic analysis of the mutant dynamics

In this section we take the case where RamR protein is mutated (i.e $\mu = 0$). We remind ourselves that this mutation results in a strain that displays MDR. Therefore, we expect the dynamics to be different to the wild-type case. In order to gain further insight into the behaviour of this strain, we must consequently undertake a new series of asymptotic analysis. We denote the scalings we must take in order to reach each timescale in Table 3.3.

3.7.1 Timescale 1: mRNA transcription

As with the wild-type case, on this first initial timescale we address the issue of the systems initial conditions of all variables being $O(\epsilon)$. We must take the following scalings

$$\begin{array}{lllll} T = \epsilon\hat{T}, & R_m = \epsilon\hat{R}_m, & A_m = \epsilon\hat{A}_m, & C_m = \epsilon\hat{C}_m, & B_m = \epsilon\hat{B}_m, \\ S_m = \epsilon\hat{S}_m, & E_m = \epsilon\hat{E}_m, & F_m = \epsilon\hat{F}_m, & R = \epsilon\hat{R}, & A = \epsilon\hat{A}, \\ C = \epsilon\hat{C}, & B = \epsilon\hat{B}, & S = \epsilon\hat{S}, & E = \epsilon\hat{E}, & F = \epsilon\hat{F}. \end{array} \tag{3.97}$$

Using these scalings, our system of equations rescaled for the first timescale is

$$\begin{aligned} \frac{d\hat{R}_m}{d\hat{T}} &= 1 - \epsilon\hat{R}_m, & \frac{d\hat{R}}{d\hat{T}} &= 0, \\ \frac{d\hat{A}_m}{d\hat{T}} &= \frac{\epsilon\hat{A}}{(\epsilon\hat{A}+1)(\epsilon\hat{R}+1)} + \epsilon\alpha - \epsilon\hat{A}_m, & \frac{d\hat{A}}{d\hat{T}} &= \theta\,\epsilon\hat{A}_m - \epsilon^{\frac{3}{2}}\upsilon\hat{A} - \epsilon^2\Delta\hat{A}, \\ \frac{d\hat{C}_m}{d\hat{T}} &= \frac{\lambda}{\epsilon\hat{A}+\lambda} - \epsilon\hat{C}_m, & \frac{d\hat{C}}{d\hat{T}} &= \gamma\,\epsilon\hat{C}_m - \epsilon^2\Delta\hat{C}, \\ \frac{d\hat{B}_m}{d\hat{T}} &= \frac{\epsilon\hat{A}+\epsilon\hat{S}}{(1+\epsilon\hat{S}+\epsilon\hat{A})(1+\epsilon\hat{E}+\epsilon\hat{C})} - \epsilon\hat{B}_m, & \frac{d\hat{B}}{d\hat{T}} &= \beta\,\epsilon\hat{B}_m - \epsilon^2\Delta\hat{B}, \\ \frac{d\hat{S}_m}{d\hat{T}} &= 1 - \epsilon\hat{S}_m, & \frac{d\hat{S}}{d\hat{T}} &= \epsilon^{3/2}\sigma\,\hat{S}_m - \epsilon^2\Delta\hat{S}, \\ \frac{d\hat{E}_m}{d\hat{T}} &= 1 - \epsilon\hat{E}_m, & \frac{d\hat{E}}{d\hat{T}} &= \epsilon^{3/2}\xi\,\hat{E}_m - \epsilon^2\Delta\hat{E}, \\ \frac{d\hat{F}_m}{d\hat{T}} &= \frac{\eta}{\eta+\epsilon\hat{E}} - \epsilon\hat{F}_m, & \frac{d\hat{F}}{d\hat{T}} &= \frac{\epsilon\hat{F}_m}{\epsilon\omega\hat{B}+1} - \epsilon^2\Delta\hat{F}. \end{aligned} \tag{3.98}$$

At leading order, we have the following system of equations

$$\begin{aligned}
\frac{d\hat{R}_m}{d\hat{T}} &= 1, & \frac{d\hat{R}}{d\hat{T}} &= 0,\\
\frac{d\hat{A}_m}{d\hat{T}} &= 0, & \frac{d\hat{A}}{d\hat{T}} &= 0,\\
\frac{d\hat{C}_m}{d\hat{T}} &= 1, & \frac{d\hat{C}}{d\hat{T}} &= 0,\\
\frac{d\hat{B}_m}{d\hat{T}} &= 0, & \frac{d\hat{B}}{d\hat{T}} &= 0,\\
\frac{d\hat{S}_m}{d\hat{T}} &= 1, & \frac{d\hat{S}}{d\hat{T}} &= 0,\\
\frac{d\hat{E}_m}{d\hat{T}} &= 1, & \frac{d\hat{E}}{d\hat{T}} &= 0,\\
\frac{d\hat{F}_m}{d\hat{T}} &= 1, & \frac{d\hat{F}}{d\hat{T}} &= 0.
\end{aligned} \tag{3.99}$$

This system of ODEs can be solved analytically and as there is no previous timescale, we match these solutions to our initial conditions to give the following asymptotic approximations

$$\begin{aligned}
&\hat{R}_m = \hat{T} + R_{m0}, && \hat{R} = R_0, && \hat{A}_m = A_{m0}, && \hat{A} = A_0,\\
&\hat{C}_m = \hat{T} + C_{m0}, && \hat{C} = C_0, && \hat{B}_m = B_{m0}, && \hat{B} = B_0,\\
&\hat{S}_m = \hat{T} + S_{m0}, && \hat{S} = S_0, && \hat{E}_m = \hat{T} + E_{m0}, && \hat{E} = E_0,\\
&\hat{F}_m = \hat{T} + F_{m0}, && \hat{F} = F_0.
\end{aligned} \tag{3.100}$$

We plot these asymptotic approximations against the numerical solutions in Figure 3.12. As expected, we see the transcription of various gene's mRNA occurring first. The transcription of *ramA* and *acrAB* mRNA are currently not active due to there being very little activator protein bound to their promoter sites to get a high level of transcription. As there is no translation of RamR protein, we see our asymptotic approximation already encompasses the full behaviour of this protein. We note that the behaviour of almost all variables on this timescale are almost identical to the wild-type timescale 1 (Section 3.6.1), with the exception of RamR protein.

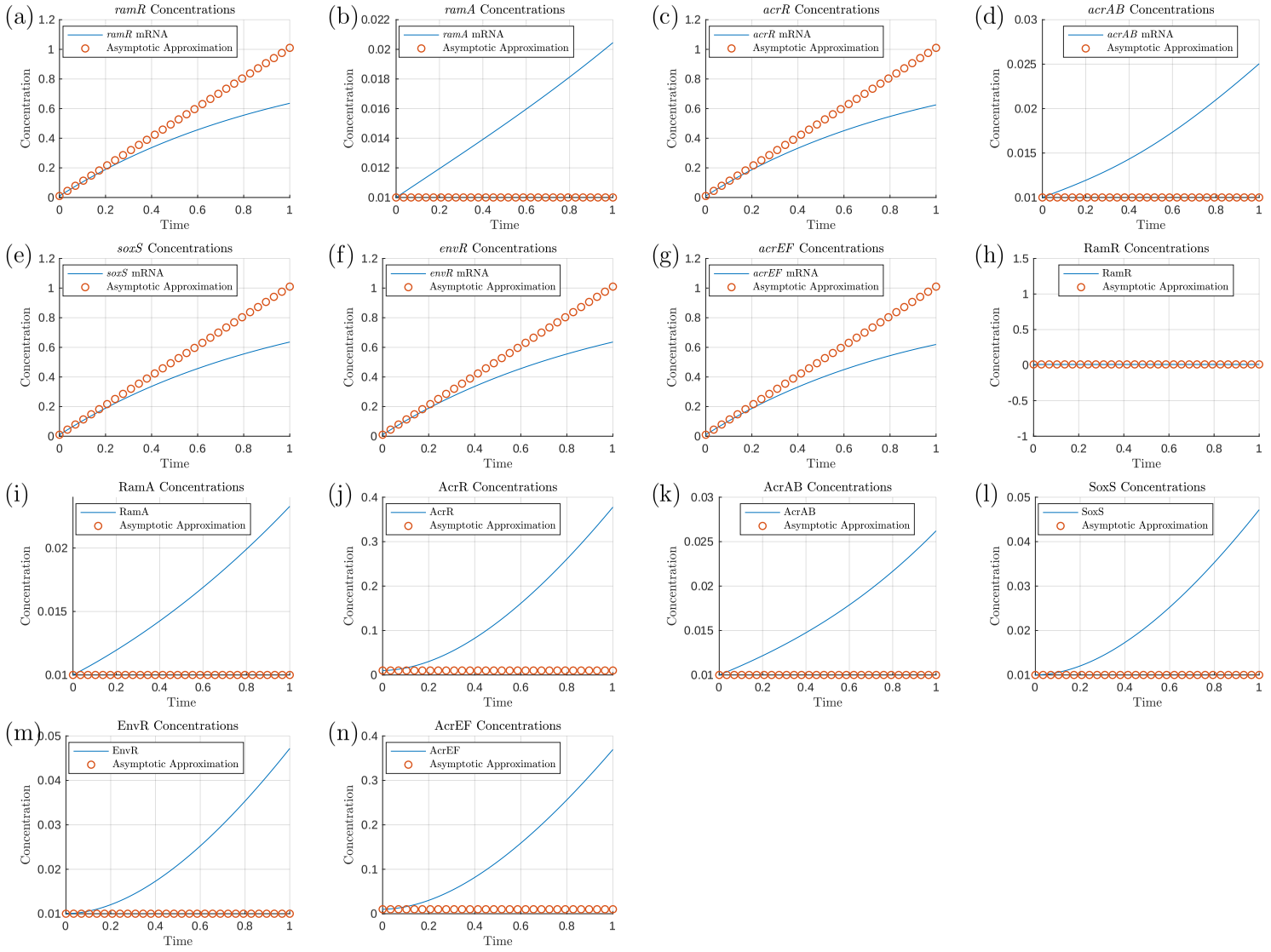

Figure 3.12: Asymptotic approximations on timescale 1 for the mutant dynamics ($\epsilon = 0.01$). On this timescale, time is $O(\epsilon)$, so we expect the asymptotics to be accurate around $T = \epsilon = 0.01$. For reference, the subsequent timescale has time at $O(\epsilon^{\frac{1}{2}})$. Most figures are still at initial condition, as no reaction terms have come into their equations at leading order.

3.7.2 Timescale 2: protein translation

For this timescale, we take the following scalings:

$$\hat{T} = \epsilon^{-\frac{1}{2}}\check{T}, \qquad \hat{R}_m = \epsilon^{-\frac{1}{2}}\check{R}_m, \qquad \hat{C}_m = \epsilon^{-\frac{1}{2}}\check{C}_m,$$
$$\hat{S}_m = \epsilon^{-\frac{1}{2}}\check{S}_m, \qquad \hat{E}_m = \epsilon^{-\frac{1}{2}}\check{E}_m, \qquad \hat{F}_m = \epsilon^{-\frac{1}{2}}\check{F}_m. \tag{3.101}$$

These scalings result in the translation terms for AcrR and AcrEF entering the leading order balance in equations (3.102)-(3.103). We note that this timescale has the same time scaling as Timescale 2 on the wild-type analysis. Our system of equations rescaled for the second timescale is

$$\begin{aligned}
\frac{d\check{R}_m}{d\check{T}} &= 1 - \epsilon^{\frac{1}{2}}\check{R}_m, & \frac{d\hat{R}}{d\check{T}} &= 0,\\
\frac{d\hat{A}_m}{d\check{T}} &= \frac{\epsilon^{\frac{1}{2}}\hat{A}}{(\epsilon\hat{A}+1)(\epsilon\hat{R}+1)} + \epsilon^{\frac{1}{2}}\alpha - \epsilon^{\frac{1}{2}}\hat{A}_m, & \frac{d\hat{A}}{d\check{T}} &= \epsilon^{\frac{1}{2}}\theta\,\hat{A}_m - \epsilon\upsilon\,\hat{A} - \epsilon^{\frac{3}{2}}\Delta\hat{A},\\
\frac{d\check{C}_m}{d\check{T}} &= \frac{\lambda}{\epsilon\hat{A}+\lambda} - \epsilon^{\frac{1}{2}}\check{C}_m, & \frac{d\hat{C}}{d\check{T}} &= \gamma\,\check{C}_m - \epsilon^{\frac{3}{2}}\Delta\hat{C},\\
\frac{d\hat{B}_m}{d\check{T}} &= \frac{\epsilon^{\frac{1}{2}}\hat{A} + \epsilon^{\frac{1}{2}}\hat{S}}{(1+\epsilon\hat{S}+\epsilon\hat{A})(1+\epsilon\hat{E}+\epsilon\hat{C})} - \epsilon^{\frac{1}{2}}\hat{B}_m, & \frac{d\hat{B}}{d\check{T}} &= \epsilon^{\frac{1}{2}}\beta\,\hat{B}_m - \epsilon^{\frac{3}{2}}\Delta\hat{B},\\
\frac{d\check{S}_m}{d\check{T}} &= 1 - \epsilon^{\frac{1}{2}}\check{S}_m, & \frac{d\hat{S}}{d\check{T}} &= \epsilon^{\frac{1}{2}}\sigma\,\check{S}_m - \epsilon^{\frac{3}{2}}\Delta\hat{S},\\
\frac{d\check{E}_m}{d\check{T}} &= 1 - \epsilon^{\frac{1}{2}}\check{E}_m, & \frac{d\hat{E}}{d\check{T}} &= \epsilon^{\frac{1}{2}}\xi\,\check{E}_m - \epsilon^{\frac{3}{2}}\Delta\hat{E},\\
\frac{d\check{F}_m}{d\check{T}} &= \frac{\eta}{\eta+\epsilon\hat{E}} - \epsilon^{\frac{1}{2}}\check{F}_m, & \frac{d\hat{F}}{d\check{T}} &= \frac{\check{F}_m}{\epsilon\omega\hat{B}+1} - \epsilon^{\frac{3}{2}}\Delta\hat{F}.
\end{aligned} \tag{3.102, 3.103}$$

At leading order, we have the following system of equations

$$\begin{aligned}
\frac{d\check{R}_m}{d\check{T}} &= 1, & \frac{d\hat{R}}{d\check{T}} &= 0,\\
\frac{d\hat{A}_m}{d\check{T}} &= 0, & \frac{d\hat{A}}{d\check{T}} &= 0,\\
\frac{d\check{C}_m}{d\check{T}} &= 1, & \frac{d\hat{C}}{d\check{T}} &= \gamma\,\check{C}_m,
\end{aligned}$$

$$\frac{d\hat{B}_m}{d\check{T}} = 0, \qquad \frac{d\hat{B}}{d\check{T}} = 0,$$
$$\frac{d\check{S}_m}{d\check{T}} = 1, \qquad \frac{d\hat{S}}{d\check{T}} = 0,$$
$$\frac{d\check{E}_m}{d\check{T}} = 1, \qquad \frac{d\hat{E}}{d\check{T}} = 0,$$
$$\frac{d\check{F}_m}{d\check{T}} = 1, \qquad \frac{d\hat{F}}{d\check{T}} = \check{F}_m. \tag{3.104}$$

Solving this reduced system of ODEs and matching to the long-term dominant behaviour on the previous timescale gives the following asymptotic approximations

$$\check{R}_m = \check{T}, \qquad \hat{R} = R_0 \qquad \hat{A}_m = A_{m0}, \qquad \hat{A} = A_0,$$
$$\check{C}_m = \check{T}, \qquad \hat{C} = \frac{\gamma}{2}\check{T}^2 + C_0, \qquad \hat{B}_m = B_{m0}, \qquad \hat{B} = B_0,$$
$$\check{S}_m = \check{T}, \qquad \hat{S} = S_0, \qquad \check{E}_m = \check{T}, \qquad \hat{E} = E_0,$$
$$\check{F}_m = \check{T}, \qquad \hat{F} = \frac{1}{2}\check{T}^2 + F_0. \tag{3.105}$$

We plot these asymptotic approximations against the numerical solutions in Figure 3.13. As expected, we see the fast translation of the genes transcribed on the previous timescale. However, as RamR protein is mutated and is not produced in a form that affects any other gene in the network, we see no translation from *ramR* mRNA. The translation is not present for EnvR and the secondary TAs as these are a homologue gene and underlying activators respectively, thus we expect less expression of these genes.

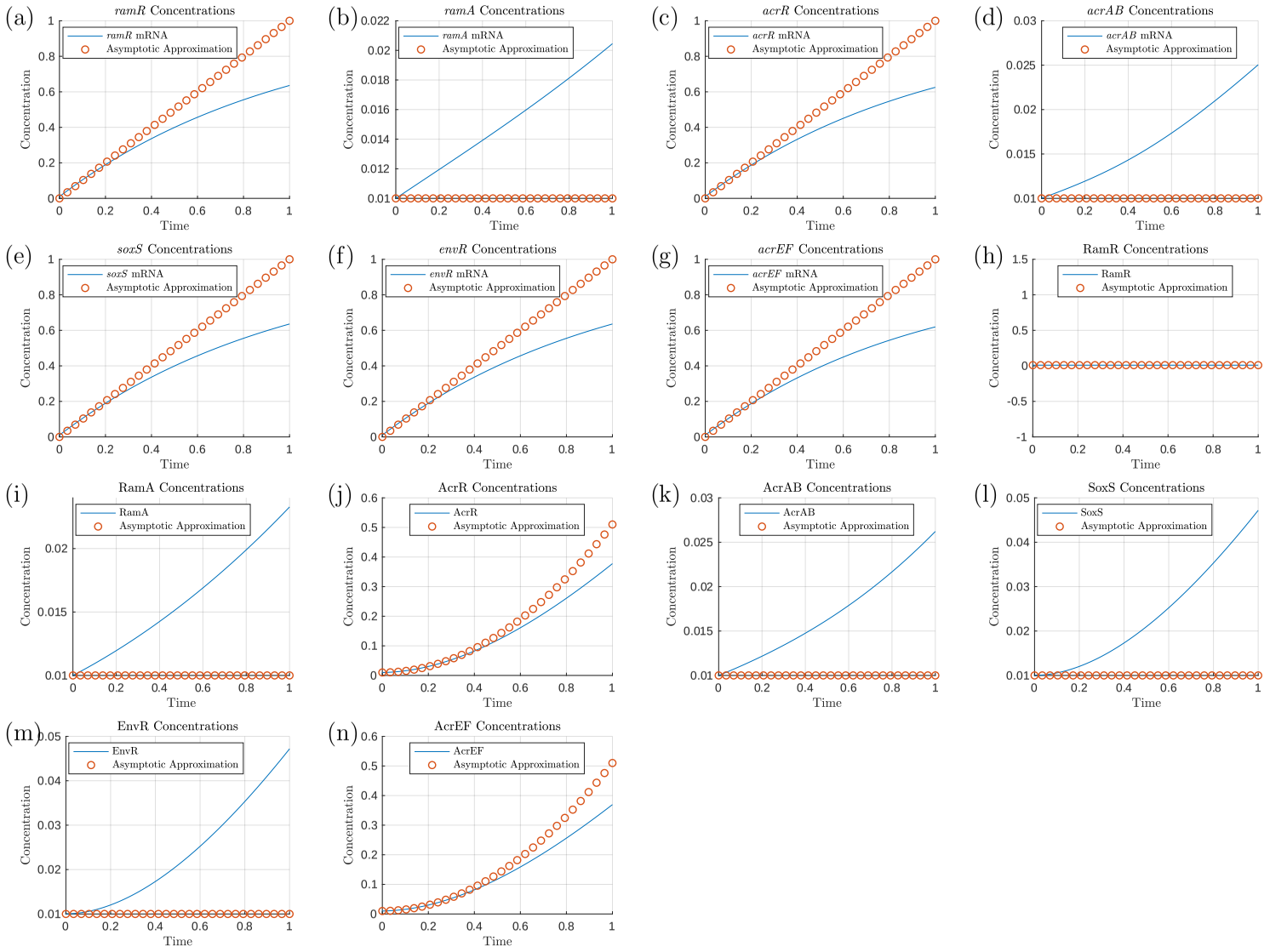

Figure 3.13: Asymptotic approximations on timescale 2 for the mutant dynamics ($\epsilon = 0.01$). On this timescale, time is $O(\epsilon^{\frac{1}{2}})$, so we expect the asymptotics to be accurate around $T = \epsilon^{\frac{1}{2}} = 0.1$. For reference, the previous and subsequent timescales have time at $O(\epsilon)$ and $O(\epsilon^{\frac{1}{4}})$ respectively.

3.7.3 Timescale 3: SoxS and EnvR translation

We move onto the third timescale, we take the following scalings based on the variables on the previous timescale's long term behaviour

$$\begin{aligned}
\check{T} &= \epsilon^{-\frac{1}{4}}\bar{T}, & \check{R}_m &= \epsilon^{-\frac{1}{4}}\bar{R}_m, & \check{C}_m &= \epsilon^{-\frac{1}{4}}\bar{C}_m,\\
\check{S}_m &= \epsilon^{-\frac{1}{4}}\bar{S}_m, & \check{E}_m &= \epsilon^{-\frac{1}{4}}\bar{E}_m, & \check{F}_m &= \epsilon^{-\frac{1}{4}}\bar{F}_m,\\
\hat{C} &= \epsilon^{-\frac{1}{2}}\bar{C}, & \hat{F} &= \epsilon^{-\frac{1}{2}}\bar{F}. & &
\end{aligned} \tag{3.106}$$

These scalings result in the rest of the translation terms for all mRNAs that are undergoing transcription entering the leading order balance in equations (3.107)-(3.108). We note that this timescale coincides with timescale 3 on the wild-type asymptotic analysis. The system of equations rescaled for the third timescale is

$$\begin{aligned}
\frac{d\bar{R}_m}{d\bar{T}} &= 1-\epsilon^{\frac{1}{4}}\bar{R}_m, & \frac{d\bar{R}}{d\bar{T}} &= 0,\\
\frac{d\hat{A}_m}{d\bar{T}} &= \frac{\epsilon^{\frac{1}{4}}\hat{A}}{(\epsilon\hat{A}+1)(\epsilon^{\frac{1}{2}}\bar{R}+1)}+\epsilon^{\frac{1}{4}}\alpha-\epsilon^{\frac{1}{4}}\hat{A}_m, & \frac{d\hat{A}}{d\bar{T}} &= \epsilon^{\frac{1}{4}}\theta\,\hat{A}_m-\epsilon^{\frac{3}{4}}\upsilon\,\hat{A}-\epsilon^{\frac{5}{4}}\Delta\hat{A},\\
\frac{d\bar{C}_m}{d\bar{T}} &= \frac{\lambda}{\epsilon\hat{A}+\lambda}-\epsilon^{\frac{1}{4}}\bar{C}_m, & \frac{d\bar{C}}{d\bar{T}} &= \gamma\,\bar{C}_m-\epsilon^{\frac{5}{4}}\Delta\bar{C},\\
\frac{d\hat{B}_m}{d\bar{T}} &= \frac{\epsilon^{\frac{1}{4}}\hat{A}+\epsilon^{\frac{1}{4}}\hat{S}}{(1+\epsilon\hat{S}+\epsilon\hat{A})(1+\epsilon\hat{E}+\epsilon^{\frac{1}{2}}\bar{C})}-\epsilon^{\frac{1}{4}}\hat{B}_m, & \frac{d\hat{B}}{d\bar{T}} &= \epsilon^{\frac{1}{4}}\beta\,\hat{B}_m-\epsilon^{\frac{5}{4}}\Delta\hat{B},\\
\frac{d\bar{S}_m}{d\bar{T}} &= 1-\epsilon^{\frac{1}{4}}\bar{S}_m, & \frac{d\hat{S}}{d\bar{T}} &= \sigma\,\bar{S}_m-\epsilon^{\frac{5}{4}}\Delta\hat{S}, \qquad (3.107)\\
\frac{d\bar{E}_m}{d\bar{T}} &= 1-\epsilon^{\frac{1}{4}}\bar{E}_m, & \frac{d\hat{E}}{d\bar{T}} &= \xi\,\bar{E}_m-\epsilon^{\frac{5}{4}}\Delta\hat{E}, \qquad (3.108)\\
\frac{d\bar{F}_m}{d\bar{T}} &= \frac{\eta}{\eta+\epsilon\hat{E}}-\epsilon^{\frac{1}{4}}\bar{F}_m, & \frac{d\bar{F}}{d\bar{T}} &= \frac{\bar{F}_m}{\epsilon\omega\hat{B}+1}-\epsilon^{\frac{5}{4}}\Delta\bar{F}.
\end{aligned}$$

At leading order, we have the following system of equations

$$\begin{aligned}
\frac{d\bar{R}_m}{d\bar{T}} &= 1, & \frac{d\hat{R}}{d\bar{T}} &= 0,\\
\frac{d\hat{A}_m}{d\bar{T}} &= 0, & \frac{d\hat{A}}{d\bar{T}} &= 0,\\
\frac{d\bar{C}_m}{d\bar{T}} &= 1, & \frac{d\bar{C}}{d\bar{T}} &= \gamma\,\bar{C}_m,
\end{aligned}$$

$$\begin{aligned}
\frac{d\hat{B}_m}{d\bar{T}} &= 0, & \frac{d\hat{B}}{d\bar{T}} &= 0,\\
\frac{d\bar{S}_m}{d\bar{T}} &= 1, & \frac{d\hat{S}}{d\bar{T}} &= \sigma\bar{S}_m,\\
\frac{d\bar{E}_m}{d\bar{T}} &= 1, & \frac{d\hat{E}}{d\bar{T}} &= \xi\bar{E}_m,\\
\frac{d\bar{F}_m}{d\bar{T}} &= 1, & \frac{d\bar{F}}{d\bar{T}} &= \bar{F}_m.
\end{aligned} \tag{3.109}$$

We solve the leading order system of ODEs and match to the long term dominant behaviour on the previous timescale, giving us the following asymptotic approximations

$$\begin{aligned}
&\bar{R}_m = \bar{T}, && \hat{R} = R_0, && \hat{A}_m = A_{m0}, && \hat{A} = A_0,\\
&\bar{C}_m = \bar{T}, && \bar{C} = \frac{\gamma}{2}\bar{T}^2, && \hat{B}_m = B_{m0}, && \hat{B} = B_0,\\
&\bar{S}_m = \bar{T}, && \hat{S} = \frac{\sigma}{2}\bar{T}^2 + S_0, && \bar{E}_m = \bar{T}, && \hat{E} = \frac{\xi}{2}\bar{T}^2 + E_0,\\
&\bar{F}_m = \bar{T}, && \bar{F} = \frac{1}{2}\bar{T}^2.
\end{aligned} \tag{3.110}$$

We plot these asymptotic approximations against the numerical solutions in Figure 3.14. Following from the previous timescale, here we introduce the fast translation of the secondary TAs and EnvR.

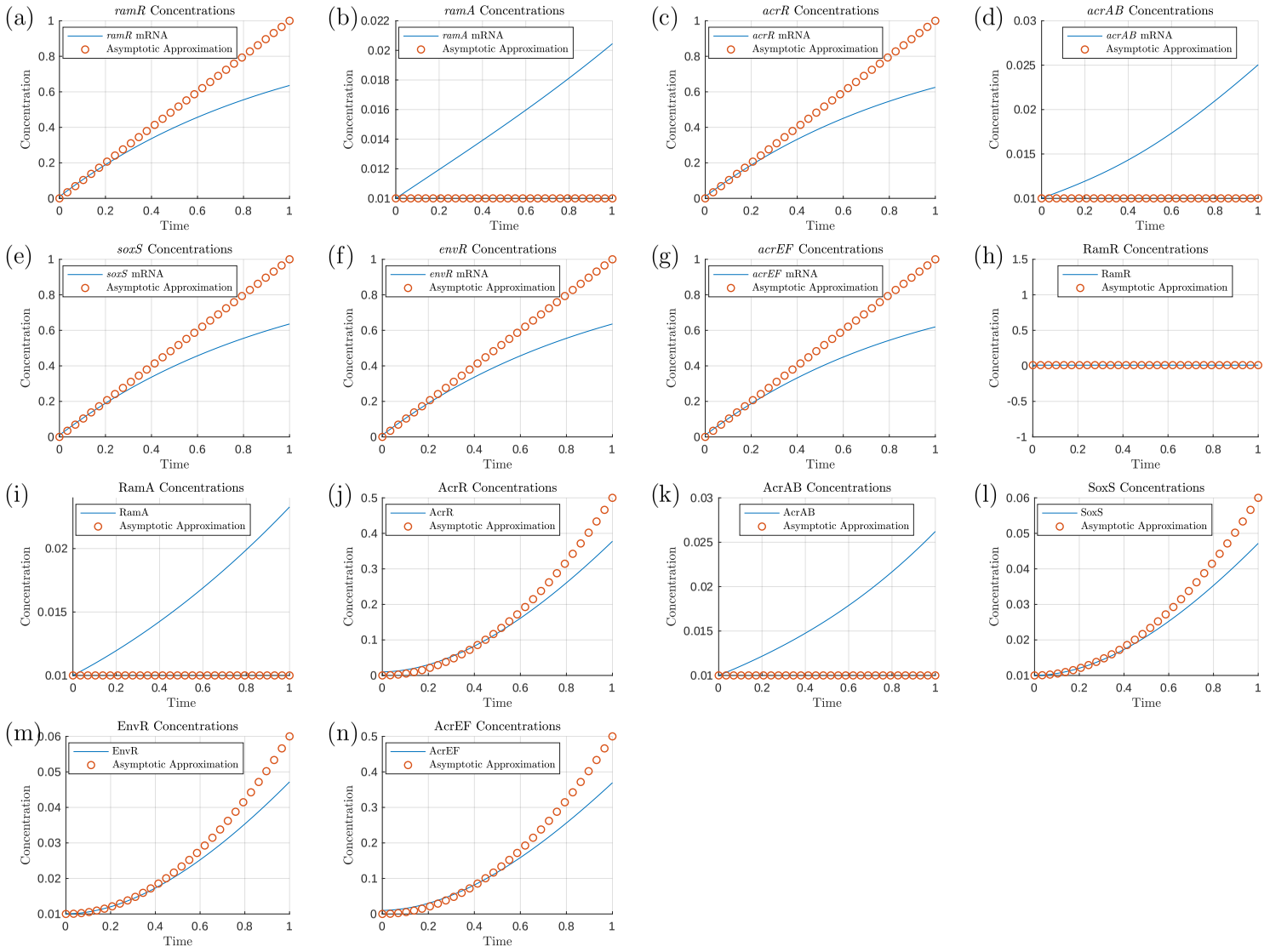

Figure 3.14: Asymptotic approximations on timescale 3 for the mutant dynamics ($\epsilon = 0.01$). On this timescale, time is $O(\epsilon^{\frac{1}{4}})$, so we expect the asymptotics to be accurate around $T = \epsilon^{\frac{1}{4}} \approx 0.3162$. For reference, the previous and subsequent timescales have time at $O(\epsilon^{\frac{1}{2}})$ and $O(\epsilon^{\frac{1}{6}})$ respectively.

3.7.4 Timescale 4: *acrAB* mRNA transcription

For this timescale, we have transcription of *acrAB* mRNA entering the leading order balance in equation (3.112). We take the following scalings:

$$\begin{aligned}
\bar{T} &= \epsilon^{-\frac{1}{12}}\tilde{T}, & \bar{R}_m &= \epsilon^{-\frac{1}{12}}\tilde{R}_m, & \bar{C}_m &= \epsilon^{-\frac{1}{12}}\tilde{C}_m, & \bar{S}_m &= \epsilon^{-\frac{1}{12}}\tilde{S}_m,\\
\bar{E}_m &= \epsilon^{-\frac{1}{12}}\tilde{E}_m, & \bar{F}_m &= \epsilon^{-\frac{1}{12}}\tilde{F}_m, & \bar{C} &= \epsilon^{-\frac{1}{6}}\tilde{C}, & \hat{S} &= \epsilon^{-\frac{1}{6}}\tilde{S},\\
\hat{E} &= \epsilon^{-\frac{1}{6}}\tilde{E}, & \bar{F} &= \epsilon^{-\frac{1}{6}}\tilde{F}. & & & & \qquad (3.111)
\end{aligned}$$

This timescale occurs at the same time as timescale 4 on the wild-type analysis. After rescaling, the system of equations for the fourth timescale is

$$\begin{aligned}
\frac{d\tilde{R}_m}{d\tilde{T}} &= 1-\epsilon^{\frac{1}{6}}\tilde{R}_m, & \frac{d\tilde{R}}{d\tilde{T}} &= 0,\\
\frac{d\hat{A}_m}{d\tilde{T}} &= \frac{\epsilon^{\frac{1}{6}}\hat{A}}{(\epsilon\hat{A}+1)(\epsilon^{\frac{1}{3}}\tilde{R}+1)}+\epsilon^{\frac{1}{6}}\alpha-\epsilon^{\frac{1}{6}}\hat{A}_m, & \frac{d\hat{A}}{d\tilde{T}} &= \epsilon^{\frac{1}{6}}\theta\,\hat{A}_m-\epsilon^{\frac{2}{3}}\upsilon\,\hat{A}-\epsilon^{\frac{7}{6}}\Delta\hat{A},\\
\frac{d\tilde{C}_m}{d\tilde{T}} &= \frac{\lambda}{\epsilon\hat{A}+\lambda}-\epsilon^{\frac{1}{6}}\tilde{C}_m, & \frac{d\tilde{C}}{d\tilde{T}} &= \gamma\,\tilde{C}_m-\epsilon^{\frac{7}{6}}\Delta\tilde{C},\\
\frac{d\hat{B}_m}{d\tilde{T}} &= \frac{\epsilon^{\frac{1}{6}}\hat{A}+\tilde{S}}{(1+\epsilon^{\frac{5}{6}}\tilde{S}+\epsilon\hat{A})(1+\epsilon^{\frac{5}{6}}\tilde{E}+\epsilon^{\frac{1}{3}}\tilde{C})}-\epsilon^{\frac{1}{6}}\hat{B}_m, & \frac{d\hat{B}}{d\tilde{T}} &= \epsilon^{\frac{1}{6}}\beta\,\hat{B}_m-\epsilon^{\frac{7}{6}}\Delta\hat{B},\\
& \qquad (3.112) & \frac{d\tilde{S}}{d\tilde{T}} &= \sigma\,\tilde{S}_m-\epsilon^{\frac{7}{6}}\Delta\tilde{S},\\
\frac{d\tilde{S}_m}{d\tilde{T}} &= 1-\epsilon^{\frac{1}{6}}\tilde{S}_m, & \frac{d\tilde{E}}{d\tilde{T}} &= \xi\,\tilde{E}_m-\epsilon^{\frac{7}{6}}\Delta\,\tilde{E},\\
\frac{d\tilde{E}_m}{d\tilde{T}} &= 1-\epsilon^{\frac{1}{6}}\tilde{E}_m, & \frac{d\tilde{F}}{d\tilde{T}} &= \frac{\tilde{F}_m}{\epsilon\omega\hat{B}+1}-\epsilon^{\frac{7}{6}}\Delta\tilde{F}.\\
\frac{d\tilde{F}_m}{d\tilde{T}} &= \frac{\eta}{\eta+\epsilon^{\frac{5}{6}}\tilde{E}}-\epsilon^{\frac{1}{6}}\tilde{F}_m, &&
\end{aligned}$$

At leading order, we have the following system of equations

$$\begin{aligned}
\frac{d\tilde{R}_m}{d\tilde{T}} &= 1, & \frac{d\hat{R}}{d\tilde{T}} &= 0,\\
\frac{d\hat{A}_m}{d\tilde{T}} &= 0, & \frac{d\hat{A}}{d\tilde{T}} &= 0,\\
\frac{d\tilde{C}_m}{d\tilde{T}} &= 1, & \frac{d\tilde{C}}{d\tilde{T}} &= \gamma\,\tilde{C}_m,
\end{aligned}$$

$$\begin{aligned}
\frac{d\hat{B}_m}{d\tilde{T}} &= \tilde{S}, & \frac{d\hat{B}}{d\tilde{T}} &= 0,\\
\frac{d\tilde{S}_m}{d\tilde{T}} &= 1, & \frac{d\tilde{S}}{d\tilde{T}} &= \sigma\tilde{S}_m,\\
\frac{d\tilde{E}_m}{d\tilde{T}} &= 1, & \frac{d\tilde{E}}{d\tilde{T}} &= \xi\tilde{E}_m,\\
\frac{d\tilde{F}_m}{d\tilde{T}} &= 1, & \frac{d\tilde{F}}{d\tilde{T}} &= \tilde{F}_m.
\end{aligned} \tag{3.113}$$

Taking this leading order balance, solving and matching to the long-term dominant behaviour on the previous timescale gives the following asymptotic approximations

$$\begin{aligned}
&\tilde{R}_m = \tilde{T}, && \hat{R} = R_0, && \hat{A}_m = A_{m0}, && \hat{A} = A_0,\\
&\tilde{C}_m = \tilde{T}, && \tilde{C} = \frac{\gamma}{2}\tilde{T}^2, && \hat{B}_m = \frac{\sigma}{6}\tilde{T}^3 + B_{m0}, && \hat{B} = B_0,\\
&\tilde{S}_m = \tilde{T}, && \tilde{S} = \frac{\sigma}{2}\tilde{T}^2, && \tilde{E}_m = \tilde{T}, && \tilde{E} = \frac{\xi}{2}\tilde{T}^2,\\
&\tilde{F}_m = \tilde{T}, && \tilde{F} = \frac{1}{2}\tilde{T}^2. &&&&
\end{aligned} \tag{3.114}$$

We plot these asymptotic approximations against the full solution in Figure 3.15. This is the first timescale where our efflux gene *acrAB* is transcribed. We notice that this is being driven by the underlying regulators Rob, SoxS and MarA binding to the promoter site of *acrAB*.

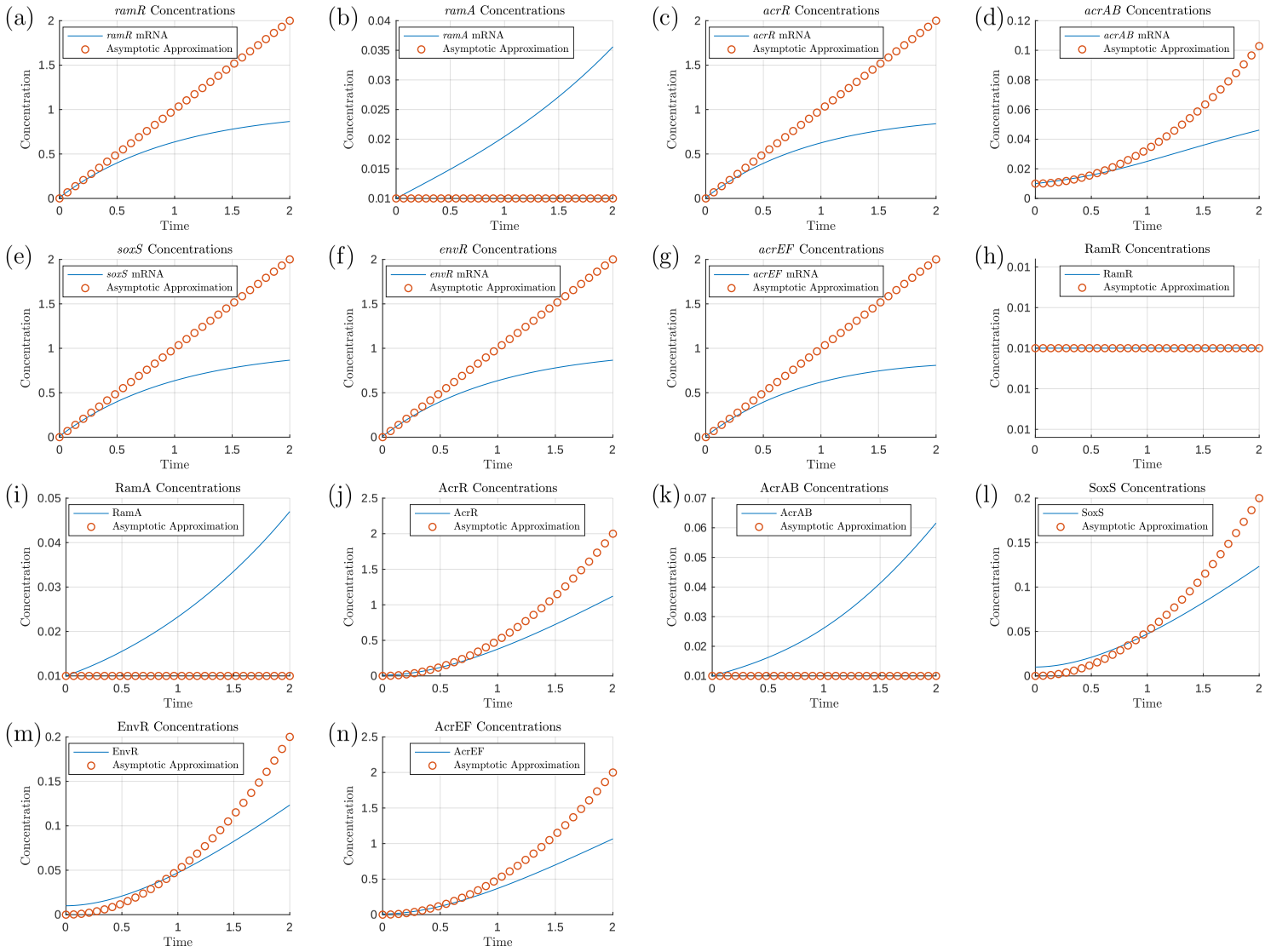

Figure 3.15: Asymptotic approximations on timescale 4 for the mutant dynamics ($\epsilon = 0.01$). On this timescale, time is $O(\epsilon^{\frac{1}{6}})$, so we expect the asymptotics to be accurate around $T = \epsilon^{\frac{1}{6}} \approx 0.4642$. For reference, the previous and subsequent timescales have time at $O(\epsilon^{\frac{1}{4}})$ and $O(\epsilon^{\frac{1}{8}})$ respectively. Note we depict the simulations over a longer period of time than earlier timescales.

3.7.5 Timescale 5: AcrAB translation

For this timescale, we take the following scalings based on the variables on the previous timescale's long term behaviour

$$\begin{aligned}
\bar{T} &= \epsilon^{-\frac{1}{24}} T', & \bar{R}_m &= \epsilon^{-\frac{1}{24}} R'_m, & \bar{C}_m &= \epsilon^{-\frac{1}{24}} C'_m, & \bar{S}_m &= \epsilon^{-\frac{1}{24}} S'_m, \\
\bar{E}_m &= \epsilon^{-\frac{1}{24}} E'_m, & \bar{F}_m &= \epsilon^{-\frac{1}{24}} F'_m, & \bar{C} &= \epsilon^{-\frac{1}{12}} C', & \hat{S} &= \epsilon^{-\frac{1}{12}} S', \\
\hat{E} &= \epsilon^{-\frac{1}{12}} E', & \bar{F} &= \epsilon^{-\frac{1}{12}} F', & \hat{B}_m &= \epsilon^{-\frac{1}{8}} B'_m
\end{aligned} \tag{3.115}$$

These scaling result in AcrAB translation terms entering the leading order balance in equation (3.116). We note that this timescale matches the same time scaling as timescale 5 in the wild-type asymptotic analysis.The system of equations rescaled for the fifth timescale is

$$\begin{aligned}
\frac{dR'_m}{dT'} &= 1 - \epsilon^{\frac{1}{8}} R'_m, & \frac{dR'}{dT'} &= 0, \\
\frac{d\hat{A}_m}{dT'} &= \frac{\epsilon^{\frac{1}{8}} \hat{A}}{(\epsilon \hat{A} + 1)(\epsilon^{\frac{1}{4}} R' + 1)} + \epsilon^{\frac{1}{8}} \alpha - \epsilon^{\frac{1}{8}} \hat{A}_m, & \frac{d\hat{A}}{dT'} &= \epsilon^{\frac{1}{8}} \theta\, \hat{A}_m - \epsilon^{\frac{5}{8}} \upsilon\, \hat{A} - \epsilon^{\frac{9}{8}} \Delta \hat{A}, \\
\frac{dC'_m}{dT'} &= \frac{\lambda}{\epsilon \hat{A} + \lambda} - \epsilon^{\frac{1}{8}} C'_m, & \frac{dC'}{dT'} &= \gamma\, C'_m - \epsilon^{\frac{9}{8}} \Delta C', \\
\frac{dB'_m}{dT'} &= \frac{\epsilon^{\frac{1}{4}} \hat{A} + S'}{(1 + \epsilon^{\frac{3}{4}} S' + \epsilon \hat{A})(1 + \epsilon^{\frac{3}{4}} E' + \epsilon^{\frac{1}{4}} C')} - \epsilon^{\frac{1}{8}} B'_m, & \frac{d\hat{B}}{dT'} &= \beta\, B'_m - \epsilon^{\frac{9}{8}} \Delta\, \hat{B}, \\
\frac{dS'_m}{dT'} &= 1 - \epsilon^{\frac{1}{8}} S'_m, & \frac{dS'}{dT'} &= \sigma\, S'_m - \epsilon^{\frac{9}{8}} \Delta\, S', \\
\frac{dE'_m}{dT'} &= 1 - \epsilon^{\frac{1}{8}} E'_m, & \frac{dE'}{dT'} &= \xi\, E'_m - \epsilon^{\frac{9}{8}} \Delta\, E', \\
\frac{dF'_m}{dT'} &= \frac{\eta}{\eta + \epsilon^{\frac{3}{4}} E'} - \epsilon^{\frac{1}{8}} F'_m, & \frac{dF'}{dT'} &= \frac{F'_m}{\epsilon \omega \hat{B} + 1} - \epsilon^{\frac{9}{8}} \Delta F'.
\end{aligned} \tag{3.116}$$

At leading order, we have the following system of equations

$$\begin{aligned}
\frac{dR'_m}{dT'} &= 1, & \frac{d\hat{R}}{dT'} &= 0, \\
\frac{d\hat{A}_m}{dT'} &= 0, & \frac{d\hat{A}}{dT'} &= 0, \\
\frac{dC'_m}{dT'} &= 1, & \frac{dC'}{dT'} &= \gamma\, C'_m,
\end{aligned}$$

$$\begin{aligned}
\frac{dB'_m}{dT'} &= S', & \frac{d\hat{B}}{dT'} &= \beta B'_m, \\
\frac{dS'_m}{dT'} &= 1, & \frac{dS'}{dT'} &= \sigma S'_m, \\
\frac{dE'_m}{dT'} &= 1, & \frac{dE'}{dT'} &= \xi E'_m, \\
\frac{dF'_m}{dT'} &= 1, & \frac{dF'}{dT'} &= F'_m.
\end{aligned} \tag{3.117}$$

This system of ODEs can be solved, matching to the long term dominant behaviour on the previous timescale gives the following asymptotic approximations

$$\begin{aligned}
R'_m &= T', & \hat{R} &= R_0, & \hat{A}_m &= A_{m0}, & \hat{A} &= A_0, \\
C'_m &= T', & C' &= \frac{\gamma}{2}T'^2, & B'_m &= \frac{\sigma}{6}T'^3, & \hat{B} &= \frac{\beta\sigma}{24}T'^4 + B_0, \\
S'_m &= T', & S' &= \frac{\sigma}{2}T'^2, & E'_m &= T', & E' &= \frac{\xi}{2}T'^2, \\
F'_m &= T', & F' &= \frac{1}{2}T'^2.
\end{aligned} \tag{3.118}$$

We plot these asymptotic approximations against the full solution in Figure 3.16. In this timescale, we have translation of AcrAB, we note that this is still being driven by the underlying regulators Rob, SoxS and MarA. We note that this is the last timescale that displays almost identical behaviour (apart from RamR protein) to the respective timescale on the wild-type asymptotic analysis.

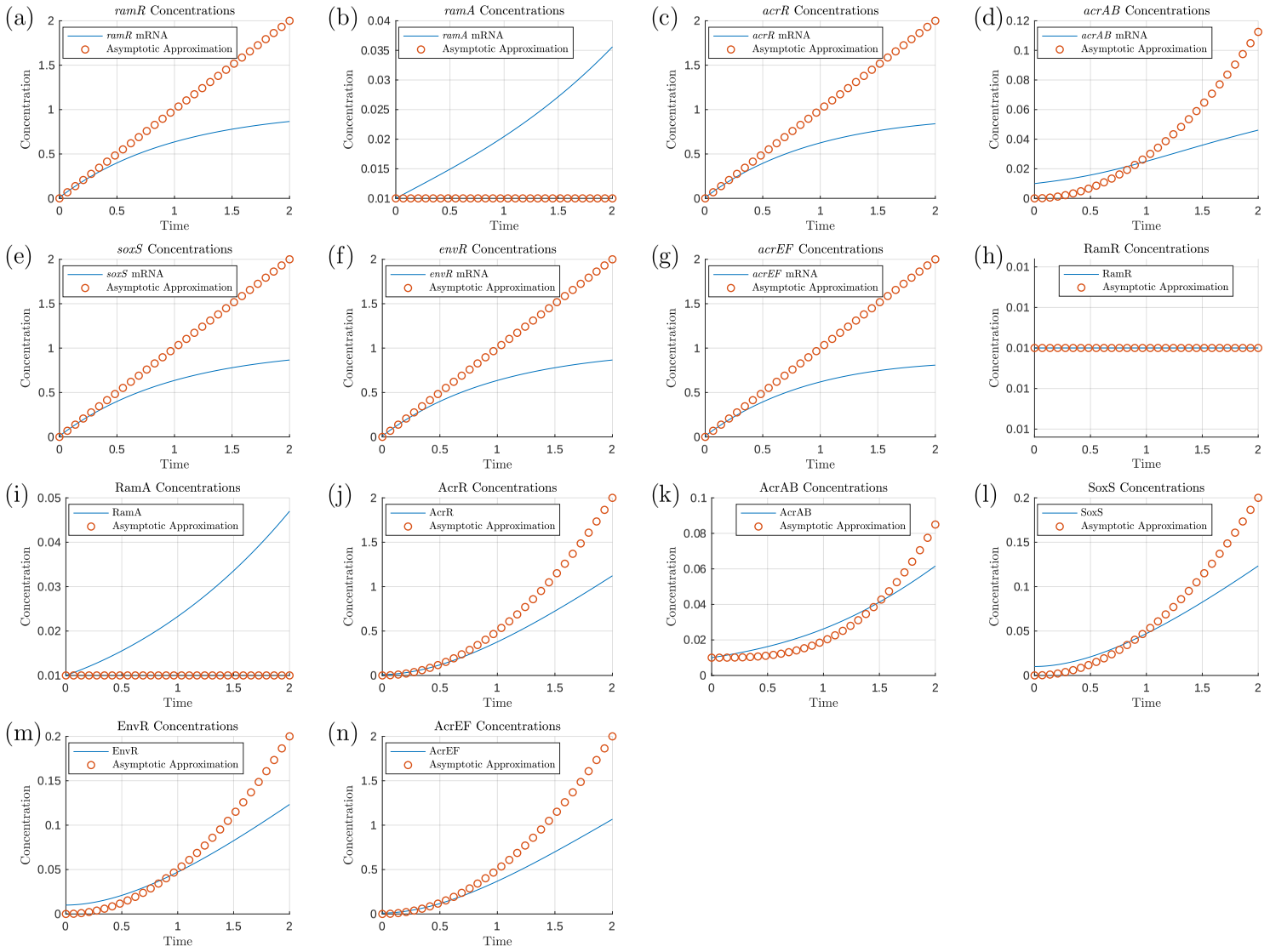

Figure 3.16: Asymptotic approximations on timescale 5 for the mutant dynamics ($\epsilon = 0.01$). On this timescale, time is $O(\epsilon^{\frac{1}{8}})$, so we expect the asymptotics to be accurate around $T = \epsilon^{\frac{1}{8}} \approx 0.5623$. For reference, the previous and subsequent timescales have time at $O(\epsilon^{\frac{1}{6}})$ and $O(1)$ respectively.

3.7.6 Timescale 6: mRNA degradation and full protein translation

We move onto the sixth timescale, here mRNA degradation and expression of *ramA* appear at leading order in all mRNA equations and (3.120). We take the following variable scalings

$$
\begin{aligned}
&T' = \epsilon^{-\frac{1}{8}} T^\dagger, \qquad R'_m = \epsilon^{-\frac{1}{8}} R^\dagger_m, \qquad C'_m = \epsilon^{-\frac{1}{8}} C^\dagger_m, \qquad S'_m = \epsilon^{-\frac{1}{8}} S^\dagger_m, \qquad E'_m = \epsilon^{-\frac{1}{8}} E^\dagger_m,\\
&F'_m = \epsilon^{-\frac{1}{8}} F^\dagger_m, \qquad C' = \epsilon^{-\frac{1}{4}} C^\dagger, \qquad S' = \epsilon^{-\frac{1}{4}} S^\dagger, \qquad E' = \epsilon^{-\frac{1}{4}} E^\dagger, \qquad F' = \epsilon^{-\frac{1}{4}} F^\dagger,\\
&B'_m = \epsilon^{-\frac{3}{8}} B^\dagger_m, \qquad \hat{B} = \epsilon^{-\frac{1}{2}} B^\dagger.
\end{aligned} \tag{3.119}
$$

This is the last timescale that matches on time scalings compared to the corresponding number timescale on the wild-type analysis. Using these scalings, our system of equations rescaled for the sixth timescale is

$$
\begin{aligned}
&\frac{dR^\dagger_m}{dT^\dagger} = 1 - R^\dagger_m, && \epsilon\frac{d\hat{R}}{dT^\dagger} = 0,\\
&\frac{d\hat{A}_m}{dT^\dagger} = \frac{\hat{A}}{(\epsilon\hat{A}+1)(\epsilon\hat{R}+1)} + \alpha - \hat{A}_m, && \frac{d\hat{A}}{dT^\dagger} = \theta\,\hat{A}_m - \epsilon^{\frac{1}{2}}\upsilon\,\hat{A} - \epsilon\Delta\hat{A},\\
&\frac{dC^\dagger_m}{dT^\dagger} = \frac{\lambda}{\epsilon\hat{A}+\lambda} - C^\dagger_m, && \frac{dC^\dagger}{dT^\dagger} = \gamma\,C^\dagger_m - \epsilon\Delta C^\dagger,\\
&\frac{dB^\dagger_m}{dT^\dagger} = \frac{\epsilon^{\frac{1}{2}}\hat{A} + S^\dagger}{(1+\epsilon^{\frac{1}{2}}S^\dagger + \epsilon\hat{A})(1+\epsilon^{\frac{1}{2}}E^\dagger + C^\dagger)} - B^\dagger_m, && \frac{dB^\dagger}{dT^\dagger} = \beta\,B^\dagger_m - \epsilon\Delta\,B^\dagger,\\
&\frac{dS^\dagger_m}{dT^\dagger} = 1 - S^\dagger_m, && \frac{dS^\dagger}{dT^\dagger} = \sigma\,S^\dagger_m - \epsilon\Delta\,S^\dagger,\\
&\frac{dE^\dagger_m}{dT^\dagger} = 1 - E^\dagger_m, && \frac{dE^\dagger}{dT^\dagger} = \xi\,E^\dagger_m - \epsilon\Delta\,E^\dagger,\\
&\frac{dF^\dagger_m}{dT^\dagger} = \frac{\eta}{\eta+\epsilon^{\frac{1}{2}}E^\dagger} - F^\dagger_m, && \frac{dF^\dagger}{dT^\dagger} = \frac{F^\dagger_m}{\epsilon^{\frac{1}{2}}\omega B^\dagger + 1} - \epsilon\Delta F^\dagger.
\end{aligned} \tag{3.120}
$$

At leading order, we have the following system of equations

$$
\begin{aligned}
\frac{dR^{\dagger}{}_m}{dT^{\dagger}} &= 1 - R^{\dagger}_m, & \frac{d\hat{R}}{dT^{\dagger}} &= 0,\\
\frac{d\hat{A}_m}{dT^{\dagger}} &= \hat{A} + \alpha - \hat{A}_m, & \frac{d\hat{A}}{dT^{\dagger}} &= \theta\hat{A}_m,\\
\frac{dC^{\dagger}_m}{dT^{\dagger}} &= 1 - C^{\dagger}_m, & \frac{dC^{\dagger}}{dT^{\dagger}} &= \gamma\, C^{\dagger}_m,\\
\frac{dB^{\dagger}{}_m}{dT^{\dagger}} &= \frac{S^{\dagger}}{1+C^{\dagger}} - B^{\dagger}_m, & \frac{dB^{\dagger}}{dT^{\dagger}} &= \beta B^{\dagger}_m,\\
\frac{dS^{\dagger}_m}{dT^{\dagger}} &= 1 - S^{\dagger}_m, & \frac{dS^{\dagger}}{dT^{\dagger}} &= \sigma S^{\dagger}_m,\\
\frac{dE^{\dagger}_m}{dT^{\dagger}} &= 1 - E^{\dagger}_m, & \frac{dE^{\dagger}}{dT^{\dagger}} &= \xi E^{\dagger}_m,\\
\frac{dF^{\dagger}_m}{dT^{\dagger}} &= 1 - F^{\dagger}_m, & \frac{dF^{\dagger}}{dT^{\dagger}} &= F^{\dagger}_m.
\end{aligned}
\tag{3.121}
$$

Solving and matching to the long term dominant behaviour on the previous timescale gives the following asymptotic approximations

$$
\begin{aligned}
&R^{\dagger}_m = 1 - e^{-T^{\dagger}}, \quad \hat{R} = R_0, && C^{\dagger}_m = 1 - e^{-T^{\dagger}}, \quad C^{\dagger} = \gamma(T^{\dagger} - e^{-T^{\dagger}} - 1),\\
&B^{\dagger}_m = \frac{\sigma T^{\dagger}}{\gamma T^{\dagger} + 1}, \quad B^{\dagger} = \frac{\beta\sigma}{\gamma}\left(T^{\dagger} - \frac{\ln(T^{\dagger}\gamma + 1)}{\gamma}\right), && S^{\dagger}_m = 1 - e^{-T^{\dagger}}, \quad S^{\dagger} = \sigma(T^{\dagger} - e^{-T^{\dagger}} - 1),\\
&E^{\dagger}_m = 1 - e^{-T^{\dagger}}, \quad E^{\dagger} = \xi(T^{\dagger} - e^{-T^{\dagger}} - 1), && F^{\dagger}_m = 1 - e^{-T^{\dagger}}, \quad F^{\dagger} = T^{\dagger} - e^{-T^{\dagger}} - 1,
\end{aligned}
$$

$$
\begin{aligned}
\hat{A}_m &= \frac{\left(\sqrt{1+4\,\theta}\alpha + \sqrt{1+4\,\theta}A_0 + 2\,A_0\theta + \alpha + A_0\right) e^{\frac{\left(-1+\sqrt{1+4\,\theta}\right)T^{\dagger}}{2}}}{2\sqrt{1+4\,\theta}} - \alpha,\\
\hat{A} &= \frac{\left((\alpha + A_0)\sqrt{1+4\,\theta} + (2\,\theta+1)\,A_0 + \alpha\right) e^{\frac{\left(-1+\sqrt{1+4\,\theta}\right)T^{\dagger}}{2}}}{2\sqrt{1+4\,\theta}}.
\end{aligned}
\tag{3.122}
$$

We plot asymptotic approximations of those variables that evolve on this timescale against the numerical solutions in Figure 3.17. In this timescale, we have most of the mRNAs' asymptotic approximations reaching near steady state as their degradation takes effect. The only mRNA not reaching steady state is *ramA* mRNA, which is exhibiting exponential growth. There is the same exponential growth for RamA protein, both of these growth behaviours are caused by the positive feedback loop with the *ramA* gene upon itself. In contrast to the wild-type system, without any presence of RamR protein to repress this feedback loop, we see rapidly increasing expression of *ramA*.

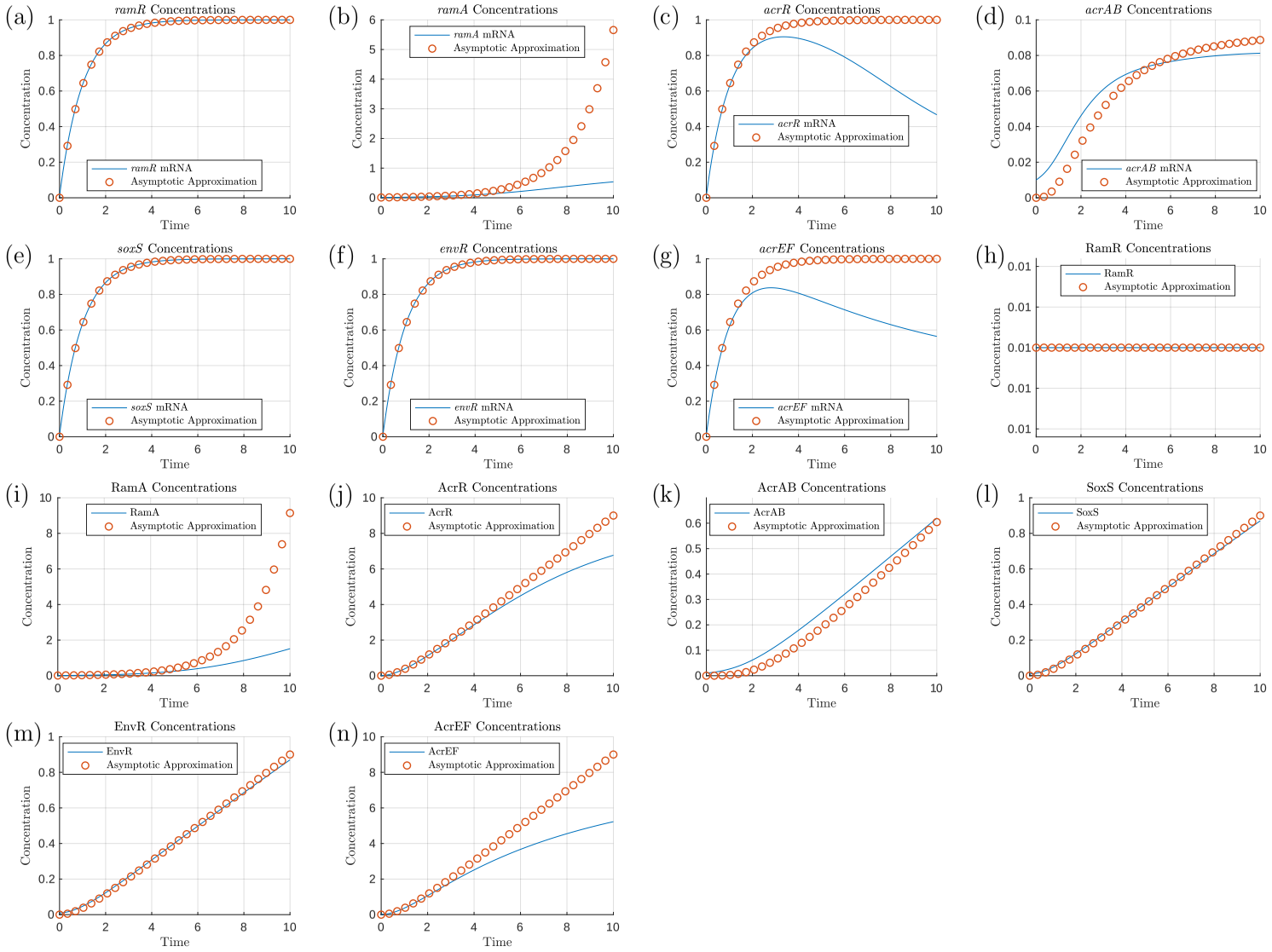

Figure 3.17: Asymptotic approximations on timescale 6 for the mutant dynamics ($\epsilon = 0.01$). On this timescale, time is $O(1)$, so we expect the asymptotics to be accurate around $T = 1$. For reference, the previous and subsequent timescales have time at $O(\epsilon^{\frac{1}{8}})$ and $O(1 + \frac{1}{2\kappa}\phi^{-1})$ respectively. Disparities in these simulations can be reduced by reducing the value of ϵ.

3.7.7 Timescale 7: activation of *acrAB* by RamA

For this timescale, we require the following values $\phi = \ln(1/\epsilon)^{-1}$ and $\kappa = \frac{1}{2}(-1+\sqrt{1+4\theta})$, resulting from the logarithmic and exponential behaviour on the previous timescale respectively. Activation of $acrAB$ mRNA transcription via RamA protein now appears in equation (3.124). We take the following variable scalings:

$$T^\dagger = \frac{1}{2\kappa}\ln(1/\epsilon) + T^\ddagger, \quad \hat{A}_m = \epsilon^{-\frac{1}{2}}A_m^\ddagger, \qquad \hat{A} = \epsilon^{-\frac{1}{2}}A^\ddagger, \qquad C^\dagger = \ln(1/\epsilon)C^\ddagger,$$
$$B^\dagger = \ln(1/\epsilon)B^\ddagger, \qquad S^\dagger = \ln(1/\epsilon)S^\ddagger, \quad E^\dagger = \ln(1/\epsilon)E^\ddagger, \quad F^\dagger = \ln(1/\epsilon)F^\ddagger. \quad (3.123)$$

This timescale takes place between timescale 6 and timescale 7 (Sections 3.6.6-3.6.7) of the wild-type asymptotic analysis. The system of equations rescaled for the seventh timescale is

$$\begin{aligned}
\frac{dR_m^\dagger}{dT^\ddagger} &= 1 - R_m^\dagger, & \epsilon\frac{d\hat{R}}{dT^\ddagger} &= 0,\\
\frac{dA_m^\ddagger}{dT^\ddagger} &= \frac{A^\ddagger}{(\epsilon^{\frac{1}{2}}A^\ddagger+1)(\epsilon\hat{R}+1)} + \epsilon^{\frac{1}{2}}\alpha - A_m^\ddagger, & \frac{dA^\ddagger}{dT^\ddagger} &= \theta\, A_m^\ddagger - \epsilon^{\frac{1}{2}}\upsilon\, A^\ddagger - \epsilon\Delta A^\ddagger,\\
\frac{dC_m^\dagger}{dT^\ddagger} &= \frac{\lambda}{\epsilon^{\frac{1}{2}}A^\ddagger+\lambda} - C_m^\dagger, & \phi^{-1}\frac{dC^\ddagger}{dT^\ddagger} &= \gamma\, C_m^\dagger - \epsilon\phi^{-1}\Delta C^\ddagger,\\
\frac{dB_m^\dagger}{dT^\ddagger} &= \frac{A^\ddagger + \phi^{-1}S^\ddagger}{(1+\epsilon^{\frac{1}{2}}\phi^{-1}S^\ddagger+\epsilon^{\frac{1}{2}}A^\ddagger)(1+\epsilon^{\frac{1}{2}}\phi^{-1}E^\ddagger+\phi^{-1}C^\ddagger)} & \phi^{-1}\frac{dB^\ddagger}{dT^\ddagger} &= \beta\, B_m^\dagger - \epsilon\phi^{-1}\Delta\, B^\ddagger,
\end{aligned} \quad (3.124)$$

$$\begin{aligned}
\frac{dS_m^\dagger}{dT^\ddagger} &= 1 - S_m^\dagger, & \phi^{-1}\frac{dS^\ddagger}{dT^\ddagger} &= \sigma\, S_m^\dagger - \epsilon\phi^{-1}\Delta\, S^\ddagger,\\
\frac{dE_m^\dagger}{dT^\ddagger} &= 1 - E_m^\dagger, & \phi^{-1}\frac{dE^\ddagger}{dT^\ddagger} &= \xi\, E_m^\dagger - \epsilon\phi^{-1}\Delta\, E^\ddagger,\\
\frac{dF_m^\dagger}{dT^\ddagger} &= \frac{\eta}{\eta+\epsilon^{\frac{1}{2}}\phi^{-1}E^\ddagger} - F_m^\dagger, & \phi^{-1}\frac{dF^\ddagger}{dT^\ddagger} &= \frac{F_m^\dagger}{\epsilon^{\frac{1}{2}}\phi^{-1}\omega B^\ddagger+1} - \epsilon\phi^{-1}\Delta F^\ddagger.
\end{aligned}$$

At leading order, we have the following system of equations

$$\begin{aligned}
\frac{dR^\dagger{}_m}{dT^\ddagger} &= 1 - R_m^\dagger, & \frac{d\hat{R}}{dT^\ddagger} &= 0,\\
\frac{dA_m^\ddagger}{dT^\ddagger} &= A^\ddagger - A_m^\ddagger, & \frac{dA^\ddagger}{dT^\ddagger} &= \theta A_m^\ddagger,\\
\frac{dC_m^\dagger}{dT^\ddagger} &= 1 - C_m^\dagger, & \frac{dC^\ddagger}{dT^\ddagger} &= \phi\gamma\, C_m^\dagger,
\end{aligned}$$

$$
\begin{aligned}
\frac{dB^{\dagger}{}_m}{dT^{\ddagger}} &= \frac{A^{\ddagger}+\phi^{-1}S^{\ddagger}}{1+\phi^{-1}C^{\ddagger}} - B^{\dagger}_m, & \frac{dB^{\ddagger}}{dT^{\ddagger}} &= \phi\beta B^{\dagger}_m,\\
\frac{dS^{\dagger}_m}{dT^{\ddagger}} &= 1 - S^{\dagger}_m, & \frac{dS^{\ddagger}}{dT^{\ddagger}} &= \phi\sigma S^{\dagger}_m,\\
\frac{dE^{\dagger}_m}{dT^{\ddagger}} &= 1 - E^{\dagger}_m, & \frac{dE^{\ddagger}}{dT^{\ddagger}} &= \phi\xi E^{\dagger}_m,\\
\frac{dF^{\dagger}_m}{dT^{\ddagger}} &= 1 - F^{\dagger}_m, & \frac{dF^{\ddagger}}{dT^{\ddagger}} &= \phi F^{\dagger}_m.
\end{aligned} \tag{3.125}
$$

We solve the leading order system of ODEs and match to the long term dominant behaviour on the previous timescale, giving us the following asymptotic approximations

$$
\begin{aligned}
&R^{\dagger}_m = 1 - e^{-T^{\ddagger}}, && \hat{R} = R_0, && C^{\dagger}_m = 1 - e^{-T^{\ddagger}}\\
&C^{\ddagger} = \phi\gamma\left(T^{\ddagger} - e^{-T^{\ddagger}} - 1\right), && B^{\dagger}_m = \frac{A_0 e^{\theta T^{\ddagger}} + \phi^{-1}\sigma T^{\ddagger}}{\phi^{-1}\gamma T^{\ddagger} + 1}, && S^{\dagger}_m = 1 - e^{-T^{\ddagger}},\\
&S^{\ddagger} = \phi\sigma\left(T^{\ddagger} - e^{-T^{\ddagger}} - 1\right), && E^{\dagger}_m = 1 - e^{-T^{\ddagger}}, && F^{\dagger}_m = 1 - e^{-T^{\ddagger}},\\
&E^{\ddagger} = \phi\xi\left(T^{\ddagger} - e^{-T^{\ddagger}} - 1\right), && F^{\ddagger} = \phi(T^{\ddagger} - e^{-T^{\ddagger}} - 1),
\end{aligned}
$$

$$
\begin{aligned}
A^{\ddagger}_m &= \frac{\left(A_0\sqrt{1+4\,\theta} + 2\,A_{m0}\theta + A_0\right)\left(-1+\sqrt{1+4\,\theta}\right)e^{\frac{\left(-1+\sqrt{1+4\,\theta}\right)T^{\ddagger}}{2}}}{4\theta\sqrt{1+4\,\theta}},\\
A^{\ddagger} &= \frac{\left(A_0\sqrt{1+4\,\theta} + 2\,A_{m0}\theta + A_0\right)e^{\frac{\left(-1+\sqrt{1+4\,\theta}\right)T^{\ddagger}}{2}}}{2\sqrt{1+4\,\theta}},\\
B^{\ddagger} &= \frac{\beta\,\phi\,A_0}{\gamma}\mathrm{e}^{-\frac{\theta}{\gamma}}Ei\left(1,\theta\,T+\frac{\theta}{\gamma}\right) + \frac{\beta\,\phi\,\sigma\,T}{\gamma} - \frac{\beta\,\phi\,\sigma\,\ln\left(T\gamma\,\phi\,\theta+\phi\,\theta\right)}{\gamma^2}.
\end{aligned} \tag{3.126}
$$

Notably here we have the function Ei that represents the exponential integral function. In order to move to the next timescale we must determine the long term dominant behaviour in terms of elementary functions by taking their series expansions at infinity. For the exponential integral function as $z \to \infty$ we have [29]

$$
Ei(z) = \frac{1}{z}\,e^{z}\left(1 + O\left(\frac{1}{z}\right)\right). \tag{3.127}
$$

We plot asymptotic approximations of those variables that evolve on this timescale against the numerical solutions in Figure 3.18. In this timescale we still have exponential

growth of *ramA* mRNA and RamA protein caused by the positive feedback of the *ramA* gene. This growth has resulted in activation of *acrAB* mRNA which now exhibits long term exponential growth. This is being translated to AcrAB protein which now also exhibits long term exponential growth. This behaviour varies from the wild-type analysis, where there is no direct activation of *acrAB* mRNA from RamA on any timescale. Comparatively, this results in a larger concentration of *acrAB* mRNA in the mutant analysis.

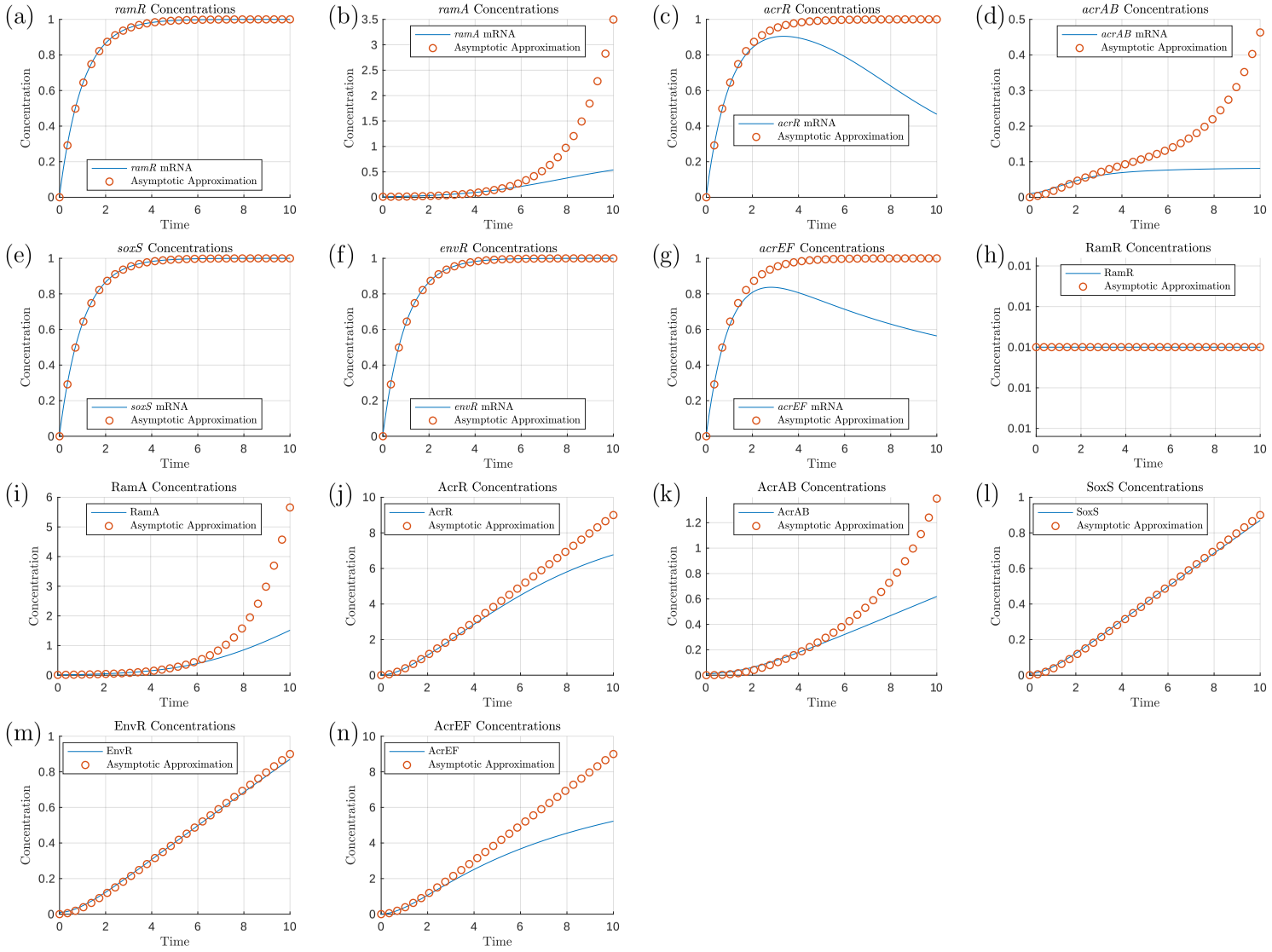

Figure 3.18: Asymptotic approximations on timescale 7 for the mutant dynamics ($\epsilon = 0.01$). On this timescale, time is $O(1+\frac{1}{2\kappa}\phi^{-1})$, so we expect the asymptotics to be accurate around $T = 1+\frac{1}{2\kappa}\phi^{-1} \approx 4.7257$. For reference, the previous and subsequent timescales have time at $O(1)$ and $O(1+\frac{1}{\kappa}\phi^{-1})$ respectively.

3.7.8 Timescale 8: *ramA* mRNA reaching steady state

For this timescale, the limitation of *ramA* activating its own expression enters the leading order balance in equation (3.129). We take the following scalings based on the variables on the previous timescale's long term behaviour

$$
\begin{aligned}
T^{\ddagger} &= \frac{1}{2\kappa}\ln(1/\epsilon) + T^{\diamond}, & A_m^{\ddagger} &= \epsilon^{-\frac{1}{2}} A_m^{\diamond}, & A^{\ddagger} &= \epsilon^{-\frac{1}{2}} A^{\diamond},\\
B_m^{\dagger} &= \epsilon^{-\frac{1}{2}}\ln(1/\epsilon)^{-1} B_m^{\diamond}, & C^{\ddagger} &= \ln(1/\epsilon) C^{\diamond}, & S^{\ddagger} &= \ln(1/\epsilon) S^{\diamond},\\
B^{\ddagger} &= \epsilon^{-\frac{1}{2}}\ln(1/\epsilon)^{-1} B^{\diamond} & E^{\ddagger} &= \ln(1/\epsilon) E^{\diamond}, & F^{\ddagger} &= \ln(1/\epsilon) F^{\diamond}.
\end{aligned}
\tag{3.128}
$$

Comparatively, this timescale takes place between timescale 6 and timescale 7 (Sections 3.6.6-3.6.7) of the wild-type asymptotic analysis. The system of equations rescaled for the eighth timescale is

$$
\begin{aligned}
\frac{dR_m^{\dagger}}{dT^{\diamond}} &= 1 - R_m^{\dagger}, & \epsilon\frac{d\hat{R}}{dT^{\diamond}} &= 0,\\
\frac{dA_m^{\diamond}}{dT^{\diamond}} &= \frac{A^{\diamond}}{(A^{\diamond}+1)(\epsilon\hat{R}+1)} + \epsilon\alpha - A_m^{\diamond}, & \frac{dA^{\diamond}}{dT^{\diamond}} &= \theta\, A_m^{\diamond} - \epsilon^{\frac{1}{2}}\upsilon\, A^{\diamond} - \epsilon\Delta A^{\diamond},\\
& & \phi^{-2}\frac{dC^{\diamond}}{dT^{\diamond}} &= \gamma\, C_m^{\dagger} - \epsilon\phi^{-2}\Delta C^{\diamond},\\
\frac{dC_m^{\dagger}}{dT^{\diamond}} &= \frac{\lambda}{A^{\diamond}+\lambda} - C_m^{\dagger}, & \frac{dB^{\diamond}}{dT^{\diamond}} &= \phi\beta\, B_m^{\diamond} - \epsilon\Delta\, B^{\diamond},\\
\phi\frac{dB_m^{\diamond}}{dT^{\diamond}} &= \frac{A^{\diamond} + \epsilon^{\frac{1}{2}}\phi^{-2}S^{\diamond}}{(1+\epsilon^{\frac{1}{2}}\phi^{-2}S^{\diamond}+A^{\diamond})(1+\epsilon^{\frac{1}{2}}\phi^{-2}E^{\diamond}+\phi^{-2}C^{\diamond})} - \phi B_m^{\diamond}, & &\\
\frac{dS_m^{\dagger}}{dT^{\diamond}} &= 1 - S_m^{\dagger}, & \phi^{-2}\frac{dS^{\diamond}}{dT^{\diamond}} &= \sigma\, S_m^{\dagger} - \epsilon\phi^{-2}\Delta\, S^{\diamond},\\
\frac{dE_m^{\dagger}}{dT^{\diamond}} &= 1 - E_m^{\dagger}, & \phi^{-2}\frac{dE^{\diamond}}{dT^{\diamond}} &= \xi\, E_m^{\dagger} - \epsilon\phi^{-2}\Delta\, E^{\diamond},\\
\frac{dF_m^{\dagger}}{dT^{\diamond}} &= \frac{\eta}{\eta+\epsilon^{\frac{1}{2}}\phi^{-2}E^{\diamond}} - F_m^{\dagger}, & \phi^{-2}\frac{dF^{\diamond}}{dT^{\diamond}} &= \frac{F_m^{\dagger}}{\omega B^{\diamond}+1} - \epsilon\phi^{-2}\Delta F^{\diamond}.
\end{aligned}
\tag{3.129}
$$

At leading order, we have the following system of equations

$$
\begin{aligned}
\frac{dR^{\dagger}{}_m}{dT^{\diamond}} &= 1 - R_m^{\dagger}, & \frac{d\hat{R}}{dT^{\diamond}} &= 0,\\
\frac{dA_m^{\diamond}}{dT^{\diamond}} &= \frac{A^{\diamond}}{A^{\diamond}+1} - A_m^{\diamond}, & \frac{dA^{\diamond}}{dT^{\diamond}} &= \theta A_m^{\diamond},\\
\frac{dC_m^{\dagger}}{dT^{\diamond}} &= \frac{\lambda}{A^{\diamond}+\lambda} - C_m^{\dagger}, & \frac{dC^{\diamond}}{dT^{\diamond}} &= \phi^2\gamma\, C_m^{\dagger},
\end{aligned}
$$

$$\begin{aligned}
\frac{dB^{\dagger}{}_m}{dT^{\diamond}} &= \phi^{-1}\frac{A^{\diamond}}{(1+A^{\diamond})(1+\phi^{-2}C^{\diamond})} - B^{\diamond}_m, & \frac{dB^{\diamond}}{dT^{\diamond}} &= \phi\beta B^{\diamond}_m,\\
\frac{dS^{\dagger}_m}{dT^{\diamond}} &= 1 - S^{\dagger}_m, & \frac{dS^{\diamond}}{dT^{\diamond}} &= \phi^2\sigma S^{\dagger}_m,\\
\frac{dE^{\dagger}_m}{dT^{\diamond}} &= 1 - E^{\dagger}_m, & \frac{dE^{\diamond}}{dT^{\diamond}} &= \phi^2\xi E^{\dagger}_m,\\
\frac{dF^{\dagger}_m}{dT^{\diamond}} &= 1 - F^{\dagger}_m, & \frac{dF^{\diamond}}{dT^{\diamond}} &= \phi^2\frac{F^{\dagger}_m}{\omega B^{\diamond}+1}.
\end{aligned} \tag{3.130}$$

Taking this leading order balance, solving and matching to the long-term dominant behaviour on the previous timescale gives the following asymptotic approximations

$$\begin{aligned}
&R^{\dagger}_m = 1 - e^{-T^{\diamond}}, && \hat{R} = R_0, && C^{\dagger}_m = 1 - e^{-T^{\diamond}}\\
&C^{\diamond} = \frac{\phi^2\gamma\,\lambda\,\ln\left(\theta\,T^{\diamond}+\lambda\right)}{\theta}, && F^{\dagger}_m = 1 - e^{-T^{\diamond}}, && S^{\dagger}_m = 1 - e^{-T^{\diamond}},\\
&S^{\diamond} = \phi^2\sigma\left(T^{\diamond} - e^{-T^{\diamond}} - 1\right), && E^{\dagger}_m = 1 - e^{-T^{\diamond}}, && E^{\diamond} = \phi^2\xi\left(T^{\diamond} - e^{-T^{\diamond}} - 1\right),
\end{aligned}$$

$$A^{\diamond}_m = \frac{\mathrm{W}\left(\frac{\left(A_0\sqrt{1+4\theta}+2A_{m0}\theta+A_0\right)e^{\theta T^{\diamond}}}{2\sqrt{1+4\theta}}\right)}{\mathrm{W}\left(\frac{\left(A_0\sqrt{1+4\theta}+2A_{m0}\theta+A_0\right)e^{\theta T^{\diamond}}}{2\sqrt{1+4\theta}}\right)+1}, \quad A^{\diamond} = \mathrm{W}\left(\frac{\left(A_0\sqrt{1+4\theta}+2A_{m0}\theta+A_0\right)e^{\theta T^{\diamond}}}{2\sqrt{1+4\theta}}\right),$$

$$B^{\diamond}_m = \frac{\phi^{-1}\theta T^{\diamond}}{(1+\theta T^{\diamond})(1+\frac{\gamma\,\lambda\,\ln(\theta\,T^{\diamond}+\lambda)}{\theta})},$$

$$B^{\diamond} = \frac{\beta}{\gamma}e^{-\frac{\theta}{\gamma\lambda}}Ei\left(1, \ln(\theta T+\lambda) + \frac{\theta}{\gamma\lambda}\right) - \frac{\beta}{\gamma}\ln\left(\gamma\lambda\ln(\theta T+\lambda)+\theta\right),$$

$$F^{\diamond} = \frac{\phi^2}{\beta\omega}\left(\frac{\gamma}{2\theta}\ln^2(\theta T^{\diamond}+\lambda) + \frac{1}{\lambda}\ln(\theta T^{\diamond}+\lambda)\right). \tag{3.131}$$

Notably here we have the functions W that represents the Lambert W function. In order to move to the next timescale we must determine the long term dominant behaviour in terms of elementary functions by taking their series expansions at infinity. For the Lambert W function as $z \to \infty$ we have [19]

$$\mathrm{W}(z) = \ln(z) + O(\ln(\ln(z))). \tag{3.132}$$

We plot asymptotic approximations of those variables that evolve on this timescale against the numerical solutions in Figure 3.19. In this timescale the *ramA* gene's positive

feedback has been limited, causing at long term the gene's mRNA to approach steady state and the gene's protein to have linear growth. This change of behaviour of RamA from exponential growth causes *acrAB* mRNA and protein to no longer display exponential behaviour. Notably this behaviour is not present in the wild-type analysis as the *ramA* gene positive feedback loop is not present at leading order on any timescale. We note that we have disparity of fit for both *acrAB* mRNA and protein. Therefore, we include additional plots (Figure 3.19 (o) and (p)) with a smaller value of ϵ ($\epsilon = 0.0001$) to prove the accuracy of the asymptotic approximations. Disparities in other simulations could also be reduced by a smaller ϵ value.

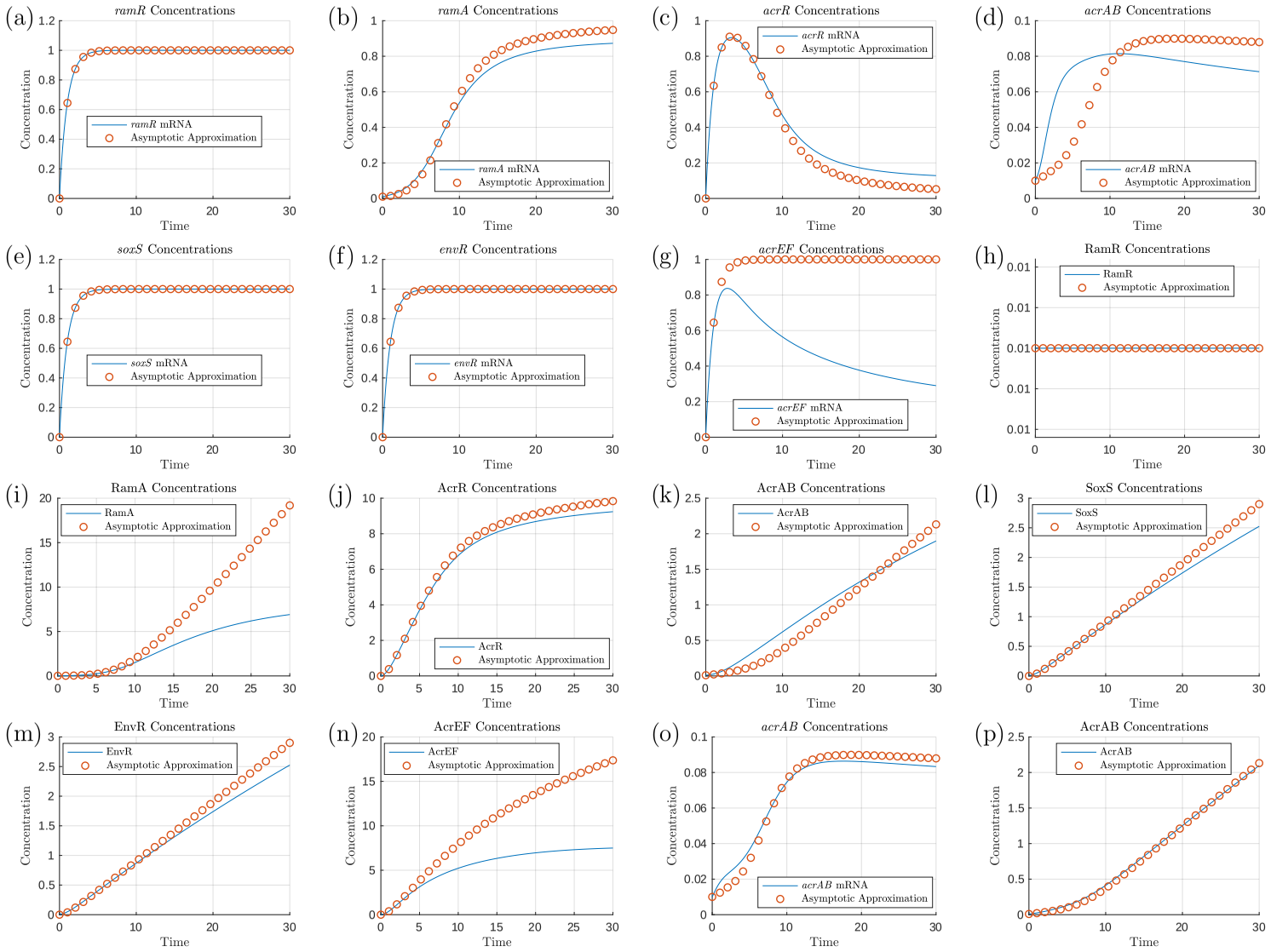

Figure 3.19: Asymptotic approximations on timescale 8 for the mutant dynamics($\epsilon = 0.01$). On this timescale, time is $O(1 + \frac{1}{\kappa}\phi^{-1})$, so we expect the asymptotics to be accurate around $T = 1 + \frac{1}{\kappa}\phi^{-1} \approx 8.4513$. For (o) and (p) we have set $\epsilon = 0.0001$ to show the validity of the asymptotic approximations for *acrAB* mRNA and protein. For reference, the previous and subsequent timescales have time at $O(1 + \frac{1}{2\kappa}\phi^{-1})$ and $O(\epsilon^{-\frac{1}{2}}(1 + \frac{1}{\kappa}\phi^{-1})$ respectively.

3.7.9 Timescale 9: degradation of RamA protein

We move onto the ninth timescale, here degradation of RamA protein caused by Lon Protease enters the leading order balance as well as EnvR repression of *acrEF* in equations (3.134)-(3.135). We take the following scalings based on the variables on the previous timescale's long term behaviour

$$\begin{aligned}
&T^{\diamond} = \epsilon^{-\frac{1}{2}} T^{+}, && A^{\diamond} = \epsilon^{-\frac{1}{2}} A^{+}, && S^{\diamond} = \epsilon^{-\frac{1}{2}} S^{+},\\
&E^{\diamond} = \epsilon^{-\frac{1}{2}} E^{+}, && B_m^{\diamond} = \ln(1/\epsilon)^{-1} B_m^{+}, && B^{\diamond} = \epsilon^{-\frac{1}{2}} \ln(1/\epsilon)^{-1} B^{+},\\
&C_m^{\dagger} = \epsilon^{\frac{1}{2}} C_m^{+}, && C^{\diamond} = \ln(1/\epsilon) C^{+}, && F^{\diamond} = \ln(1/\epsilon)^{2} F^{+}.
\end{aligned} \tag{3.133}$$

In relation to the wild-type asymptotic analysis, this timescale transpires between timescale 8 and timescale 9 (Sections 3.6.8-3.6.9) . The system of equations rescaled for the ninth timescale is

$$\begin{aligned}
\epsilon^{\frac{1}{2}} \frac{dR_m^{\dagger}}{dT^{+}} &= 1 - R_m^{\dagger}, & \epsilon^{\frac{3}{2}} \frac{d\hat{R}}{dT^{+}} &= 0,\\
\epsilon^{\frac{1}{2}} \frac{dA_m^{\diamond}}{dT^{+}} &= \frac{\epsilon^{-\frac{1}{2}} A^{+}}{(\epsilon^{-\frac{1}{2}} A^{+} + 1)(\epsilon \hat{R} + 1)} + \epsilon\alpha - A_m^{\diamond}, & \frac{dA^{+}}{dT^{+}} &= \theta\, A_m^{\diamond} - \upsilon\, A^{+} - \epsilon^{\frac{1}{2}} \Delta A^{+},\\
\epsilon \frac{dC_m^{+}}{dT^{+}} &= \frac{\lambda}{\epsilon^{-\frac{1}{2}} A^{+} + \lambda} - \epsilon^{\frac{1}{2}} C_m^{+}, & \phi^{-3} \frac{dC^{+}}{dT^{+}} &= \gamma\, C_m^{+} - \epsilon^{\frac{1}{2}} \phi^{-3} \Delta C^{+},\\
\epsilon^{\frac{1}{2}} \phi^{2} \frac{dB_m^{+}}{dT^{+}} &= \frac{\epsilon^{-\frac{1}{2}} A^{+} + \phi^{-2} S^{+}}{(1 + \phi^{-2} S^{+} + \epsilon^{-\frac{1}{2}} A^{+})(1 + \phi^{-2} E^{+} + \phi^{-3} C^{+})} - \phi^{2} B_m^{+}, & \frac{dB^{+}}{dT^{+}} &= \phi\beta\, B_m^{+} - \epsilon^{\frac{1}{2}} \Delta\, B^{+},\\
\epsilon^{\frac{1}{2}} \frac{dS_m^{\dagger}}{dT^{+}} &= 1 - S_m^{\dagger}, & & \\
\epsilon^{\frac{1}{2}} \frac{dE_m^{\dagger}}{dT^{+}} &= 1 - E_m^{\dagger}, & \phi^{-2} \frac{dS^{+}}{dT^{+}} &= \sigma\, S_m^{\dagger} - \epsilon^{\frac{1}{2}} phi^{-2} \Delta\, S^{+},\\
\epsilon^{\frac{1}{2}} \frac{dF_m^{\dagger}}{dT^{+}} &= \frac{\eta}{\eta + \phi^{-2} E^{+}} - F_m^{\dagger}, & \phi^{-2} \frac{dE^{+}}{dT^{+}} &= \xi\, E_m^{\dagger} - \epsilon^{\frac{1}{2}} \phi^{-2} \Delta\, E^{+},\\
& & \phi^{-4} \frac{dF^{+}}{dT^{+}} &= \frac{F_m^{\dagger}}{\phi\omega B^{+} + \epsilon^{\frac{1}{2}}} - \epsilon^{\frac{1}{2}} \phi^{-4} \Delta F^{+}.
\end{aligned} \tag{3.134}$$

At leading order, we have the following system of equations

$$\begin{aligned}
R_m^{\dagger} &= 1, & \frac{d\hat{R}}{dT^{+}} &= 0,\\
A_m^{\diamond} &= 1, & \frac{dA^{+}}{dT^{+}} &= \theta A_m^{\diamond} - \upsilon A^{+},
\end{aligned}$$

$$
\begin{aligned}
C_m^+ &= \frac{\lambda}{A^+}, \\
B_m^+ &= \phi^{-2}\frac{1}{(1+\phi^{-2}E^+ + \phi^{-3}C^+)}, \\
S_m^\dagger &= 1, \\
E_m^\dagger &= 1, \\
F_m^\dagger &= \frac{\eta}{\eta + \phi^{-2}E^+},
\end{aligned}
\qquad\qquad
\begin{aligned}
\frac{dC^+}{dT^+} &= \phi^3\gamma\, C_m^+, \\
\frac{dB^+}{dT^+} &= \phi\beta B_m^+, \\
\frac{dS^+}{dT^+} &= \phi^2\sigma S_m^\dagger, \\
\frac{dE^+}{dT^+} &= \phi^2\xi E_m^\dagger, \\
\frac{dF^+}{dT^+} &= \phi^3\frac{F_m^\dagger}{\omega B^+}.
\end{aligned}
\tag{3.136}
$$

Solving and matching to the long term dominant behaviour on the previous timescale gives the following asymptotic approximations

$$
\begin{aligned}
A^\diamond &= \frac{\theta}{\upsilon}(1-e^{-\upsilon T^+}), & A_m^\diamond &= 1, & R_m^\dagger &= 1, & \hat{R} &= R_0, \\
C_m^+ &= \frac{\lambda\upsilon}{\theta(1-e^{-\upsilon T^+})}, & C^+ &= \frac{\phi^3\gamma\lambda\upsilon}{\theta}T^+, & S_m^\dagger &= 1, & S^+ &= \phi^2\sigma T^+, \\
B_m^+ &= \frac{1}{\phi^2(1+\xi T^+ + \frac{\gamma\lambda\upsilon}{\theta}T^+)}, & E_m^\dagger &= 1, & E^+ &= \phi^2\xi T^+, & F_m^\dagger &= \frac{\eta}{\eta+\xi T^+}, \\
B^+ &= \frac{\beta\,\phi^2\theta\,\ln\left((\phi^3\gamma\,\lambda\,\upsilon + \phi^3\theta\,\xi)\,T^+ + \phi^3\theta\right)}{\phi^3\gamma\,\lambda\,\upsilon + \phi^3\theta\,\xi}, & & & F^+ &= \frac{\phi^4\eta(\gamma\lambda\upsilon+\theta\xi)}{\omega\xi\beta\theta}\ln(\phi^3\ln(T^+ + 1)).
\end{aligned}
\tag{3.137}
$$

We plot asymptotic approximations of those variables that evolve on this timescale against the numerical solutions in Figure 3.20. In this timescale we have RamA protein reaching steady state from degradation via Lon Protease. With this, we have *acrR* mRNA also reaching steady state. With less RamA protein due to degradation, the repressors dominate expression of *acrAB*, causing its inhibition. We also have EnvR protein causing inhibition of *acrEF* mRNA. This inhibition of mRNAs causes logarithmic behaviour for both AcrAB and AcrEF. Comparatively to the wild-type analysis, for both strains we see the emergence of repressor proteins on the latter timescales. Interestingly though however is the repression of *acrR* mRNA transcription by RamA, which is not present in the wild-type analysis.

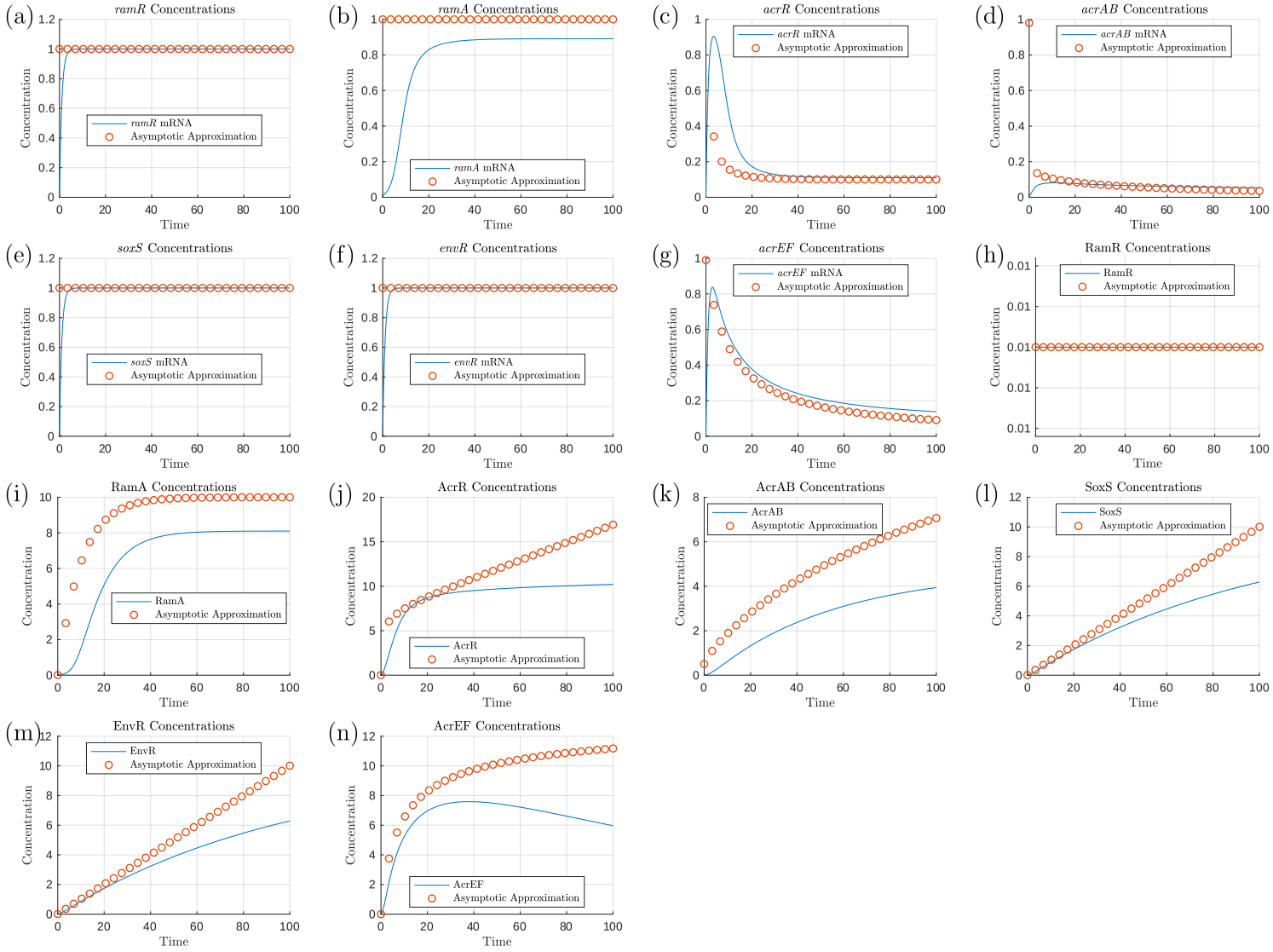

Figure 3.20: Figures showing asymptotic approximations using timescale 9 to the full solutions for $\epsilon = 0.01$. Here the time scaling is $O(\epsilon^{-\frac{1}{2}}(1+\frac{1}{\kappa}\phi^{-1}))$, so we expect the asymptotics to be accurate around $T = \epsilon^{-\frac{1}{2}}(1+\frac{1}{\kappa}\phi^{-1}) \approx 84.5132$. For reference, the previous and subsequent timescales have time at $O(1+\frac{1}{\kappa}\phi^{-1})$ and $O(\epsilon^{-1}(1+\frac{1}{\kappa}\phi^{-1})$ respectively.

3.7.10 Timescale 10: full protein degradation, with all proteins reaching steady state

For this timescale, we use $\delta = \ln(\ln(1/\epsilon))^{-1}$, emerging from the logarithmic behaviour on the previous timescale. On this timescale protein degradation emerges for the rest of our proteins. We take the following variable scalings:

$$\begin{aligned} T^+ &= \epsilon^{-\frac{1}{2}}\breve{T}, & C^+ &= \epsilon^{-\frac{1}{2}}\breve{C}, & S^+ &= \epsilon^{-\frac{1}{2}}\breve{S}, \\ E^+ &= \epsilon^{-\frac{1}{2}}\breve{E}, & B_m^+ &= \epsilon^{\frac{1}{2}}\breve{B}_m, & F_m^\dagger &= \epsilon^{\frac{1}{2}}\breve{F}_m, \\ B^+ &= \ln(1/\epsilon)\breve{B}, & F^+ &= \ln(\ln(1/\epsilon))\breve{F}. \end{aligned} \tag{3.138}$$

Comparatively, this timescale takes place after timescale 9 (Section 3.6.9) of the wild-type asymptotic analysis. The system of equations rescaled for the tenth timescale is

$$\begin{aligned} \epsilon\frac{dR_m^\dagger}{d\breve{T}} &= 1 - R_m^\dagger, & \epsilon^2\frac{d\hat{R}}{d\breve{T}} &= 0, \\ \epsilon\frac{dA_m^\diamond}{d\breve{T}} &= \frac{\epsilon^{-\frac{1}{2}}A^+}{(\epsilon^{-\frac{1}{2}}A^+ + 1)(\epsilon\hat{R} + 1)} + \epsilon\alpha - A_m^\diamond, & \epsilon^{\frac{1}{2}}\frac{dA^+}{d\breve{T}} &= \theta\, A_m^\diamond - \upsilon\, A^+ - \epsilon^{\frac{1}{2}}\Delta A^+, \\ \epsilon^{\frac{3}{2}}\frac{dC_m^+}{d\breve{T}} &= \frac{\lambda}{\epsilon^{-\frac{1}{2}}A^+ + \lambda} - \epsilon^{\frac{1}{2}}C_m^+, & \phi^{-3}\frac{d\breve{C}}{d\breve{T}} &= \gamma\, C_m^+ - \phi^{-3}\Delta\breve{C}, \\ & & \frac{d\breve{B}}{d\breve{T}} &= \phi^2\beta\,\breve{B}_m - \Delta\,\breve{B}, \\ \epsilon^{\frac{3}{2}}\phi^2\frac{d\breve{B}_m}{d\breve{T}} &= \frac{\epsilon^{-\frac{1}{2}}A^+ + \epsilon^{-\frac{1}{2}}\phi^{-2}\breve{S}}{(1 + \epsilon^{-\frac{1}{2}}\phi^{-2}\breve{S} + \epsilon^{-\frac{1}{2}}A^+)(1 + \epsilon^{-\frac{1}{2}}\phi^{-2}\breve{E} + \epsilon^{-\frac{1}{2}}\phi^{-3}\breve{C})} - \epsilon^{\frac{1}{2}}\phi^2\breve{B}_m, & & \\ \epsilon\frac{dS_m^\dagger}{d\breve{T}} &= 1 - S_m^\dagger, & \phi^{-2}\frac{d\breve{S}}{d\breve{T}} &= \sigma\, S_m^\dagger - \phi^{-2}\Delta\,\breve{S}, \\ \epsilon\frac{dE_m^\dagger}{d\breve{T}} &= 1 - E_m^\dagger, & \phi^{-2}\frac{d\breve{E}}{d\breve{T}} &= \xi\, E_m^\dagger - \phi^{-2}\Delta\,\breve{E}, \\ \epsilon^{\frac{3}{2}}\frac{d\breve{F}_m}{d\breve{T}} &= \frac{\eta}{\eta + \epsilon^{-\frac{1}{2}}\phi^{-2}\breve{E}} - \epsilon^{\frac{1}{2}}\breve{F}_m, & \phi^{-4}\delta^{-1}\frac{d\breve{F}}{d\breve{T}} &= \frac{\breve{F}_m}{\phi\omega\breve{B} + \epsilon^{\frac{1}{2}}} - \phi^{-4}\delta^{-1}\Delta\breve{F}. \end{aligned} \tag{3.139}$$

At leading order, we have the following system of equations

$$R_m^\dagger = 1, \qquad \frac{d\hat{R}}{d\breve{T}} = 0,$$

$$
\begin{aligned}
A_m^{\diamond} &= 1, & A^{+} &= \frac{\theta}{\upsilon} A_m^{\diamond},\\
C_m^{+} &= \frac{\lambda}{A^{+}}, & \frac{d\breve{C}}{d\breve{T}} &= \phi^3 \gamma\, C_m^{+} - \Delta \breve{C},\\
\breve{B}_m &= \phi^{-2} \frac{1}{(\phi^{-2}\breve{E} + \phi^{-3}\breve{C})}, & \frac{d\breve{B}}{d\breve{T}} &= \phi^2 \beta \breve{B}_m - \Delta \breve{B},\\
S_m^{\dagger} &= 1, & \frac{d\breve{S}}{d\breve{T}} &= \phi^2 \sigma S_m^{\dagger} - \Delta \breve{S},\\
E_m^{\dagger} &= 1, & \frac{d\breve{E}}{d\breve{T}} &= \phi^2 \xi E_m^{\dagger} - \Delta \breve{E},\\
\breve{F}_m &= \frac{\eta}{\phi^{-2}\breve{E}}, & \frac{d\breve{F}}{d\breve{T}} &= \phi^4 \delta \frac{\breve{F}_m}{\omega \breve{B}} - \Delta \breve{F}.
\end{aligned} \tag{3.140}
$$

This system of ODEs can be solved, matching to the long term dominant behaviour on the previous timescale gives the following asymptotic approximations.

$$
\begin{aligned}
R_m^{\dagger} &= 1, & \hat{R} &= R_0, & A_m^{+} &= 1,\\
A^{+} &= \frac{\theta}{\upsilon}, & \breve{C} &= \phi^3 \frac{\gamma\lambda\upsilon}{\Delta\theta}(1 - e^{-\Delta\breve{T}}), & C_m^{+} &= \frac{\lambda\upsilon}{\theta},\\
\breve{B}_m &= \frac{1}{\phi^2(\frac{\xi}{\Delta} + \frac{\gamma\lambda\upsilon}{\Delta\theta})(1 - e^{-\Delta\breve{T}})}, & \breve{B} &= \frac{\beta\theta}{\gamma\lambda\upsilon + \theta\xi}(1 - e^{-\Delta\breve{T}}), & S_m^{\dagger} &= 1,\\
\breve{S} &= \phi^2 \frac{\sigma}{\Delta}(1 - e^{-\Delta\breve{T}}), & \breve{E} &= \phi^2 \frac{\xi}{\Delta}(1 - e^{-\Delta\breve{T}}), & E_m^{\dagger} &= 1,
\end{aligned}
$$

$$
\breve{F}_m = \frac{\eta}{\frac{\xi}{\Delta}(1 - e^{-\Delta\breve{T}})}, \qquad \breve{F} = \frac{\phi^4 \delta\eta\,(\gamma\,\lambda\,\upsilon + \theta\xi)}{\xi\omega\beta\theta}(1 - e^{-\Delta\breve{T}}). \tag{3.141}
$$

We plot asymptotic approximations of those variables that evolve on this timescale against the numerical solutions in Figure 3.21. In this timescale we have all variables reaching steady state. We note that compared to the wild-type analysis, the steady state values for RamA and AcrAB are much larger in the mutant strain. The disparity in the asymptotic approximations of some variables could be reduced using a smaller value for ϵ. However, we have instead opted to include the second order asymptotic approximation steady state values. This achieves an accurate approximation to the steady state whilst not having to alter the value of ϵ. Alternatively, we could solve for the full solutions of the second

order correction terms, however, this is the final timescale where the only evolution of behaviour is the variables approaching steady state. Thus, the main importance on this timescale is in the accuracy of the approximations to the steady state of the system. To obtain these values, we have taken the following asymptotic expansions

$$\begin{aligned}
A_m^{\dagger} &= a_{m0} + \epsilon^{\frac{1}{2}} a_{m1} + \epsilon a_{m2} + ..., & A^{+} &= a_0 + \epsilon^{\frac{1}{2}} a_1 + \epsilon a_2 + \dots, \\
C_m^{+} &= c_{m0} + \epsilon^{\frac{1}{2}} c_{m1} + \epsilon c_{m2} + ..., & \breve{C} &= c_0 + \epsilon^{\frac{1}{2}} c_1 + \epsilon c_2 + \dots, \\
\breve{B}_m &= b_{m0} + \epsilon^{\frac{1}{2}} b_{m1} + \epsilon b_{m2} + ..., & \breve{B} &= b_0 + \epsilon^{\frac{1}{2}} b_1 + \epsilon b_2 + \dots, \\
\breve{F}_m &= f_{m0} + \epsilon^{\frac{1}{2}} f_{m1} + \epsilon f_{m2} + ..., & \breve{F} &= f_0 + \epsilon^{\frac{1}{2}} f_1 + \epsilon f_2 + \dots .
\end{aligned} \tag{3.142}$$

Substituting into the equations (3.139) we achieve the leading order system of equations (3.140) and the following system for the second order correction terms

$$\begin{aligned}
a_{m1} &= -\frac{1}{a_0}, & a_1 &= \frac{1}{\upsilon}\left(\theta a_{m1} - \Delta a_0 - \frac{da_0}{d\breve{T}}\right), \\
c_{m1} &= -\frac{\lambda(\lambda + a_1)}{a_0^2}, & \frac{dc_1}{d\breve{T}} &= \phi^3 \gamma\, c_{m1} - \Delta c_1, \\
b_{m1} &= -\phi^{-2}\frac{\phi\breve{E} + c_0 + (\phi^3 + c_1)(a_0 + \phi^{-2}\breve{S})}{(\phi\breve{E} + c_0)(a_0 + \phi^{-2}\breve{S})(\phi^{-2}\breve{E} + \phi^{-3}c_0)}, & \frac{db_1}{d\breve{T}} &= \phi^2 \beta\, b_{m1} - \Delta b_1, \\
f_{m1} &= -\frac{\eta^2}{\phi^{-4}\breve{E}^2}, & \frac{df_1}{d\breve{T}} &= \phi^4 \delta\left(\frac{f_{m1}}{\omega b_0} - \frac{f_{m0}(\omega b_1 + 1)}{\omega^2 b_0^2}\right) - \Delta f_1.
\end{aligned} \tag{3.143}$$

By assuming that $\breve{T} \to \infty$ such that $\dfrac{d}{d\breve{T}} \approx 0$, we are left with a system of equations that can be solved trivially to obtain the steady states for the correction terms (ommited here for brevity). By summing with the limit of the leading order solutions as $\breve{T} \to \infty$ in (3.141), we then achieve the steady state values for the expanded variables.

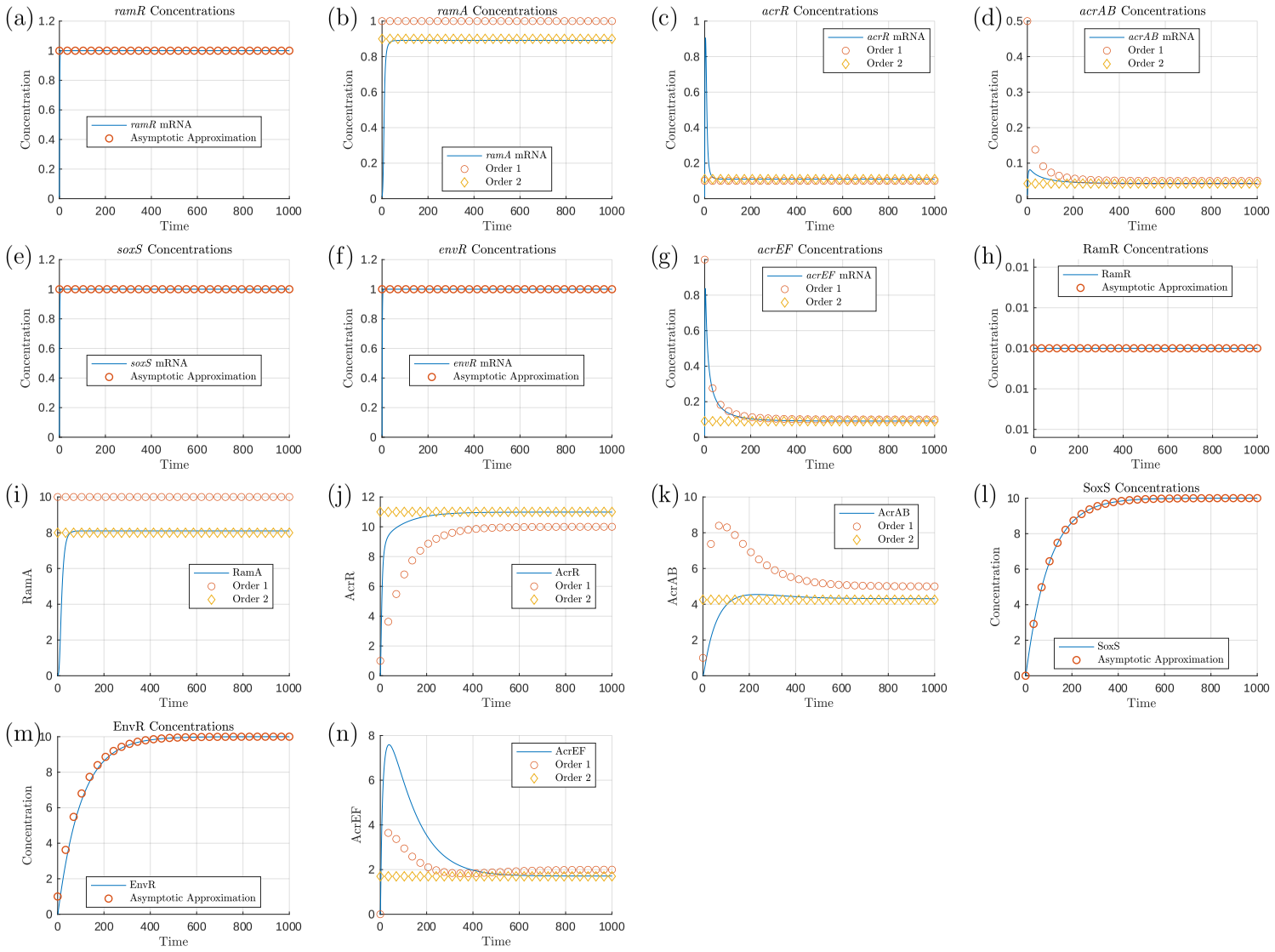

Figure 3.21: Asymptotic approximations on timescale 10 ($\epsilon = 0.01$). The order 2 approximations display the steady state value for all time. On this timescale, time is $O(\epsilon^{-1}(1+\frac{1}{\kappa}\phi^{-1}))$, so we expect the asymptotics to be accurate around $T = \epsilon^{-1}(1+\frac{1}{\kappa}\phi^{-1})) \approx 845.1322$. For reference, the previous timescale has time at $O(\epsilon^{-\frac{1}{2}}(1+\frac{1}{\kappa}\phi^{-1})$ respectively.

3.7.11 Summary

In Figure 3.22 we exhibit the leading order processes in timescale order from our asymptotic analysis for the mutant case. We note that the schematics are not on identical timescales to the wild-type case as the scalings to reach each of the timescales are different. Here we detail the differences in the order of dominant processes shown in the schematics compared to the wild-type case. As predicted by the analysis:

- In this case, functional RamR is not produced. This allows the positive feedback loop on *ramA* expression to dominate at leading order, resulting in high production of RamA and activation of *acrAB* expression.
- Any activation by secondary TAs (that may occur under the appropriate stress) is overshadowed by RamA and relegated to lower order behaviour. RamA also lowers AcrR levels, yielding higher expression of *acrAB* in the analysis.
- RamA is regulated by degradation through the Lon protease, allowing AcrR and EnvR to dominate acrAB expression.
- Degradation of all proteins brings the system to a steady state.

At steady state, as expected this mutant strain also has RamA dominating the behaviour (in addition to those considered in the wild type strain). The analysis therefore identifies *ramA*, *acrR*, *envR*, *acrAB* and *acrEF* as the most likely potential targets for efflux pump inhibition. In regards to the other timescales, this breakdown highlights the importance of the positive feedback loop of *ramA*. With the release of *ramA* expression in this mutant case, various different interactions between genes and proteins become dominant. In particular, we see direct and indirect activation of *acrAB*, with the latter as a result of its local repressor, *acrR*, itself being inhibited (by RamA). It is interesting to note that the direct activation from RamA only dominates at leading order prior to steady state and without undergoing our time-dependent analysis we may have not identified this key mechanism in the activation of the efflux pump genes under this parameter

set. Reducing the activation from RamA may be enough to minimise early expression of *acrAB*, enabling the antibiotic to kill bacteria before its efflux pumps are overexpressed. For example, an efflux inhibiting adjuvant targeting RamA may be more successful if administered with or before antibiotic. It is also important to note that in the wild-type case we see no leading order activation processes caused by RamA (though this will be present at lower orders). Thus whilst choosing *ramA* as an inhibition target seems plausible, this may only revert the GRN to the wild-type case rather than knocking out efflux expression entirely. This concludes the mutant asymptotic analysis. We have broken down the system into ten timescales. For each of these timescales we have obtained full analytical solutions.

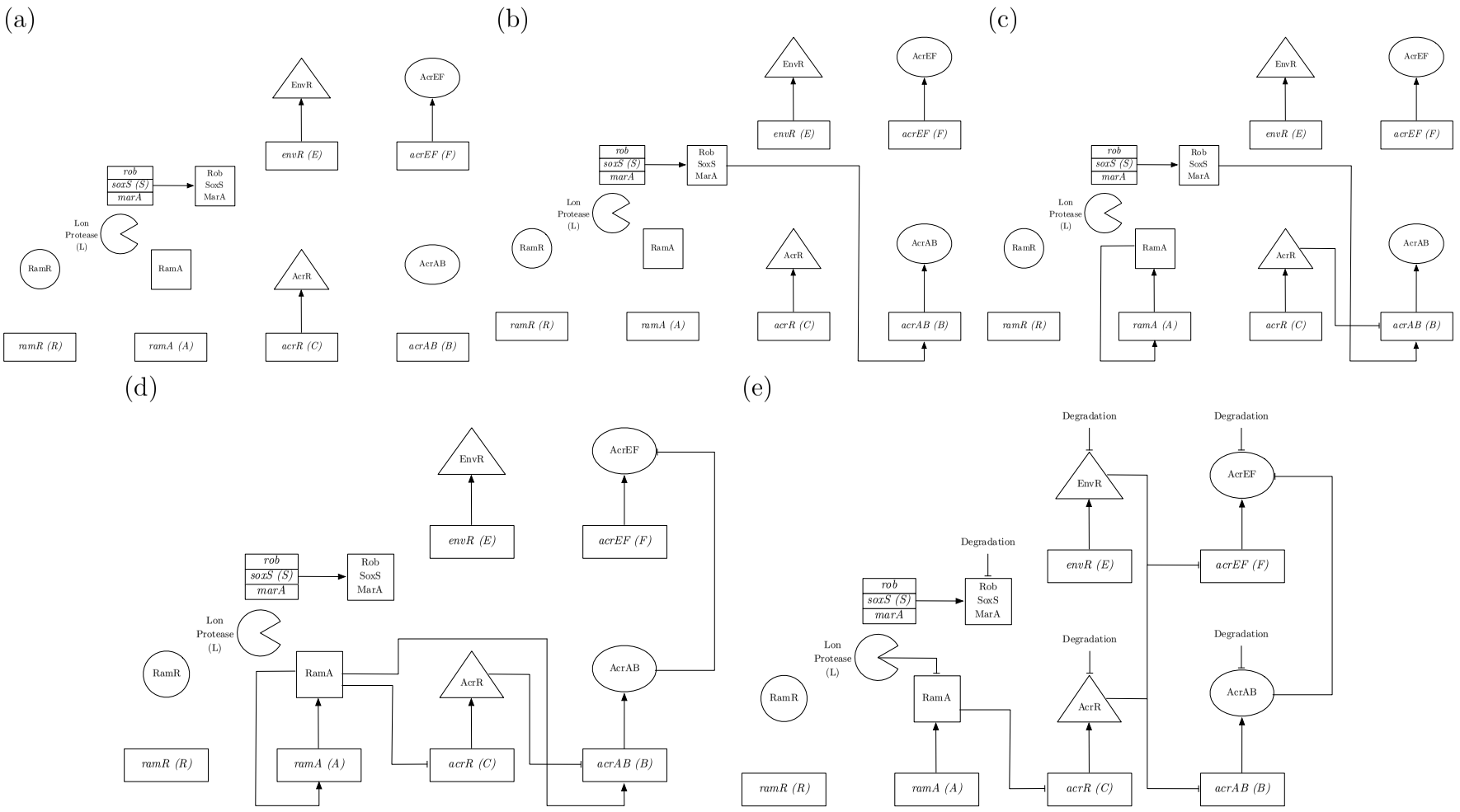

Figure 3.22: Schematic diagrams showing the order in which processes appear at leading order in the asymptotic analysis for the mutant case. We show these processes in timescale order, starting from initial processes and finishing at steady state in (e). As we evolve the schematic, we insert and remove arrows or lines depending on which terms enter or leave the leading order balance.

3.8 Steady State Analysis

Upon reaching the final timescale, all of our variables attain a steady state. For the full nondimensionalised model it is not possible to derive a set of analytically solvable steady states. However, in both wild-type and mutant cases we can achieve analytical expressions for the asymptotic approximation of the steady states. We know from our GRN that reducing the concentration of the main efflux pump protein AcrAB results in increased concentration of the homologue efflux pump protein AcrEF. Thus we must consider both efflux pump protein concentrations simultaneously. We perform a sensitivity analysis of the sum of the asymptotic approximations of the steady states of AcrAB (including second order terms) and AcrEF, the proteins that form the efflux pump complexes (i.e. this reflects the total efflux "power" of the bacteria). By conducting this analysis we hope to identify potential targets for efflux inhibition. Here, we use relative sensitivity in order to draw comparisons on how much individually changing a parameter affects the overall efflux. We define our equation for the relative sensitivity as

$$\varsigma = \frac{d(\bar{B} + \bar{F})}{dP}, \tag{3.144}$$

where $d(\bar{B} + \bar{F})$ represents the change of the efflux pump genes steady state and dP represents the change of the nondimensional parameter being varied.

To conduct our sensitivity analysis, we vary all our nondimensional parameters in a bounded parameter space. For both wild-type and mutant strains, the space is bounded to the range of $\epsilon^{\frac{1}{5}}$ to $\epsilon^{-\frac{1}{5}}$ to maintain consistency with the parameter sizes used in the asymptotic analysis. By using a Latin hypercube method of sampling, we choose 10000 points in the parameter space for each parameter and find the relative sensitivity for each point. The resulting relative sensitivities are then plotted on box plots in order for us to view the distribution of sensitivity. We exhibit the results of the sensitivity analysis in Figure 3.23.

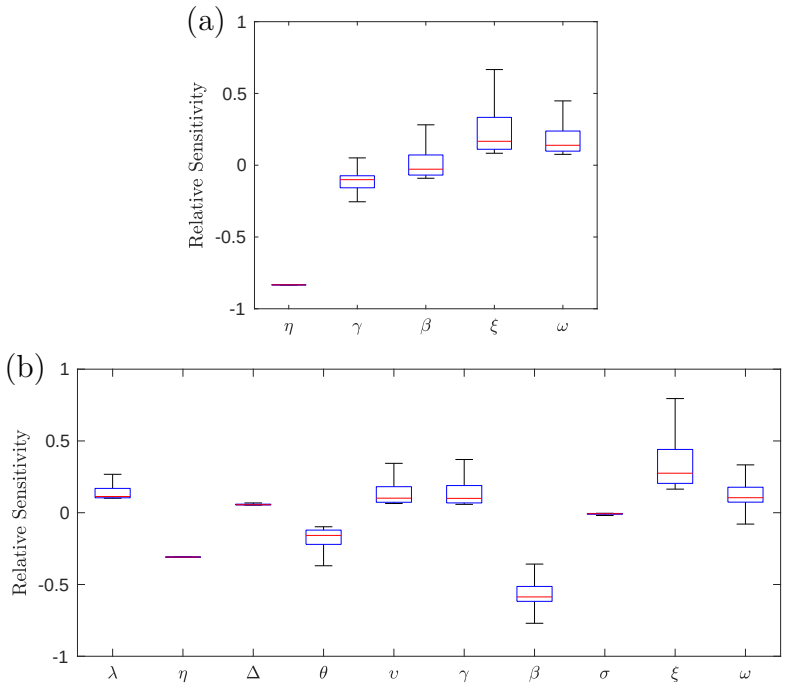

Figure 3.23: Box plots showing the relative sensitivity of nondimensional parameters on the combined asymptotic approximated steady states of AcrAB and AcrEF. In (a) we denote the sensitivity in the wild-type case whereas in (b) we denote the mutant case. For (b), mutations to RamR protein results in more parameters involved in our steady state approximation.

We can see from the wild-type case (a), that the parameter to which efflux is most sensitive is η, here all points correspond to the same value as this grouping only affects AcrEF and does so linearly. Our next most sensitive parameter is ξ, which also has the largest spread of sensitivity of all parameters in this case. We note that our most sensitive parameter groupings η and ξ relate to the binding coefficients of EnvR to the two efflux pump genes, and the expression of *envR* respectively. Since both of these parameters involve *envR* mRNA or protein, the analysis suggests that this gene could be a possible target for inhibition of efflux in this case. Our next most sensitive parameter is ω relating to the link between the concentration of AcrAB and activation/repression of *acrEF* the homologue efflux pump gene. Unfortunately as we do not know the full mechanisms involved causing this link, this does not provide a realistic target for inhibition. However, this does lead us to believe that with more biological knowledge of this link there could be a potential inhibition target worth pursuing. Finally with similar sensitivities are

γ (*acrR* expression) and β (*acrAB* expression). Since the former of these parameters has a relatively low sensitivity compared to other parameters, the analysis predicts that this may not be a target worth pursuing. The latter is an expected target, relating to direct expression of one of the efflux pump genes. It is interesting to note that some parameters in the system (that do not affect the efflux pump genes directly) provide a greater sensitivity than β, that is directly related to AcrAB concentration.

In the mutant case (b), it comes to note that we have double the amount of parameters that affect the efflux pump steady states compared to the wild-type case. This is partially due to including second order terms, however it is only the parameters Δ and σ that do not appear at leading order. With only one change in the GRN (to RamR protein), the change in the amount of parameters demonstrates the unpredictability and sensitive nature of this network. We note that here, the parameter to which the steady state of efflux proteins is most sensitive is ξ (*envR* expression). Additionally we also see high sensitivity to the parameter η (EnvR binding affinity). This similarity with the wild-type system further highlights the case for targeting the gene *envR* for inhibiting efflux. Our next most sensitive parameter is β (*acrAB* expression) which differs from the wild-type case where it was one of the least sensitive parameters. This could be due to the overexpression of *acrAB* in this mutant case. The parameters λ (RamA binding affinity), θ (*ramA* expression), υ (RamA degradation from Lon Protease), γ (*acrR* expression) and ω (AcrAB and *acrEF* link) all show a degree of sensitivity, meaning that any of these parameters could prove to be a realistic target to inhibit efflux. However it is interesting to note that parameters associated with *ramA*, which is over expressed in this mutant case, is not the most sensitive target for inhibiting efflux. The rest of the parameters Δ (degradation of mRNA and proteins) and σ (*soxS* mRNA expression) have a low sensitivity in this case, which we should expect as these parameters are only prevalent in the second order terms. Thus the analysis suggests that these parameters may not be realistic targets for inhibiting efflux.

3.9 Discussion

Antimicrobial resistance is a topic with ever increasing importance. With the threat to human health worsening as more bacteria evolve resistance to antibiotics, it is clear we must urgently seek novel treatment methods in order to combat antibiotic resistance. By delving into GRNs governing resistance mechanisms, it is possible to identify certain targets to potentially prevent resistance in bacteria. We believe that our asymptotic analysis has given us useful insights into the network governing efflux pump expression.

We first nondimensionalised our model, resulting in nondimensional parameter groupings. By using information from the biology of the network and consultations with the Piddock Laboratory (University Of Birmingham), we were able to estimate sizes for these parameter groupings and focus on relative parameter sizes rather than absolute parameter values. We performed two independent series of time dependent asymptotic analyses, modelling the dynamics of the wild-type and mutant strains. This enabled us to break down our nondimensional model (which does not have a full set of analytical solutions) onto various timescales, exhibiting the order of dominant processes within the network. In both cases on the early timescales, genes that are not highly regulated are transcribed and quickly translated. On the middle timescales we see translated proteins inhibiting and activating expression of other genes within the network. Finally on the later timescales we have degradation of proteins bringing the system to a steady state. We noted that for the mutant strain, as non-functional RamR is produced, the expression of *ramA* and resulting reactions feature heavily in the dominant processes within the network. This ultimately results in a steady state where more genes are active at leading order than the wild-type case. Notably RamA only directly affected *acrAB* expression on the middle timescales, whereas on the later timescales *acrAB* expression was affected indirectly. This leads us to believe that if we were to choose *ramA* as an inhibition target, the timing of an adjuvant in relation to antibiotic administration could be crucial.

After achieving asymptotically approximated steady states for the system in both strains. We have performed parameter sensitivity analysis upon the steady state values.

This enabled us to determine which parameter groupings the strains are most sensitive to for inhibiting efflux. We saw that amongst both strains, the most sensitive parameters were linked to the gene *envR*. This closely aligned with the biology of the network as the gene's protein is capable of directly inhibiting both *acrAB* and *acrEF* expression. Many other parameter groupings displayed reasonable sensitivity and hence showed us multiple inhibitory targets. It was interesting to note the sensitivity of the link between the concentration of AcrAB and the activation / repression of *acrEF*. Although we do not know the full biology behind this mechanism, this sensitivity gives us strong reason to further delve into the processes causing this link.

CHAPTER 4

A SPATIAL MODEL OF SUBSTRATE EFFLUX

4.1 Motivation

The Resistance-Nodulation-Division (RND) family of transporters are common to extrude a range of antibiotics and can account for multi drug resistance (MDR) [69]. From genomic analysis, it has been shown that *Salmonella* strains contain five RND efflux pump systems. Various antibiotics have been shown to be substrates of multiple of these efflux pump systems [61]. Thus inhibition of one of the efflux pump systems could mean that substrate extrusion will be picked up by another efflux pump system.

In the previous chapters we have modelled and analysed the GRN governing expression of two members of the RND family of transporters. This model has given us useful insights into potential inhibitory targets for the aforementioned efflux pumps. However, our model does not consider the link between efflux pump gene expression and the resulting effects on substrate concentration. In this chapter we will consider a cellular model of substrate efflux governed by multiple members of the RND family, with the aim of linking this model to our gene regulatory model in further chapters. We will attempt to parametrise this model in order for us to replicate the experimental data. By successfully parametrising our model, we will then be able to conduct analysis into the role of efflux upon the bacterial cell and its environment.

4.2 Experimental Protocol

We base our mathematical model upon experiments completed by the Blair laboratory, based at the University of Birmingham [56]. Cultures of *Salmonella* are adjusted to an optical density (measured at a wavelength of $600nm$, OD600) of the value 0.2 and are placed into standard 96 well plates. *Salmonella* are rod shaped bacteria and generally range between 2-5μm long and 0.5-1.5μm wide [4]. Individual cultures are loaded with high concentrations of ethidium bromide (a substrate of multiple RND efflux pumps). At this stage, an efflux inhibitor is present which prevents proton motive force of the RND efflux pumps, resulting in substrate accumulation. Ethidium bromide is a DNA-intercalating agent that fluoresces when it is bound to DNA [28]. Due to this fluorescing, the concentration of ethidium bromide within a culture can be approximated. Once the cells are washed to remove extracellular substrate the fluorescence is measured. The cells are then re energized so that the efflux pumps begin to extrude the substrate. The fluorescence is then monitored and measured over various time points [11]. Experiments have taken place on various different cultures of *Salmonella*, including a wild-type case and various cases with efflux gene knock outs. By comparing multiple experiments, we are able to see the effects of the efflux pump systems. For these experiments four RND efflux pumps have been considered: AcrAB, AcrEF, MdsAB and MdtAB. All of these efflux pump proteins share the same outer membrane protein TolC, with MdtAB having the ability to also form a system with the outer membrane protein MdtC [61].

4.3 Cell model formulation

We choose to model these experiments using partial differential equations (PDEs). Whilst currently the spatial effects may not have a huge bearing on the results, by choosing PDEs it gives us the potential to apply the model to situations where spatial effects could be more important, such as *in vivo* experiments. To formulate our model, we assume that each cell in a population acts identically. We also assume that the concentration of ethidium

bromide is evenly distributed in the population such that every cell has an identical initial concentration of ethidium bromide. We assume this distributed concentration of ethidium bromide is independent to each cell, meaning that if the substrate has been expelled into the extracellular space, it can only diffuse back into the original cell. Since we do not know the correlation between fluorescence of ethidium bromide and the concentration of ethidium bromide within the culture, we assume a directly proportional relation between the two. By making these assumptions, we are able to model the full culture population via a single cell model where that cell displays the typical behaviour of all cells in the population. We exhibit a schematic of our single cell model in Figure 4.1. To model the cell, we follow a similar method to Carr and Pontrelli [15]. We use spherical coordinates to model an axisymmetric spherical cell with radius R_M surrounded by extracellular (outside of a cell) space with an outer boundary of radius R_B. At the cell radius (R_M), we have a thin permeable membrane which contains all of the efflux pump systems that expel substrate from the intracellular (inside of a cell) space to the extracellular space. This limit to the amount of extracellular space is represented by the outer boundary radius (R_B). The equations for this model are as follows

$$\begin{aligned} \frac{\partial c_I}{\partial t} &= D_I \left(\frac{\partial^2 c_I}{\partial r^2} + \frac{2}{r} \frac{\partial c_I}{\partial r} \right), \\ \frac{\partial c_E}{\partial t} &= D_E \left(\frac{\partial^2 c_E}{\partial r^2} + \frac{2}{r} \frac{\partial c_E}{\partial r} \right). \end{aligned} \tag{4.1}$$

Here we have split the ethidium bromide into two concentrations for intracellular (c_I) and extracellular (c_E) concentration under the assumption that the ethidium bromide diffuses at a different rate within the intracellular space (with coefficient D_I) to the extracellular space (with coefficient D_E) [20].

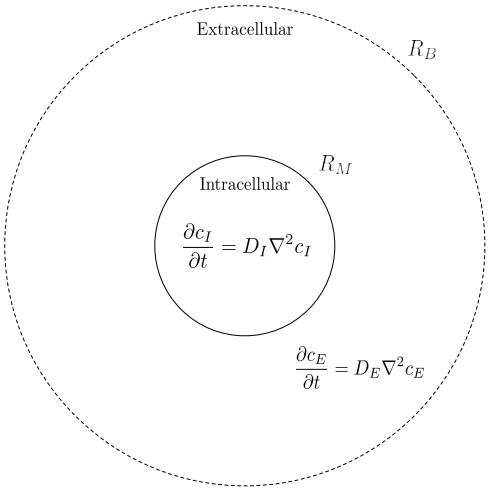

Figure 4.1: A schematic of the single cell efflux model. The solid circle denotes our membrane boundary at the distance from the centre R_M, whilst the dotted line denotes our outer boundary at distance R_B. We place our model equations in the intracellular and extracellular regions where they apply.

4.3.1 Boundary Conditions

The first boundary conditions for our system is

$$D_I \frac{\partial c_I}{\partial r}\bigg|_{r=0} = 0. \tag{4.2}$$

Here we assume axisymmetric properties of the cell for the intracellular concentration. Our secondary boundary condition is at the membrane R_M, which we demonstrate in Figure 4.2. We choose to model our membrane with small but finite thickness δ, with the fictitious points R_M^- and R_M^+ being the intracellular and extracellular membrane points respectively. We can see that we have both diffusion and efflux through the membrane and thus the total flux through the membrane will be a combination of both diffusive flux and advective flux (via efflux). Via Fick's law [33], we can calculate the diffusive flux

through the membrane via the following approximation (valid for $\delta \ll 1$):

$$\begin{aligned} J_D &= -D_M \nabla c(R_M, T), \\ &= -D_M \frac{c(R_M^+, T) - c(R_M^-, T)}{\delta}, \\ &= -D_M \frac{c_E(R_M, T) - c_I(R_M, T)}{\delta}, \\ &= \frac{D_M}{\delta}(c_I(R_M, T) - c_E(R_M, T)). \end{aligned} \tag{4.3}$$

Here D_M denotes the diffusion coefficient inside the membrane which we assume to be constant throughout. In regards to the advective flux, this is proportional to the concentration times the volume flow from efflux X [46]

$$\begin{aligned} J_A &= X\, c(R_M^-, T), \\ &= X\, c_I(R_M, T). \end{aligned} \tag{4.4}$$

Therefore the total flux through the membrane is

$$\begin{aligned} J &= J_D + J_A, \\ &= P\,(c_I(R_M, T) - c_E(R_M, T)) + X\, c_I(R_M, T). \end{aligned} \tag{4.5}$$

Here $P = \dfrac{D_M}{\delta}$ is a mass transfer coefficient related to the permeability of the membrane. Finally, we require continuity of flux at the membrane and therefore the boundary condition at $R = R_M$ can be written as

$$-\,D_I \frac{\partial c_I}{\partial r}\bigg|_{r=R_M} = -\,D_E \frac{\partial c_E}{\partial r}\bigg|_{r=R_M} = (P + X)\, c_I(R_M, t) - P\, c_E(R_M, t). \tag{4.6}$$

In summation, this condition encompasses flux continuity between the intracellular and extracellular space, with interface conditions that characterise the properties of the membrane which we assume are constant for the full duration of our simulations [21]. If we set $X = 0$ such that there is no efflux, we can see that as $P \to 0$ this condition becomes a no

flux boundary condition (which is expected with no membrane permeability), in contrast as $P \to \infty$ we approach $c_I(R_M, t) = c_E(R_M, t)$ which models the case with no membrane. In addition to the above boundary conditions, we have the outer boundary condition (at $r = R_B$). There are two methods by which we choose to model this:

1. We assume that the culture is surrounded by enough extracellular space that the substrate dissipates. Here we set the outer boundary to be at the far field where the concentration is always zero,

$$c_E(R_B, t) \to 0 \text{ as } R_B \to \infty. \tag{4.7}$$

2. We assume that the extracellular space is limited, such that substrate expelled out of the cell will always be within range to diffuse back in. Here we set the outer boundary to be a closer boundary with no flux,

$$D_E \frac{\partial c_E}{\partial r}\bigg|_{r=R_B} = 0. \tag{4.8}$$

Whilst we expect the extracellular space to be limited meaning our secondary boundary condition would be more relevant to the experiments, we do not know the extent of the extracellular space in comparison to the individual cell and thus our first boundary condition would provide a simpler model for numerical simulations in the case of a large extracellular space [31].

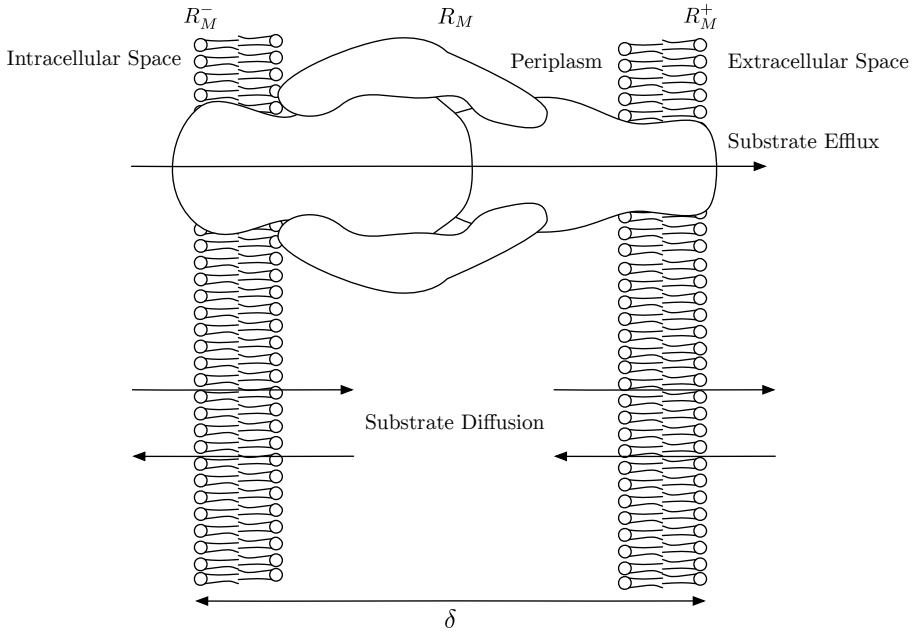

Figure 4.2: A schematic showing the processes involved at the membrane R_M with small finite thickness δ. We show fictitious points R_M^- and R_M^+ that are part of the intracellular and extracellular space respectively. We show the process of efflux of substrate from the intracellular space direct to the extracellular space through the RND efflux pumps. In addition we exhibit diffusion of substrate in both directions through each membrane from the intracellular and extracellular spaces into the periplasm.

4.3.2 Initial Conditions

As the cultures are washed to remove extracellular substrate before the initial fluorescence is measured, we assume that there is no substrate in the extracellular space initially. In regards to the intracellular space, we assume that all substrate fluoresces. The initial conditions for the model are therefore

$$c_I(r,0) = C_0 \qquad\qquad c_E(r,0) = 0, \tag{4.9}$$

where here C_0 denotes a constant for the initial intracellular concentration of substrate.

4.3.3 Model Solution

We adopt the method of separation of variables to obtain a solution to this PDE model, adopting an approach that has been used to solve similar spherical models [43]. By proposing separated solutions $c_i(r,t) = F_i(r)\,G_i(t)$ for $i = I, E$ and substituting into (4.1) we obtain

$$F_i\,G_i' = D_i\left(F_i''\,G_i + \frac{2}{r}F_i' G_i\right), \tag{4.10}$$

which rearranges to

$$\frac{1}{D_i}\frac{G_i'}{G_i} = \frac{F_i''}{F_i} + \frac{2}{r}\frac{F_i'}{F_i}. \tag{4.11}$$

We set both sides equal to a negative constant

$$\frac{1}{D_i}\frac{G_i'}{G_i} = -\lambda_i^2, \qquad\qquad \frac{F_i''}{F_i} + \frac{2}{r}\frac{F_i'}{F_i} = -\lambda_i^2, \tag{4.12}$$

admitting the following general solutions

$$F_I(r) = k_1\frac{\cos(\lambda_I\,r)}{r} + k_2\frac{\sin(\lambda_I\,r)}{r}, \qquad G_I(t) = e^{-D_I\lambda_I^2 t}, \tag{4.13}$$

$$F_E(r) = k_3\frac{\cos(\lambda_E\,r)}{r} + k_4\frac{\sin(\lambda_E\,r)}{r}, \qquad G_E(t) = e^{-D_E\lambda_E^2 t}. \tag{4.14}$$

By setting $G_I(t) = G_E(t)$ such that $\lambda_E = \sqrt{\dfrac{D_E}{D_I}}\lambda_I$, the boundary conditions (4.2)-(4.8) (using the no flux outer boundary condition) become:

$$F_I'(0) = 0, \tag{4.15}$$

$$-D_I F_I'(R_M) = (P+X)\,F_I(R_M) - P\,F_E(R_M), \tag{4.16}$$

$$-D_E F_E'(R_M) = (P+X)\,F_I(R_M) - P\,F_E(R_M), \tag{4.17}$$

$$F_E'(R_B) = 0. \tag{4.18}$$

From the boundary condition (4.15), we get $k_1 = 0$, giving us the updated solution

$$F_I(r) = k_2 \frac{\sin(\lambda_I\, r)}{r}, \tag{4.19}$$

The remaining boundary conditions (4.16)-(4.18) leave us with a system of equations with unknown constants k_2, k_3, k_4. To find a non trivial solution of this system of equations we require the determinant of a coefficient matrix of system to be non zero. We can use this condition to determine an infinite set of eigenvalues $\lambda_{I,n}$ $(n = 1, 2, ...)$ with the following eigenfunctions and time solutions

$$F_{I,n}(r) = k_{2,n} \frac{\sin(\lambda_{I,n}\, r)}{r}, \tag{4.20}$$

$$F_{E,n}(r) = k_{3,n} \frac{\cos(\sqrt{\frac{D_E}{D_I}}\lambda_{I,n}\, r)}{r} + k_{4,n} \frac{\sin(\sqrt{\frac{D_E}{D_I}}\lambda_{I,n}\, r)}{r}, \tag{4.21}$$

$$G_{I,n}(t) = G_{E,n}(t) = e^{-D_I \lambda_{I,n}^2 t}. \tag{4.22}$$

The general solution to (4.1) is therefore

$$c_i(r,t) = \sum_{n=1}^{\infty} a_{i,n} F_{i,n}(r) e^{-D_I (\lambda_{I,n})^2 t}. \tag{4.23}$$

Here $i = I, E$ and the constants $a_{i,n}$ are Fourier coefficients that are determined by the initial conditions (4.9). Notably this solution is only valid if the parameters P and X are constant. In Section 5, we introduce variable efflux X and thus this general solution will not be valid for the models presented in the section. Furthermore, to solve the determinant matrix to find the unknown coefficients and eigenvalues we must employ the use of numerical methods. In this thesis we have instead opted to use finite difference numerical methods to produce numerical simulations of the model, which can be utilised on both models in this section as well as Section 5.

4.4 Numerical Method

In order to produce numerical simulations of the model, we use a combination of finite difference methods [49, 92]. We discretise both time and space into a finite grid with spacing Δt and Δr respectively, resulting in the coordinates $r_i = i\Delta r$ and $t_n = n\Delta t$ for $i = 0, 1, ..., R$ (where $R = \dfrac{R_B}{\Delta r}$) and for $n = 0, 1, ..., T$. We then use forwards time centralised space (FTCS) scheme to approximate our model as

$$\begin{aligned}
\frac{c_{I,i}^{n+1} - c_{I,i}^{n}}{\Delta t} &= D_I \left(\frac{c_{I,i+1}^{n} - 2c_{I,i}^{n} + c_{I,i-1}^{n}}{\Delta r^2} + \frac{2}{r_i} \frac{c_{I,i+1}^{n} - c_{I,i-1}^{n}}{2\Delta r} \right) + O(\Delta t) + O(\Delta x^2), \\
\frac{c_{E,i}^{n+1} - c_{E,i}^{n}}{\Delta t} &= D_E \left(\frac{c_{E,i+1}^{n} - 2c_{E,i}^{n} + c_{E,i-1}^{n}}{\Delta r^2} + \frac{2}{r_i} \frac{c_{E,i+1}^{n} - c_{E,i-1}^{n}}{2\Delta r} \right) + O(\Delta t) + O(\Delta x^2).
\end{aligned} \tag{4.24}$$

Here $c_{I,i}^{n}$ and $c_{E,i}^{n}$ denote the intracellular and extracellular concentrations respectively. Discarding the truncation error terms and solving (4.24) for $c_{I,i}^{n+1}$ and $c_{E,i}^{n+1}$ gives

$$\begin{aligned}
c_{I,i}^{n+1} &= c_{I,i}^{n} + D_I \Delta t \left(\frac{c_{I,i+1}^{n} - 2c_{I,i}^{n} + c_{I,i-1}^{n}}{\Delta r^2} + \frac{2}{r_i} \frac{c_{I,i+1}^{n} - c_{I,i-1}^{n}}{2\Delta r} \right), \\
c_{E,i}^{n+1} &= c_{E,i}^{n} + D_E \Delta t \left(\frac{c_{E,i+1}^{n} - 2c_{E,i}^{n} + c_{E,i-1}^{n}}{\Delta r^2} + \frac{2}{r_i} \frac{c_{E,i+1}^{n} - c_{E,i-1}^{n}}{2\Delta r} \right).
\end{aligned} \tag{4.25}$$

The model discretisation simplifies to

$$\begin{aligned}
c_{I,i}^{n+1} &= \theta_I \left(1 + \frac{\Delta r}{r_i} \right) c_{I,i+1}^{n} + (1 - 2\theta_I)\, c_{I,i}^{n} + \theta_I \left(1 - \frac{\Delta r}{r_i} \right) c_{I,i-1}^{n}, \\
c_{E,i}^{n+1} &= \theta_E \left(1 + \frac{\Delta r}{r_i} \right) c_{E,i+1}^{n} + (1 - 2\theta_E)\, c_{E,i}^{n} + \theta_E \left(1 - \frac{\Delta r}{r_i} \right) c_{E,i-1}^{n}.
\end{aligned} \tag{4.26}$$

where

$$\theta_I = \frac{D_I \Delta t}{\Delta r^2}, \qquad \theta_E = \frac{D_E \Delta t}{\Delta r^2}. \tag{4.27}$$

These discretisations will apply to all spatial points not at the boundaries, which we must incorporate using different approximations. For the point $r_0 = 0$, we need to

consider the singularity from the term $\frac{2}{r}\frac{\partial c}{\partial r}$. We use L'Hopital's rule to approximate this term:

$$\lim_{r\to 0}\frac{1}{r}\frac{\partial c_I}{\partial r} = \frac{\partial^2 c_I}{\partial r^2} \tag{4.28}$$

substituting this approximation into equation (4.25) we have

$$\frac{c_{I,0}^{n+1} - c_{I,0}^{n}}{\Delta t} = 3D_I\left(\frac{c_{I,1}^{n} - 2c_{I,0}^{n} + c_{I,-1}^{n}}{\Delta r^2}\right). \tag{4.29}$$

We now discretise the no flux boundary condition using central difference, involving a ghost point (a point out of the concentration's spatial domain) $c_{I,-1}^{n}$

$$\frac{c_{I,1}^{n} - c_{I,-1}^{n}}{2\Delta r} = 0, \tag{4.30}$$

achieving $c_{I,-1}^{n} = c_{I,1}^{n}$. We can then substitute this into (4.29) to achieve the discretisation for this boundary point

$$c_{I,0}^{n+1} = (1-6\theta)c_{I,0}^{n} + 6\theta c_{I,1}^{n}. \tag{4.31}$$

For our outer boundary condition (the coordinate $r_R = R_B$) we have two possibilities of boundary condition, a far field boundary condition and a no flux boundary condition. The far field condition is simply a perfect sink condition

$$c_{E,R}^{n} = 0. \tag{4.32}$$

For the no flux boundary condition, we follow a similar method to the boundary at r_0, discretising the no flux boundary condition using central difference

$$\frac{c_{E,R+1}^{n} - c_{E,R-1}^{n}}{2\Delta r} = 0, \tag{4.33}$$

obtaining $c_{E,R+1}^{n} = c_{E,R-1}^{n}$, which substituting into (4.26) simplifies to

$$c_{E,R}^{n+1} = (1-2\theta_E)c_{E,R}^{n} + 2\theta_E c_{E,R-1}^{n}. \tag{4.34}$$

Finally we have our membrane boundary condition which we define to be at the point $r_M = R_M$. We discretise this boundary condition using central difference

$$\begin{aligned} -D_I \frac{c^n_{I,M+1} - c^n_{I,M-1}}{\Delta r} &= (P+X)c^n_{I,M} - Pc^n_{E,M}, \\ -D_E \frac{c^n_{E,M+1} - c^n_{E,M-1}}{\Delta r} &= (P+X)c^n_{I,M} - Pc^n_{E,M}. \end{aligned} \tag{4.35}$$

By solving this condition as a system of simultaneous equations, we are able to find equations for the ghost points of each of the concentrations $c^n_{I,M+1}$ and $c^n_{E,M-1}$. These are ghost points as c_I does not exist in the extracellular space and c_E does not exist in the intracellular space.

$$\begin{aligned} c^n_{I,M+1} &= \frac{2P\Delta r}{D_I} c^n_{E,M} - \frac{2(P+X)\Delta r}{D_I} c^n_{I,M} + c^n_{I,M-1} \\ &= \lambda_I c^n_{E,M} - \eta_I c^n_{I,M} + c^n_{I,M-1}, \end{aligned} \tag{4.36}$$

$$\begin{aligned} c^n_{E,M-1} &= -\frac{2P\Delta r}{D_I} c^n_{E,M} + \frac{2(P+X)\Delta r}{D_I} c^n_{I,M} + c^n_{E,M+1}, \\ &= -\lambda_E c^n_{E,M} + \eta_E c^n_{I,M} + c^n_{E,M+1}, \end{aligned} \tag{4.37}$$

where here we have used the following for simplicity in presentation

$$\lambda_I = \frac{2P\Delta r}{D_I}, \qquad \eta_I = \frac{2(P+X)\Delta r}{D_I}, \tag{4.38}$$

$$\lambda_E = \frac{2P\Delta r}{D_E}, \qquad \eta_E = \frac{2(P+X)\Delta r}{D_E}. \tag{4.39}$$

Now that we have these equations, we can apply them to our finite difference method by

substituting into equations (4.26)

$$c_{I,M}^{n+1} = \theta_I \lambda_I \left(1 + \frac{\Delta r}{r_i}\right) c_{E,M}^n + \left(1 - 2\theta_I - \eta_I \theta_I - \frac{\eta_I \theta_I \Delta r}{r_i}, \right) c_{I,M}^n + 2\theta_I c_{I,M-1}^n,$$
$$c_{E,i}^{n+1} = \theta_E \eta_E \left(1 + \frac{\Delta r}{r_i}\right) c_{I,M}^n + \left(1 - 2\theta_E - \lambda_E \theta_E - \frac{\lambda_E \theta_E \Delta r}{r_i}\right) c_{E,M}^n + 2\theta_E c_{E,M+1}^n. \tag{4.40}$$

Thus by collating our approximations our full finite difference method to approximate our model is represented in equation (4.41). We implement this method in MATLAB to produce various different simulations of our model. Unless otherwise stated we set our spatial step $\Delta r = 0.1\mu m$, with membrane at radius $2\mu m$. Furthermore in order to maintain stability of our finite difference method we set $\Delta t = \frac{\Delta r^2}{4D_{MAX}}$, where $D_{MAX} = \max(D_I, D_E)$ [78]. The model has also been tested at different resolutions using smaller values for Δr, the size of Δr here provides a sufficient degree of accuracy whilst not taking an extensive time to produce simulations.

$$
c_{I,i}^{n+1} = \begin{cases} (1-6\theta_I)c_{I,i}^n + 6\theta_I c_{I,i+1}^n, & i=0, \\ \theta_I \left(1+\dfrac{\Delta r}{r_i}\right) c_{I,i+1}^n + (1-2\theta_I)\, c_{I,i}^n + \theta_I \left(1-\dfrac{\Delta r}{r_i}\right) c_{I,i-1}^n, & i=1,...,M-1, \\ \theta_I\, \lambda_I \left(1+\dfrac{\Delta r}{r_i}\right) c_{E,i}^n + \left(1-2\,\theta_I - \eta_I\,\theta_I - \dfrac{\eta_I\,\theta_I\,\Delta r}{r_i},\right) c_{I,i}^n + 2\,\theta_I\, c_{I,i-1}^n, & i=M, \end{cases}
$$

$$
c_{E,i}^{n+1} = \begin{cases} \theta_E\,\eta_E \left(1+\dfrac{\Delta r}{r_i}\right) c_{I,i}^n + \left(1-2\,\theta_E - \lambda_E\,\theta_E - \dfrac{\lambda_E\,\theta_E\,\Delta r}{r_i}\right) c_{E,i}^n + 2\,\theta_E\, c_{E,i+1}^n, & i=M, \\ \theta_E \left(1+\dfrac{\Delta r}{r_i}\right) c_{E,i+1}^n + (1-2\theta_E)\, c_{E,i}^n + \theta_E \left(1-\dfrac{\Delta r}{r_i}\right) c_{E,i-1}^n, & i=M+1,...,R-1, \\ (1-2\theta_E)c_{E,i}^n + 2\theta_E c_{E,i-1}^n, & i=R. \end{cases} \tag{4.41}
$$

4.4.1 Numerical Simulations

As we are modelling the *Salmonella* cells as spheres rather than rods, we choose a cell radius ($2\mu m$) that yields a similar spherical volume and surface area to the maximum cylindrical volume and surface area of *Salmonella*'s typical rod shaped dimensions.

We exhibit simulations of the single cell model with a zero far field outer boundary in Figure 4.3. Here we have set the far field boundary (at $10\mu m$) to be far enough from the membrane (at $2\mu m$). We also set the initial intracellular concentration to be $1\,\mathrm{mol}/\mu m^3$. For simplicity, we have set the diffusivity coefficients of the intracellular and extracellular substrate to be identical ($0.1\mu m^2 s^{-1}$).

In Figure 4.3 (a), we can see the results of an impermeable membrane with no efflux. We see no transfer of substrate from the intracellular space, with a uniform distribution throughout for all time. In (b), we see the introduction of a permeable membrane. Here we can immediately see that substrate is able to diffuse across the membrane. This results in a decrease in the intracellular concentration. The rate of expulsion from the intracellular space slows as time gets larger, as the membrane surrounding extracellular concentrations become similar to the intracellular concentration. In (c), we see an impermeable membrane with active efflux pumps. Whilst being similar to the simulations in (b), we note that substrate is not free to diffuse back into the intracellular space once being expelled. This results in almost all substrate being expelled from the intracellular space, even with higher extracellular concentrations surrounding the membrane. In (d) we exhibit a permeable membrane with active efflux pumps. In this simulation, we see a combination of the characteristics of simulations (b) and (c). Whilst the efflux pumps expel a large concentration of substrate, some substrate is able to diffuse back into the intracellular space through the permeable membrane. We note that in the latter simulations (b), (c) and (d) the extracellular concentration dissipates due to the zero far field boundary condition. Thus the system will only reach steady state once there is zero concentration in all regions.

We exhibit simulations of the single cell model with a no flux outer boundary in

Figure 4.4. Here we have set the outer boundary (at $4\mu m$) to be close to the membrane (at $2\mu m$). We note that the simulations in each case are similar to those in Figure 4.3. We see however with the introduction of a no flux boundary, the simulations approach steady state as time grows. In Figure 4.4 (b) the substrate is free to diffuse across the membrane. However as the extracellular space is limited and is not depleting, we see the intracellular and extracellular concentrations approaching steady state at the same concentration. In (c) we see the impermeable membrane with active efflux; here the extracellular concentration approaches a steady state but is unable to diffuse back into the cell. Thus we see the intracellular concentration being completely expelled via the cell's efflux pumps. Finally in (d) we see the mixture of diffusion and expulsion via efflux pumps, with a steady state being approached for both intracellular and extracellular concentrations. However, we note that the intracellular concentration steady state is higher than the intracellular concentration in (c), due to the membrane permeability enabling substrate to diffuse back in from the extracellular to the intracellular space.

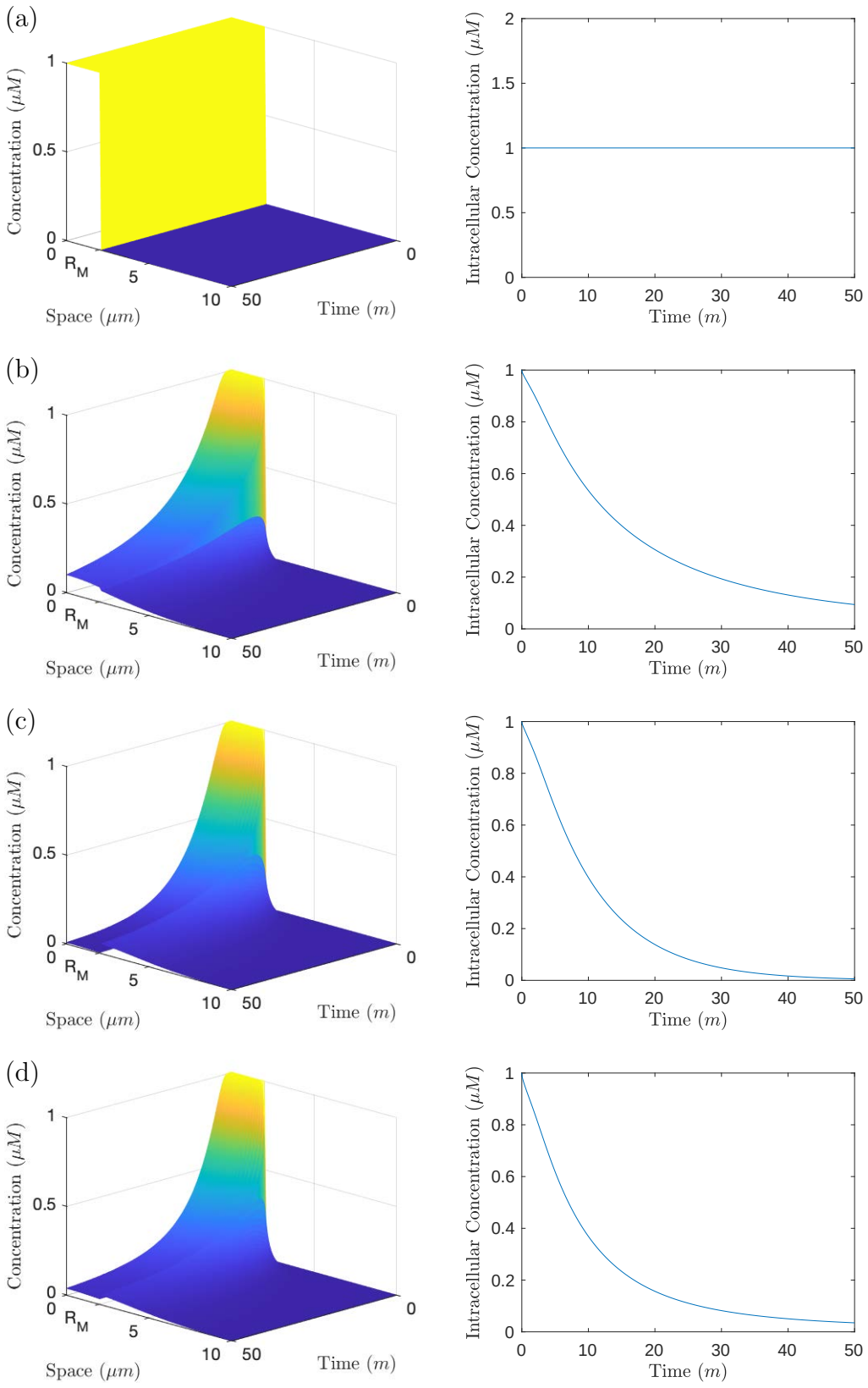

Figure 4.3: Simulations of the cell model with a zero far field outer boundary condition, with $R_M = 2\mu m$ and $R_B = 10\mu m$. We exhibit the distribution profiles on the left, with resulting averaged intracellular concentrations on the right. In simulation (a) $P = 0\mu m, X = 0\mu m$, (b) $P = 0.1\mu m, X = 0\mu m$, (c) $P = 0\mu m, X = 0.1\mu m$ and (d) $P = 0.1\mu m, X = 0.1\mu m$.

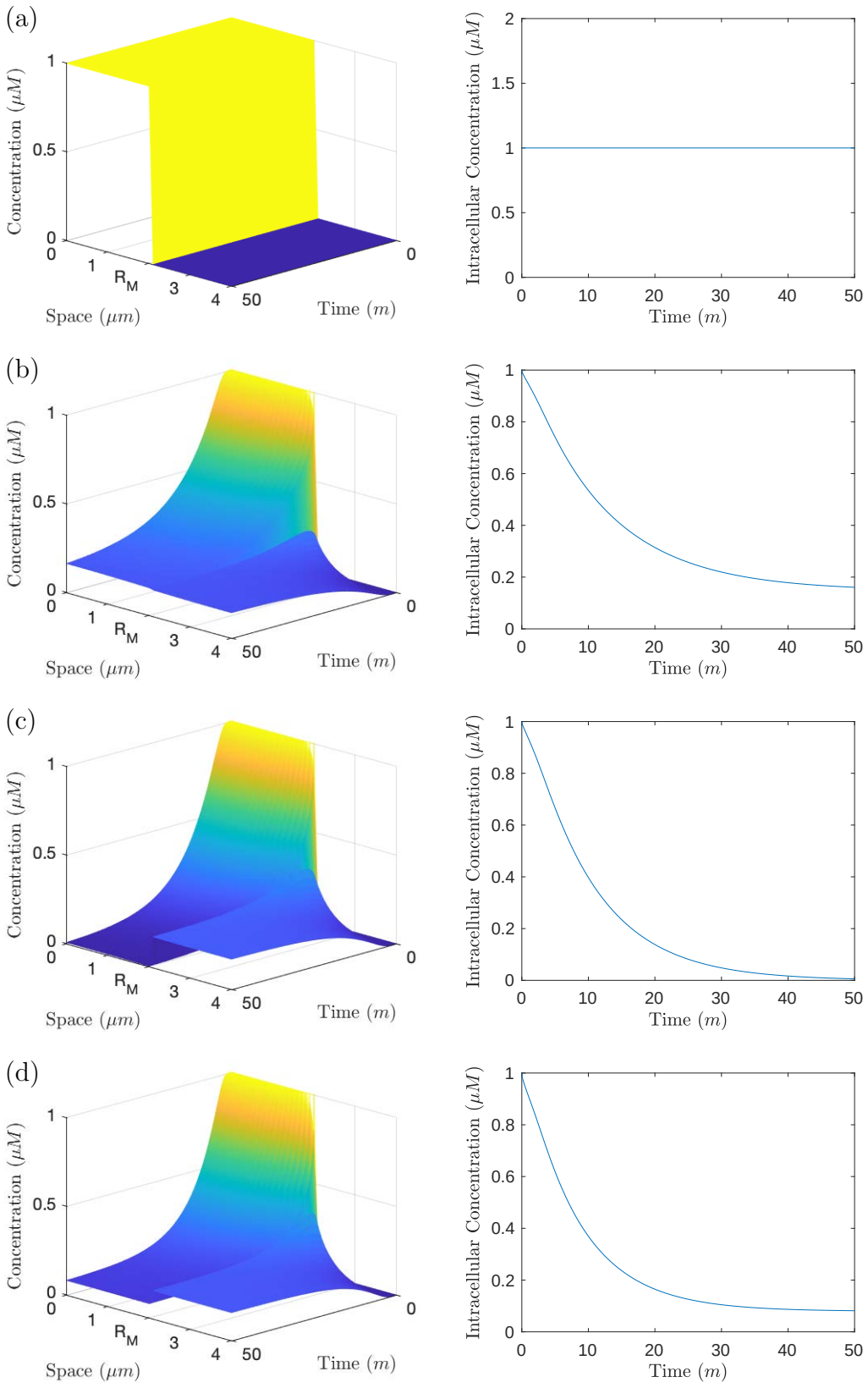

Figure 4.4: Simulations of the cell model with a no flux outer boundary condition with $R_M = 2\mu m$ and $R_B = 4\mu m$. We exhibit the distribution profiles on the left, with resulting averaged intracellular concentrations on the right. In simulation (a) $P = 0\mu m, X = 0\mu m$, (b) $P = 0.1\mu m, X = 0\mu m$, (c) $P = 0\mu m, X = 0.1\mu m$ and (d) $P = 0.1\mu m, X = 0.1\mu m$.

4.5 Parametrisation Data

Experiments have taken place on various different cultures of *Salmonella*, with various efflux pump knockouts as described in Section 4.2. We detail the strains used in the experiments as:

- Wild-type strain; in this strain we have all four efflux pump systems active.
- AcrAB knockout strain (A Knockout); in this strain we have only AcrEF, MdsAB and MdtAB active.
- AcrEF knockout strain (E Knockout); in this strain we have only AcrAB, MdsAB and MdtAB active.
- MdsAB knockout strain (S Knockout); in this strain we have only AcrAB, AcrEF and MdtAB active.
- MdtAB knockout strain (T Knockout); in this strain we have only AcrAB, AcrEF and MdsAB active.
- AcrAB and AcrEF knockout strain (AE Knockout); in this strain we have only MdsAB and MdtAB active.
- Full RND knockout strain (AEST Knockout); in this strain we have none of our four efflux pumps active. Thus the only transfer of substrate will be through the cell membrane or through other lesser efflux pump systems.

We summarise all of these strains and their corresponding efflux parameters in Table 4.1. In regards to efflux parameter notation, we list the efflux pumps that are still active in the subscript (e.g. A knockout would be noted by X_{EST}). We include each strain's efflux parameter in the following parameter fitting exercises by modifying the membrane boundary condition for each strain:

$$-D_I \frac{\partial c_I}{\partial r}\bigg|_{r=R_M} = -D_E \frac{\partial c_E}{\partial r}\bigg|_{r=R_M} = (P + X_I)c_I(R_M, t) - Pc_E(R_M, t), \tag{4.42}$$

Strain Name	Active Efflux Pumps	Efflux Constant
Wild-type	AcrAB, AcrEF, MdsAB, MdtAB	X_{AEST}
A Knockout	AcrEF, MdsAB, MdtAB	X_{EST}
E Knockout	AcrAB, MdsAB, MdtAB	X_{AST}
S Knockout	AcrAB, AcrEF, MdtAB	X_{AET}
T Knockout	AcrAB, AcrEF, MdsAB	X_{AES}
AE Knockout	MdsAB, MdtAB	X_{ST}
AEST Knockout	N/A	N/A

Table 4.1: A summary of the strains involved in the experiments. We list each strain's active efflux pumps as well as their corresponding efflux rate constant.

here X_I denotes the efflux for the strain of which the pump(s) I are active. This enables us to find the corresponding efflux value for each strain through multiple parameter fitting exercises.

For each experiment with a given strain, we have multiple assays (biological repeats). Within these individual assays, we have technical repeats for each strain. The mean and standard deviations are found of these technical repeats and we plot these in Figures 4.5-4.11. Under advice from the Blair laboratory, we have taken each assay's initial data point to be the start of the final peak of fluorescence. This is due to unknown experimental errors upon measuring fluorescence on very early time points. Fluorescence for each assay is measured in arbitrary units. In order to combine the data from all assays we normalise our data by dividing the fluorescence over time by the peak initial fluorescence. In Figures 4.12 and 4.13, we show the results of normalising our data. As not all assays run for the same length of time, we split our combinations into three time periods (short, medium and long time). Whilst the short time plots include data of all assays, the medium and long time plots are restricted to the assays that reach the final time point on the corresponding plot.

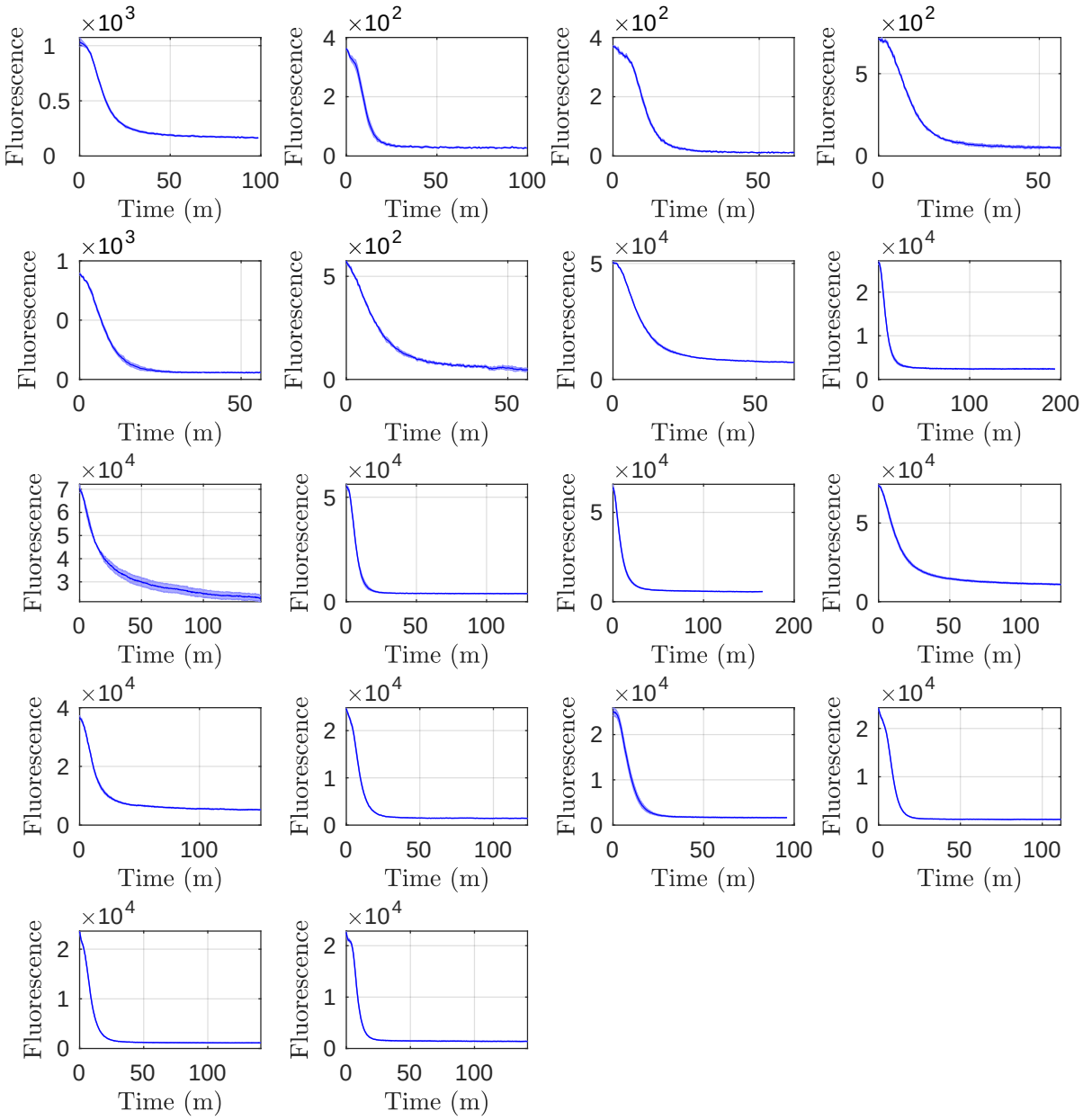

Figure 4.5: Experiments taken upon the wild-type strain consisting of 18 assays. In each individual assay we have plotted the mean (solid line) and standard deviation (shaded error bar) of three technical repeats.

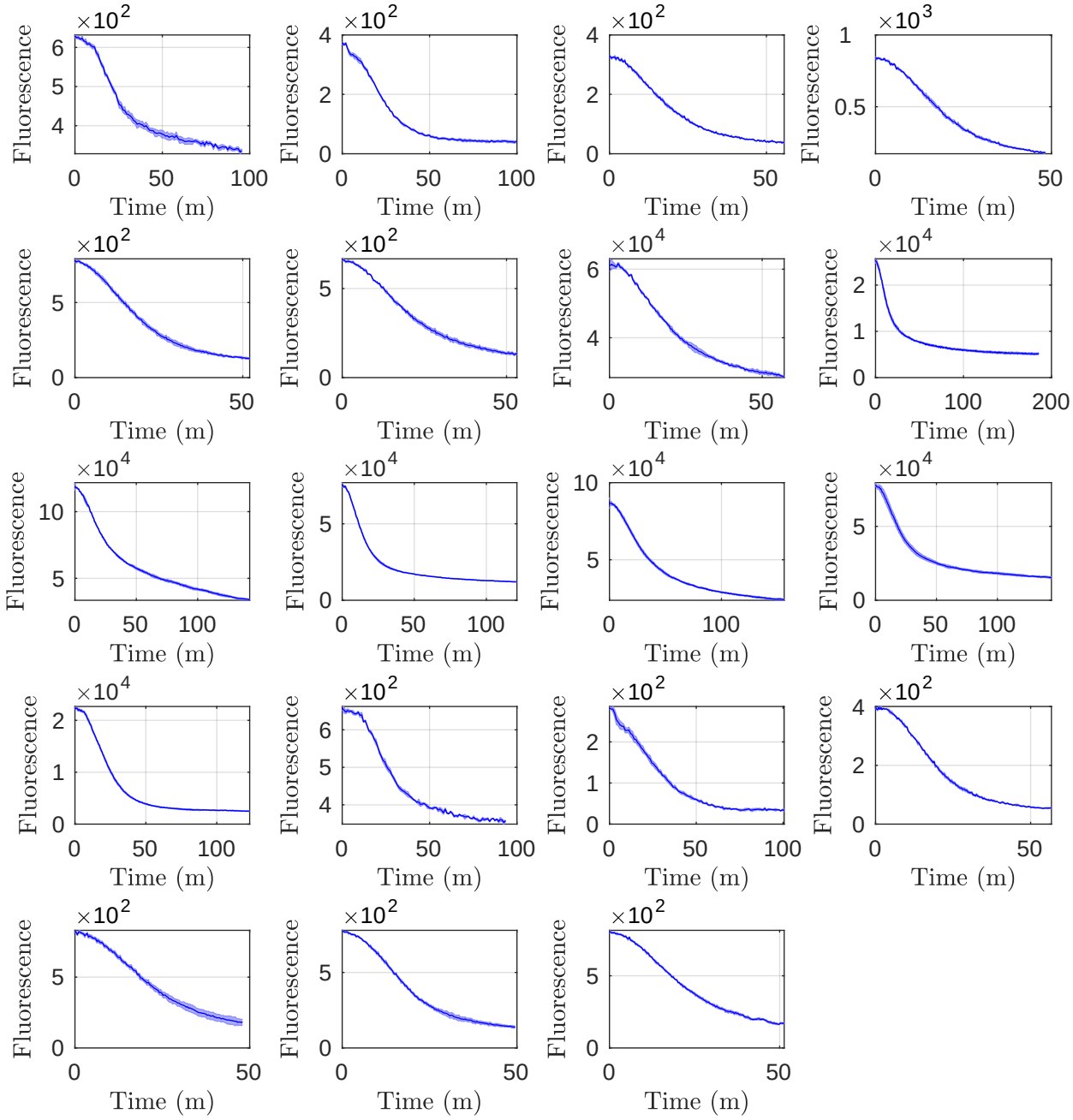

Figure 4.6: Experiments taken upon the A knockout strain consisting of 19 assays. In each individual assay we have plotted the mean (solid line) and standard deviation (shaded error bar) of three technical repeats.

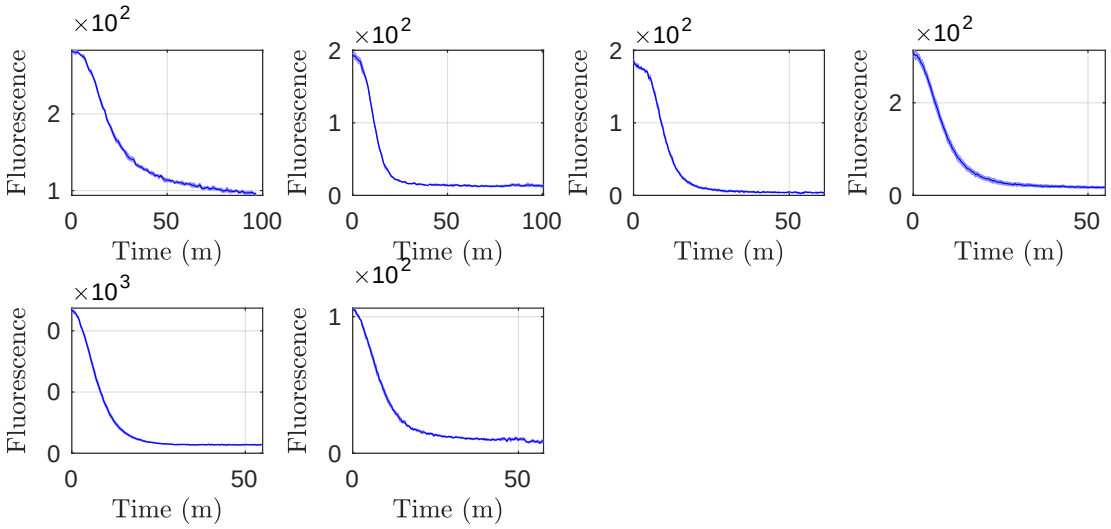

Figure 4.7: Experiments taken upon the E knockout strain consisting of 6 assays. In each individual assay we have plotted the mean (solid line) and standard deviation (shaded error bar) of three technical repeats.

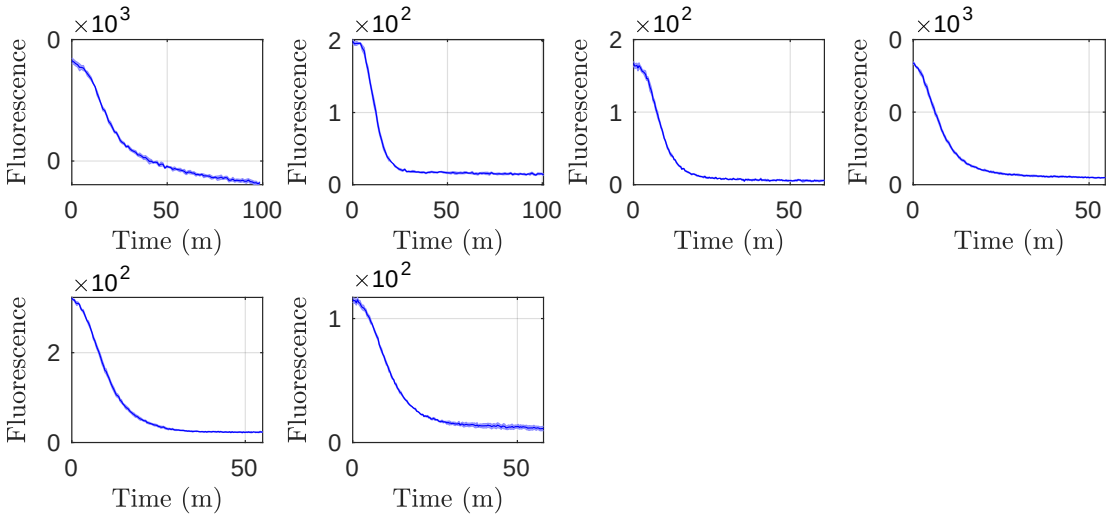

Figure 4.8: Experiments taken upon the S knockout strain consisting of 6 assays. In each individual assay we have plotted the mean (solid line) and standard deviation (shaded error bar) of three technical repeats.

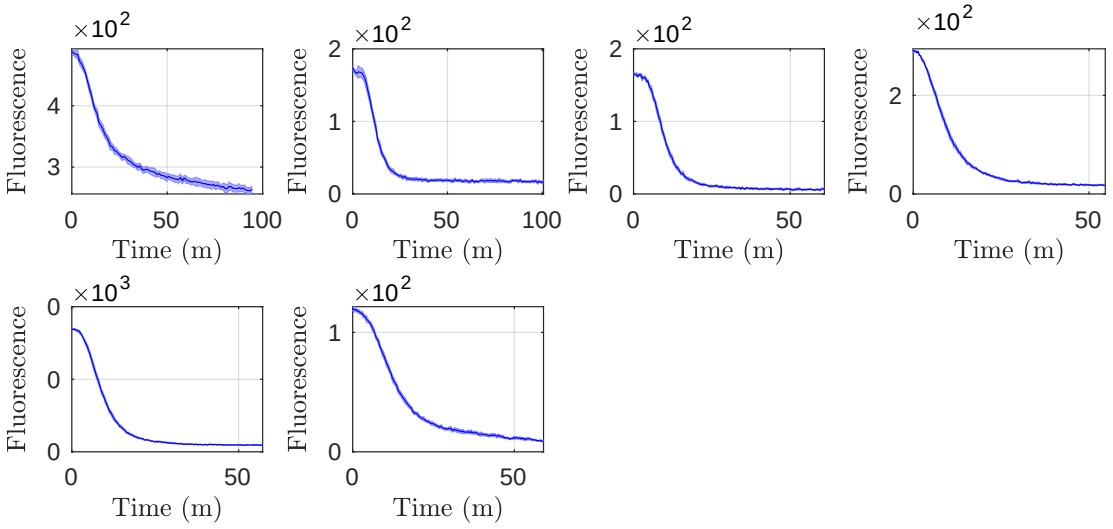

Figure 4.9: Experiments taken upon the T knockout strain consisting of 6 assays. In each individual assay we have plotted the mean (solid line) and standard deviation (shaded error bar) of three technical repeats.

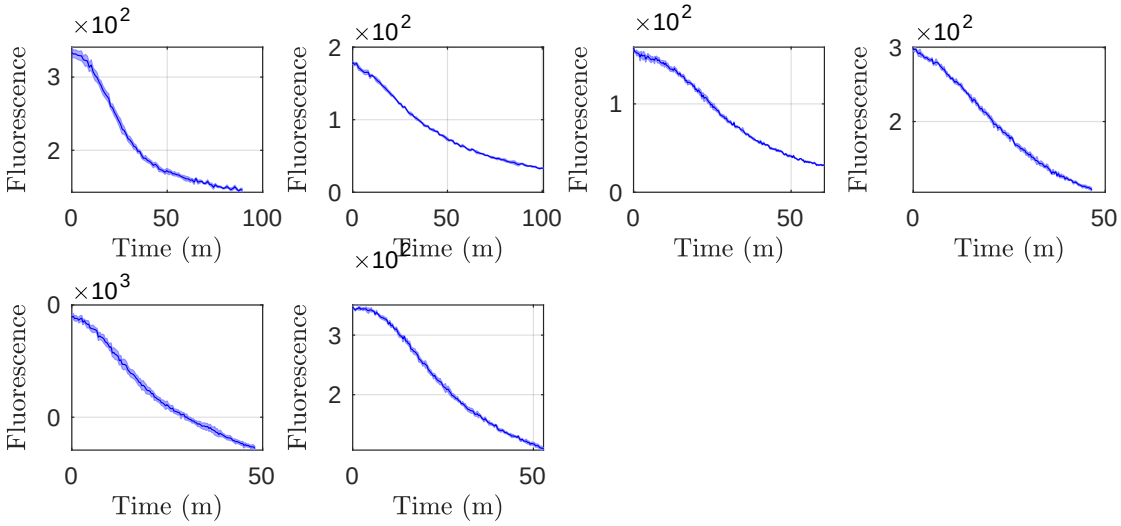

Figure 4.10: Experiments taken upon the AE knockout strain consisting of 6 assays. In each individual assay we have plotted the mean (solid line) and standard deviation (shaded error bar) of three technical repeats.

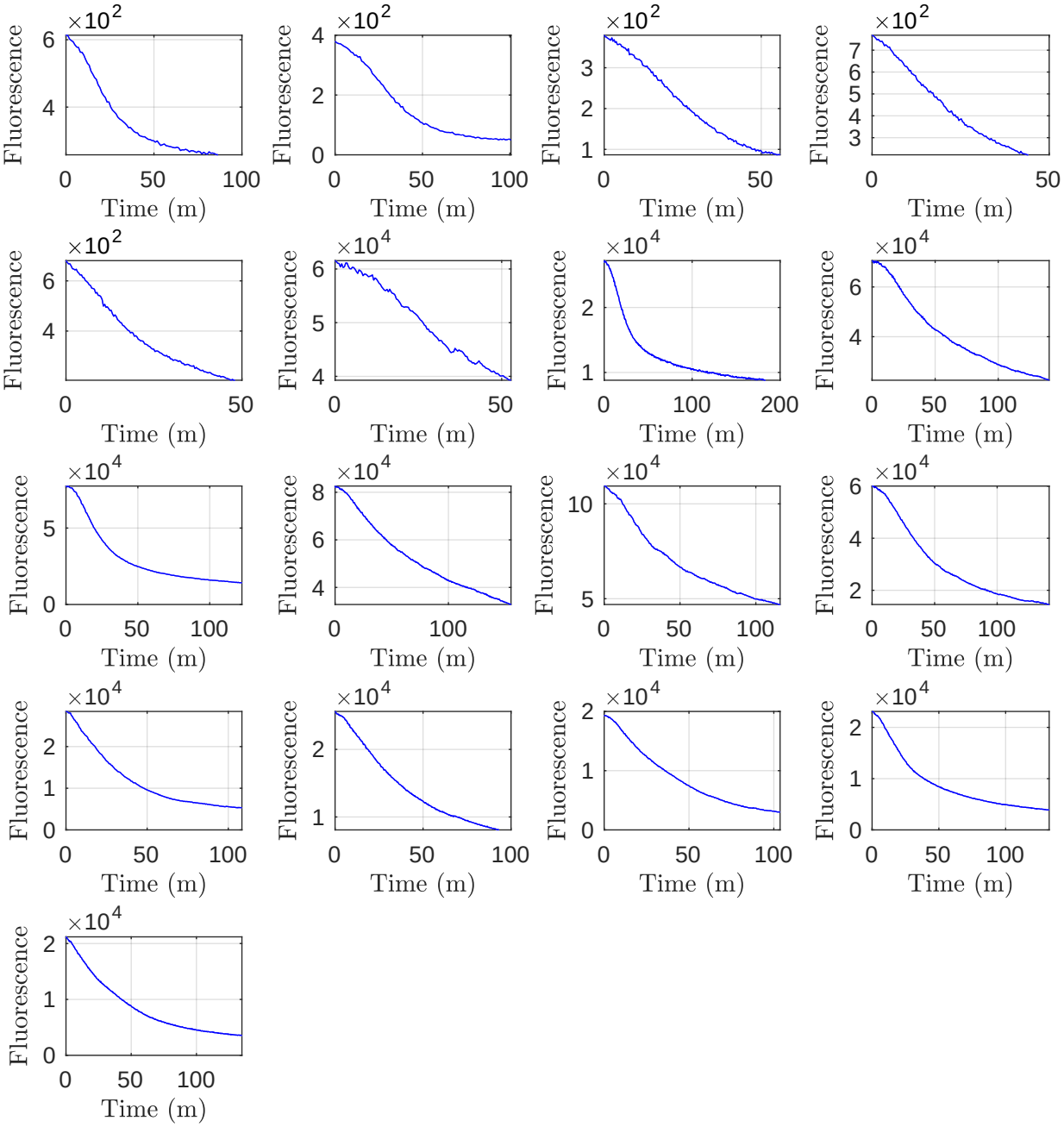

Figure 4.11: Experiments taken upon the AEST knockout strain consisting of 17 assays. In each individual assay we have plotted the mean (solid line) and standard deviation (shaded error bar) of three technical repeats.

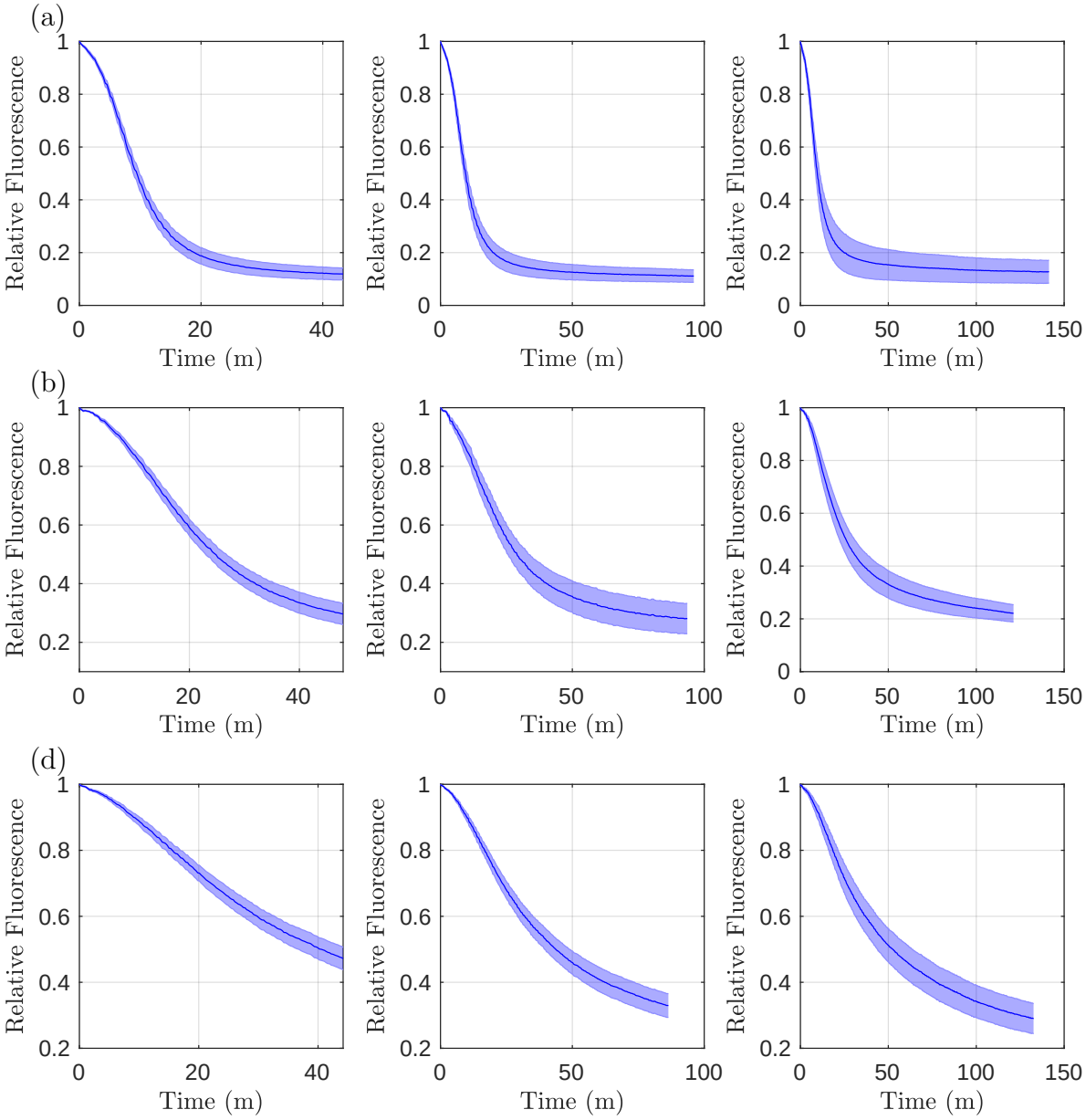

Figure 4.12: Normalised efflux assay data, for each plot we have the mean of the assays (solid line) and standard deviation (shaded error bar). We have combined (a) Wild-type, (b) A Knockout and (c) AEST knockout. We have split the data of each strain into three time regions, only including the assays that reach the maximum time point.

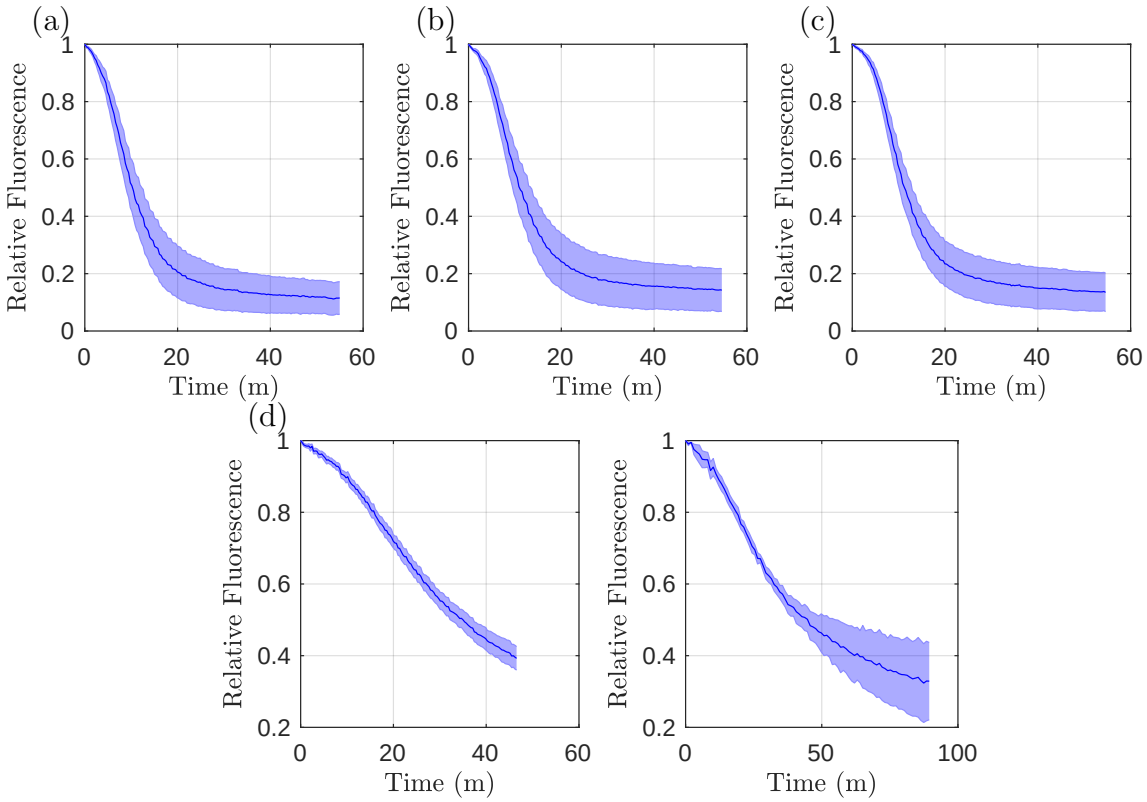

Figure 4.13: Normalised efflux assay data, for each plot we have the mean of the assays (solid line) and standard deviation (shaded error bar). We have combined (a) E knockout, (b) S knockout, (c) T knockout and (d) ST knockout. For (d) we have split the data for the strain into two time regions, only including the assays that reach the maximum time point.

4.6 Parametrisation Methods

We employ the use of the function *fminsearch* in MATLAB to obtain our parameter estimates. The function uses the Nelder-Mead simplex method (described in [47]) to minimize a given objective function starting from initial parameter guesses. In order to obtain these parameter guesses, we use a latin hypercube method of sampling as described by McKay in [55]. By establishing realistic upper and lower parameter bounds, we create a parameter space from which a range of initial parameter guesses are chosen. We use this sampling method in order to choose a well-spread distribution of initial parameter guesses (something that is not guaranteed from using a random method of sampling).

Our objective function that we attempt to minimise is as follows:

$$f = \frac{1}{t_{max}} \int_0^{t_{max}} \mid y(t) - I(t)) \mid dt \tag{4.43}$$

where

$$\begin{aligned} I(t) &= \frac{1}{\frac{4}{3}\pi R_M^3} \iiint_V r^2 \, \sin(\theta) \, c_I(r,t) \, dr \, d\theta \, d\phi \\ &= \frac{3}{R_M^3} \int_0^{R_M} r^2 \, c_I(r,t) \, dr. \end{aligned}$$

Here y denotes the experimental data, I denotes the averaged intracellular concentration of substrate, R_M denotes the distance from the cell centre to the cell membrane and t_{max} is the maximum time for the simulations. We have opted to divide our objective function by the amount of data points in the corresponding assay to which we are fitting. This gives us a comparison point between the accuracy of fits to different strains that differ in assay length. In addition we have applied a constraint to our parameters to be non-negative, we have included this by ensuring that the absolute value of each parameter is taken through every iteration of finding the objective function. We note that our data values are measured in relative fluorescence and our model in concentration. However, as we have assumed a directly proportional relationship between the fluorescence and intracellular concentration of substrate, we choose to model in terms of relative concentration so we can directly fit the model to the data. Finally, we list all parameters used in this model, noting the parameters being varied in Table 4.2. For simplicity in presentation, we will omit the units of each fitted parameter in our following optimal parameter sets.

4.7 Results

As in our numerical simulations in section 4.4, for the following we set the cell to have a radius of $2\mu m$. Since we do not know the link between fluorescence and concentration

Parameter	Description	Value	Units
R_M	Membrane Radius	2	μm
R_B	Outer Boundary Radius	Not Set	μm
P	Permeability Mass Transfer Coefficient	Not Set	$\mu m\, min^{-1}$
X_{AEST}	Efflux Conversion Constant For Wild-type Case	Not Set	$\mu m\, min^{-1}$
X_{EST}	Efflux Conversion Constant For A Knockout Case	Not Set	$\mu m\, min^{-1}$
X_{AST}	Efflux Conversion Constant For E Knockout Case	Not Set	$\mu m\, min^{-1}$
X_{AST}	Efflux Conversion Constant For S Knockout Case	Not Set	$\mu m\, min^{-1}$
X_{AES}	Efflux Conversion Constant For T Knockout Case	Not Set	$\mu m\, min^{-1}$
X_{ST}	Efflux Conversion Constant For AE Knockout Case	Not Set	$\mu m\, min^{-1}$
D_I	Diffusion Coefficient Of Intracellular Substrate	Not Set	$\mu m^2\, min^{-1}$
D_E	Diffusion Coefficient Of Extracellular Substrate	Not Set	$\mu m^2\, min^{-1}$

Table 4.2: All parameters used in our single cell model and their respective units. If we vary a parameter we will list it as "Not Set" in the "Value" column, otherwise if the parameter is not varied we list its fixed value.

of substrate, we assume that the fluorescence is directly proportional to the averaged internal concentration of ethidium bromide such that the relative fluorescence and relative concentration of substrate is equivalent. By modelling in terms of relative concentration, we can then produce a fit to the relative fluorescence. For the parameter fitting exercises in this chapter, unless otherwise stated we have taken 1000 sets of initial parameter guesses, finding the local minimum objective function and corresponding optimised parameters for each parameter set. By then comparing the resulting objective functions, we have been able to deduce the optimal set of fitted parameters. We have taken the step sizing $\Delta r = 0.25$ and $\Delta t = \dfrac{\Delta r^2}{4D_{MAX}}$ for efficiency to reduce the time taken to run parameter fits of all of the samples whilst maintaining small enough step sizes to produce accurate simulations. For all parameter fits, we fit to the long time data only, withholding the short time and medium time assays for testing of the accuracy of the fit.

4.7.1 Zero far field boundary condition

We first run exercises upon our model with a zero far field boundary condition. For the simulations in this subsection, we have taken our far field boundary to be at a radius of $10\mu m$.

AEST knockout

In order to start fitting our model to the data, we initially fit to the data where no RND efflux pumps are active in the strain. Whilst there is the possibility of less significant efflux pump systems being active in this case, we choose to assume that the efflux contributed from these pumps will be negligible compared to the efflux caused by the RND efflux pumps and membrane permeability. Thus by initially fitting to this data we can construct a base for the diffusion parameters and membrane permeability as these should not vary between experiments. We plot the optimal parameter fit in Figure 4.14 which corresponds with the following parameters:

$$[D_I, D_E, P] = [2.45 \times 10^{-2}, 1.01 \times 10^{-2}, 2.72 \times 10^{-2}], \tag{4.44}$$

given to three significant figures and resulting in an objective function of 8.07×10^{-4}. We note that in general the fit for long time is reasonable, with the model residing within the standard deviation error bars for the majority of long time. We do however note that whilst the data appears to be reaching some kind of steady state, the model does not encapsulate this and by the end of the simulation the concentration appears to be decreasing faster than in the data. When comparing to the (b) medium time and (c) short time assays, we can see that the early time behaviour is missing. Quite prominently the data suggests a delay in the decreasing of concentration, however there is no delay in the model as the concentration clearly undershoots this.

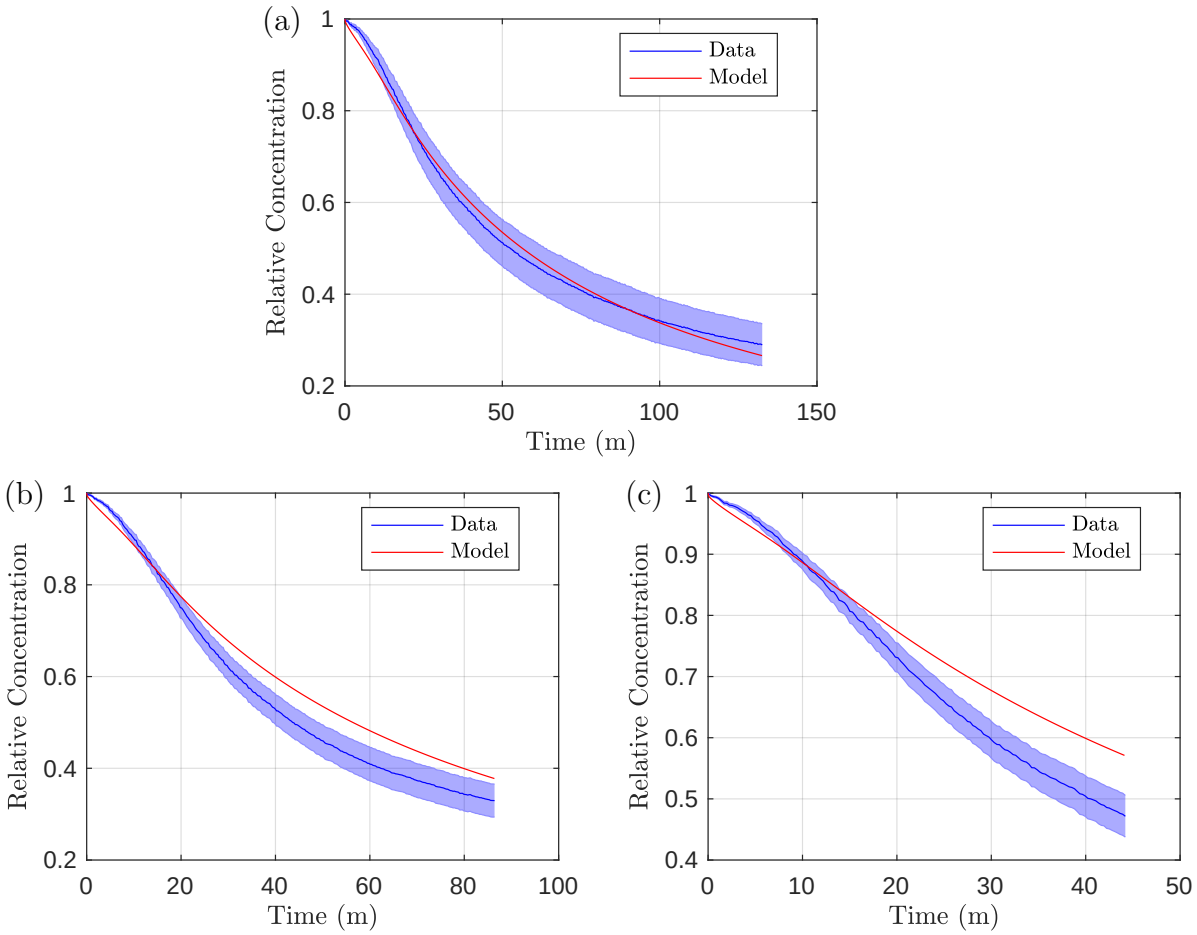

Figure 4.14: Parameter fitting results of the model with a zero far field boundary condition to the AEST knockout data. In (a) we show the fit to the assays that reach long time, (b) the assays that reach medium time and (c) all assays shown upon short time.

Individual efflux knockouts

By fixing our optimal parameters from the AEST knockout case, we can continue to find the remaining efflux parameters from the other strains. As a reminder for efflux parameter notation, we list the efflux pumps that are active in the subscript. For the following fits, we include the individual pump knockouts, meaning in each strain three other RND efflux pumps will be active. We exhibit the optimal fits in Figure 4.15 with the corresponding parameters:

$$[X_{EST}, X_{AST}, X_{AET}, X_{AES}] = [2.50 \times 10^{-2}, 6.68, 0.729, 0.718], \tag{4.45}$$

given to 3 significant figures and a combined objective function of 2.16×10^{-2}. We note that whilst the fit for the A knockout is similar to the data, the E, S and T knockouts are not reasonable fits and exhibit largely different dynamics to the data. As the A knockout corresponds to the strain containing a knockout of the most dominant efflux pump AcrAB-TolC, we expect this case to be the closest to the AEST knockout in that we expect little efflux, which could explain the closeness of fit. Whilst this case does provide the most realistic fit, the key dynamics are missing, with the model not approaching a steady state at long time and no delay of decrease of concentration in the early time.

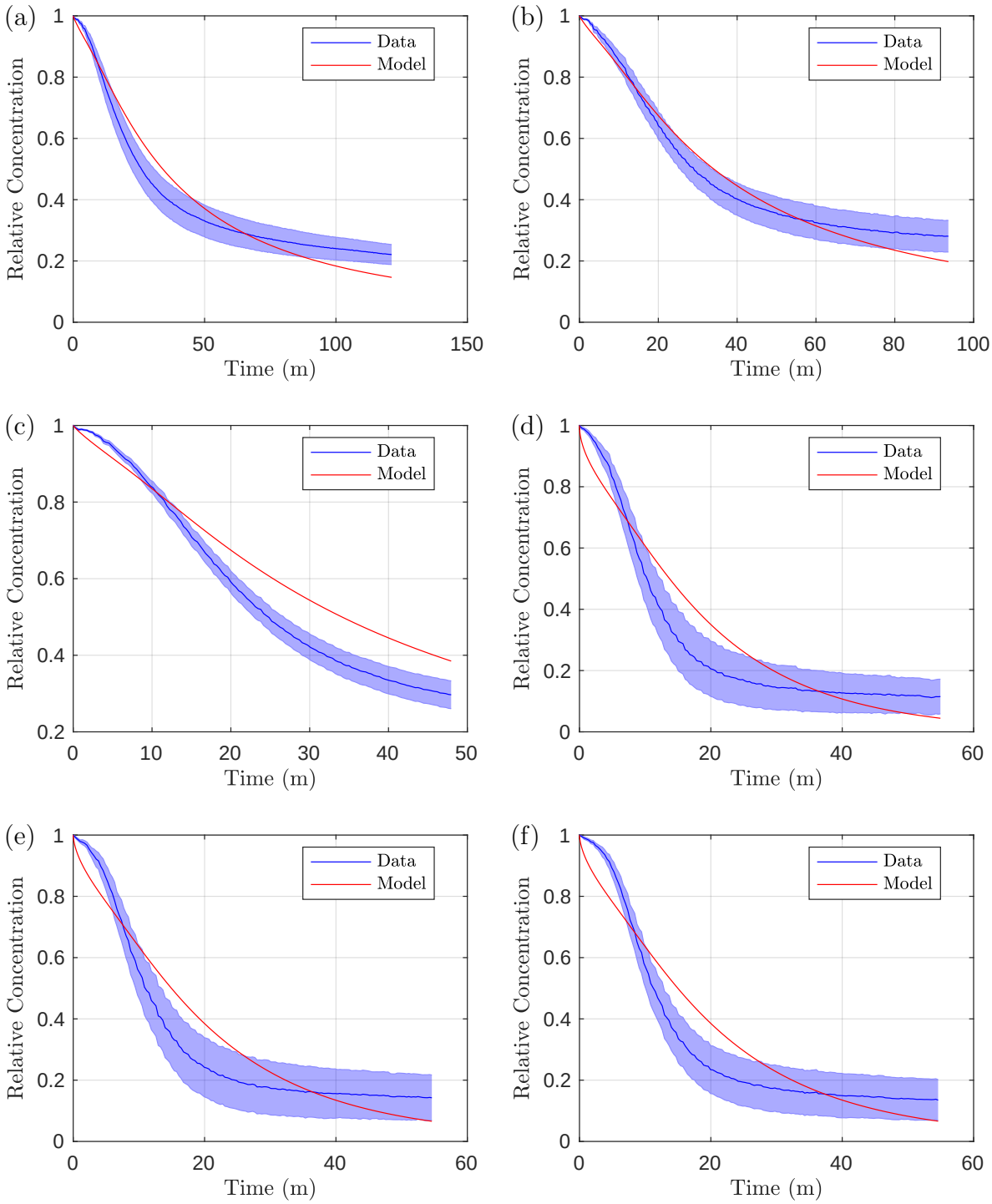

Figure 4.15: Parameter fitting results of the model with a zero far field boundary condition to the individual knockout strains after fixing AEST parameters (4.44). We exhibit the A knockout strain in (a) long time, (b) medium time and (c) short time. The rest of the strains are exhibited as (d) E knockout, (e) S knockout and (f) T knockout.

Wild-type strain

Since we have estimated parameters for efflux of the individual knockouts, if we assume that all efflux is additive, we can use simultaneous equations to find efflux parameters for the individual pumps. From these individual parameters, we can produce an approximation for the efflux parameter for the wild-type strain. If we assume that

$$X_E + X_S + X_T = X_{EST}, \tag{4.46}$$

$$X_A + X_S + X_T = X_{AST}, \tag{4.47}$$

$$X_A + X_E + X_T = X_{AET}, \tag{4.48}$$

$$X_A + X_E + X_S = X_{AES}, \tag{4.49}$$

$$X_A + X_E + X_S + X_T = X_{AEST}, \tag{4.50}$$

then we can solve for

$$X_A = \frac{1}{3}(X_{AST} + X_{AET} + X_{AES} - 2X_{EST}), \tag{4.51}$$

$$X_E = \frac{1}{3}(X_{EST} + X_{AET} + X_{AES} - 2X_{AST}), \tag{4.52}$$

$$X_S = \frac{1}{3}(X_{EST} + X_{AST} + X_{AES} - 2X_{AET}), \tag{4.53}$$

$$X_T = \frac{1}{3}(X_{EST} + X_{AST} + X_{AET} - 2X_{AES}). \tag{4.54}$$

Using the optimal parameters from our individual knockouts strains $(X_{EST}, X_{AST}, X_{AET}, X_{AES})$ we are able to find the efflux values of our individual efflux pumps (X_A, X_E, X_S, X_T) and combine them to estimate the efflux in the wild-type case:

$$[X_A, X_E, X_S, X_T, X_{AEST}] = [2.69, -3.96, 1.99, 2.00, 2.72], \tag{4.55}$$

given to three significant figures. We plot our model with the estimated wild-type parameter in Figure 4.16. It is clear to note that in the long time the simulated efflux is larger than measured in the data, with the concentration reaching null values at long time. We

also note that the individual efflux value for X_E is negative, this leads us to believe that in this model efflux from each individual pump is not additive as negative efflux is not possible.

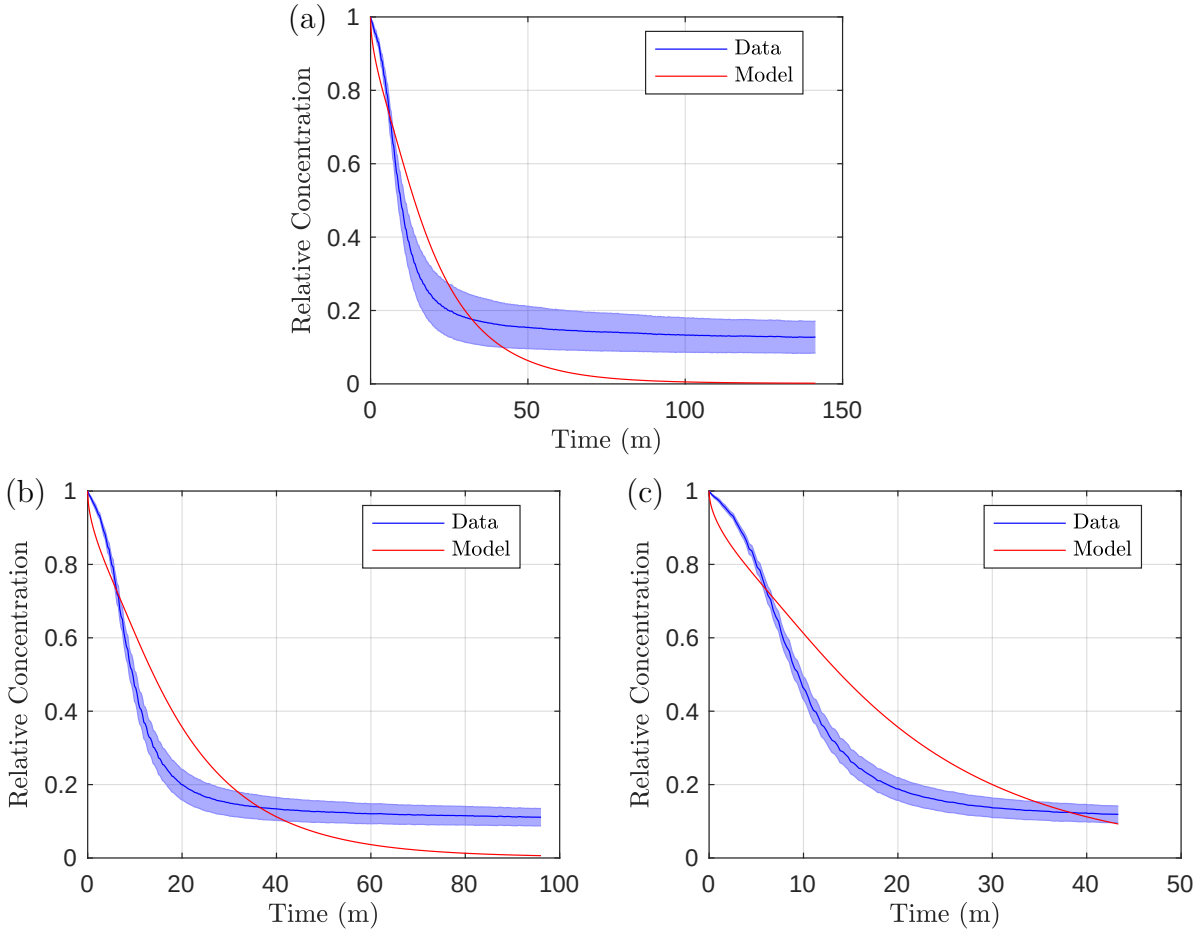

Figure 4.16: Comparison of the estimated wild-type efflux constant (4.55) applied to our model with a zero far field boundary condition to the wild-type data after fixing AEST parameters (4.44). In (a) we show the fit to the assays that reach long time, (b) the assays that reach medium time and (c) all assays in the short time.

Since our estimated efflux parameter does not provide a realistic fit, we run a parameter fit for the wild-type efflux parameter. We plot this in Figure 4.17 with the corresponding parameter:

$$[X_{AEST}] = [0.247], \tag{4.56}$$

given to three significant figures and an objective function of 4.50×10^{-3}. Here we note that the fit at long time is better than our previous estimated parameter, with the concentration

not reaching null values. However, again like the individual knockouts the dynamics of the data is missing, especially shown against the short time assays. Finally, we note that the efflux parameter is less than those fitted of the individual knockouts. We believe this to be because we are fitting to a longer time region in this wild-type data compared to the individual knockout data. In addition compared to the individual efflux knockouts in Figure 4.15, we see that at longer time the individual knockout fits would likely hit null values quicker than the wild-type case, which should not be possible as the wild-type case is where efflux should be at a maximum compared to other strains as all pumps are active.

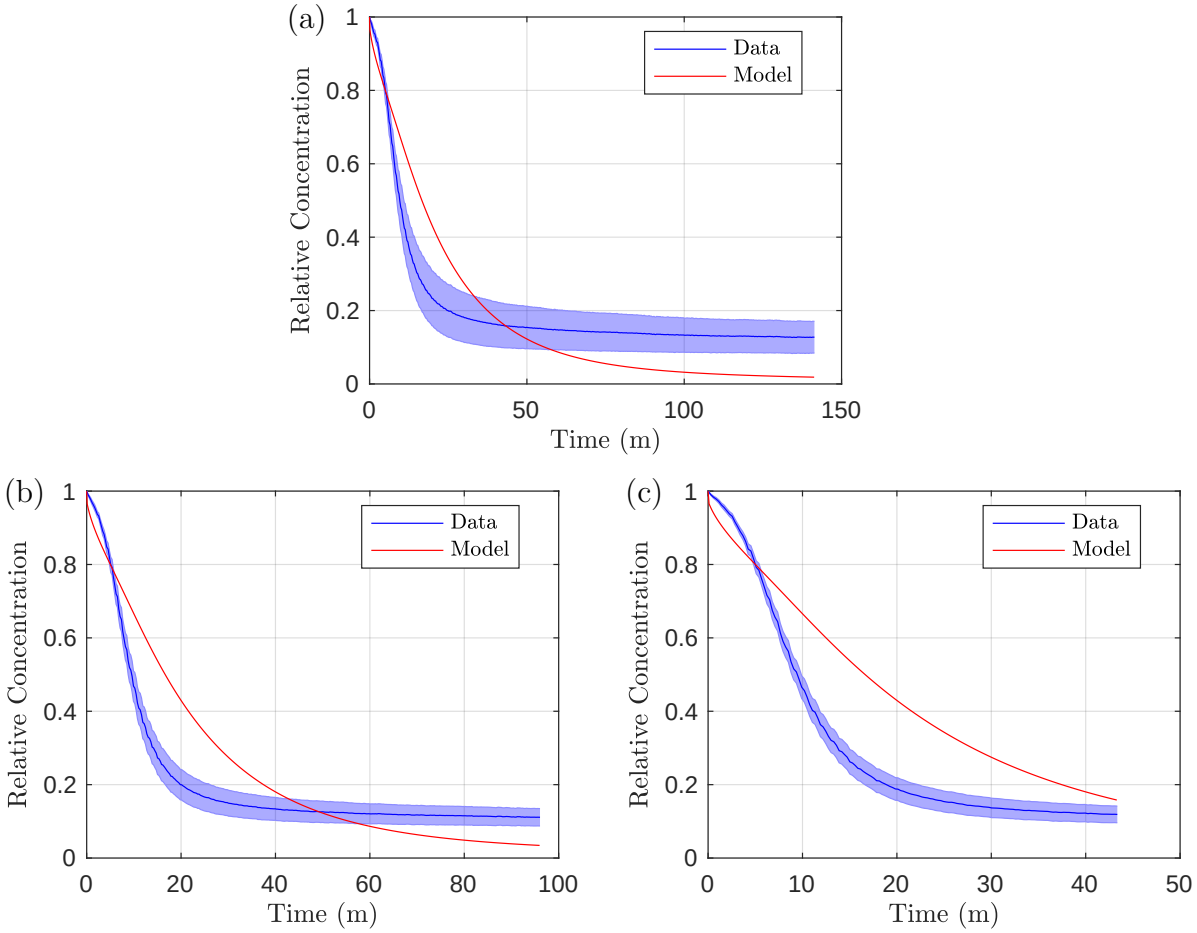

Figure 4.17: Parameter fitting results of the model with a zero far field boundary condition to the wild-type data after fixing our AEST parameters (4.44) and using a parameter fitted efflux rate constant (4.56). In (a) we show the fit to the assays that reach long time, (b) the assays that reach medium time and (c) all assays in the short time.

4.7.2 No-flux boundary condition

Whilst the fit for the zero far field boundary condition model was reasonable in the AEST knockout case, the model failed to capture the dynamics of all cases with efflux. Given that one element of this was the model's failure to reach a steady state (guided by our results of section 4.7.1) we now fit our model with a no-flux outer boundary condition. For the following fits we also vary the position of the extracellular boundary (R_B), by using 125 initial parameter guesses into *fminsearch* for each integer between $3\mu m$ and $10\mu m$ inclusive, resulting in 1000 sets of optimal parameters.

AEST knockout

As with the zero far field boundary model, we set our baseline parameters in the AEST knockout case where we assume that efflux is not active. We plot the optimal fit in Figure 4.18, with corresponding parameters:

$$[R_B, D_I, D_E, P] = [4, 0.102, 7.00 \times 10^{-2}, 9.42 \times 10^{-3}], \tag{4.57}$$

given to 3 significant figures and an objective function of 7.2×10^{-4}. We note that in regards to the objective function, the fit here is better than the previous model for this strain in Section 4.7.1. However we note that the fit is still very similar and is notably still missing the early and mid time dynamics, with only a small improvement to the long term dynamics.

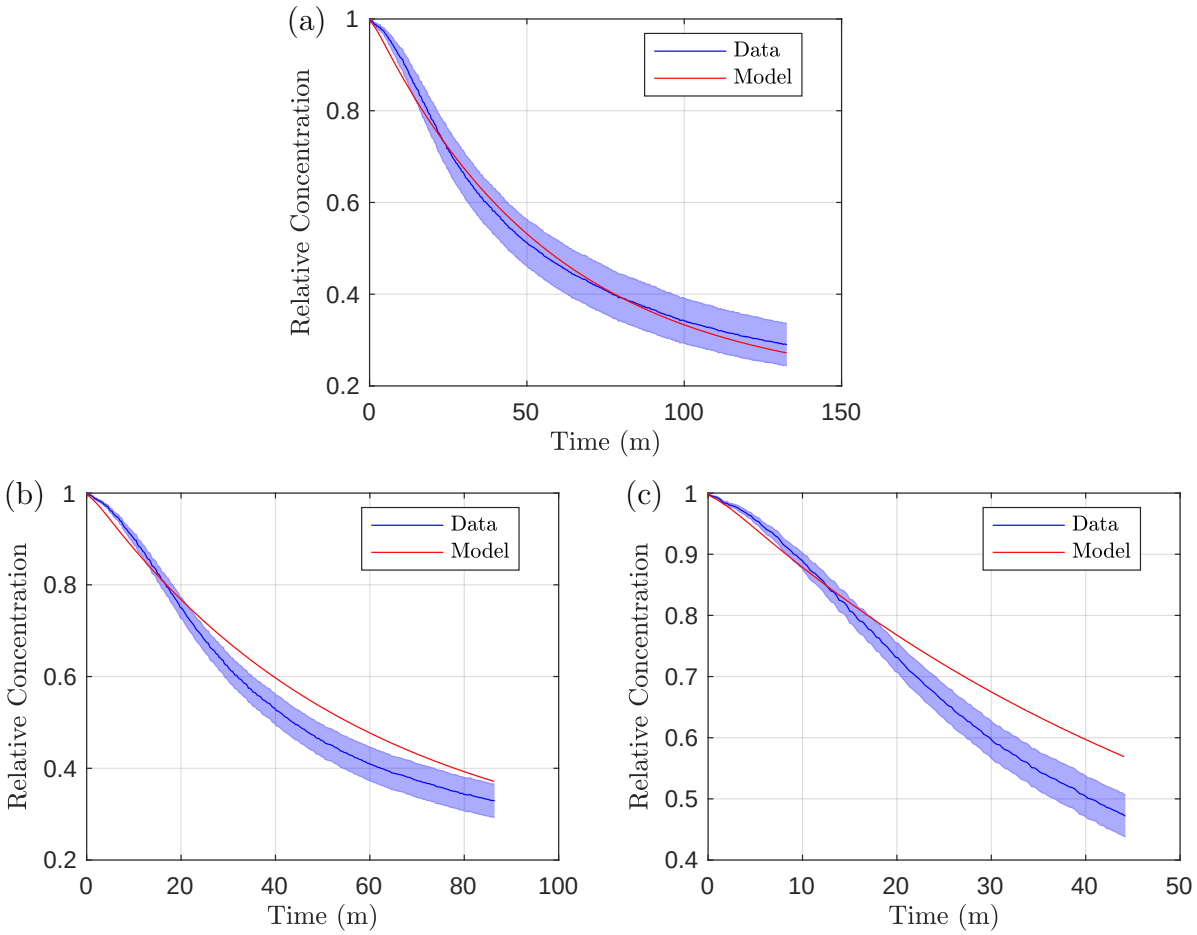

Figure 4.18: Parameter fitting results of the model with a no flux outer boundary condition to the AEST knockout data. In (a) we show the fit to the assays that reach long time, (b) the assays that reach medium time and (c) all assays in the short time.

Individual efflux knockouts

For the individual efflux knockouts, we again follow the method used in Section 4.7.1. By fixing our parameters gained from the AEST knockout case, we are able to find the efflux parameters for our individual efflux knockout strains. We plot these fits in Figure 4.19 and the corresponding parameters are:

$$[X_{EST}, X_{AST}, X_{AET}, X_{AES}] = [6.54 \times 10^{-3}, 4.94 \times 10^{-2}, 4.10 \times 10^{-2}\, 4.07 \times 10^{-2}], \quad (4.58)$$

given to 3 significant figures and a combined objective function of 1.56×10^{-2}. We note that the combined objective function is immediately improved compared to the zero far field boundary model. Our fit for the A knockout model in (a) still undershoots the data in the long term, however it is closer to reaching a steady state than the previous model. Again we note that the early dynamics are missing in the short and medium time. The fits for the E, S and T knockouts (d)-(f) are also improved compared to section 4.7.1, with the model approaching a steady state that fits within the standard error of the data.

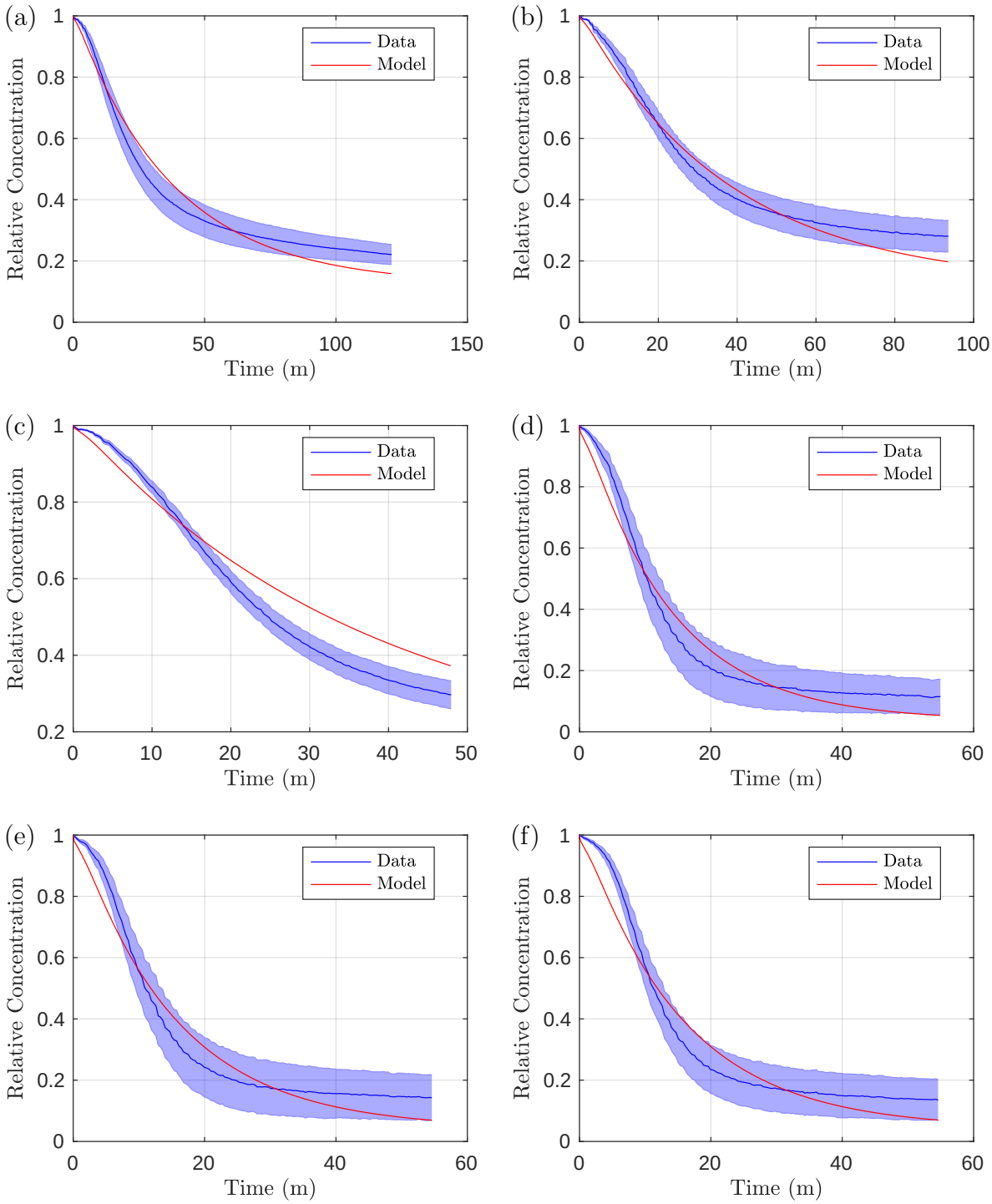

Figure 4.19: Parameter fitting results of the model with a no flux outer boundary condition to the individual knockout strains having fixed our AEST parameters (4.57). We exhibit the A knockout strain in (a) long time, (b) medium time and (c) short time. The rest of the strains are exhibited as such (d) E knockout, (e) S knockout and (f) T knockout.

Wild-type strain

By following the method in Section 4.7.1, we are able to estimate the efflux parameters for each of the individual efflux pumps. We plot our estimated wild-type efflux in Figure 4.20, with the following corresponding parameters

$$[X_A, X_E, X_S, X_T, X_{AEST}] = [3.94\times10^{-2}, -3.54\times10^{-3}, 4.90\times10^{-3}, 5.18\times10^{-3}, 4.59\times10^{-2}], \tag{4.59}$$

given to three significant figures. We note that the estimated wild-type parameter (X_{AEST}) causes the model to undershoot the data, however the model does approach a steady state as the experimental data suggests. Again early dynamics are missing as there is no delay in concentration decreasing and past this delay the decrease in concentration is not fast enough to encapsulate the behaviour shown by the data. In addition, as for the individual efflux values, our parameter for efflux by AcrEF (X_E) is again negative. This again leads us to believe that for our current model the individual efflux parameters are not additive and may differ from strain to strain. Since our estimated efflux parameter again does not provide a realistic fit, we run a parameter fit for the wild-type efflux parameter in Figure 4.21 with the corresponding parameter:

$$[X_{AEST}] = [3.57 \times 10^{-2}], \tag{4.60}$$

given to three significant figures and an objective function of 3.48×10^{-3}. This parameter is similar to our estimated wild-type efflux parameter and the resulting model has similar dynamics. Whilst in the long time the model reaches a steady state, the early dynamics exhibited by the data are still missing.

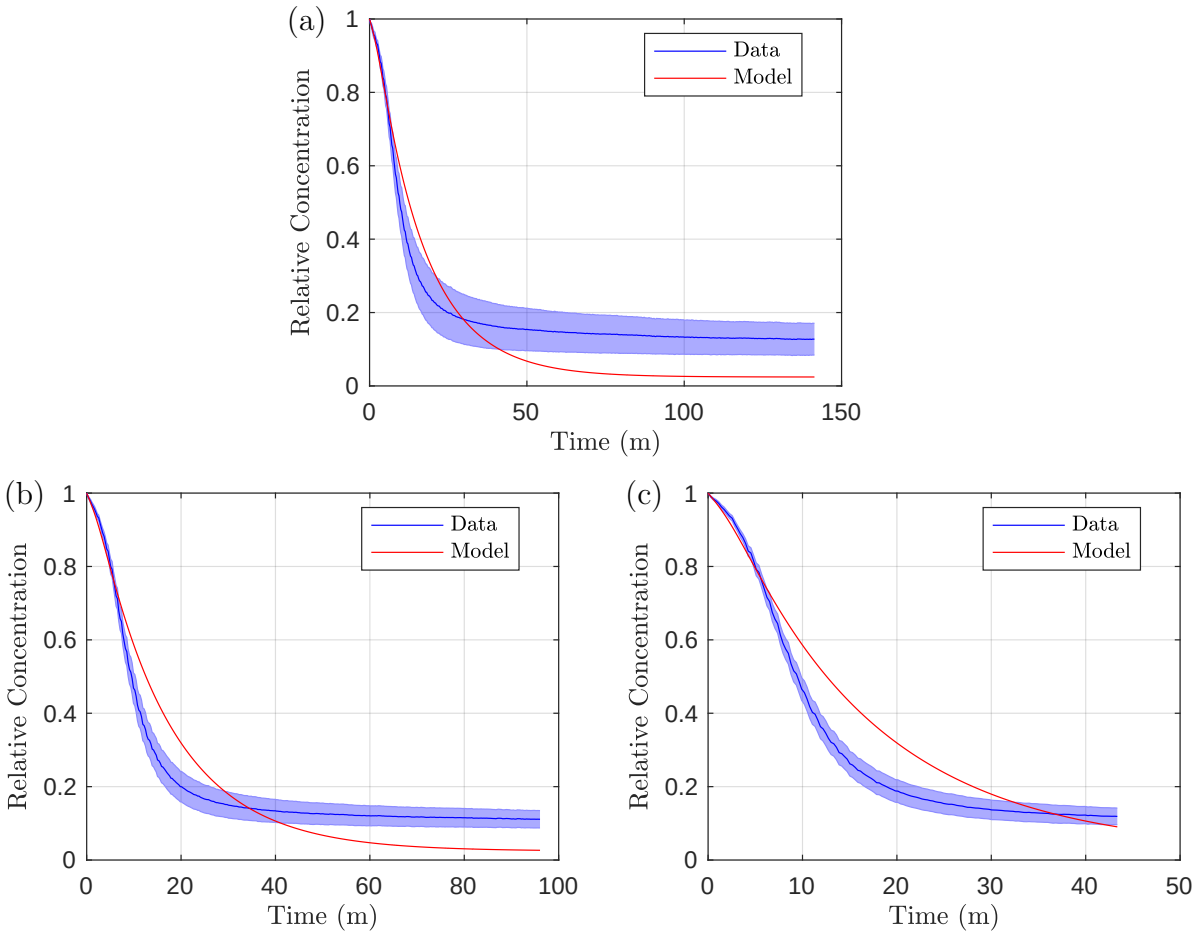

Figure 4.20: Comparing our estimated wild-type efflux constant (4.59) in our model with a no flux outer boundary condition to the wild-type data with fixed AEST parameters (4.57). In (a) we show the fit to the assays that reach long time, (b) the assays that reach medium time and (c) all assays in the short time.

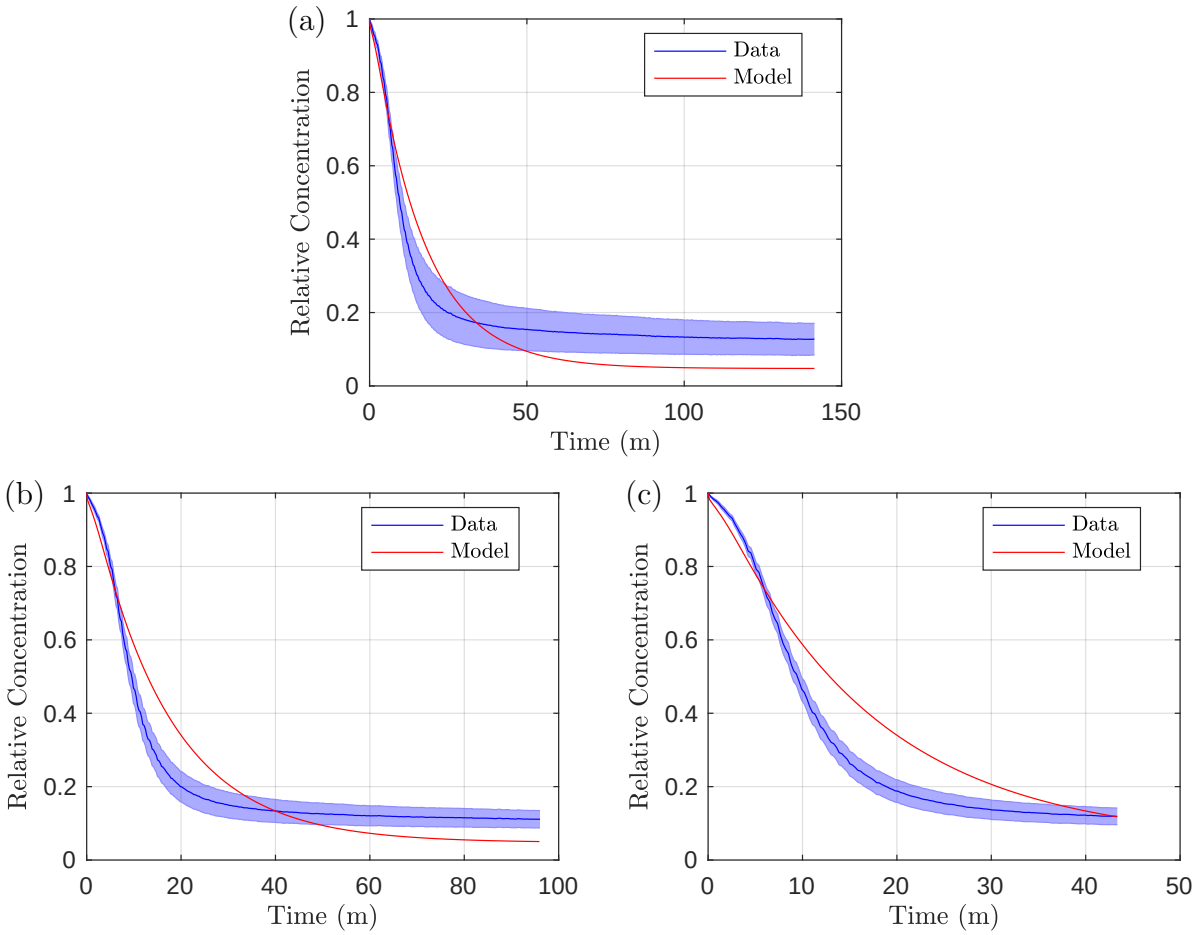

Figure 4.21: Parameter fitting results of the model with a no flux outer boundary condition to the wild-type data using using (4.57) having fixed our AEST parameters (4.57). In (a) we show the fit to the assays that reach long time, (b) the assays that reach medium time and (c) all assays in the short time.

4.8 Discussion

We have formulated a spatial model that encapsulates the behaviour of substrate concentration of a single cell, demonstrating the physical effects of efflux pump activity upon substrate concentration. By making assumptions on the far field boundary conditions for this model, we have created a single cell model that can potentially encapsulate the behaviour of a *Salmonella* culture.

By using finite difference methods, we have discretised our domain and produced numerical solutions for our model. These simulations have presented insights into the

behaviour of the mass transfer coefficients, showing clear differences between the coefficient related to efflux and the coefficient related to permeability. By producing likewise simulations for the model with differing outer boundary conditions (zero far field and no flux), we have been able to show the effects these give to our model. With the zero far field boundary condition, we see the intracellular concentration more likely to fully deplete. In the long term, the model with this boundary condition would achieve a steady state of fully depleted concentration in all space, unless we have no transfer of substrate through the membrane. This would physically represent a *Salmonella* population that has plentiful extracellular space, such that once substrate is expelled from the cells it disperses and does not diffuse back into the population. With the no flux condition, the system may reach a non zero steady state. Since there is no depletion at the far field, at long time both intracellular and extracellular concentrations will reach steady state. This represents physically a *Salmonella* population that has limited extracellular space, such that we see diffusion of expelled substrate back into the cell.

We have implemented parameter fitting techniques for the efflux model to experimental data consisting of various different strains with different efflux pumps active. By varying the extracellular boundary condition, we have been able to fit two versions of the model to the data. Whilst the zero far field boundary model provided a reasonable fit to the AEST knockout data, the flaws in the model were realised upon adding efflux. Not only were efflux dynamics missing upon early time, upon long time the model concentration would keep on decreasing when the data suggests an approach to a steady state. In regards to the no flux boundary model, we saw better fits across all strains, shown by the objective functions of each of the fits. Whilst again, short time dynamics were missing upon our fits, the long time fits were improved in all strains. The model in all fits appeared to reach or be approaching a steady state at long time. Whilst the fits would give a reasonable approximation to modelling the experimental data, it is clear that our model needs adaptation to encapsulate the data better and primarily the short and medium time dynamics. In the next chapter, we will attempt to adapt our existing model to greater

encapsulate the dynamics of the data.

CHAPTER 5

SPATIAL MODEL IMPROVEMENTS

5.1 Motivation

In the previous chapter we have modelled our efflux data via a single cell model, including variations upon the model's extracellular boundary condition. However, when attempting to fit the model to data, flaws were exhibited. Early time and medium time dynamics in particular did not correspond with the data. It is clear that our current model is oversimplified and needs adaptation.

As stated in the previous model, ethidium bromide is a DNA-intercalating agent that fluoresces when it is bound to DNA. Due to this fluorescing, the concentration of ethidium bromide within a culture can be approximated. However in our previous model, we have made assumptions that the fluorescence is directly proportional to the concentration of ethidium bromide. In reality, we will have two states of ethidium bromide; bound ethidium bromide that is fluorescing and unbound ethidium bromide that is not fluorescing. In addition, as we know from our gene regulatory model the expression of efflux pump genes is not constant. In our previous model, we have taken efflux to be constant and to be fully expressed from the start of the assay, when in reality this may not be the case. This may be a reason for the disparity in results for strains that included efflux. By considering these aspects we adapt our previous model with the hope of finding a better fit to our data.

5.2 Bound ethidium bromide model formulation

We formulate our model in a manner similar to the previous model by again assuming that each cell acts identically. We also assume that the concentration of ethidium bromide is evenly distributed in the population such that every cell has an identical initial concentration of ethidium bromide. We assume this distributed concentration of ethidium bromide is independent to each cell, meaning that if the substrate has been expelled into the extracellular space, it can only diffuse back into the original cell. In this model however we consider ethidium bromide in two states. The first state is ethidium bromide that fluoresces because it is bound to DNA, we will further refer to this state as bound ethidium bromide. In this state the ethidium bromide cannot pass through the cell membrane via efflux or diffusion. The second state is ethidium bromide that is not bound to DNA. We will further refer to this state as unbound ethidium bromide. In this state, ethidium bromide does not fluoresce but can move freely through the cell membrane via efflux or diffusion. Since one state is bound, we assume that the two states will diffuse at different rates and hence apply a different diffusion coefficient for each state. Again similar to the previous model, we do not know the correlation between fluorescence of ethidium bromide and the concentration of bound ethidium bromide within the culture, we thus assume a directly proportional relation between the two.

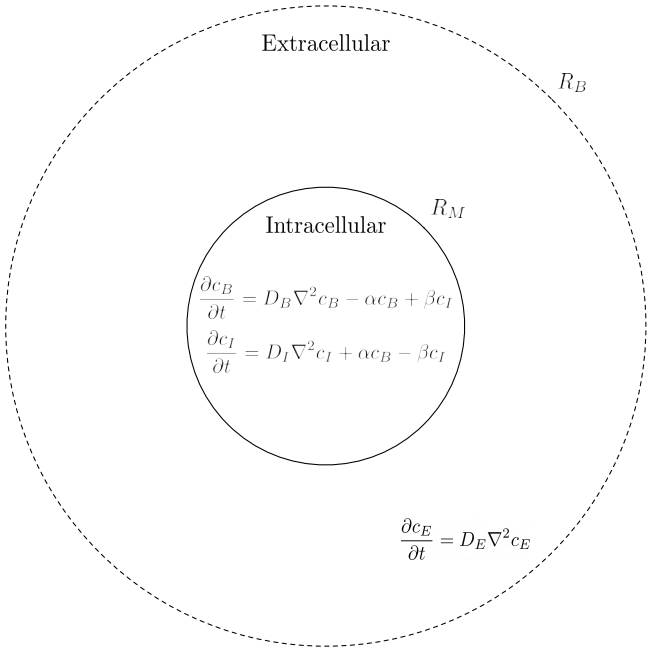

Figure 5.1: A schematic of the bound ethidium bromide model. The solid line represents our cell membrane at radius R_M, whereas the dashed line represents our outer boundary at radius R_B. We have placed our equations where they apply in the intracellular and extracellular space.

We exhibit a schematic of our model in Figure 5.1. Again, we use spherical coordinates to model an axisymmetric spherical cell with radius R_M surrounded by extracellular space with an outer boundary of radius R_B. At the cell radius, we have a thin permeable membrane which contains all of our efflux pump systems that expel unbound substrate from the intracellular to the extracellular space. The equations for this model are as follows

$$\frac{\partial c_B}{\partial t} = D_B \nabla^2 c_B - \alpha c_B + \beta c_I, \tag{5.1}$$

$$\frac{\partial c_I}{\partial t} = D_I \nabla^2 c_I + \alpha c_B - \beta c_I, \tag{5.2}$$

$$\frac{\partial c_E}{\partial t} = D_E \nabla^2 c_E. \tag{5.3}$$

Here c_B denotes the bound concentration of substrate, c_I denotes the intracellular unbound concentration of substrate and c_E denotes the extracellular unbound concentration of substrate. The intracellular ethidium bromide undergoes DNA binding at rate β and

unbinding at rate α. We assume that there is always a sufficient concentration of DNA that is well mixed throughout the cell such that ethidium bromide is able to bind at all times.

5.2.1 Boundary Conditions

The first boundary conditions are

$$D_B \frac{\partial c_B}{\partial r}\bigg|_{r=0} = 0, \qquad D_I \frac{\partial c_I}{\partial r}\bigg|_{r=0} = 0, \tag{5.4}$$

$$-D_I \frac{\partial c_I}{\partial r}\bigg|_{r=R_M} = -D_E \frac{\partial c_E}{\partial r}\bigg|_{r=R_M} = (P+X)c_I(R_M,t) - Pc_E(R_M,t), \tag{5.5}$$

$$D_B \frac{\partial c_B}{\partial r}\bigg|_{r=R_M} = 0. \tag{5.6}$$

Similar to the previous model, we assume axisymmetry of the cell, resulting in two boundary conditions at the cell centre for both bound and unbound ethidium bromide concentrations. We also uphold flux continuity between the intracellular and extracellular space for the unbound substrate. The bound ethidium bromide however, cannot pass through the membrane via either efflux or diffusion, thus we introduce the no flux boundary condition (5.6).

In addition to the above boundary conditions, we have the outer boundary condition. After analysing parameter fitting results from the previous model we discount the zero far field boundary condition. Thus we assume that the extracellular space is limited, such that substrate expelled out of the cell will always be within range to diffuse back in. Here we set the outer boundary to be a closer boundary with no flux,

$$D_E \frac{\partial c_E}{\partial r}\bigg|_{r=R_B} = 0. \tag{5.7}$$

5.2.2 Initial Conditions

As with the previous model, we assume that there is no substrate in the extracellular space. In regards to the intracellular space, we do not know the ratio of unbound to bound substrate, thus we introduce the parameter γ into our initial conditions that will define the ratio of unbound to bound substrate. The initial conditions for each concentration are as follows

$$c_B(r,0) = C_{B0}, \qquad c_I(r,0) = \gamma\, C_{B0}, \qquad c_E(r,0) = 0, \tag{5.8}$$

where C_{B0} is the initial concentration of bound substrate.

5.2.3 Variable Efflux

In our previous model, we chose our rate of efflux to be constant. In reality we know that the rate of efflux is not likely to be constant as expression of the proteins that constitute the efflux pumps can vary. We model efflux as a simple efflux pump formation model with the following equation and initial condition

$$\frac{dX}{dt} = \phi - \delta X, \qquad X(0) = X_0, \tag{5.9}$$

where ϕ is our efflux pump formation rate, δ is our efflux pump degradation rate and X_0 is a constant determining the initial rate of efflux. In addition, the formation of efflux could be dependent upon the antibiotic concentration within the cell, we could model this as

$$\frac{dX}{dt} = \phi_I\, I - \delta X, \qquad X(0) = X_0, \qquad I(t) = \frac{1}{R_M}\int_0^{R_M} c_B(r,t)dr, \tag{5.10}$$

where ϕ_I is the efflux pump formation rate dependent on substrate concentration and I is the averaged intracellular concentration of substrate. We will consider both cases of

efflux in our simulations, hoping to give us further insights into the dynamics of efflux over the course of the experiments.

5.3 Numerical Method

We follow a similar method for discretisation as used on the previous model in Section 4.4. In the interests of brevity, we omit most trivial steps, only exhibiting the main differences in the FTCS numerical method. By introducing the notation:

$$\theta_B = \frac{D_B \Delta t}{\Delta r^2}, \qquad \theta_I = \frac{D_I \Delta t}{\Delta r^2}, \qquad \theta_E = \frac{D_E \Delta t}{\Delta r^2}, \tag{5.11}$$

the model discretisation in this case simplifies to:

$$c_{B,i}^{n+1} = \theta_B \left(1 + \frac{\Delta r}{r_i}\right) c_{B,i+1}^n + (1 - 2\theta_B - \alpha\Delta t)\, c_{B,i}^n + \theta_B \left(1 - \frac{\Delta r}{r_i}\right) c_{B,i-1}^n + \beta \Delta t c_{I,i}^n, \tag{5.12}$$

$$c_{I,i}^{n+1} = \theta_I \left(1 + \frac{\Delta r}{r_i}\right) c_{I,i+1}^n + (1 - 2\theta_I - \beta\Delta t)\, c_{I,i}^n + \theta_I \left(1 - \frac{\Delta r}{r_i}\right) c_{I,i-1}^n + \alpha \Delta t c_{B,i}^n, \tag{5.13}$$

$$c_{E,i}^{n+1} = \theta_E \left(1 + \frac{\Delta r}{r_i}\right) c_{E,i+1}^n + (1 - 2\theta_E)\, c_{E,i}^n + \theta_E \left(1 - \frac{\Delta r}{r_i}\right) c_{E,i-1}^n. \tag{5.14}$$

In regards to our boundary conditions, we omit our conditions due to following similar discretisation to the boundary conditions in Section 4.4. By collating our approximations our full finite difference method to approximate our model is represented in equation (5.15). We implement this method in MATLAB to produce various different simulations of our model. Unless otherwise stated we set our spatial step $\Delta r = 0.1$ with $R_M = 2\mu m$. Again, in order to maintain stability of our finite difference method we set $\Delta t = \dfrac{\Delta r^2}{4D_{MAX}}$, where $D_{MAX} = \max(D_I, D_E, D_B)$.

$$
c_{B,i}^{n+1} = \begin{cases} (1-6\theta_B-\alpha\Delta t)c_{B,i}^n + 6\theta_B c_{B,i+1}^n + \beta\Delta t c_{I,i}^n, & i=0, \\ \theta_B\left(1+\dfrac{\Delta r}{r_i}\right)c_{B,i+1}^n + (1-2\theta_B-\alpha\Delta t)\,c_{B,i}^n + \theta_B\left(1-\dfrac{\Delta r}{r_i}\right)c_{B,i-1}^n + \beta\Delta t c_{I,i}^n, & i=1,...,M-1, \\ (1-2\theta_B-\alpha\Delta t)c_{B,i}^n + 2\theta_B c_{B,i-1}^n + \beta\Delta t c_{I,i}^n, & i=M, \end{cases}
$$

$$
c_{I,i}^{n+1} = \begin{cases} (1-6\theta_I-\beta\Delta t)c_{I,i}^n + 6\theta_I c_{I,i+1}^n + \alpha\Delta t c_{B,i}^n, & i=0, \\ \theta_I\left(1+\dfrac{\Delta r}{r_i}\right)c_{I,i+1}^n + (1-2\theta_I-\beta\Delta t)\,c_{I,i}^n + \theta_I\left(1-\dfrac{\Delta r}{r_i}\right)c_{I,i-1}^n + \alpha\Delta t c_{B,i}^n, & i=1,...,M-1, \\ \theta_I\,\lambda_I\left(1+\dfrac{\Delta r}{r_i}\right)c_{E,i}^n + \left(1-2\,\theta_I-\eta_I\,\theta_I-\dfrac{\eta_I\,\theta_I\,\Delta r}{r_i}, -\beta\Delta t\right)c_{I,i}^n + 2\,\theta_I\,c_{I,i-1}^n + \alpha\Delta t c_{B,i}^n, & i=M, \end{cases}
$$

$$
c_{E,i}^{n+1} = \begin{cases} \theta_E\,\eta_E\left(1+\dfrac{\Delta r}{r_i}\right)c_{I,i}^n + \left(1-2\,\theta_E-\lambda_E\,\theta_E-\dfrac{\lambda_E\,\theta_E\,\Delta r}{r_i}\right)c_{E,i}^n + 2\,\theta_E\,c_{E,i+1}^n, & i=M, \\ \theta_E\left(1+\dfrac{\Delta r}{r_i}\right)c_{E,i+1}^n + (1-2\theta_E)\,c_{E,i}^n + \theta_E\left(1-\dfrac{\Delta r}{r_i}\right)c_{E,i-1}^n, & i=M+1,...,R-1, \\ (1-2\theta_E)c_{E,i}^n + 2\theta_E c_{E,i-1}^n, & i=R. \end{cases} \tag{5.15}
$$

5.3.1 Numerical Simulations

For the following simulations, we choose our cell radius to be $2\mu m$, with a far field boundary at $4\mu m$. We set the diffusivity of unbound ethidium bromide to be equal at $D_I, D_E = 1\mu m^2 \min^{-1}$, whilst we set the bound ethidium bromide to have diffusivity of $D_B = 0.1\mu m^2 \min^{-1}$. Finally, we set the initial intracellular concentrations of bound and unbound ethidium bromide to be equal at $1 \,\mathrm{mol}\, /m^3$. We exhibit various simulations of our bound ethidium bromide model, exhibiting various features of the model's dynamics in Figures 5.2-5.4. In these simulations, we vary membrane permeability, efflux rate and finally the binding and unbinding rates of the intracellular ethidium bromide.

In Figure 5.2 (a), we see the results of an impermeable membrane with no efflux and equal binding and unbinding coefficients. We see no transfer of substrate from the intracellular space, with a uniform distribution of both concentrations throughout for all time due to equal rates of binding and unbinding. In (b), we maintain an impermeable membrane, however here the unbinding rate dominates the binding rate. We see the bound substrate concentration decrease over time and unbound substrate concentration increase until both concentrations reach a steady state.

In Figure 5.3 (a), we maintain an impermeable membrane, however here the binding rate dominates the unbinding rate. We see the opposite to the previous simulations, with the bound substrate concentration increasing until reaching steady state. In (b), we set the binding and unbinding rates to be equal but introduce a permeable membrane. We can see here that the unbound substrate concentration quickly disperses into the extracellular space until a steady state is reach between the unbound and bound substrate concentrations. We note that on very early time the bound substrate concentration has a delay upon unbinding, with the bound substrate concentration only reaching a maximum unbinding rate when the unbound intracellular concentration has decreased and reached steady state. When the unbound substrate concentration has reached its lowest point, we see the greatest decrease of bound substrate concentration, due to there being the minimal intracellular unbound substrate concentration available to form bound sub-

strate concentration. Finally at long time both concentrations reach a steady state as the unbound substrate concentration has fully dispersed and unbound and bound substrate concentrations have reached an equilibrium point.

In Figure 5.4 (a), we introduce efflux to the permeable membrane. We note that the simulation is similar to Figure 5.3 (b), however with the efflux rate only expelling unbound substrate concentration from the intracellular to extracellular space, the intracellular and extracellular concentrations reach different steady states at long time. Due to introducing efflux the unbound intracellular substrate concentration reaches a steady state lower than achieved via diffusion through the membrane alone (i.e. Figure 5.3 (b)). This has a resulting effect on the bound substrate concentration as we reach a lower concentration and equilibrium point between both concentrations at long time. Finally in (b), we maintain our efflux values but exhibit a case of the unbinding rate dominating the binding rate. Again, we have similar dynamics to the previous simulation, however instead of the intracellular and extracellular concentrations reaching an equilibrium at the same steady state concentration, we see the bound substrate concentration continuing to unbind and almost fully depleting at long time.

We can compare the dynamics of these simulations to the previous single cell model (with no flux outer boundary condition) simulations in Section 4.4.1 by comparing the intracellular bound concentration of substrate in this model against the concentration of intracellular substrate of the single cell model. By comparing the cases with active efflux (Figure 5.4 against Figure 4.4 (c) and (d)), it is notable that the long term dynamics are very similar, with the concentration of substrate appearing to reach a steady state in both models. However, the main differences are noted upon the early and mid time dynamics, with the bound ethidium bromide model having a delay in decrease of substrate concentration during early dynamics. A maximum decrease of substrate concentration is then reached which then slows upon mid time. This is promising as our parameter fitting results with the previous model showed that the long term dynamics matched, however the model was not able to replicate the early and mid time dynamics of the data.

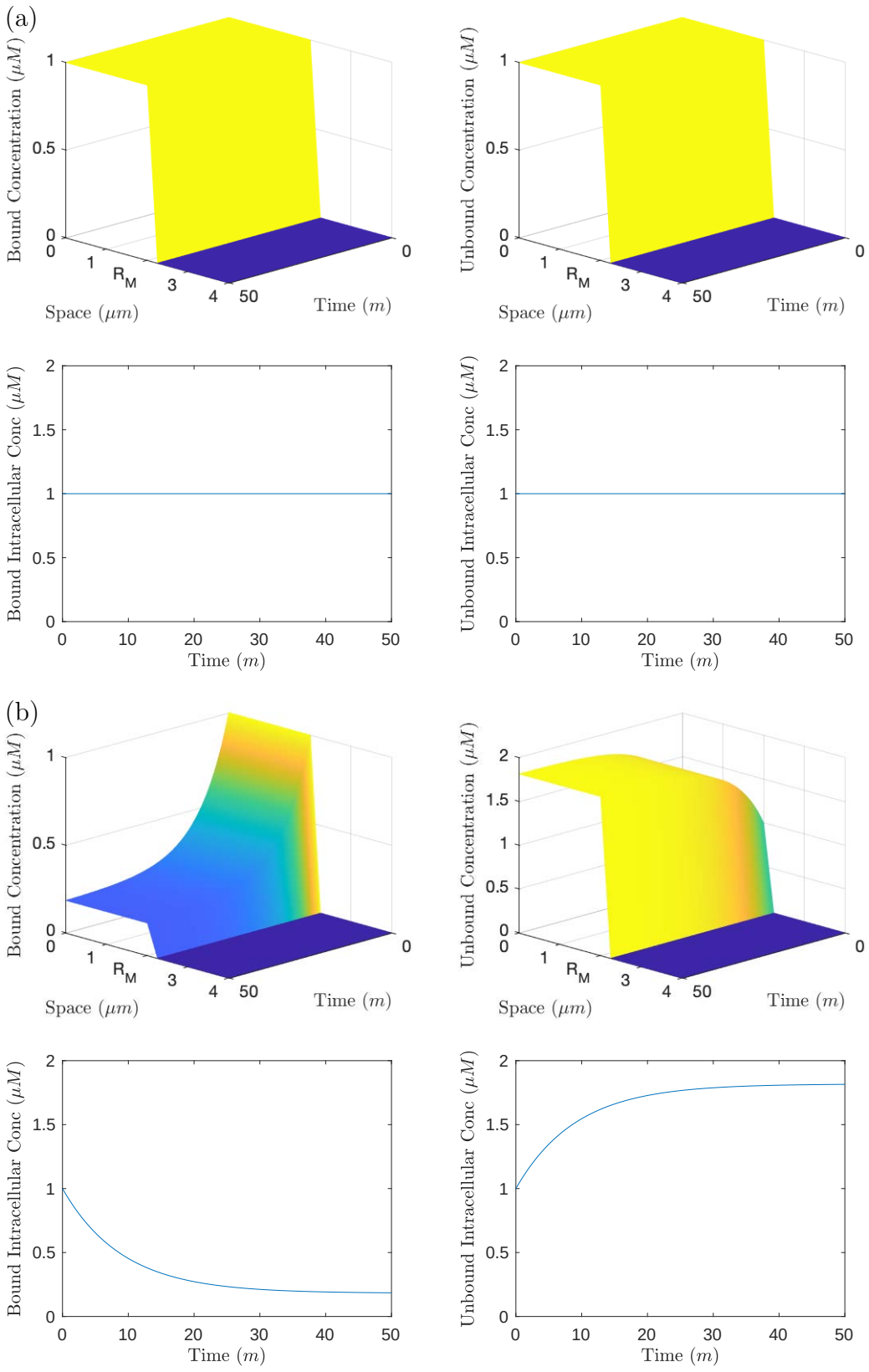

Figure 5.2: Simulations of the bound ethidium bromide model with a no flux far field outer boundary condition and $R_M = 2\mu m$. We exhibit bound and unbound distribution profiles, with averaged intracellular concentrations below. We vary permeability, efflux, unbinding and binding rates. In (a) we have $P, X = 0$ and $\alpha, \beta = 0.1$. In (b) we have $P, X = 0$ and $\alpha = 0.1$, $\beta = 0.01$.

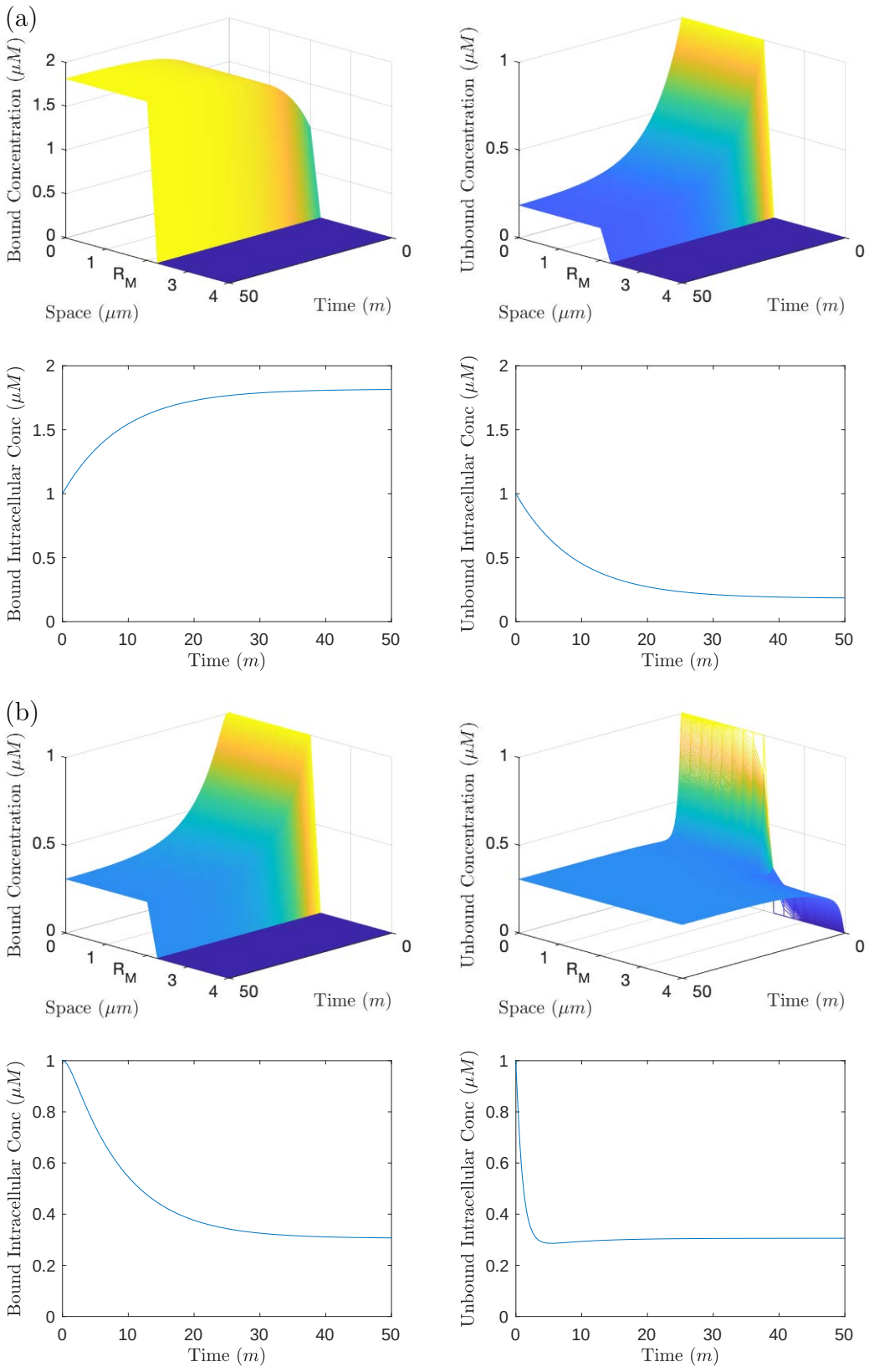

Figure 5.3: Further simulations of the bound ethidium bromide model with a no flux far field outer boundary condition and $R_M = 2\mu m$. In simulation (a) we have $P, X = 0$ and $\alpha = 0.01$, $\beta = 0.1$. In simulation (b) we have $P = 1, X = 0$ and α, $\beta = 0.1$.

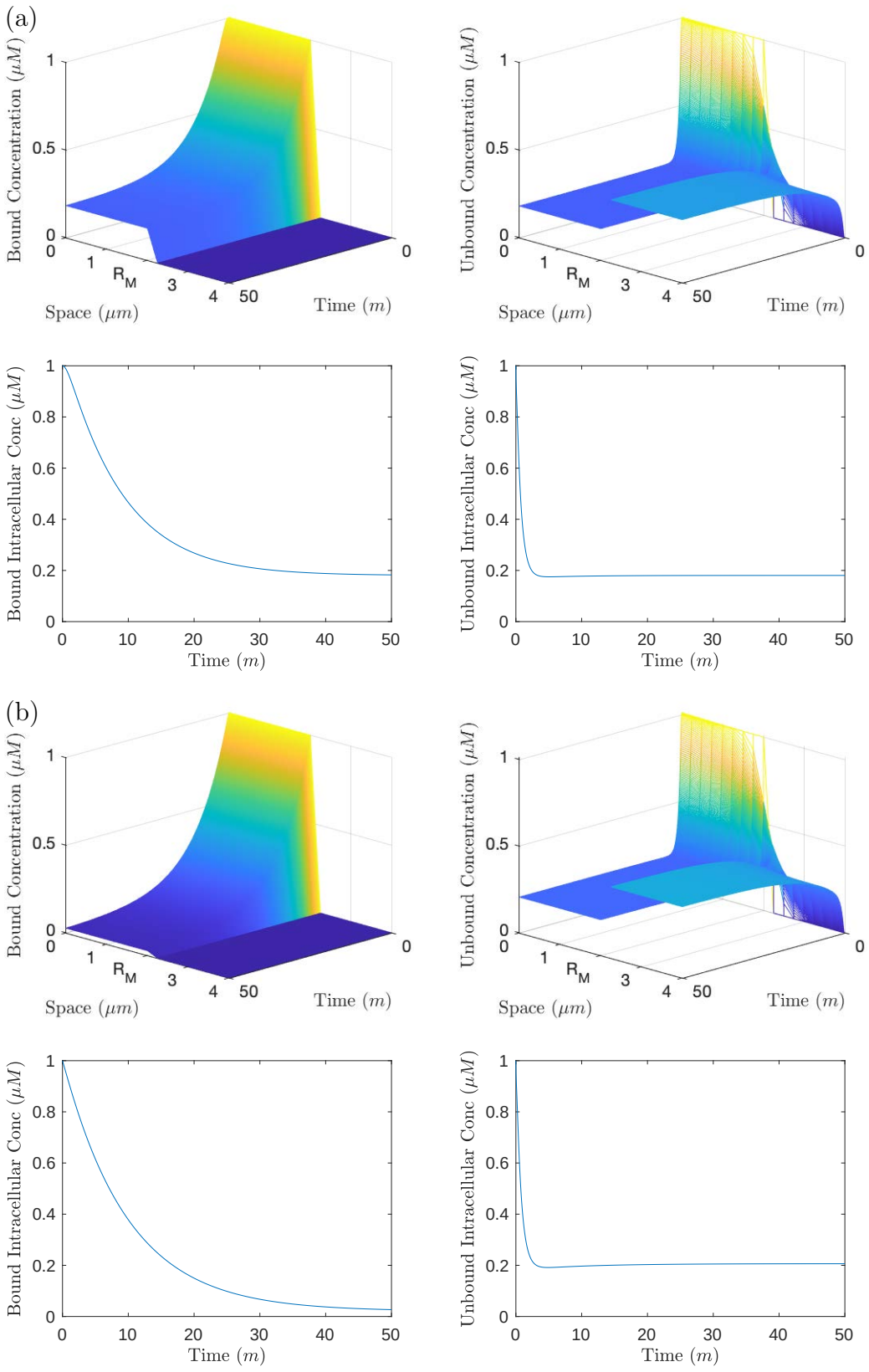

Figure 5.4: Final set of simulations of the bound ethidium bromide model with a no flux far field outer boundary condition. In simulation (a) we have $P = 1, X = 1$ and α, $\beta = 0.1$. In simulation (b) we have $P = 1, X = 1$ and $\alpha = 0.1$, $\beta = 0.01$.

5.4 Parametrisation Methods

We follow similar methods to our previous parameter fitting exercises in Section 4.6. We again employ the use of the function *fminsearch* in MATLAB with a latin hypercube method of sampling to produce initial parameter guesses, with the only difference being our objective function. Our objective function that we are attempting to minimise for this model using our initial parameter guesses in *fminsearch* is as follows:

$$f = \frac{1}{t_{max}} \int_0^{t_{max}} \mid y(t) - I(t)) \mid dt \tag{5.16}$$

where

$$I(t) = \frac{3}{R_M^3} \int_0^{R_M} r^2 \, c_B(r,t) \, dr.$$

Here y denotes the experimental data, I denotes the averaged intracellular concentration of the bound substrate, R_M denotes the distance from the cell centre to the cell membrane and t_{max} is the maximum time for the simulations. Again, we note that our data values are measured in relative fluorescence and our model in concentration. However, as we have assumed a directly proportional relationship between the fluorescence and intracellular bound concentration of substrate, we choose to model in terms of relative concentration so we can directly fit the model to the data. We list all parameters used in this model, noting the parameters being varied and their respective units in Table 5.1. For simplicity in presentation, we will omit the units of each fitted parameter in our following optimal parameter sets.

5.5 Results

As with our previous parameter fitting methods, we set the cell to have a radius of $2\mu m$. We have taken the step sizing $\Delta r = 0.25$ and $\Delta t = \dfrac{\Delta r^2}{4D_{MAX}}$. For most parameter fitting exercises we have taken 1000 sets of initial parameter guesses, finding the optimal case,

Parameter	Description	Value	Units
R_M	Membrane Radius	2	μm
R_B	Outer Boundary Radius	Not Set	μm
P	Permeability Mass Transfer Coefficient	Not Set	$\mu m\, min^{-1}$
X_{AEST}	Efflux Conversion Constant For Wild-type Case	Not Set	$\mu m\, min^{-1}$
X_{EST}	Efflux Conversion Constant For A Knockout Case	Not Set	$\mu m\, min^{-1}$
X_{AST}	Efflux Conversion Constant For E Knockout Case	Not Set	$\mu m\, min^{-1}$
X_{AST}	Efflux Conversion Constant For S Knockout Case	Not Set	$\mu m\, min^{-1}$
X_{AES}	Efflux Conversion Constant For T Knockout Case	Not Set	$\mu m\, min^{-1}$
X_{ST}	Efflux Conversion Constant For AE Knockout Case	Not Set	$\mu m\, min^{-1}$
D_B	Diffusion Coefficient Of Bound Substrate	0	$\mu m^2\, min^{-1}$
D_I	Diffusion Coefficient Of Unbound Intracellular Substrate	Not Set	$\mu m^2\, min^{-1}$
D_E	Diffusion Coefficient Of Unbound Extracellular Substrate	Not Set	$\mu m^2\, min^{-1}$
α	Unbinding Rate Of Bound Substrate	Not Set	min^{-1}
β	Binding Rate Of Unbound Substrate	Not Set	min^{-1}
γ	Initial Ratio Of Unbound To Bound Substrate Concentrations	Not Set	N/A

Table 5.1: All parameters used in our bound ethidium bromide model and their respective units. If we vary a parameter we will list it as "Not Set" in the "Value" column, otherwise if the parameter is not varied we list its fixed value.

fitting to the long time data only. We withhold the short time and medium time assays for testing of the accuracy of the fit. For simplicity of our parameter fitting exercises, we set our bound ethidium bromide diffusion rate to be zero ($D_B = 0$) reducing the number of parameters in the following fits. This is under the assumption that the bound molecules will be large compared to unbound molecules such that the diffusion will be negligible compared to the unbound state. Initially, we will consider efflux to be constant for all parameter fitting exercises in this section. We do this in order for us to gain more insights firstly into the binding dynamics by drawing comparisons against the single cell model in Chapter 4.

AEST knockout

We follow parameter fitting exercises to the AEST knockout strain with the previous models in Sections 4.7.1 and 4.7.2 by continuing to assume that there is no efflux in this case. We plot the optimal parameter fit in Figure 5.5 which has the following parameters:

$$[R_B, D_I, D_E, P, \alpha, \beta, \gamma] = [4, 5.26, 6.47 \times 10^{-3}, 6.63, 9.15 \times 10^{-2}, 2.38 \times 10^{-2}, 39.4], \quad (5.17)$$

given to three significant figures and resulting in an objective function of 1.23×10^{-4}. We note that in Figure 5.5 (a) the fit is near perfect, with almost all of the model fitting within the standard error of the data. The model differs in very early time, where the bound substrate concentration increases and peaks before decreasing. We can see from (d) and (e) that with a high initial unbound substrate concentration (caused by the fitted ratio γ), that the binding process dominates over unbinding. Over time the unbound substrate concentration diffuses out of the cell into the extracellular space, resulting in a lower intracellular unbound substrate concentration. At this point the unbinding processes dominate as the unbound substrate cannot bind when it is situated in the extracellular space. Finally, as the expulsion of intracellular unbound substrate concentration slows, this means that both intracellular concentrations appear to reach an equilibrium with its unbinding and binding processes. This results in a near steady state of bound substrate concentration at the end of the simulation. Testing the fit including the medium and short time assays in (b) and (c), shows improved results to the previous model in Section 4.7.2. Whilst the model may not fit within the standard error of the data for both medium and short time, the model closely mimics the dynamics of the data.

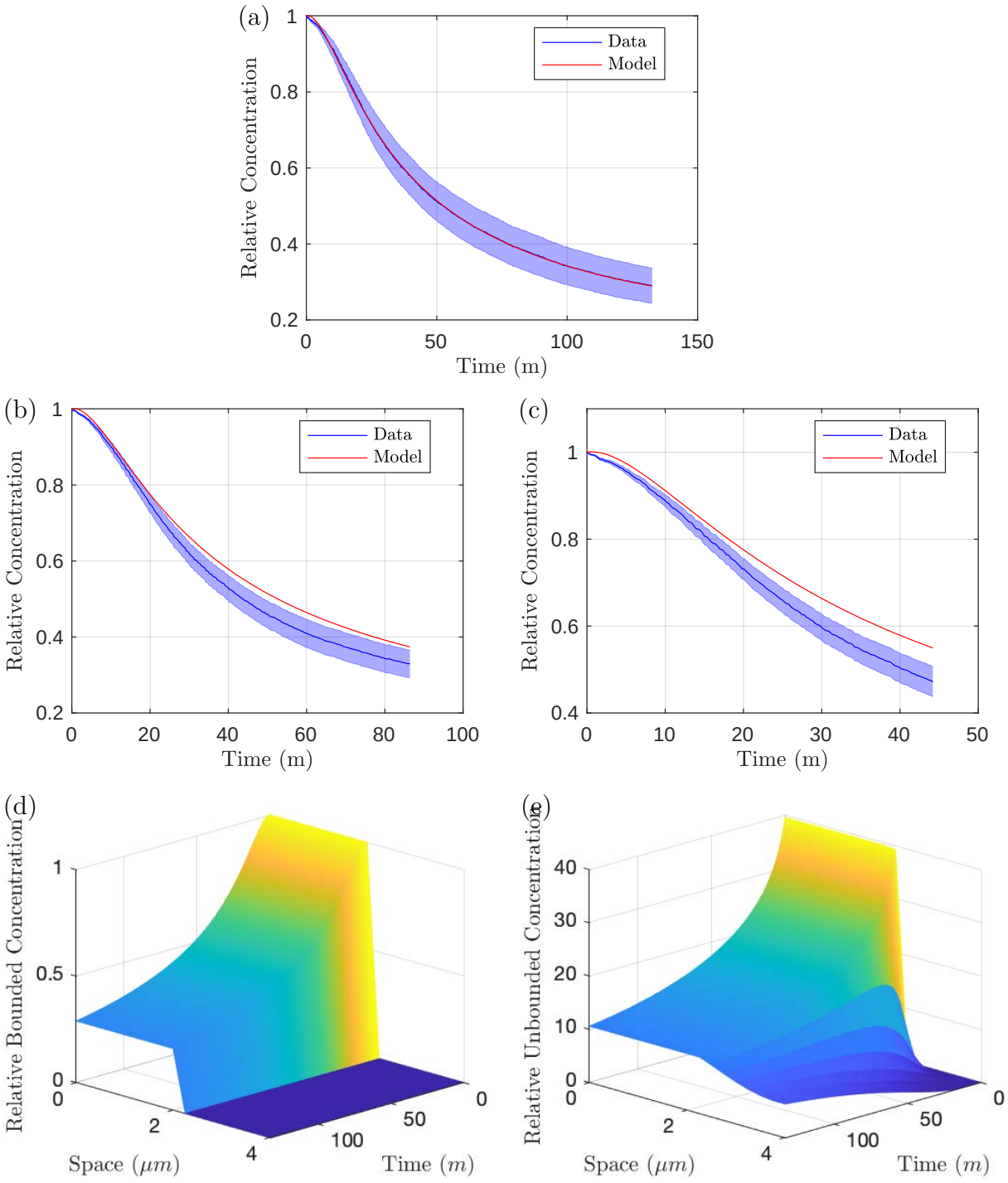

Figure 5.5: Parameter fitting results of the bound ethidium bromide model to the AEST knockout data. In (a) we show the fit to the assays that reach long time, (b) the assays that reach medium time and (c) all assays in the short time. Finally in (d) and (e) we demonstrate the distribution profiles for both concentrations upon fitting to the long time data.

Wild-type strain

Similar to the previous model, we fix our optimal parameters from the AEST knockout case, as we assume these should not vary in each strain. Since our individual knockout cases did not give insight into predicting the wild-type case in Chapter 4, we skip parameter fitting to the individual knockout cases instead immediately providing a parameter fit to the wild-type case. We will instead use our individual knockout cases in later parameter fitting exercises to help ascertain estimates of individual efflux parameters. We plot our optimal fit for the wild-type strain in Figure 5.6, with the corresponding optimal parameter

$$[X_{AEST}] = [37.5], \tag{5.18}$$

given to three significant figures and resulting in an objective function value of 3.65×10^{-3}. We note that although the earlier dynamics are improved, the overall objective function of this fit is larger than the best fit to this wild-type strain of the previous model in Section 4.7.2. As with the AEST knockout case, a high initial unbound substrate concentration causes a delay on early time in the decreasing of bound substrate concentration. The efflux parameter is comparatively much larger than the permeability parameter, however even with this large efflux rate, our bound substrate concentration cannot unbind quickly enough to follow the dynamics of the data. We can see from the distribution profile in (e) the intracellular concentration is expelled extremely rapidly such that there is a large localised concentration in the extracellular space close to the membrane of the cell. The bound intracellular concentration decreases until the bound and unbound intracellular concentrations have reached an equilibrium point. We note that although the model's bound substrate concentration steady state does not fit in the standard error of the data at long term in (a), the model still achieves a steady state. It is clear from this parameter fit that the optimal parameters fixed from the AEST knockout case do not provide realistic dynamics to the wild-type case.

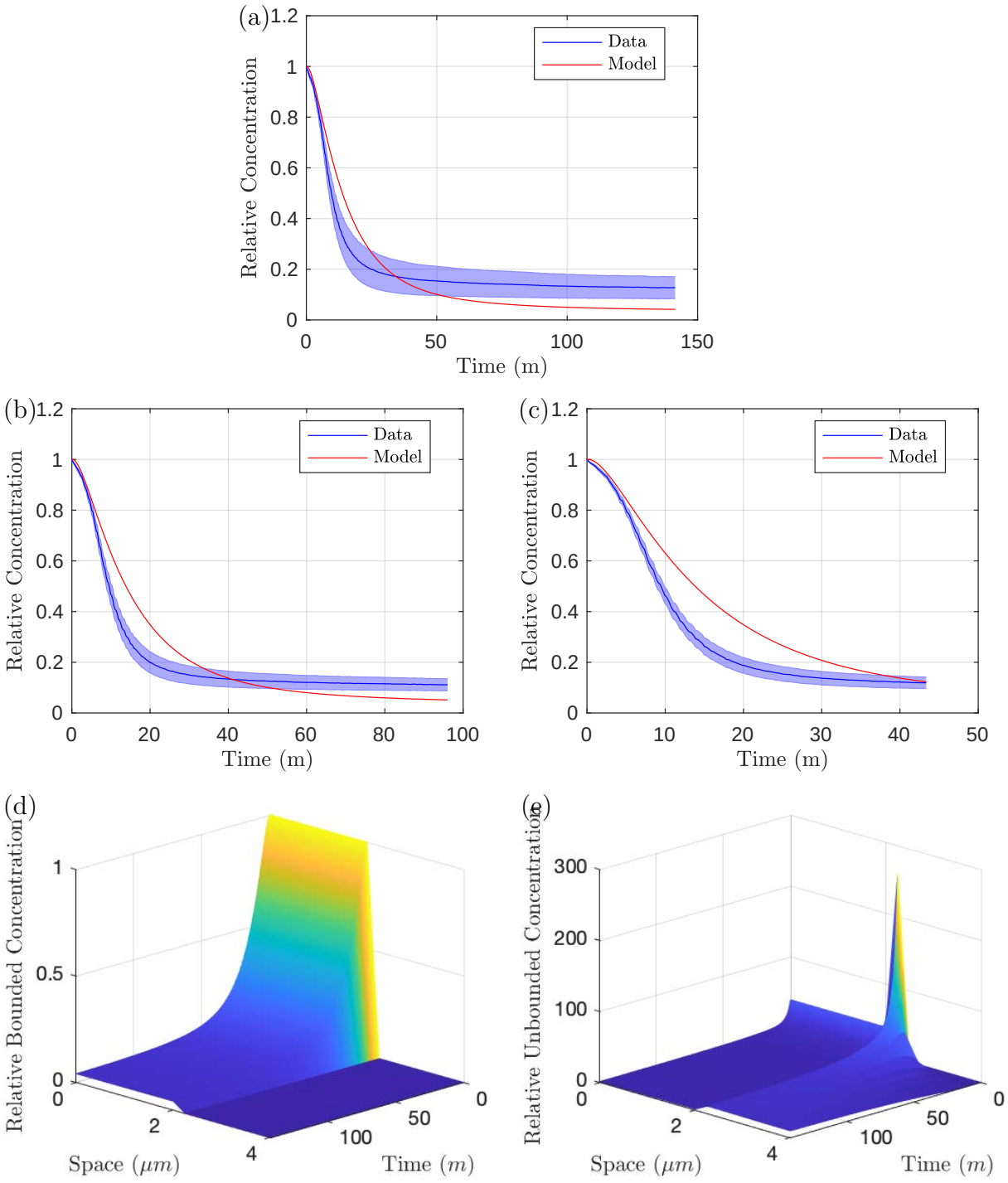

Figure 5.6: Parameter fitting results of the bound ethidium bromide model to the wild-type strain data having fixed our AEST parameters (5.17). In (a) we show the fit to the assays that reach long time, (b) the assays that reach medium time and (c) all assays in the short time. Finally in (d) and (e) we demonstrate the distribution profiles for both concentrations upon fitting to the long time data

AEST knockout and wild-type strain

Since the previous optimal parameters for the AEST knockout case did not provide a base for a realistic fit to the wild-type case, we now produce fits for both cases simultaneously. For this parameter fitting exercise, we minimise the combined sum of the objective functions calculated for each data set. We plot the optimal parameter fits for the AEST knockout in Figure 5.7 and wild-type strain in Figure 5.8 using the following parameters:

$$[R_B, D_I, D_E, P, \alpha, \beta, \gamma, X_{AEST}] = [4, 7.44, 1.65, 2.00 \times 10^{-2}, 1.32, 0.86, 1.75, 5.70 \times 10^{-2}], \tag{5.19}$$

given to three significant figures and resulting in a combined objective function of 2.58×10^{-3}. We can immediately see that the fit to the wild-type case (Figure 5.8) has much improved, with the majority of the model fitting within the standard error of the data in (a). In terms of parameters, the binding and unbinding rates are much faster enabling the bound substrate concentration to unbind and therefore be expelled from the intracellular space at a faster rate. We also have a lower initial concentration of unbound substrate concentration (γ), which in turn results in smaller permeability (P) and efflux activity parameters X_{AEST}. We thus now do not see a spike in the external unbound substrate concentration at early time near the membrane. Whilst the fit for the wild-type case has improved, further shown by comparing to the test data of short time and medium time assays (b) and (c), we have compromised the fit for the AEST knockout (Figure 5.7). In (a)-(c) we now have a large peak upon early time where the intracellular unbound substrate concentration is still at high concentrations such that binding is dominating. We also have reduced similarities in behaviour in the long term as (although the model still fits within the region of standard error for the data) the model looks as though it will hit a steady state much earlier than the data suggests and at a higher concentration.

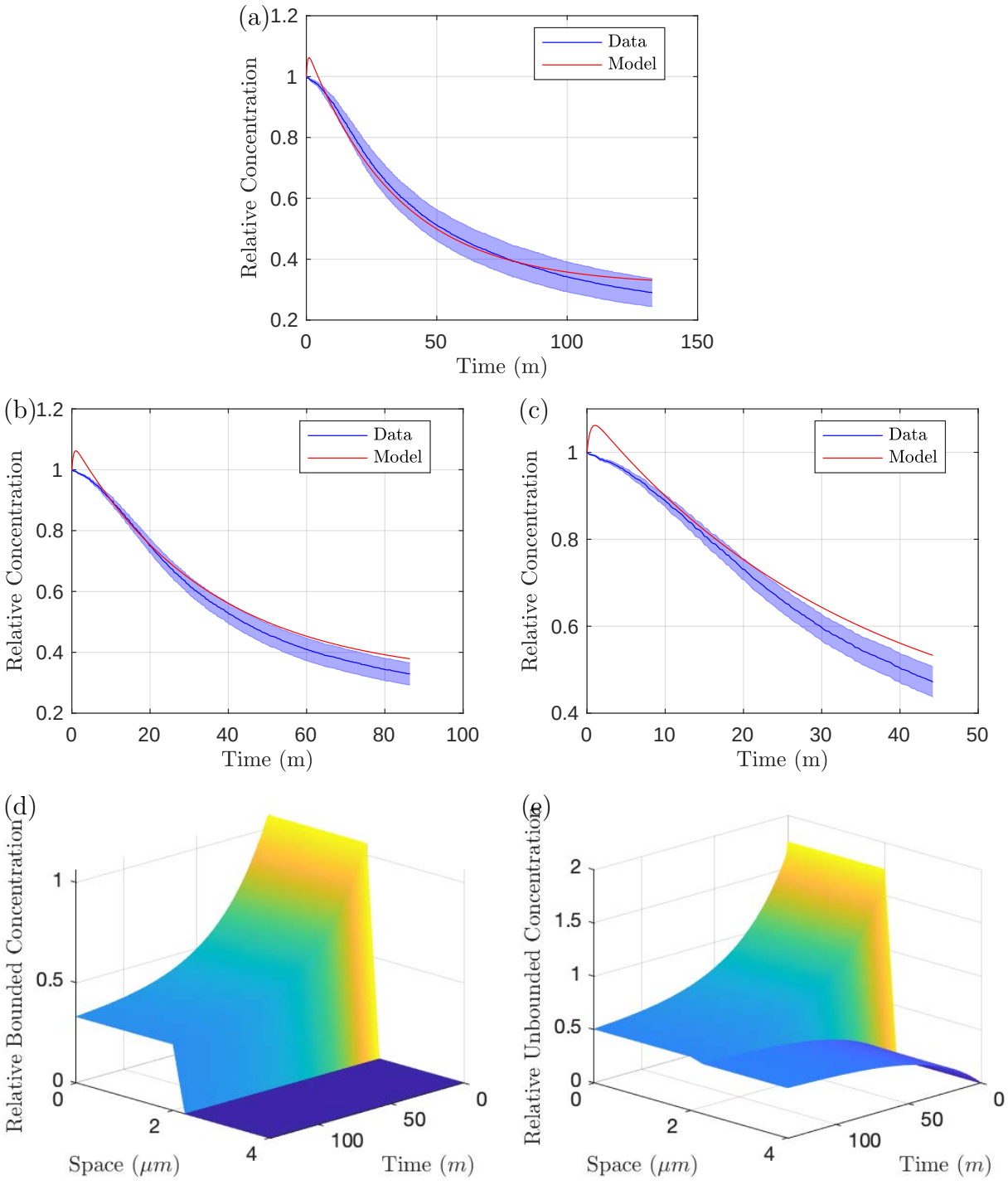

Figure 5.7: Parameter fitting results of the bound ethidium bromide model to both the AEST knockout and wild-type data simultaneously, comparing against the AEST data. In (a) we show the fit to the assays that reach long time, (b) the assays that reach medium time and (c) all assays in the short time. Finally in (d) and (e) we demonstrate the distribution profiles for both concentrations upon fitting to the long time data.

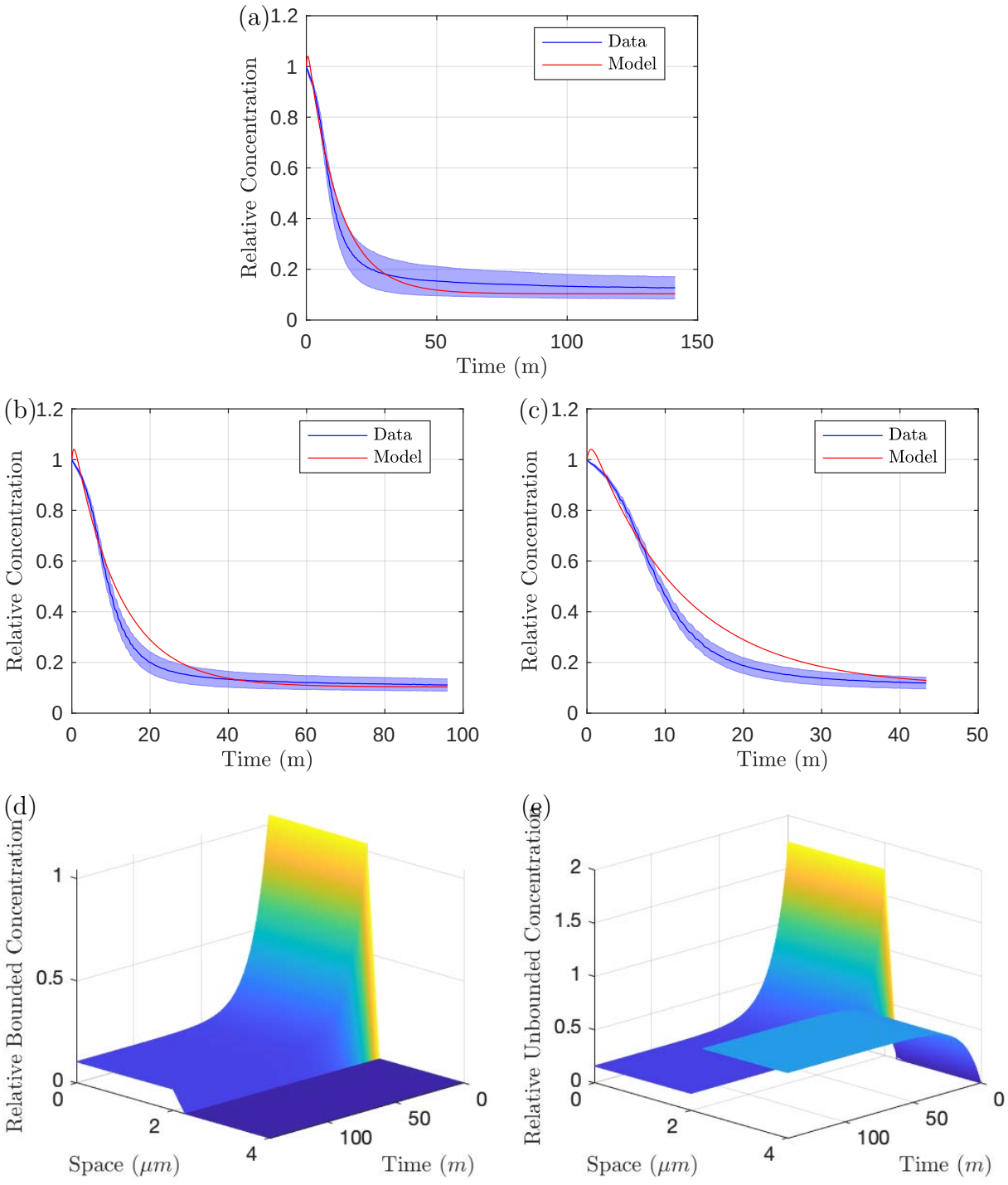

Figure 5.8: Parameter fitting results of the model to both the AEST knockout and wild-type data simultaneously, comparing against the wild-type data. In (a) we show the fit to the assays that reach long time, (b) the assays that reach medium time and (c) all assays in the short time. Finally in (d) and (e) we demonstrate the distribution profiles for both concentrations upon fitting to the long time data

5.6 Improving the wild-type fit

Whilst simultaneous parameter fits have improved our fit for modelling the dynamics of the wild-type case, it is clear that the efflux knockout is compromised. Thus it is possible that we are not encapsulating the effect of efflux with our constant efflux parameter. For the next parameter fits, we look into improving the fits for the wild-type case upon the model with no bound substrate diffusion and variable efflux.

5.6.1 Variable Efflux

AEST Optimal Parameters

Initially, as these parameters provided a realistic fit to the AEST case, we fix the following parameters from the AEST knockout

$$[R_B, D_I, D_E, P, \alpha, \beta, \gamma] = [4, 5.26, 6.47 \times 10^{-3}, 6.63, 9.15 \times 10^{-2}, 2.38 \times 10^{-2}, 39.4], \quad (5.20)$$

given to three significant figures and resulting in an objective function of 1.23×10^{-4}. We then fit our efflux parameters. Since we do not know the initial condition of efflux, we include this in the parameter fit. Our following fitted parameters are:

$$[X_0, \phi, \delta] = [149, 0.31, 0.085], \quad (5.21)$$

given to three significant figures and resulting in an objective function of 7.58×10^{-4}. We plot the optimal fit in Figure 5.9. We note that here with variable efflux, the overall objective function has significantly decreased. This is mainly due to the increased accuracy of replicating the data's steady state in (a). Whilst we note here the long term dynamics are much improved, the short term dynamics are still not being encapsulated. The initial condition of efflux is set to a very large value causing the model to undershoot the data.

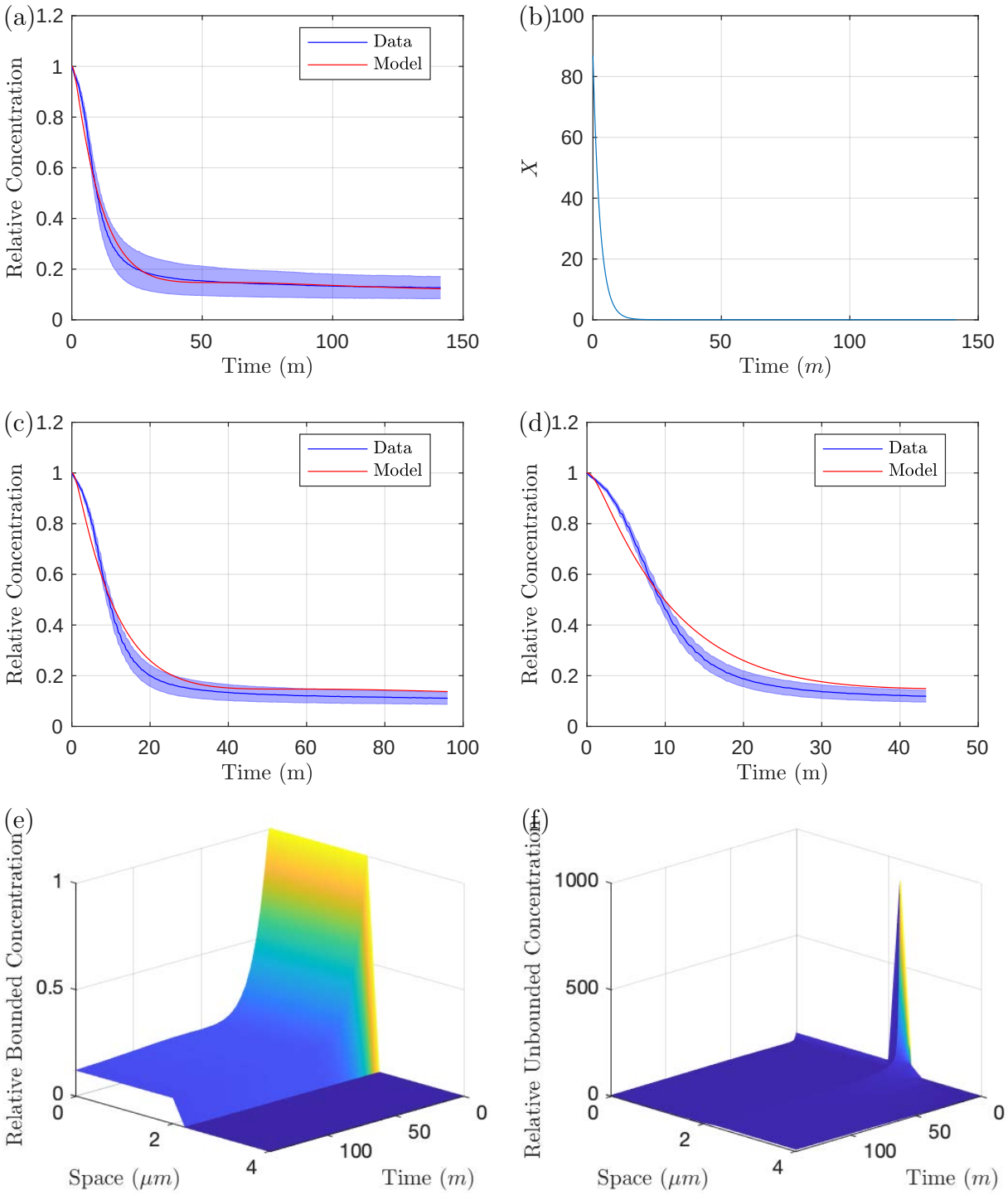

Figure 5.9: Parameter fitting results of the bound ethidium bromide model with variable efflux to the wild-type strain data, fixing AEST parameters from (5.20). In (a) we show the fit to the assays that reach long time, (c) the assays that reach medium time and (d) all assays in the short time. In (b) we exhibit the resulting efflux profile, with (e) and (f) demonstrating the distribution profiles for both concentrations upon fitting to the long time data.

Combined Optimal Parameters

Since the optimal AEST parameters did not produce a realistic fit for the wild-type case upon early and mid time, we now produce fits for the wild-type case by considering each of the top 100 sets of parameters for the fit to the AEST data. Then by combining their objective functions, we choose a case that is optimal and realistic to both the AEST and wild-type cases. The parameters we fix from the AEST data are

$$[R_B, D_I, D_E, P, \alpha, \beta, \gamma] = [4, 6.13 \times 10^{-2}, 1.14 \times 10^{-2}, 4.26 \times 10^{-2}, 0.21, 3.44 \times 10^{-2}, 6.15], \tag{5.22}$$

given to three significant figures and resulting in an objective function of 2.15×10^{-4}. This results in the following parameters when fitting to the wild-type case:

$$[X_0, \phi, \delta] = [86.9, 9.17 \times 10^{-3}, 0.34], \tag{5.23}$$

given to three significant figures and resulting in an objective function of 4.55×10^{-4}. We plot the fits for the AEST and wild-type case in Figures 5.10 and 5.11 respectively. We note here, we have made barely any compromise to the fit to the AEST data but have achieved a much more realistic fit for the wild-type case. For the wild-type (Figure 5.11), the short time behaviour is much improved, with the model only just undershooting the data. In regards to the efflux dynamics in (b) we note that the initial condition of efflux is initially very large and greatly decreases over time.

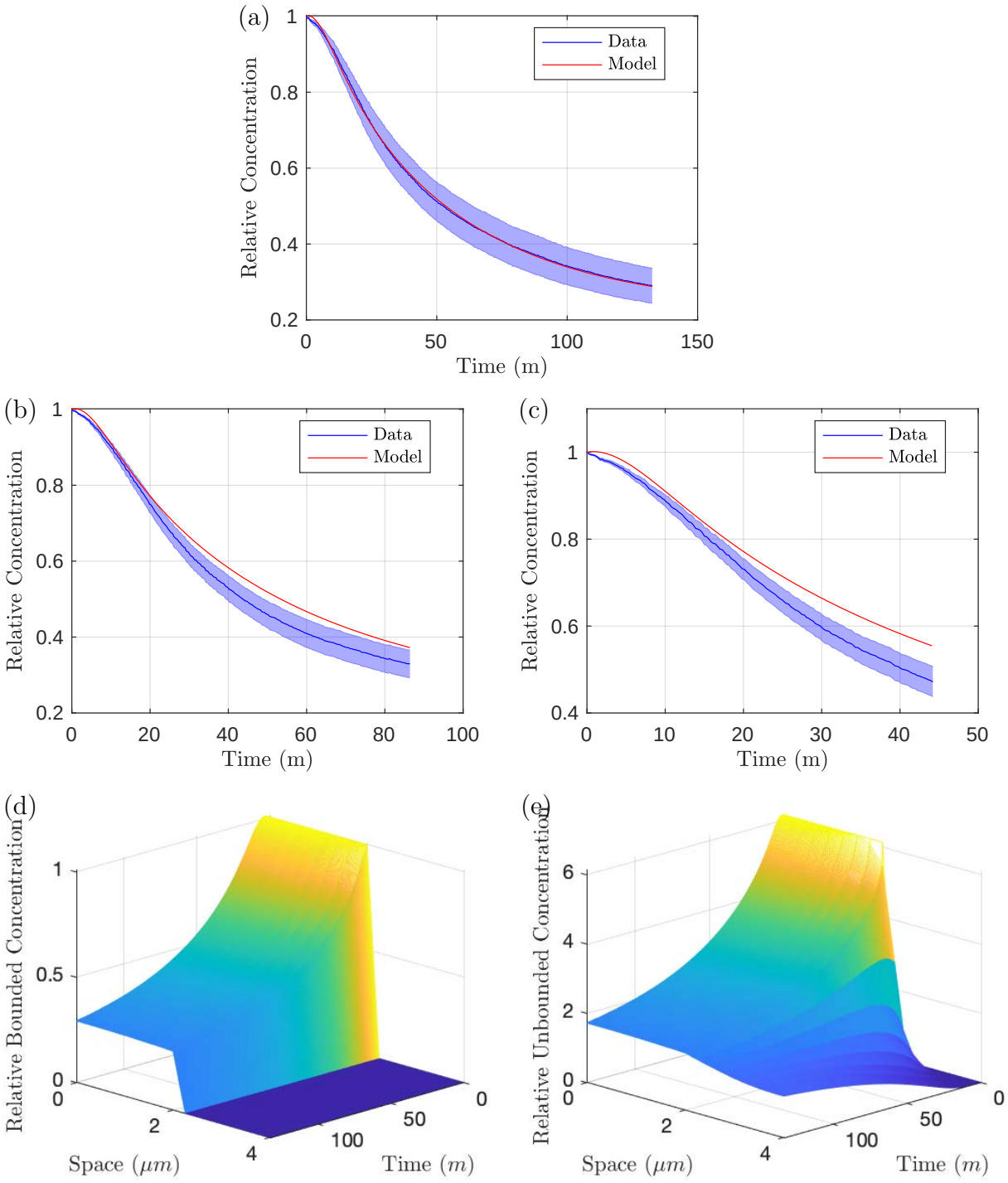

Figure 5.10: Parameter fitting results of the bound ethidium bromide model with variable efflux using the top 100 fits to the AEST data and fitting to the wild-type data, shown against the AEST knockout data. In (a) we show the fit to the assays that reach long time, (b) the assays that reach medium time and (c) all assays in the short time. Finally in (d) and (e) we demonstrate the distribution profiles for both concentrations upon fitting to the long time data.

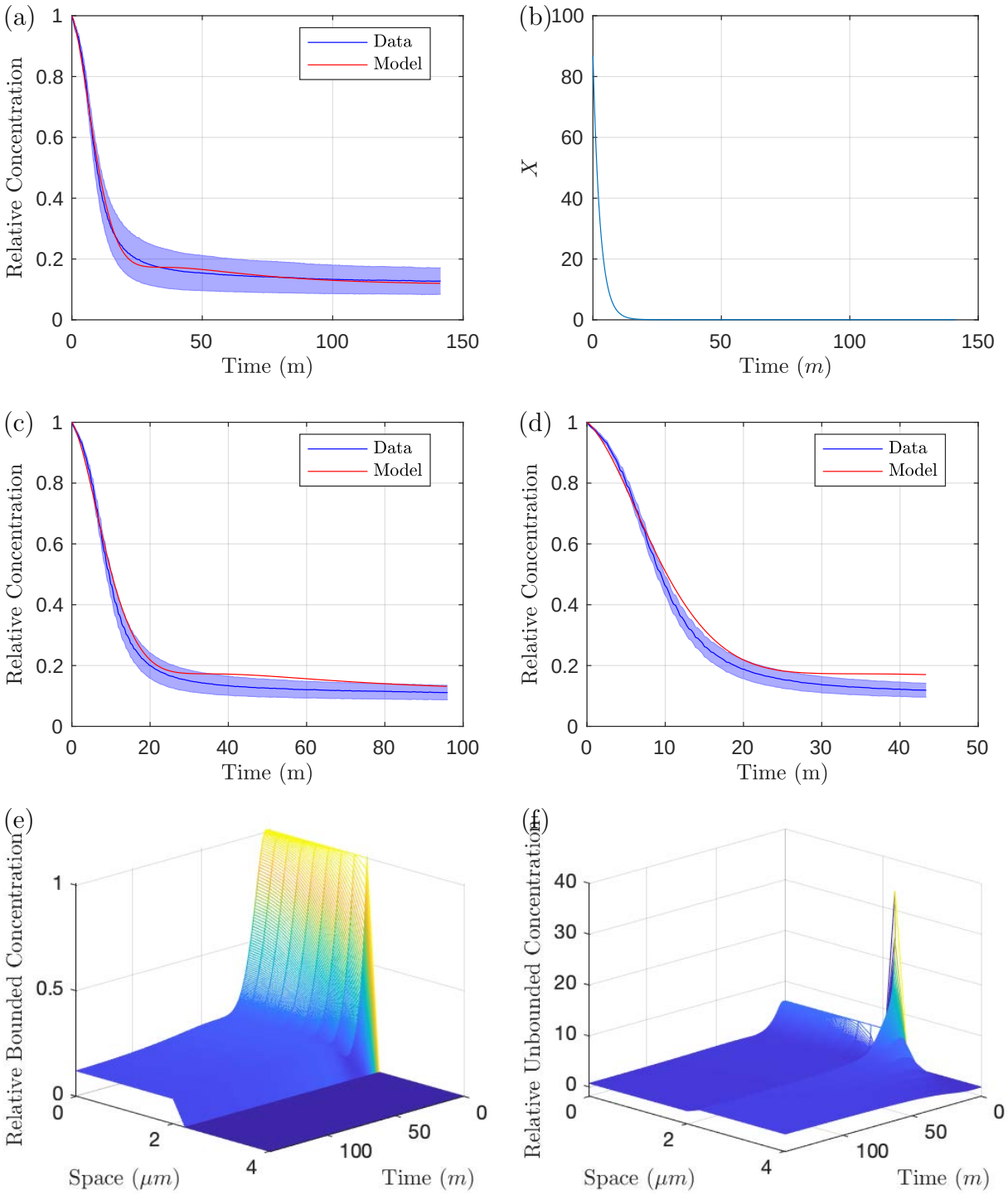

Figure 5.11: Parameter fitting results of the bound ethidium bromide model with variable efflux using the top 100 fits to the AEST data and fitting to the wild-type data, shown against the wild-type data. In (a) we show the fit to the assays that reach long time, (c) the assays that reach medium time and (d) all assays in the short time. In (b) we exhibit the resulting efflux profile, with (e) and (f) demonstrating the distribution profiles for both concentrations upon fitting to the long time data

5.6.2 Substrate Dependent Efflux

Combined Optimal Parameters

It is clear from the previous fits that not only is efflux unlikely to be constant, the optimal fits start with a high level of efflux that decreases over time. We note that the efflux rate very closely matches the concentration of internal antibiotic, thus we produce a fit to a model where the rate of efflux is dependent on the internal antibiotic concentration using (5.10). As with the previous fit, we consider each of the 100 best sets of parameters for the AEST case for the wild-type case, finding the minimal combined objective function. The parameters we choose from the AEST data are

$$[R_B, D_I, D_E, P, \alpha, \beta, \gamma] = [4, 2.30, 1.01, 1.47 \times 10^{-2}, 0.22, 8.89 \times 10^{-2}, 2.59], \tag{5.24}$$

given to three significant figures and resulting in an objective function of 2.44×10^{-4}. Fitting to the wild-type we achieve the parameters

$$[X_0, \phi, \delta] = [4.00 \times 10^{-2}, 7.99 \times 10^{-2}, 0.60], \tag{5.25}$$

given to three significant figures and resulting in an objective function of 3.76×10^{-4}. We plot the resulting parameter fits in Figures 5.12 and 5.13. We note again that there is barely any compromise in regards to fitting to the AEST knockout data (Figure5.12). However the fit to the wild-type case is much improved (Figure 5.13). We note that the long term dynamics are well approximated in (a), whilst the short term dynamics are further encapsulated with a small delay in the initial decrease of bound substrate concentration. We can see that the time course of the efflux rate is very different in (b) to previous fits. The initial condition of efflux is small, however there is a sharp increase in efflux before decreasing to reach a steady state. We note that we have seen similar behaviour to this when simulating the protein expression of these efflux pumps in our GRN model in Chapter 2.

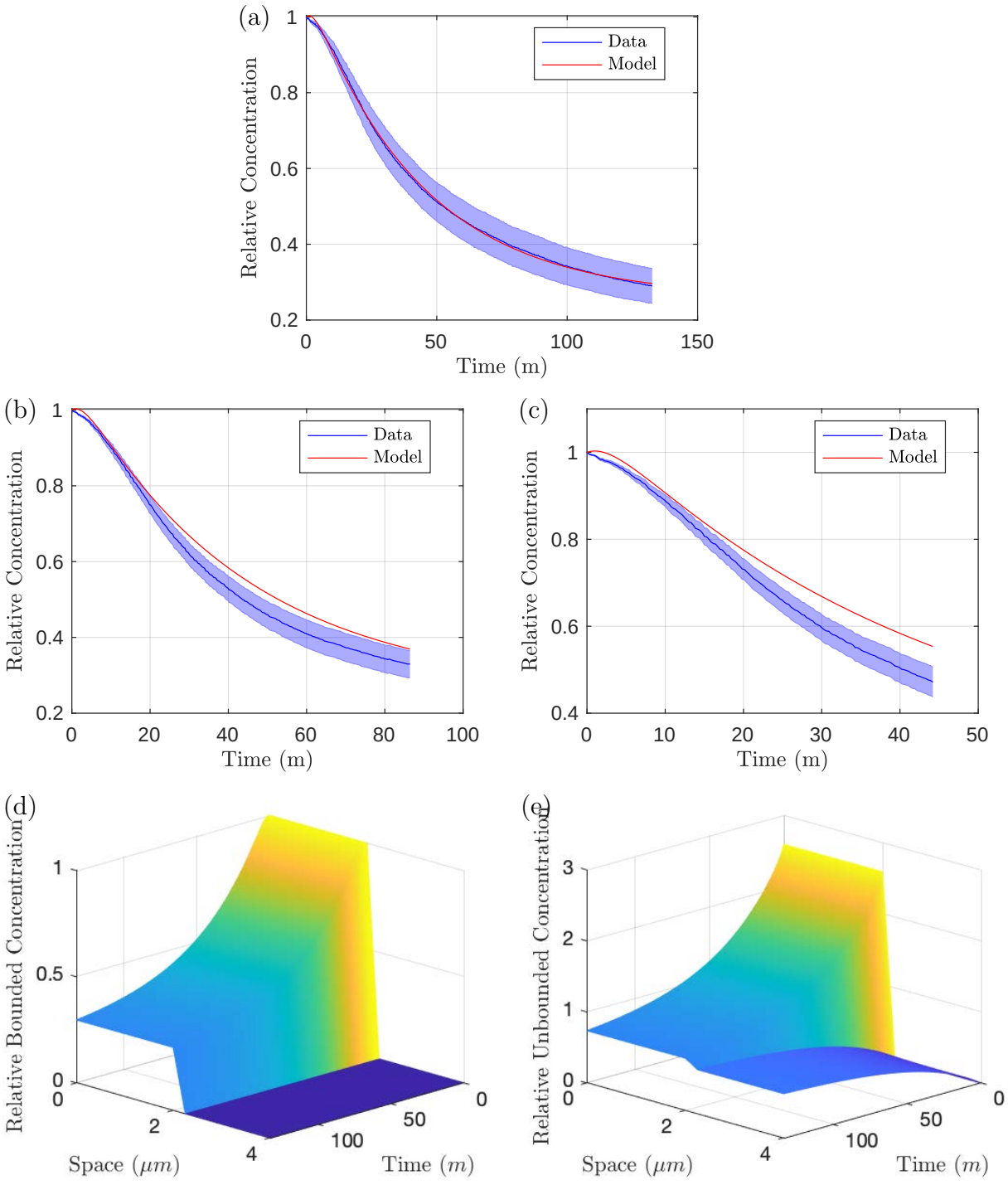

Figure 5.12: Parameter fitting results of the bound ethidium bromide model with variable efflux dependent on substrate using the top 100 fits to the AEST data and fitting to the wild-type data, shown against the AEST data. In (a) we show the fit to the assays that reach long time, (b) the assays that reach medium time and (c) all assays in the short time. Finally in (d) and (e) we demonstrate the distribution profiles for both concentrations upon fitting to the long time data.

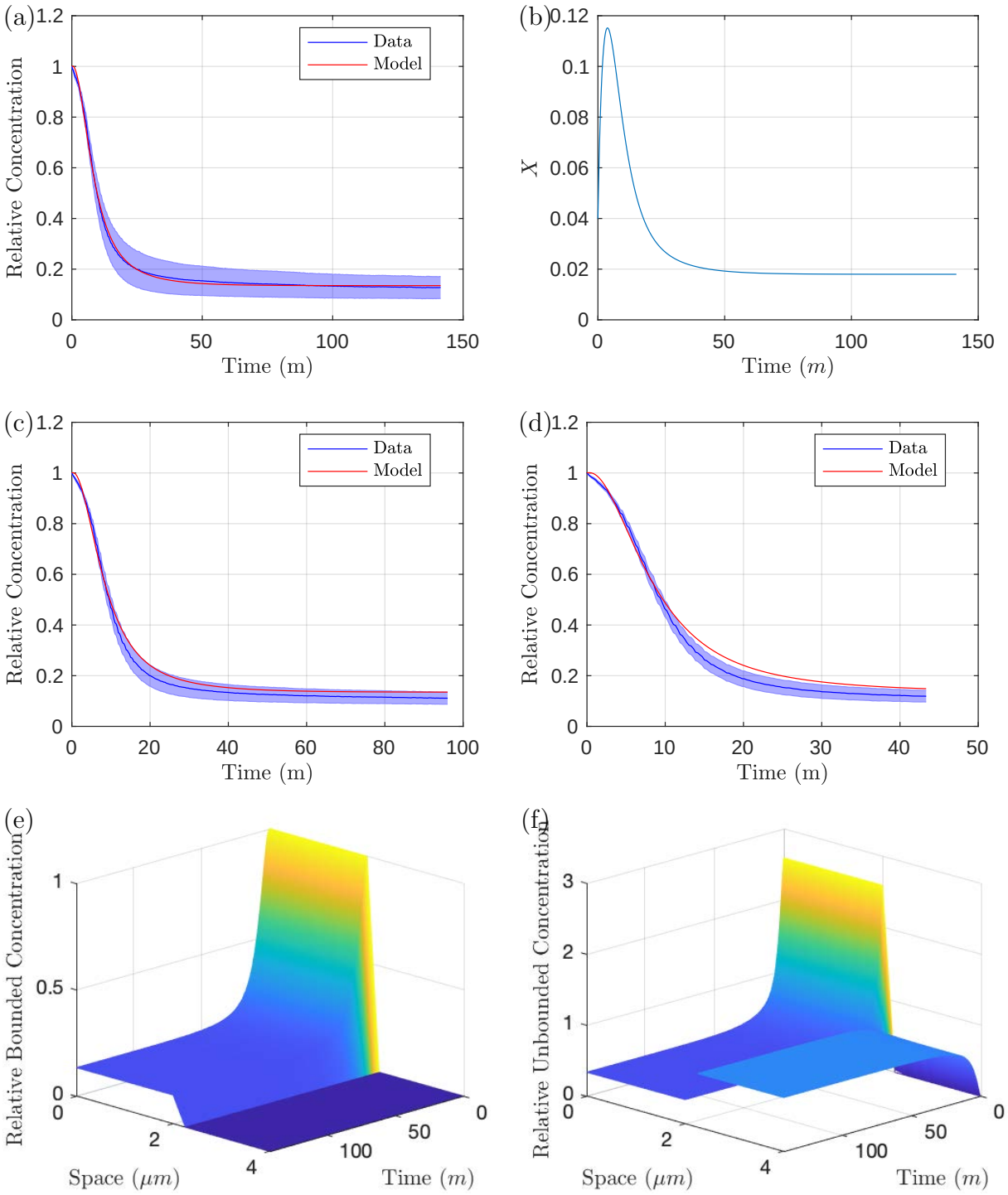

Figure 5.13: Parameter fitting results of the bound ethidium bromide model with variable efflux dependent on substrate using the top 100 fits to the AEST data and fitting to the wild-type data, shown against the wild-type data. In (a) we show the fit to the assays that reach long time, (c) the assays that reach medium time and (d) all assays in the short time. In (b) we exhibit the resulting efflux profile, with (e) and (f) demonstrating the distribution profiles for both concentrations upon fitting to the long time data.

Individual Efflux Knockouts

Since we have found parameters that encapsulate the behaviour of the two most extreme cases (AEST knockout and wild-type) we fix the AEST parameters (5.24) and fit new efflux parameters for each case of efflux knockouts. For notation, we list all fitted parameters as X_{G0}, ϕ_G and δ_G together with their corresponding objective function θ_G, where G represents the efflux pumps that are active in that case. The parameters we achieve are

$$[X_{EST0}, \phi_{EST}, \delta_{EST}, \theta_{EST}] = [8.99 \times 10^{-3}, 4.89 \times 10^{-3}, 0.26, 4.53 \times 10^{-4}], \tag{5.26}$$

$$[X_{AST0}, \phi_{AST}, \delta_{AST}, \theta_{AST}] = [1.35 \times 10^{-2}, 4.18 \times 10^{-2}, 0.24, 6.15 \times 10^{-4}], \tag{5.27}$$

$$[X_{AET0}, \phi_{AET}, \delta_{AET}, \theta_{AET}] = [7.01 \times 10^{-8}, 4.30 \times 10^{-2}, 0.32, 6.53 \times 10^{-4}], \tag{5.28}$$

$$[X_{AES0}, \phi_{AES}, \delta_{AES}, \theta_{AES}] = [7.87 \times 10^{-8}, 3.42 \times 10^{-2}, 0.25, 9.53 \times 10^{-4}], \tag{5.29}$$

$$[X_{ST0}, \phi_{ST}, \delta_{ST}, \theta_{ST}] = [2.12 \times 10^{-4}, 1.57 \times 10^{-4}, 2.94 \times 10^{-2}, 1.30 \times 10^{-3}], \tag{5.30}$$

given to three significant figures and resulting in a combined objective function of 3.98×10^{-3}. Notably we have very small values for X_{AET0} and X_{AES0} which could depend on the resolution of the numerical method. These initial conditions however have been tested these at value zero and have obtained similar results. We plot the resulting fits in Figures 5.14 and 5.15. We can immediately see that for each efflux knockout case, the dynamics are closely matched with the majority of the model fitting within the standard error of the data. It is also interesting to note that nearly all efflux profiles (barring the AE knockout) start off at a low value, then rapidly increase before decreasing to a steady state value (Figure 5.14 (d), (f), Figure 5.15 (b) and (d)). The efflux profile for the AE knockout in Figure 5.15 (e) and (f) we note has a very different efflux profile to the other cases. This could be due to the fact that in this case only the efflux pumps MdsAB and MdtAB are active, these are both lesser efflux pumps compared to AcrAB and AcrEF and we should

expect less efflux and hence a lesser or no initial peak of efflux caused by these pumps.

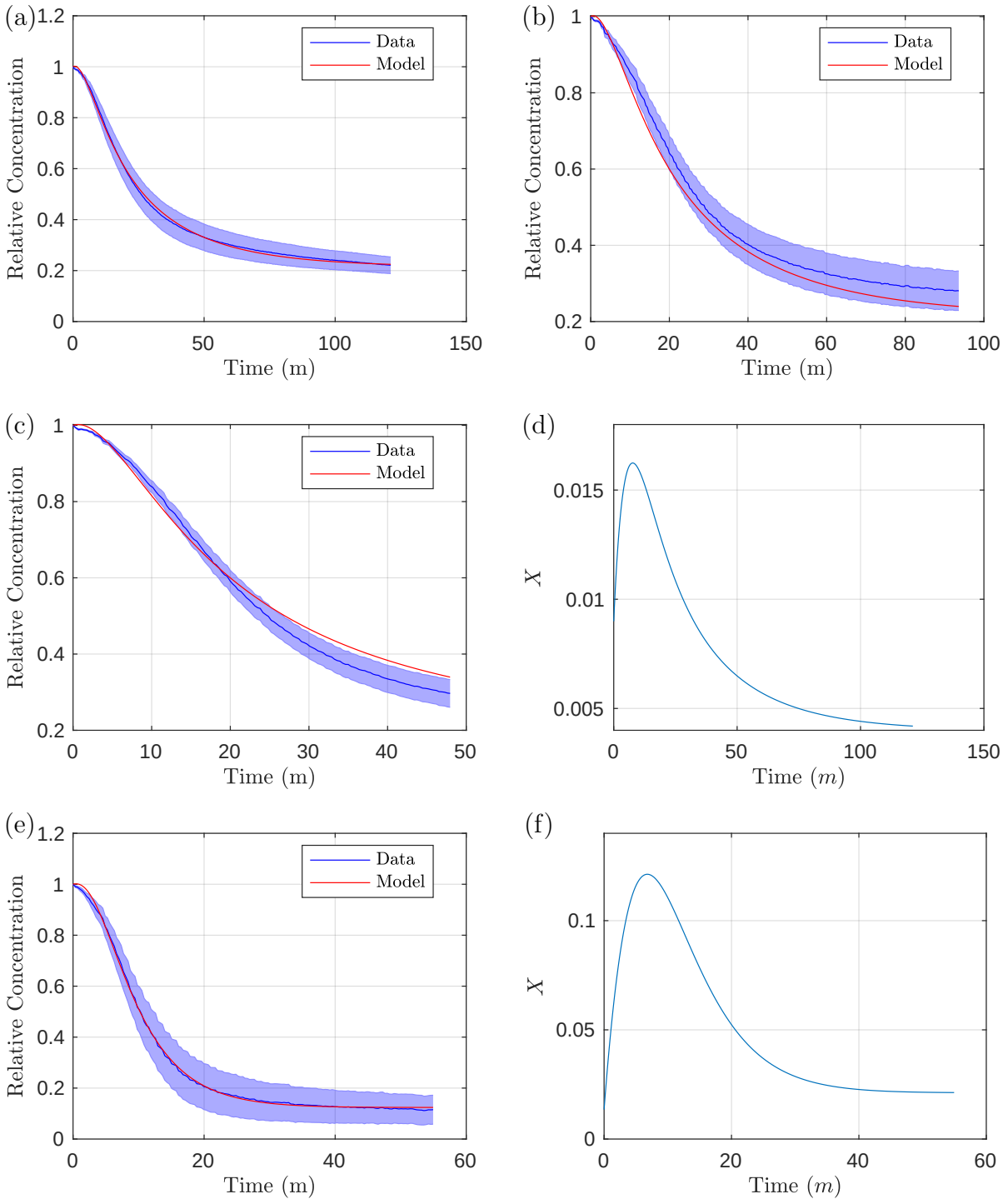

Figure 5.14: Parameter fitting results of the bound ethidium bromide model to the data of individual knockouts, having fixed AEST parameters (5.24). In (a), (b) and (c) we show the model fitting to the A knockout, firstly to long time and then testing against medium and short time data respectively. In (d) we show the resulting efflux variable. In (e) we show the fit to the E knockout and resulting efflux parameter (f).

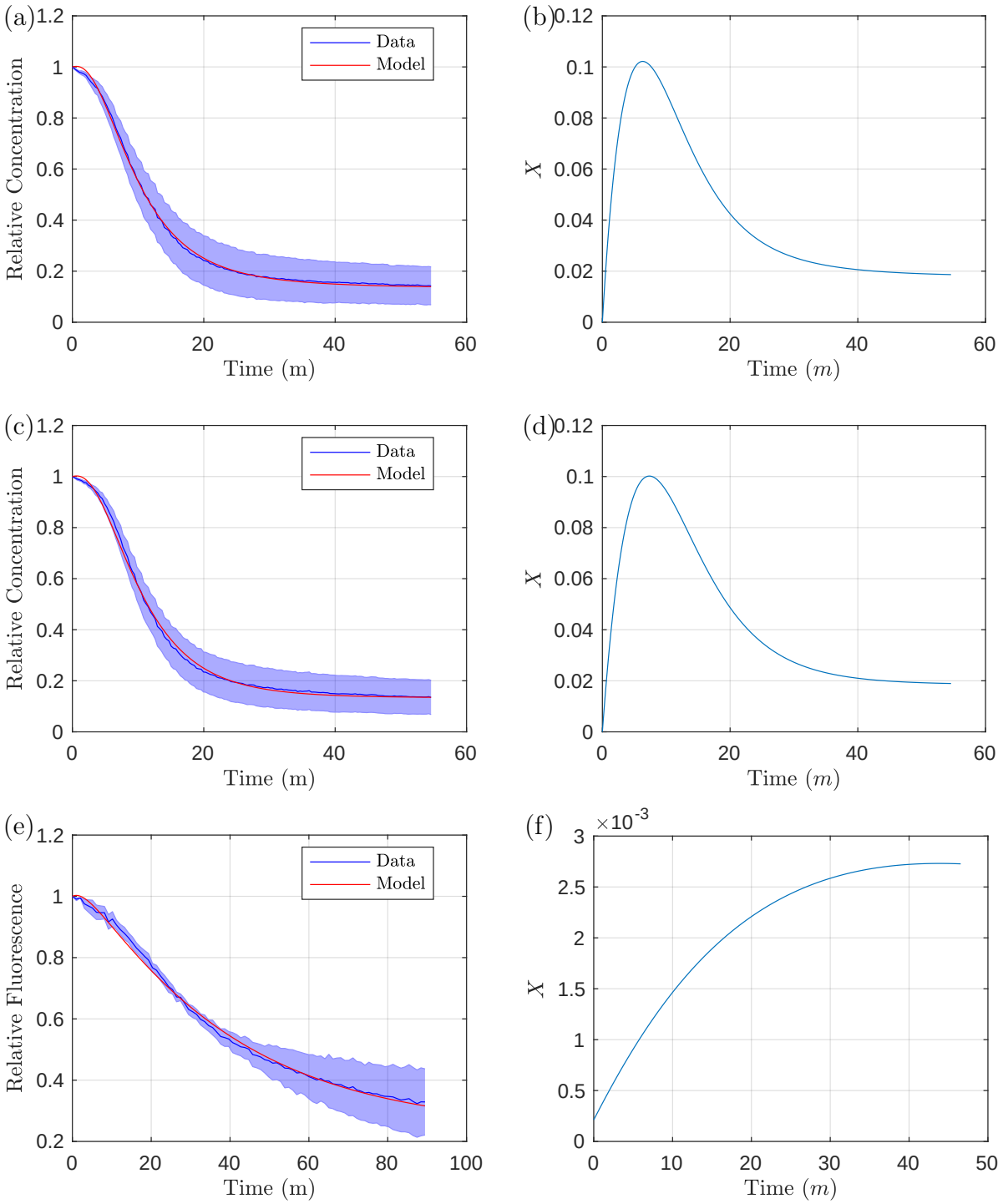

Figure 5.15: Further parameter fitting results of the bound ethidium bromide model to the data of individual knockouts, having fixed AEST parameters (5.24). In (a) we show the S knockout with resulting efflux parameter in (b). In (c) we show the T knockout with resulting efflux parameter in (d). Finally, in (e) we show the AE knockout with resulting efflux parameter in (f).

In Figure 5.16 (a) we show all of our fitted efflux profiles compiled onto one plot. Similar to Section 4.7.1, we assume that efflux from each individual efflux pump is the same from strain to strain (when said efflux pump is active) and is additive, we can find the level of efflux from each efflux pump by solving a system of simultaneous equations. In (b) we plot the individual efflux variables derived under this assumption.

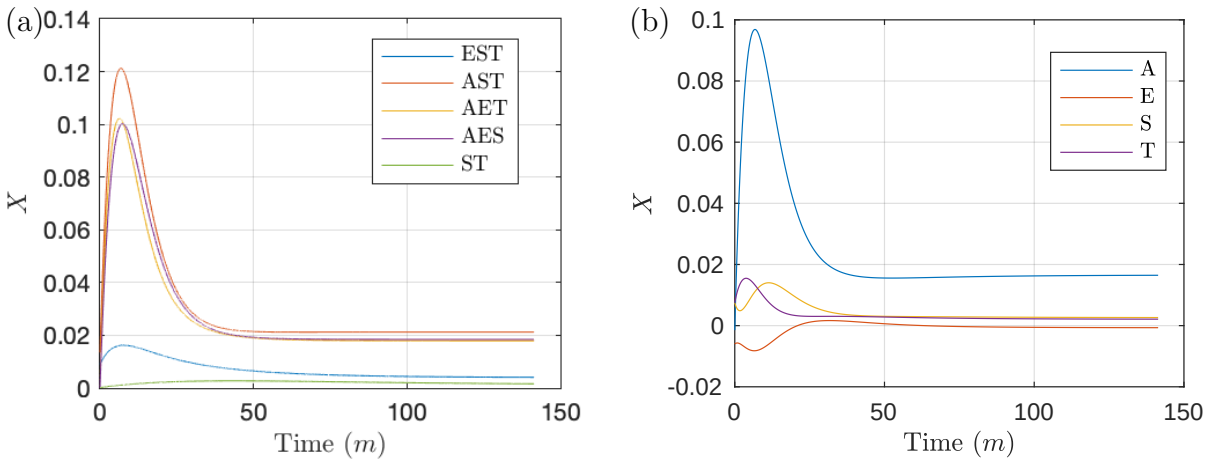

Figure 5.16: Compiled efflux profiles from our parameter fitting results of the ethidium bromide model with substrate dependent efflux. In (a) we show the profiles of our efflux knockout strains, in (b) we show the profiles of our estimated individual efflux profiles.

We can see that this puts the value from the efflux pump AcrEF (X_E) to be negative. We know this is not possible and thus the assumption made above must not be correct. However, we know from our GRN model that if AcrAB levels are high AcrEF levels are low and there is a switch between these pumps. Thus we make another assumption that there is no AcrEF ($X_E = 0$) when AcrAB (X_A) is active and also group MdsAB and MdtAB as one pump ($X_S + X_T = X_{ST}$), due to both pumps not being involved in our GRN model. Thus our simultaneous equations to be solved are

$$X_A + X_{ST} = X_{AST}, \tag{5.31}$$

$$X_E + X_{ST} = X_{EST}, \tag{5.32}$$

which results in the efflux values

$$X_A = X_{AST} - X_{ST}, \tag{5.33}$$

$$X_E = X_{EST} - X_{ST}. \tag{5.34}$$

We plot these values in Figure 5.17, showing the efflux profile for AcrEF only when AcrAB is not active. All profiles are now positive which could possibly suggest that there is interplay between the efflux pumps and that when a pump is knocked out, there is a noticeable effect upon the other pumps in the cell. In addition the behaviour for the two main efflux pumps is very similar, showing an early increase before rapidly decreasing to reach a steady state. These factors could be due to many mechanisms, however our GRN-model efflux proteins (AcrAB and AcrEF) do exhibit similar behaviour to these efflux profiles. Therefore the interaction of genes that govern expression of the efflux pumps could be prominent in determining the efflux profiles of the RND pumps. Thus the GRN behaviour may provide a pivotal role in substrate efflux over long time and determining the spatial distribution of substrate concentration within the *Salmonella* cells and their environment.

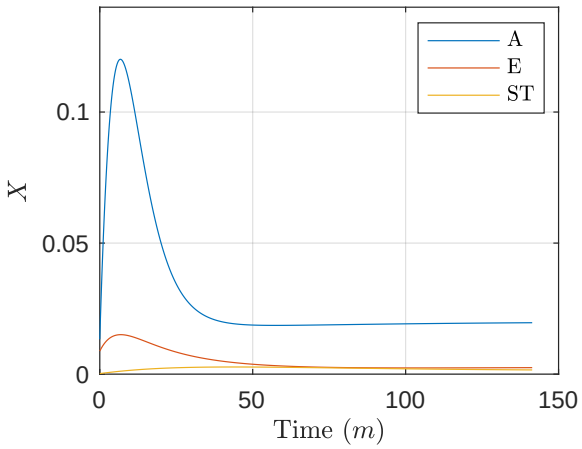

Figure 5.17: Efflux profiles from our parameter fitting results of the ethidium bromide model with substrate dependent efflux. Here we show the profiles of our estimated efflux profiles for AcrAB and AcrEF, with strain results for ST (MdsAB and MdtAB).

5.7 Compartmental Model

In the previous subsections, we have produced a PDE model and applied parameter fitting techniques on the spatial average of the intracellular concentration to fit to experimental data. An alternative approach however, could have been taken utilising compartmental models using ODEs. In this section, we compartmentalise our model (5.1)-(5.3) and compare the differences in simulations between the ODE and PDE models. In order to compartmentalise our PDE model we must first define our spatial average

$$\begin{aligned}\bar{c}_i &= \frac{1}{V}\iiint_V r^2\,\sin(\theta)\,c_i(r,t)\,dr\,d\theta\,d\phi \\ &= \frac{3}{(R_{max}^3 - R_{min}^3)}\int_{R_{min}}^{R_{max}} r^2\,c_i(r,t)\,dr, \end{aligned} \tag{5.35}$$

which has the time derivative

$$\frac{\partial \bar{c}_i}{\partial t} = \frac{3}{(R_{max}^3 - R_{min}^3)}\int_{R_{min}}^{R_{max}} r^2\,\frac{\partial c_i}{\partial t}\,dr, \tag{5.36}$$

where $i = B, I, E$. If we take the volume integral of our equation for bound ethidium bromide (5.1) we have

$$\frac{1}{V}\iiint_V r^2\,\sin(\theta)\frac{\partial c_B}{\partial t}\,dr\,d\theta\,d\phi = \frac{1}{V}\iiint_V r^2\,\sin(\theta)\,(D_B\nabla^2 c_B - \alpha c_B + \beta c_I)\,dr\,d\theta\,d\phi, \tag{5.37}$$

which by substituting (5.35) and (5.36), simplifies to

$$\frac{\partial \bar{c}_B}{\partial t} = \frac{1}{V}\iiint_V r^2\,\sin(\theta)\,D_B\nabla^2 c_B\,dr\,d\theta\,d\phi - \alpha\bar{c}_B + \beta\bar{c}_I \tag{5.38}$$

$$= \frac{3}{R_M^3}\left[D_B\,r^2\frac{\partial c_B}{\partial r}\right]_0^{R_M} - \alpha\bar{c}_B + \beta\bar{c}_I, \tag{5.39}$$

$$= \frac{3}{R_M}\,D_B\frac{\partial c_B}{\partial r}\bigg|_{r=R_M} - \alpha\bar{c}_B + \beta\bar{c}_I, \tag{5.40}$$

Now by using the no flux boundary condition at $r = R_M$ for bound ethidium bromide (5.6), we have

$$\frac{d\bar{c}_B}{dt} = -\alpha\bar{c}_B + \beta\bar{c}_I. \tag{5.41}$$

Next, we assume that all rates of diffusion are much faster compared to other reaction rates such that the concentrations within the compartments are constantly uniform ($\bar{c}_i = c_i$), we can write:

$$\frac{dc_B}{dt} = -\alpha c_B + \beta c_I. \tag{5.42}$$

Now following the same method for the unbound ethidium bromide (5.2), we achieve

$$\frac{\partial\bar{c}_I}{\partial t} = \frac{3}{R_M} D_I \frac{\partial c_B}{\partial r}\bigg|_{r=R_M} - \alpha\bar{c}_B + \beta\bar{c}_I, \tag{5.43}$$

In this case, we substitute our membrane boundary condition for unbound intracellular ethidium bromide at $r = R_M$ (5.5), to get

$$\frac{\partial\bar{c}_I}{\partial t} = \frac{3}{R_M}(-(P+X)c_I(R_M,t) + Pc_E(R_M,t)) - \alpha\bar{c}_B + \beta\bar{c}_I, \tag{5.44}$$

We again assume that the compartment concentrations are uniform (hence $\bar{c}_i = c_i$ and $c_i(R_M,t) = c_i$), thus we can write:

$$\frac{dc_I}{dt} = \frac{3P}{R_M}c_E - \frac{3(P+X)}{R_M}c_I + \alpha c_B - \beta c_I, \tag{5.45}$$

Finally we apply this method to the extracellular ethidium bromide (5.3), giving us

$$\frac{\partial\bar{c}_E}{\partial t} = \frac{3}{(R_B^3 - R_M^3)}\left(D_E\, R_B^2\, \frac{\partial c_B}{\partial r}\bigg|_{r=R_B} - D_E\, R_M^2\, \frac{\partial c_B}{\partial r}\bigg|_{r=R_M}\right). \tag{5.46}$$

In this case, we use our boundary conditions for the extracellular ethidium bromide. We have a no flux boundary at $r = R_B$ (5.7), and the membrane condition at $r = R_M$ (5.5).

Substituting and assuming that the compartment concentrations are uniform gives us

$$\frac{dc_E}{dt} = \frac{3R_M^2(P+X)}{(R_B^3 - R_M^3)}c_I - \frac{3R_M^2 P}{(R_B^3 - R_M^3)}c_E. \tag{5.47}$$

We have now derived our compartmental model and the corresponding ODE equations are as follows

$$\frac{dc_B}{dt} = -\alpha c_B + \beta c_I, \tag{5.48}$$

$$\frac{dc_I}{dt} = \frac{3P}{R_M}c_E - \frac{3(P+X)}{R_M}c_I + \alpha c_B - \beta c_I, \tag{5.49}$$

$$\frac{dc_E}{dt} = \frac{3R_M^2(P+X)}{(R_B^3 - R_M^3)}c_I - \frac{3R_M^2 P}{(R_B^3 - R_M^3)}c_E. \tag{5.50}$$

We note that this model retains the majority of the parameters from the PDE model, however there is no dependence on the diffusion coefficients D_B, D_I and D_E. In Figure 5.18, we exhibit the simulations comparing the ODE and PDE models, using the optimal parameters for the AEST and wild-type cases in Section 5.6.2. We can see from the simulations that for the chosen parameters the ODE model encapsulates the behaviour of the PDE model well, with little difference in their simulations. In Figure 5.19 however, we exhibit the simulations with slower diffusion rates (by a factor of 100). We can see that there are large differences between the model simulations, with the ODE model not being able to encapsulate the changes in behaviour to the PDE model. In Figure 5.20, we exhibit a parameter variation plot comparing the root mean square error (RMSE) of all concentrations between ODE and PDE models, using the optimal wild-type parameters. We can see that when either diffusion rate is small enough, the assumption of a uniform concentration within the compartments fails and thus the behaviour in the ODE model does not match up to the behaviour in the PDE model. Therefore, whilst for the optimal parameters chosen the ODE model may be sufficient, if we were to model a different substrate that diffuses differently we may not encapsulate the substrate's full behaviour. In addition if we were to introduce a synthetic molecule to try to combat substrate efflux

the ODE model may not be sufficient i.e. a molecule that binds to the substrate affecting its diffusion dynamics. For these reasons, we continue using the PDE model for the remaining sections.

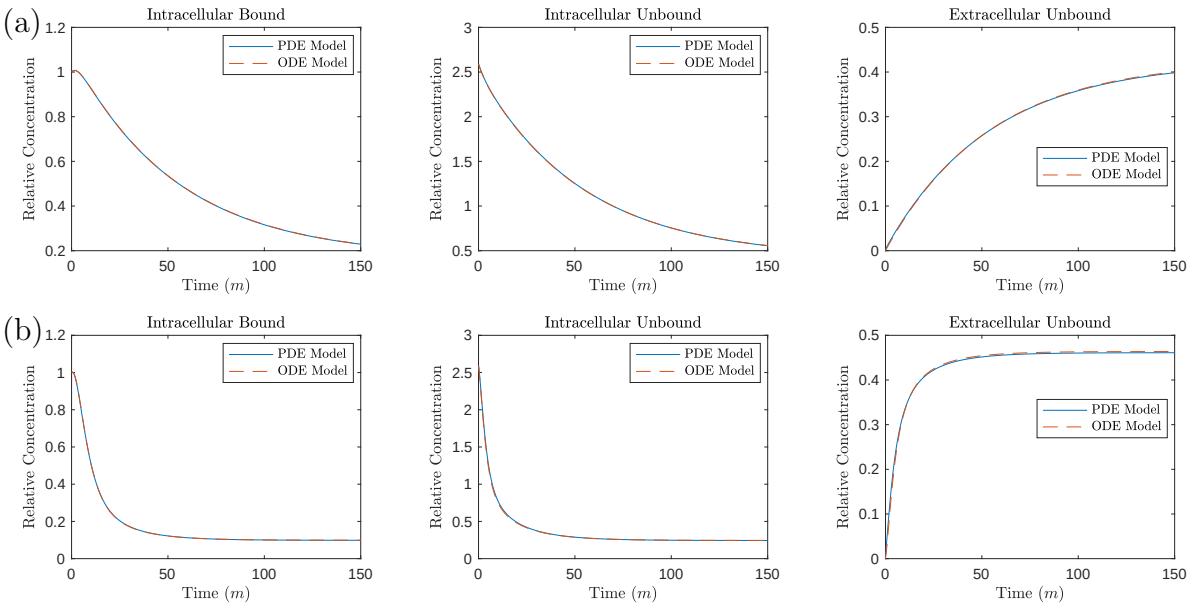

Figure 5.18: Simulations comparing the compartmental ODE and spatial PDE model. In (a) we exhibit simulations using the AEST optimal parameters, whilst in (b) we use the optimal wild-type parameters.

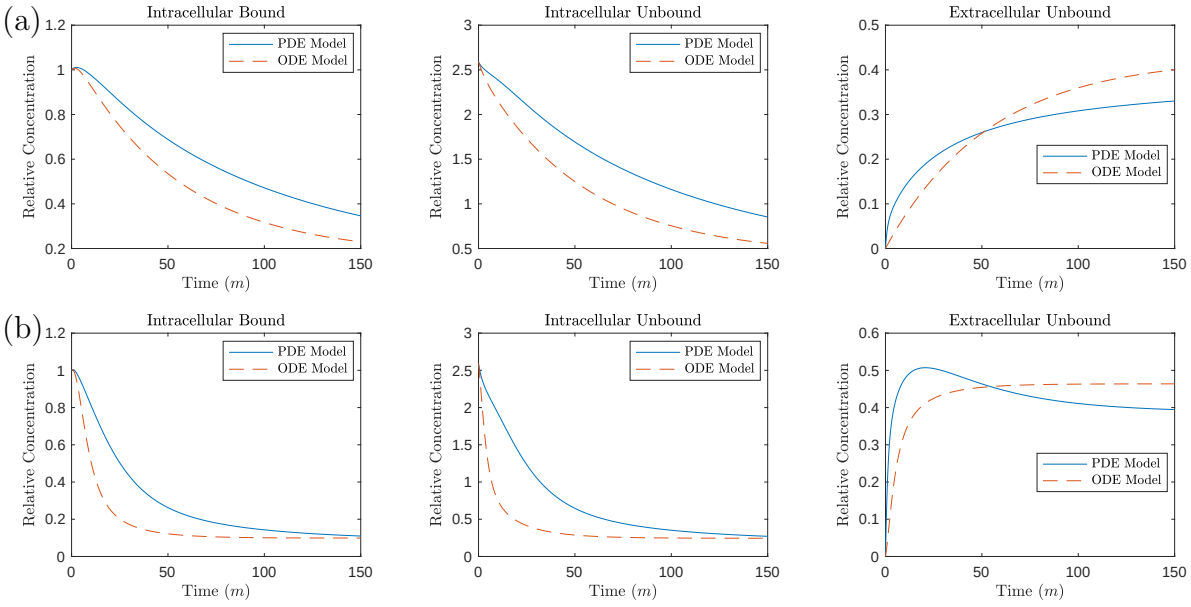

Figure 5.19: Simulations comparing the compartmental ODE and spatial PDE model with slower substrate diffusion (by a factor of 100). In (a) we exhibit simulations using the AEST optimal parameters, whilst in (b) we use the optimal wild-type parameters.

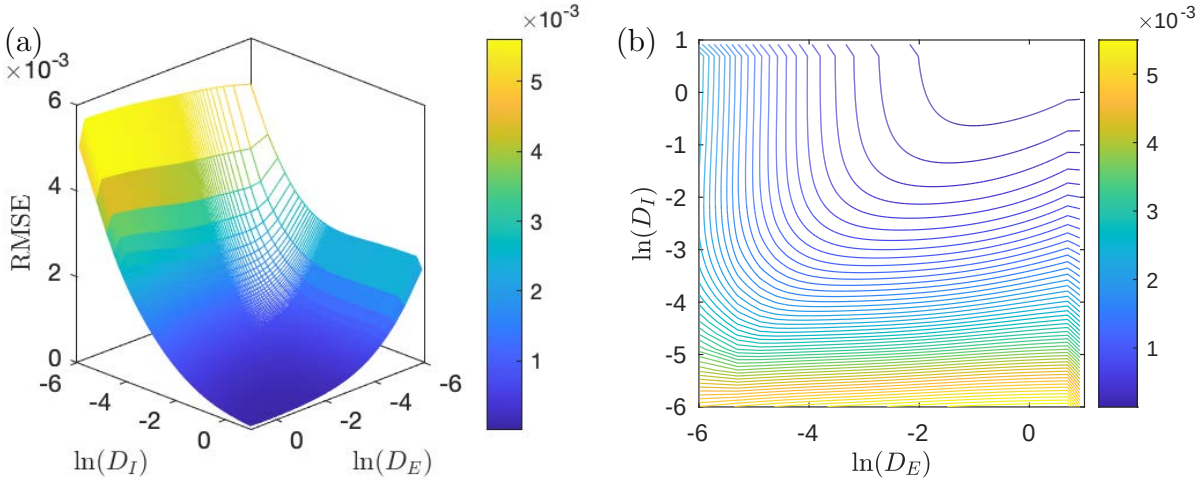

Figure 5.20: Parameter variation plots exhibiting the RMSE between the ODE and PDE models for all concentrations, varying the log of diffusion parameters D_I and D_E to greater show the differences in RMSE for small values of diffusion. In (a) we exhibit a 3D mesh and (b) a contour plot.

5.8 Discussion

We have adapted our previous spatial model to greater encapsulate the dynamics of substrate expulsion of a single cell by including the binding dynamics of ethidium bromide. By using finite difference methods, we have discretised our domain and produced numerical solutions for both concentrations of bound and unbound ethidium bromide, including the interplay between both concentrations. We have produced multiple simulations, varying parameters to best present insights into the model. Whilst the long term dynamics are similar to the original model, it is shown that the short and medium term dynamics have changed. By introducing two states of ethidium bromide we have caused the fluorescing intracellular substrate concentration to decrease more slowly at early time, with the depreciation depending on the binding and unbinding rates as well as the membrane permeability and efflux parameters.

We have then implemented parameter fitting techniques using our more in depth bound ethidium bromide model. Upon initial parameter fitting exercises, it was shown that although the model fitted well to the AEST knockout data, it struggled to model

the wild-type dynamics when including an efflux parameter. We have conducted joint parameter fitting exercises, minimising a combined objective function for both data sets. Whilst the fit for the wild-type case was much improved, the fit for the AEST knockout was compromised, with a greater peak at initial concentration and the model appearing to reach a steady state at a higher concentration than the data suggests.

It is clear that the efflux behaviour in the model was not fully accurate, with the constant efflux parameter unable to fully replicate the dynamics of the drop in substrate concentration seen in the data. By including efflux as a variable instead, we have been able to improve our model fits for both cases of knockout and wild-type, with the model demonstrating the difference in dynamics between both cases. By again fitting to both cases simultaneously with a joint objective function, we have further been able to improve our fits, with minimal compromise to the fit of the AEST case. Furthermore, we have produced fits where efflux is dependent on the internal substrate. This has provided us with our optimal fits and also interesting profiles for our efflux variables. We noted that the efflux profiles are similar to simulations of the expression of genes in our GRN model, leading us to believe that gene expression could be the cause of this efflux profile on this time period. This suggests that combining our GRN model with our spatial model is an appropriate next step and will enable us to make predictions about adaptations to the GRN and how they could affect the antibiotic concentration within the cell. In addition, we have compartmentalised our model, simplifying our existing PDE model into an ODE model. Whilst the ODE model provided good simulations with our optimal parameters, we have shown the limitations of the ODE model for modelling different substrates or manipulations. Therefore in the following sections we opt to use our PDE model rather than the compartmental ODE model.

CHAPTER 6

MULTISCALE MODEL

6.1 Introduction

In the previous chapters, we have constructed two independent models. The first in Chapter 2, is a model of the GRN governing the expression of efflux proteins that constitute the efflux pumps AcrAB and AcrEF for a *Salmonella* cell. The second model in Chapter 5, is a spatial model of substrate efflux from a *Salmonella* culture, exhibiting the efflux caused by four RND efflux pumps AcrAB, AcrEF, MdsAB and MdtAB. Upon parameter fitting of the spatial model, we were able to gain insights into the efflux dynamics over time when a culture was subject to a stressor, namely Ethidium Bromide. From multiple parameter fitting exercises, it was shown that these dynamics in the spatial model were similar to the expression of efflux pump proteins in the GRN model. It was also shown that substrate dependent efflux best captured the dynamics of the data, agreeing with our knowledge that bacteria can react to their environment. One way that we already know bacteria can do this is by varying expression of genes that control aspects of the bacterial behaviour. In this chapter, we will combine the GRN model with the spatial model, in order to create a multiscale model of the *Salmonella* population and its environment. This model will enable us to draw hypotheses on manipulating aspects of the GRN and the resulting effect upon substrate concentration in a culture. By creating this multiscale model, we have a more realistic and complete model that should capture more of the important aspects of the population's behaviour than the previous models.

6.2 GRN Model Adaptation

Following our asymptotic analysis in Chapter 3, we have identified the genes that dominate processes within the network. Thus for simplicity, in this section we use this analysis to create a simplified version of the GRN in Chapter 2. One change is to remove the secondary TAs *soxS*, *marA* and *rob*. Our asymptotic analysis concluded that once *ramA* is expressed, these secondary TAs did not produce a noticeable effect at long time on the expression of the efflux pump genes. The second change to the network is to remove the post transcriptional activator CsrA. Since this protein was not linked to other mechanisms within the network, mathematically we can easily incorporate the effect of this protein by altering the translation rate of *acrAB* mRNA. Thus for simplicity, we choose to omit this protein from the network.

Since our initial construction of the GRN, the knowledge of the mechanisms within the network has been broadened [27]. In order for our model to fully encapsulate the new mechanisms within the network, we further adapt our GRN model. We exhibit our updated network in Figure 6.1, with the following changes exhibited by dashed lines:

- RamA activates *acrEF* as well as *acrAB* [5].
- The link between the expression of *acrAB* and *acrEF*, is governed by heat-stable nucleoid-structuring protein (H-NS) [62].

In regards to the first change, previously the expression of *acrEF* was only governed by EnvR. Thus we should see new interesting dynamics to the network with *acrEF* now also being dependent on the activator protein RamA to be transcribed. In regards to the second change, we have replaced our theoretical link between both efflux pumps in our previous GRN model with the molecule H-NS. We exhibit the interactions that involve H-NS in Figure 6.2. When H-NS is active, it inhibits expression of both *envR* and *acrEF* [12]. H-NS is believed to be involved in the experimentally observed switching dynamics of the two efflux pumps, such that *acrEF* expression is activated when *acrAB* expression is low. We include these switching dynamics by assuming that a high concentration of

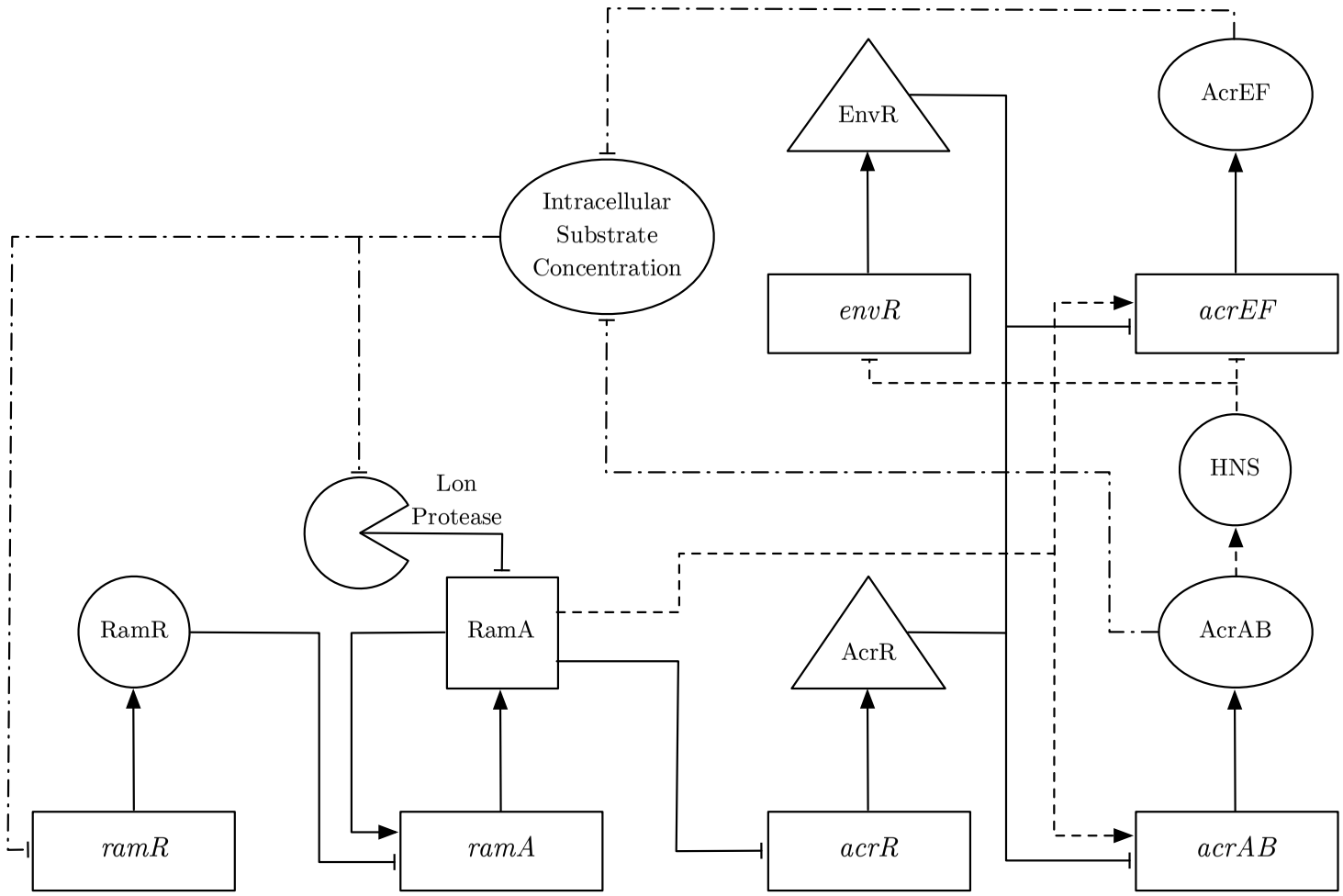

Figure 6.1: Updated GRN model schematic incorporating simplifications drawn from the time dependent asymptotic analysis, updates from broadened knowledge of the GRN mechanisms and updates to incorporate dependence on internal substrate concentration. The solid lines represent original mechanisms from our previous GRN model. The dashed lines represent updates based on recent information about the network from biological experiments. The dot dashed lines represent updates to include GRN influence by the internal substrate concentration from our spatial PDE model.

AcrAB will activate the molecule H-NS, hence inhibiting the expression of both *acrEF* and *envR*. To include this into our model we assume that the variable H-NS will vary between 1 (when active) and 0 (when inactive). We represent the variable for H-NS through the following equation

$$\frac{dH}{dt} = k_h B(1 - H) - m_h H, \tag{6.1}$$

where k_h is the activation rate of H-NS linked to AcrAB concentration and m_h is the deactivation rate of H-NS. For simplicity, we take (6.1) to be in quasi steady state, with $K_H = \frac{m_h}{k_h}$:

$$H = \frac{B}{B + K_H}. \tag{6.2}$$

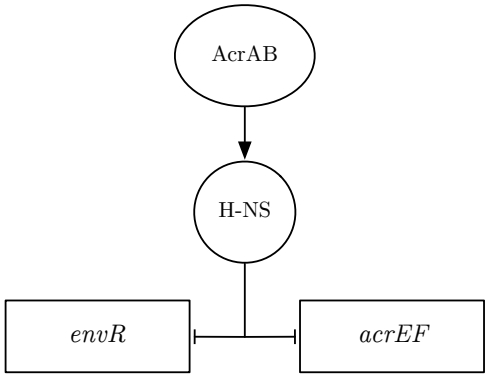

Figure 6.2: A schematic of a section of the GRN model, demonstrating the interactions that involve H-NS. This includes the proteins AcrAB and H-NS, and the genes *envR* and *acrEF*.

From our parameter fitting exercises, we achieved the best results when efflux was dependent upon the substrate concentration. To combine the two models, rather than choosing the substrate concentration to have a direct effect upon the expression of both efflux pumps, we choose to target the areas in the network that are most likely to be affected by a stressor, backed up by consultations with the Blair group and Piddock group at the University of Birmingham. We plot our updated GRN model that has substrate concentration as a signal in Figure 6.1, with the following changes exhibited by

dot dashed lines:

- The internal substrate concentration inhibits expression of *ramR* [39].
- The internal substrate concentration inhibits the concentration of Lon Protease within the cell [39].

In regards to the first change, *ramR* is the local repressor of *ramA*, the primary activator of both efflux pumps. By targeting *ramR*, we should see an indirect effect upon *ramA* expression. For the second change, by targeting Lon Protease concentration, we indirectly affect RamA concentration by altering the protein's degradation. In regards to the efflux of the substrate, we assume that efflux will correspond with both translation of AcrAB and AcrEF. We incorporate this by assuming that the efflux rate is proportional to the combined concentrations of these efflux pump proteins. In addition, since both MdsAB and MdtAB (which were both involved in the experiments) and their corresponding genes are not involved in this GRN, we include their corresponding efflux rates from their parameter fitted equations in the previous chapter. The equations for the combined GRN model are as follows:

$$\frac{dR_m}{dt} = k_1 \frac{K_I}{K_I + I} - \delta_m R_m, \tag{6.3}$$

$$\frac{dA_m}{dt} = k_2 \frac{K_R A + K_R K_A}{(A + K_{A_1})(R + K_R)} - \delta_m A_m, \tag{6.4}$$

$$\frac{dC_m}{dt} = k_3 \frac{K_{A_2}}{A + K_{A_2}} - \delta_m C_m, \tag{6.5}$$

$$\frac{dB_m}{dt} = k_4 \frac{K_{E_2} K_C A}{(K_C E + K_{E_2} K_C + K_{E_2} C)(K_{A_1} + A)} - \delta_m B_m, \tag{6.6}$$

$$\frac{dE_m}{dt} = k_5 \frac{K_H}{K_H + B} - \delta_m E_m, \tag{6.7}$$

$$\frac{dF_m}{dt} = k_6 \frac{K_H K_{E_1} A}{(K_H + B)(K_{E_1} + E)(K_{A_3} + A)} - \delta_m F_m, \tag{6.8}$$

$$\frac{dR}{dt} = \mu(m_1 R_m - \delta_p R), \tag{6.9}$$

$$\frac{dA}{dt} = m_2 A_m - \delta_p A - d_1 \frac{K_I}{K_I + I} A, \tag{6.10}$$

$$\frac{dC}{dt} = m_3 C_m - \delta_p C, \tag{6.11}$$

$$\frac{dB}{dt} = m_4 B_m - \delta_p B, \tag{6.12}$$

$$\frac{dE}{dt} = m_5 E_m - \delta_p E, \tag{6.13}$$

$$\frac{dF}{dt} = m_6 F_m - \delta_p F, \tag{6.14}$$

$$\frac{dX_{ST}}{dt} = \phi_{ST}\, I - \delta_{ST} X_{ST}, \tag{6.15}$$

$$\frac{\partial c_B}{\partial t} = D_B \nabla^2 c_B - \alpha c_B + \beta c_I, \tag{6.16}$$

$$\frac{\partial c_I}{\partial t} = D_I \nabla^2 c_I + \alpha c_B - \beta c_I, \tag{6.17}$$

$$\frac{\partial c_E}{\partial t} = D_E \nabla^2 c_E, \tag{6.18}$$

$$I(t) = \frac{3}{R_M^3} \int_0^{R_M} r^2\, c_B(r,t)\, dr. \tag{6.19}$$

Here I denotes the averaged internal concentration of bound substrate. As the mRNAs and proteins in the GRN only exist in the intracellular space, for simplicity of reducing the number of unknown parameters we have opted to not include spatial effects on these variables. In regards to our GRN equations, these have been modified compared to our model equations in Chapter 2. Firstly by using insights into the asymptotic analysis we have adapted equations (6.6) and (6.12). From the former we have removed activation from SoxS (also removing *soxS* mRNA and SoxS entirely from the model) whilst the latter we have removed CsrA from the translation terms of *acrAB*. By using updates from further knowledge into the GRN, we have updated equations (6.7) and (6.8), including the assumption that H-NS must not be active for mRNA transcription in both equations, whilst including dependence on RamA concentration on the latter. In addition, we have modified our basal *ramA* transcription rate in (6.4). Rather than including a standard basal transcription rate regardless of whether a protein is bound to the promoter region of *ramA*, we have chosen to only include transcription in the times where RamA or no proteins are bound to the promoter region. Finally, we have included the GRN influence from internal bound substrate by regulating *ramR* mRNA transcription in (6.3) and regulating Lon Protease degradation in (6.10). Whilst MdsAB and MdtAB do not feature within the GRN we include their rate of efflux in (6.15), this is in order for us to replicate

the full dynamics of the spatial model shown from the parameter fitting results in Chapter 5. The boundary conditions used in the above model are

$$D_B \frac{\partial c_B}{\partial r}\bigg|_{r=0} = 0, \qquad D_I \frac{\partial c_I}{\partial r}\bigg|_{r=0} = 0, \tag{6.20}$$

$$D_I \frac{\partial c_I}{\partial r}\bigg|_{r=R_M} = D_E \frac{\partial c_E}{\partial r}\bigg|_{r=R_M} = \left(P + \frac{B+F}{X_C} + X_{ST}\right) c_I(R_M, t) - P c_E(R_M, t), \tag{6.21}$$

$$D_B \frac{\partial c_B}{\partial r}\bigg|_{r=R_M} = 0, \qquad D_E \frac{\partial c_E}{\partial r}\bigg|_{r=R_B} = 0. \tag{6.22}$$

The first set of boundary conditions (6.20) represent axisymmetry in both angular dimensions for bound and unbound substrate. The boundary condition (6.21) represents our membrane boundary condition for unbound substrate. In this boundary condition we set our efflux rate $X = \dfrac{B+F}{X_C} + X_{ST}$. We have included the efflux rate of MdsAB and MdtAB directly as X_{ST} in this equation, however for AcrAB (B) and AcrEF (F) we link their concentrations to their efflux rates by assuming a directly proportional relationship, dividing both concentrations by an efflux rate constant X_C. The final set of boundary conditions (6.22) represents no flux boundary conditions, for bound substrate at the membrane and unbound substrate at the outer boundary. The initial conditions for each concentration are as follows

$$c_B(r,0) = \begin{cases} C_{B0}, & 0 \le r \le R_M, \\ 0, & R_M < r \le R_B, \end{cases} \qquad c_I(r,0) = \begin{cases} \gamma\, C_{B0}, & 0 \le r \le R_M, \\ 0, & R_M < r \le R_B, \end{cases} \tag{6.23}$$

where C_{B0} is the initial concentration of bound substrate. These initial conditions denote the concentrations for bound and unbound substrate. We express the initial condition for the unbound substrate as a ratio of the bound substrate using γ. In regards to the initial conditions for the GRN and efflux we have down-regulated initial conditions for the mRNAs and proteins of all repressor genes (*ramR*, *acrR* and *envR*). For the mRNAs and

proteins of the remaining genes (*ramA*, *acrAB* and *acrEF*), we will estimate their initial conditions in order to replicate the experiments. In the experiments, the cell has had a short amount of time to react to the substrate before the first measurement is taken and thus we should expect some activation of expression of the efflux genes and their activator genes. This behaviour is also shown in the parameter fitted efflux dynamics, as the initial conditions for the efflux rates of individual pumps are not fully down regulated. Finally, the initial condition for the efflux rate of MdsAB and MdtAB follows from our fitted initial condition in the previous chapter. The notation for the initial conditions are then as follows:

$$R_m(0) = C_m(0) = E_m(0) = G_{m0}, \quad R(0) = C(0) = E(0) = G_0, \quad X_{ST}(0) = X_{ST0}, \tag{6.24}$$

$$A_m(0) = A_{m0}, \qquad B_m(0) = B_{m0}, \qquad F_m(0) = F_{m0}, \tag{6.25}$$

$$A(0) = A_0, \qquad B(0) = B_0, \qquad F(0) = F_0. \tag{6.26}$$

We will provide the exact values in the following section. We list all of the variables and parameters used in our model in Tables 6.1 and 6.2. In all future simulations, we will be using the finite difference method in Chapter 5 to approximate our model, using spatial step $\Delta r = 0.25$ and time step $\Delta t = \dfrac{\Delta r^2}{4D_{MAX}}$, where $D_{MAX} = \max(D_I, D_E, D_B)$.

6.3 Numerical Simulations

In this section, we will exhibit numerical simulations of the multiscale model, attempting to replicate similar results from fitting to the same data used in Chapter 5. As we have assumed a directly proportional relationship between the fluorescence and intracellular bound concentration of substrate, we again model our substrate in terms of relative concentration so we can compare the model directly against the data. Since we have data for both wild-type and EST knockout strains, we compare the model against the data of these strains using parameter values from Table 6.2. We have aimed to keep parameters as similar as possible to those in the previous GRN model in Chapter 2 and have main-

Variables	Description	Units
R_m	Concentration of *ramR* mRNA	nM
R	Concentration of RamR	nM
A_m	Concentration of *ramA* mRNA	nM
A	Concentration of RamA	nM
C_m	Concentration of *acrR* mRNA	nM
C	Concentration of AcrR	nM
B_m	Concentration of *acrAB* mRNA	nM
B	Concentration of AcrAB	nM
E_m	Concentration of *envR* mRNA	nM
E	Concentration of EnvR	nM
F_m	Concentration of *acrEF* mRNA	nM
F	Concentration of AcrEF	nM
X	Combined efflux rate of all pumps	$\mu m\, min^{-1}$
X_{ST}	Efflux rate of MdsAB and MdtAB	$\mu m\, min^{-1}$
c_B	Relative concentration of bound substrate	N/A
c_I	Relative concentration of unbound substrate	N/A
N	Averaged intracellular concentration of bound substrate	N/A

Table 6.1: Variables used in our multiscale model along with their respective units.

Parameter	Description	Estimate	Units
k_1	Transcription Rate of *ramR* mRNA	10	nM min^{-1}
m_1	Translation Rate of RamR	1	min^{-1}
k_2	Transcription Rate of *ramA* mRNA	10	nM min^{-1}
m_2	Translation Rate of RamA	1	min^{-1}
k_3	Transcription Rate of *acrR* mRNA	10	nM min^{-1}
m_3	Translation Rate of AcrR	1	min^{-1}
k_4	Transcription Rate of *acrAB* mRNA	10	nM min^{-1}
m_4	Translation Rate of AcrAB	1	min^{-1}
k_5	Transcription Rate of *envR* mRNA	10	nM min^{-1}
m_5	Translation Rate of EnvR	1	min^{-1}
k_6	Transcription Rate of *acrEF* mRNA	10	nM min^{-1}
m_6	Translation Rate of AcrEF	1	min^{-1}
δ_m	Degradation Rate of mRNA	1	min^{-1}
δ_p	Degradation Rate of proteins	0.05	min^{-1}
$d_1 L$	Degradation caused by Lon Protease	0.37	min^{-1}
K_R	Dissociation Constant of RamR	6.58	nM
K_{A_1}	Dissociation Constant of RamA with *ramA* and *acrAB*	2	nM
K_{A_2}	Dissociation Constant of RamA with *acrR*	2	nM
K_{A_3}	Dissociation Constant of RamA with *acrEF*	60	nM
K_C	Dissociation Constant of AcrR	20.2	nM
K_{E_1}	Dissociation Constant of EnvR with *acrEF*	20.2	nM
K_{E_2}	Dissociation Constant of EnvR with *acrAB*	20.2	nM
K_I	Saturation Constant of Substrate	0.3	nM
K_H	Dissociation Constant of H-NS	1	nM
μ	Mutation Coefficient	0 or 1	N/A
P	Permeability Mass Transfer Coefficient	0.01	$\mu m\, min^{-1}$
X_C	Efflux Conversion Constant	500	nM $min\, \mu m^{-1}$
D_B	Diffusion Coefficient Of Bound Substrate	0	$\mu m^2\, min^{-1}$
D_I	Diffusion Coefficient Of Unbound Intracellular Substrate	2.30 or 1	$\mu m^2\, min^{-1}$
D_E	Diffusion Coefficient Of Unbound Extracellular Substrate	1.01	$\mu m^2\, min^{-1}$
R_M	Membrane Radius	2	μm
R_B	Outer Boundary Radius	4	μm
α	Unbinding Rate Of Bound Substrate	0.22	min^{-1}
β	Binding Rate Of Unbound Substrate	0.09	min^{-1}
ϕ_{ST}	Increase In MdsAB And MdtAB Efflux Rate	1.57×10^{-4}	$\mu m\, min^{-1}$
δ_{ST}	Decrease In MdsAB And MdtAB Efflux Rate	2.94×10^{-2}	$\mu m\, min^{-1}$

Table 6.2: Parameters used in our multiscale model with their estimated values and units.

tained the fitted spatial parameters from Chapter 5. We opt not to compare against the data of the remaining strains: AST (AcrAB, MdsAB and MdtAB), AET (AcrAB, AcrEF and MdtAB), AES (AcrAB, AcrEF and MdsAB), ST (MdsAB and MdtAB). We do not use this data as the first three strains (which have AcrAB active) do not hugely differ in dynamics to the wild-type strain. Furthermore for the last strain, the genes that govern MdsAB and MdtAB do not feature within our GRN. For comparing against the data for the EST strain, we have knocked out $acrAB$ in the GRN by setting $k_4, m_4 = 0$. Although we do not have the data for any RamR mutant strain, we will run simulations to predict the behaviour of the strain by mutating RamR in the GRN, setting $\mu = 0$. Recall that this mutation is known for causing the strain to confer MDR. In total we simulate four strains: wild-type, EST knockout, RamR mutant and EST RamR mutant, detailing them in Table 6.3.

Strain Name	Active Efflux Pumps	Mutations
Wild-type	AcrAB, AcrEF, MdsAB, MdtAB	N/A
EST	AcrEF, MdsAB, MdtAB	N/A
RamR Mutant	AcrAB, AcrEF, MdsAB, MdtAB	RamR
EST RamR mutant	AcrEF, MdsAB, MdtAB	RamR

Table 6.3: A summary of the strains involved in this section. We list each strain's active efflux pumps and any mutations to their GRNs.

For the following simulations, we set down-regulated initial conditions for the repressor mRNAs and proteins ($G_{m0} = G_0 = 0.01$nM) and set the initial condition for the efflux rate of MdsAB and MdtAB from the parameter fitting results ($X_{ST0} = 2.12 \times 10^{-4}$nM). For the mRNAs and proteins of the remaining genes *ramA*, *acrAB* and *acrEF*, their initial conditions will vary depending on the strain we are modelling. To choose these initial conditions, we first run a simulation for each strain with down-regulated initial conditions for all mRNAs and proteins ($A_{m0} = A_0 = B_{m0} = B_0 = F_{m0} = F_0 = 0.01$nM). For the wild-type and RamR mutant strains, we expect *acrEF* expression to be down-regulated as *acrAB* is active, so we maintain the initial conditions $F_{m0} = F_0 = 0.01$nM. For the EST and EST RamR mutant strains, the gene *acrAB* is knocked out entirely so we set $B_{m0} = B_0 = 0$. For the remaining variables, in the wild-type and EST strains, we choose the initial condition of the variables to be half of the maximum value over the full time course in the down-regulated simulation i.e. the system has had a short period of time to react from a down-regulated state. For the RamR mutant and EST RamR mutant strains, we choose the initial condition of the variables to be the steady state values in the down-regulated simulation i.e. with RamR mutated there is always high expression of *ramA* and *acrAB* or *acrEF*. In addition, as RamR is mutated in the latter two strains, we set the initial condition of RamR protein $R(0) = 0$nM. We display these initial conditions in Table 6.4. We produce simulations using these initial conditions in Figures 6.3-6.6 for the wild-type strain, EST (AcrAB knockout) strain, RamR mutant strain and EST RamR mutant strain respectively.

Strain Name	A_{m0} (nM)	A_0 (nM)	B_{m0} (nM)	B_0 (nM)	F_{m0} (nM)	F_0 (nM)	G_0 (nM)	$R(0)$ (nM)
Wild-type	3.6256	12.1458	3.1665	36.9524	0.01	0.01	0.01	0.01
EST	3.5985	12.2401	0	0	0.4798	3.5434	0.01	0.01
RamR Mutant	10	25.3726	5.0964	102.0014	0.01	0.01	0.01	0
EST RamR mutant	10	33.5428	0	0	0.3297	6.7758	0.01	0

Table 6.4: Initial condition values for strains involved in this section.

For the wild-type strain mRNAs (Figure 6.3 (a)) and proteins (Figure 6.3(b)), at early time we see low concentrations of *ramR* mRNA and RamR as the gene is inactive in the presence of a high internal substrate concentration. This in turn allows fast expression of *ramA*, resulting in large concentrations of RamA protein, activating the expression of the efflux pump gene *acrAB*. Since the local efflux repressor *acrR* is inhibited by a large concentration of RamA, we see higher expression of *acrAB*. This leads to an increase in efflux rate (Figure 6.3(d)) and resulting expulsion of substrate from within the cell (Figure 6.3(c)). Once the intracellular bound substrate concentration is sufficiently low, we see increased activation of *ramR* expression resulting in inhibition of the expression of the network's main activator *ramA*. The local efflux repressor *acrR* is able to express at a faster rate due to a lower concentration of RamA. The lower concentration of RamA and larger AcrR concentration result in less *acrAB* expression both indirectly and directly respectively. This results in a decrease in efflux rate and results in an equilibrium between the transfer of intracellular and extracellular substrate. We note that the model comparison to the data (Figure 6.3(c)) is not perfect, with mid time dynamics appearing outside the standard error of the data. However, we have opted not to largely differ our GRN parameter choices from Chapter 2 by manually editing parameters as little as possible. Alternatively, we could run new parameter fitting exercises including the GRN parameters, however due to the high number of parameters within the network compared to the available data, there will likely be many non identifiable parameters.

We show the simulation of the EST strain in Figure 6.4. For (a) and (b), we note that for all time there is no expression of *acrAB* due to the gene being knocked out in this strain. Without the presence of AcrAB in this strain, there is no activation of H-NS meaning that both *envR* and *acrEF* can be expressed freely. Thus at early time, similar to the wild-type strain, with low concentrations of *ramR* mRNA and RamR due to a high internal substrate concentration, we see activation of *ramA* expression, with RamA this time activating expression of *acrEF*. Due to the difference in the dissociation constants of RamA with *acrEF* and *acrAB*, we see less *acrEF* expression compared to the expression

of *acrAB* in the wild-type strain (Figure 6.3(a) and (b)). The expression of *acrEF* is also reduced by the constitutive expression of *envR* and hence we see a lower efflux rate (Figure 6.4 (d)) than in the wild-type strain (Figure 6.3 (d)). Thus substrate is expelled from the intracellular space at a slower rate (Figure 6.4 (c)). There is also less expression of *ramR* due to a higher intracellular substrate concentration, which reaches an equilibrium steady state with the extracellular substrate at a higher concentration than that of the wild-type strain. We note that we have achieved a good model fit to the data in this case (Figure 6.4 (c)), with almost all of the model fitting within the standard error of the data.

We show the simulation of the RamR mutant strain in Figure 6.5, exhibited against the simulation of the wild-type strain in 6.5 (c) as a comparison (recall that there is no experimental data for this strain). Following from Chapter 2, we have assumed that RamR protein is mutated and thus there is no functional RamR in the system (Figure 6.5 (a) and (b)). This means that there is no inhibition of *ramA* expression, resulting in large concentrations of RamA activating *acrAB* expression. This results in a large efflux rate (Figure 6.5 (d)), comparatively larger than the wild-type strain (Figure 6.3 (d)). As the intracellular bound concentration of substrate decreases (Figure 6.5 (c)), we see increased degradation of RamA caused by an increased concentration of Lon Protease. At long time we see both concentrations of RamA and AcrAB reach steady state, with almost all substrate expelled from the intracellular space. Compared to the wild-type strain (Figure 6.5 (c)), we can see that there is less feedback from the internal substrate concentration within the GRN on mid and long time. Mainly, the intracellular bound substrate reaches a steady state that is below the concentration shown by the wild-type, clearly exhibiting the strains ability to display MDR.

We show the simulation of the RamR mutant EST strain in Figure 6.6, exhibited against the EST strain simulation for comparison in Figure 6.6 (c). Similar to the previous strain there is no restriction upon expression of *ramA* due to no presence of RamR (Figure 6.6 (a) and (b)). However in this strain as *acrAB* is knocked out, we see RamA activating *acrEF* expression. Whilst early time does not hugely differ from the normal EST strain,

we see that with a higher RamA concentration, the concentration of AcrEF achieves a higher steady state. This results in an efflux rate (Figure 6.6 (d)) similar to the wild-type case (Figure 6.3 (d)) and a steady state of intracellular bound substrate concentration (Figure 6.6 (c)) lower than the normal EST strain (Figure 6.4 (c)) i.e. this strain is predicted to have a higher efflux capability.

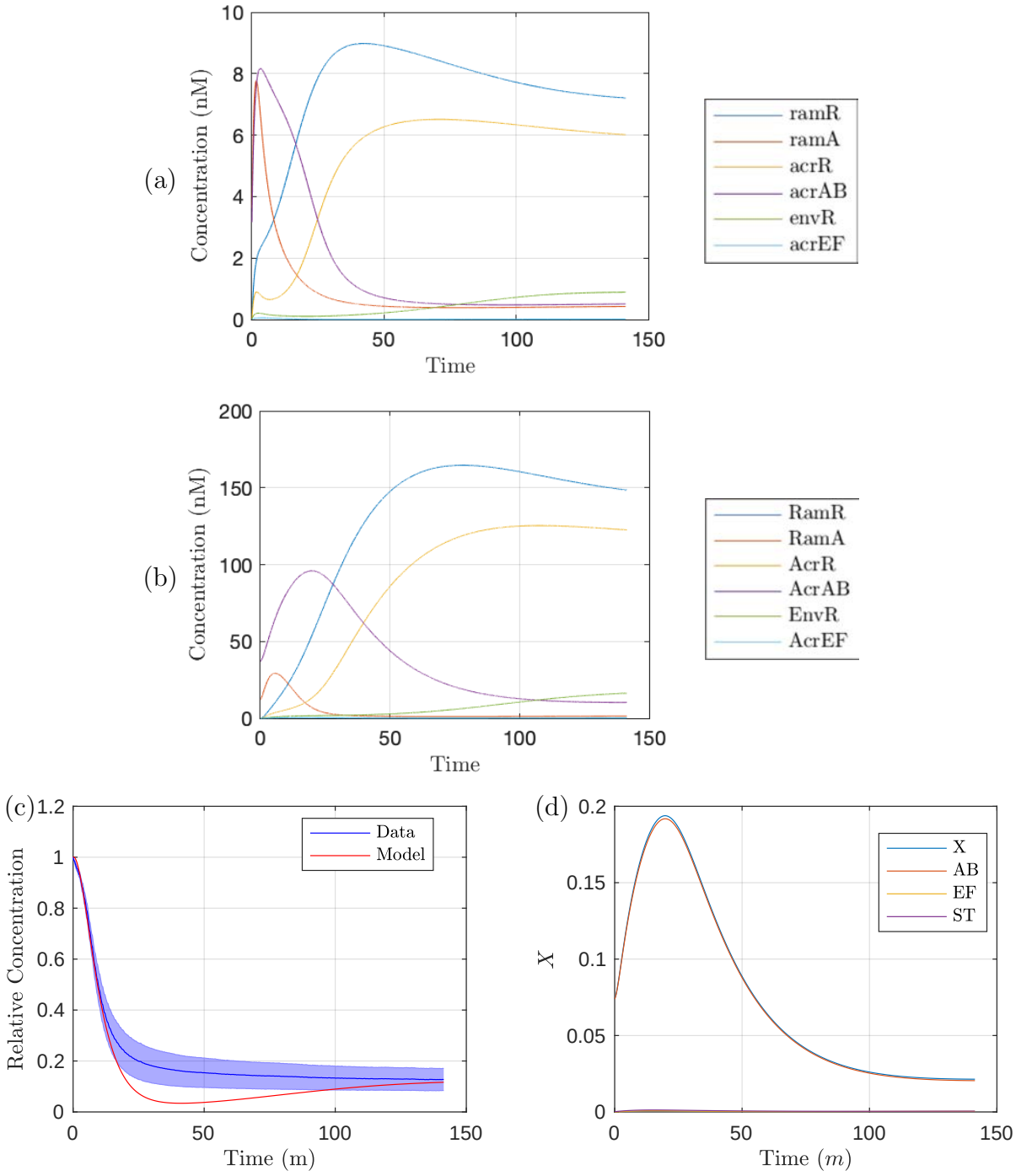

Figure 6.3: Our multiscale model of the wild-type strain, run for the time course of the wild-type data. In (a) we show the concentration of mRNAs over time, (b) we show the concentration of proteins. In (c) we exhibit the substrate concentration over time against the experimental data and (d) the corresponding efflux rate X, with efflux rate contributed by AcrAB (AB), AcrEF (EF) and the sum of MdsAB and MdtAB (ST).

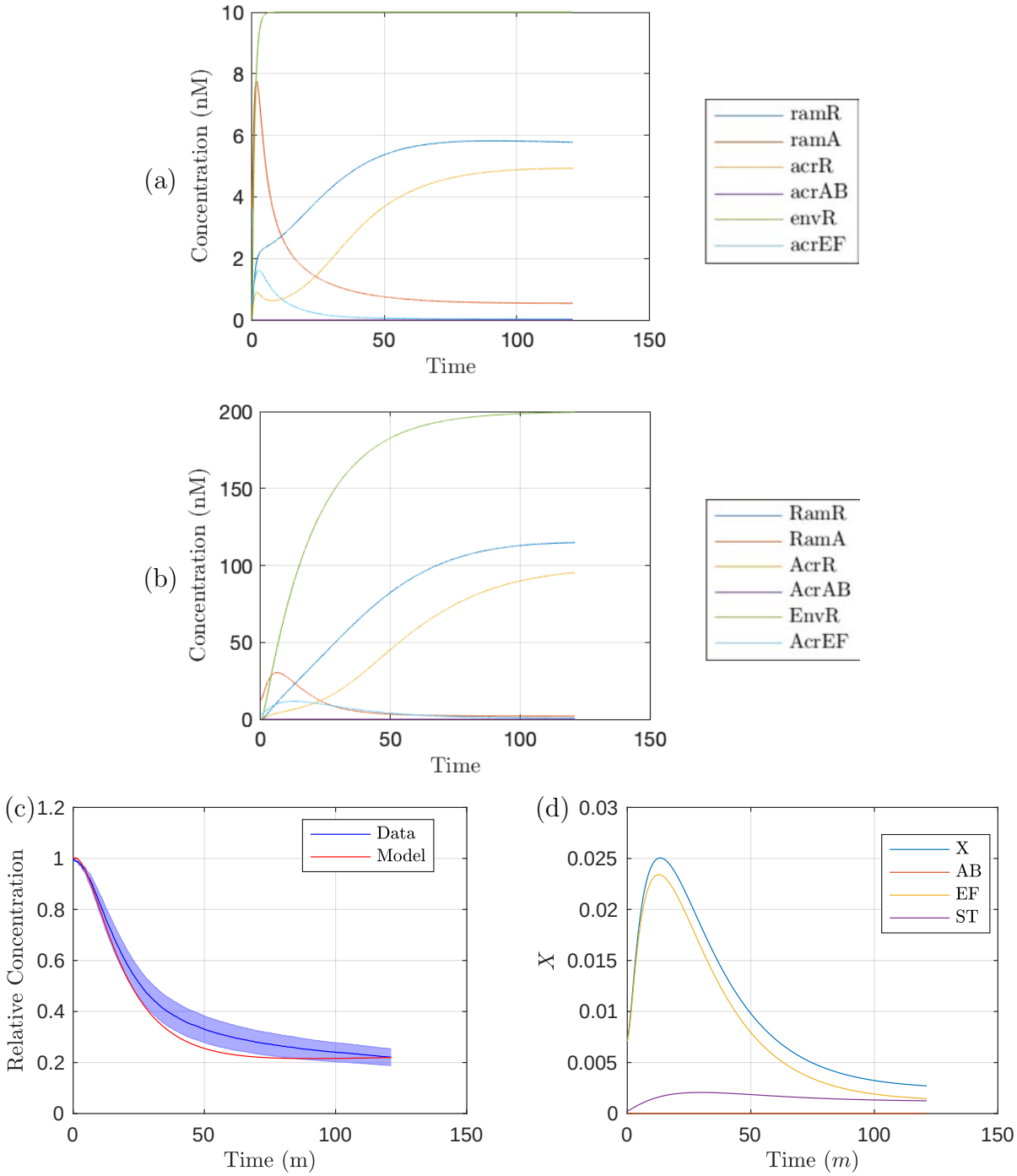

Figure 6.4: Our multiscale model of the EST strain (*acrAB* knockout, $k_4, m_4, B_m(0), B(0) = 0$), run for the time course of the EST data. In (a) we show the concentration of mRNAs over time, (b) we show the concentration of proteins. In (c) we exhibit the substrate concentration over time against the experimental data and (d) the corresponding efflux rate X, with efflux rate contributed by AcrAB (AB), AcrEF (EF) and the sum of MdsAB and MdtAB (ST).

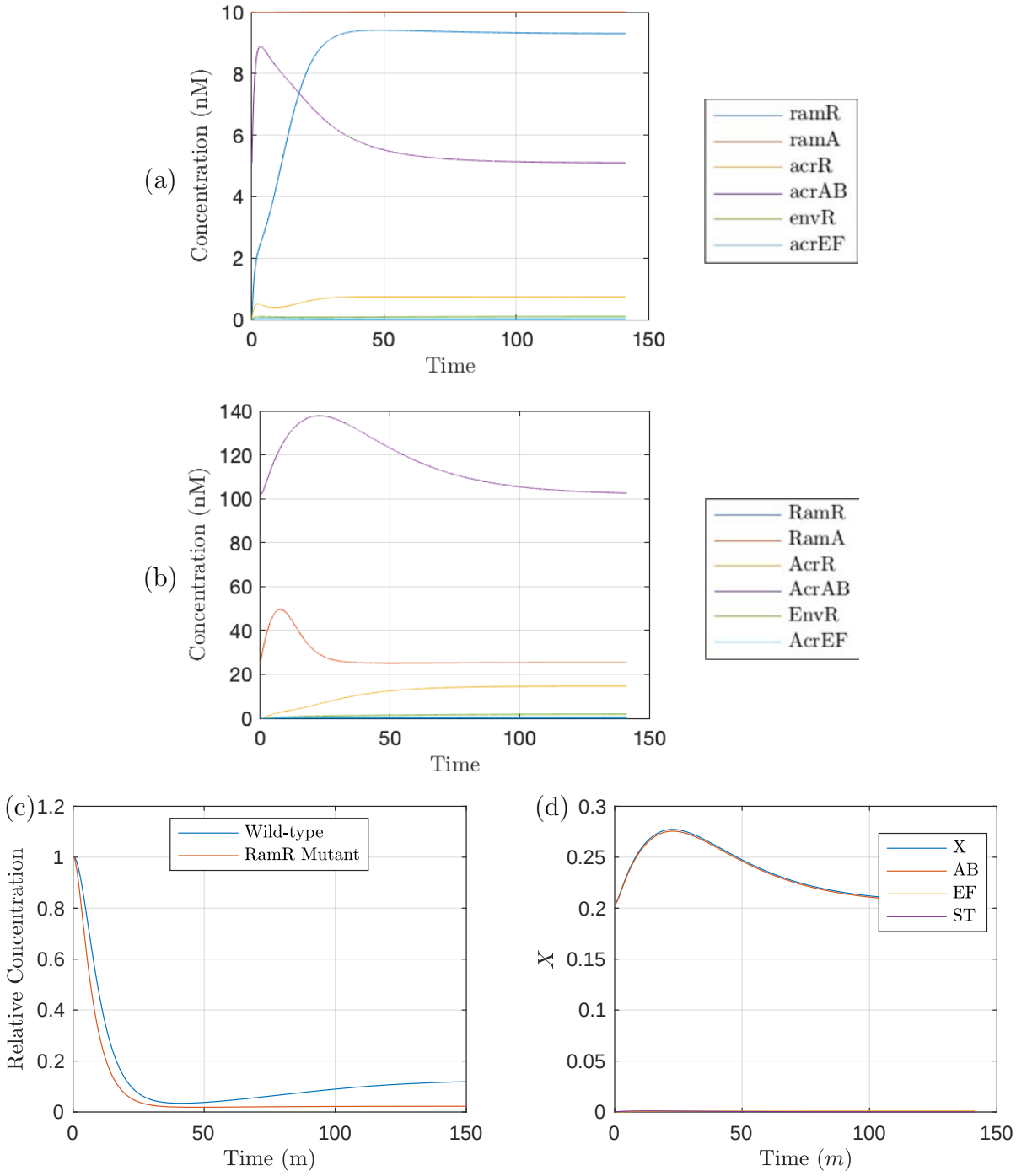

Figure 6.5: Our multiscale model showing a RamR mutant strain ($\mu, R(0) = 0$), run for the time course of the wild-type data. In (a) we show the concentration of mRNAs over time, (b) we show the concentration of proteins. In (c) we exhibit the substrate concentration over time compared against the simulation from the wild-type strain and (d) the corresponding efflux rate X, with efflux rate contributed by AcrAB (AB), AcrEF (EF) and the sum of MdsAB and MdtAB (ST).

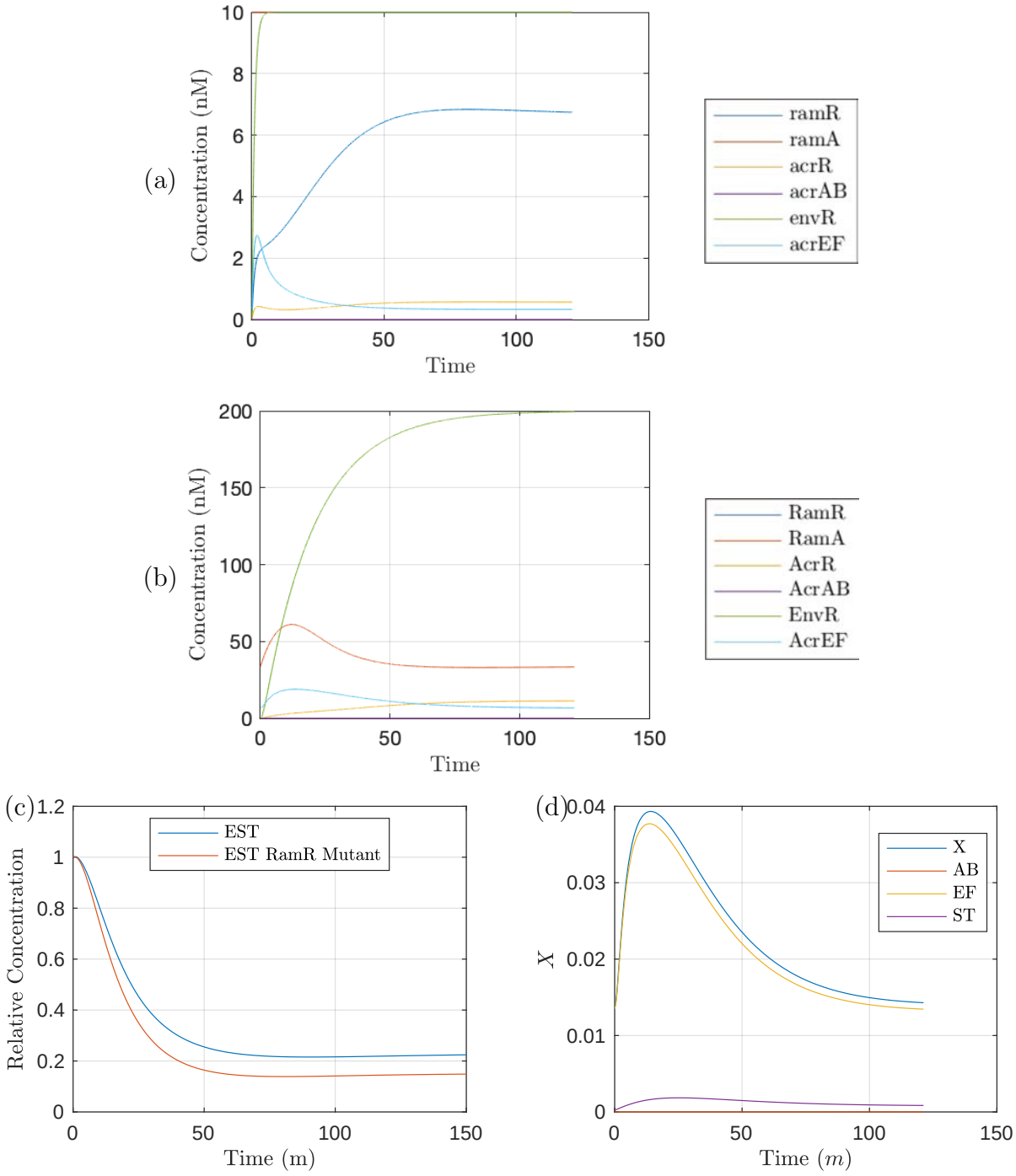

Figure 6.6: Our multiscale model showing the RamR mutant EST strain ($k_4, m_4, B_m(0)$, $B(0), \mu, R(0) = 0$), run for the time course of the EST data. In (a) we show the concentration of mRNAs over time, (b) we show the concentration of proteins. In (c) we exhibit the substrate concentration over time compared against the simulation from the EST case and (d) the corresponding efflux rate X, with efflux rate contributed by AcrAB (AB), AcrEF (EF) and the sum of MdsAB and MdtAB (ST).

Finally, in Figure 6.7, we compare the substrate expulsion of all strains. In (a) we plot all time dependent simulations of the strains on one plot. In (b) we use the trapezium rule (function "trapz" in MATLAB) to approximate the area under the curve (AUC) of each strain simulated in (a). The AUC shows us the overall relative substrate exposure over the simulated time course [90]. Immediately we can clearly see the benefits of the RamR mutation for both strains as there is a clear reduction in substrate over all time for strains with this mutation over their counterparts (Figure 6.7(b)). It is also interesting to note that at steady state the EST RamR mutant achieves a similar value to that of the wild-type strain (Figure 6.7(a)). This shows that even with *acrAB* knocked out, the strain (which has mutated RamR) is able to compensate by using the secondary pump system *acrEF* to achieve similar efflux in the long term to that of the wild-type. Finally we note that, initially, the wild-type strain and RamR mutant display similar levels of efflux (albeit the RamR mutant exhibiting slightly faster expulsion). However in the long term, the RamR mutant maintains high levels of efflux, almost eliminating all substrate from the intracellular space. This clearly shows the advantages of the RamR mutation, the strain is able to prevent large concentrations of intracellular substrate and this is a huge contributor to its ability to exhibit MDR.

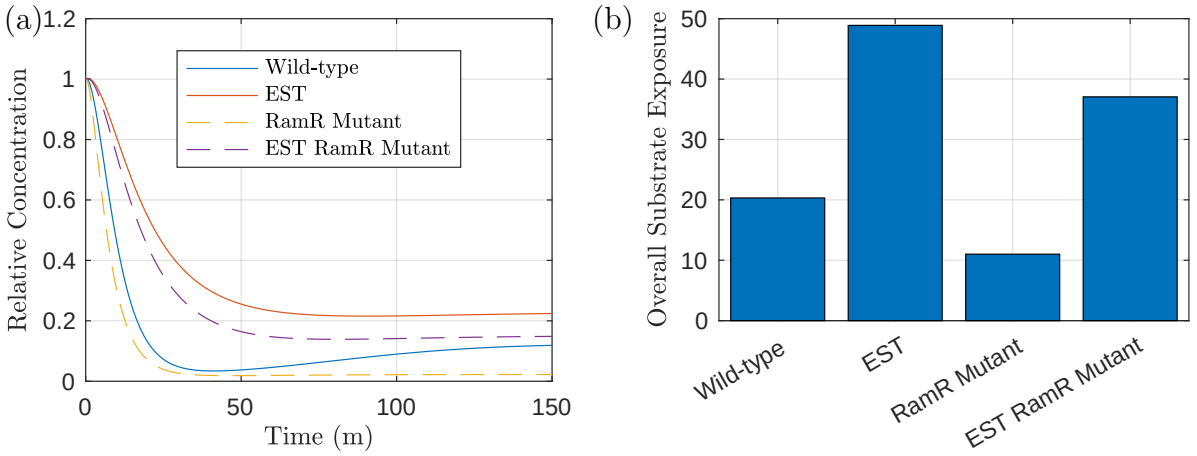

Figure 6.7: Our multi scale model showing the intracellular bound substrate concentration over time for all strains. In (a) we show time dependent plots of all strains, in (b) we approximate the AUC of the strains in (a) using the trapezium rule, to show the overall relative substrate exposure. The wild-type strain is simulated using all parameters values in Table 6.2, the EST case has $k_4, m_4 = 0$, RamR mutant $\mu = 0$, and EST RamR mutant $k_4, m_4, \mu = 0$.

6.4 Parameter Sensitivity

Similar to analysis in previous chapters, we conduct a sensitivity analysis of the parameters in our model. Here our equation for the relative sensitivity is

$$S = \frac{\delta \bar{I}}{\delta P}, \tag{6.27}$$

where $\delta \bar{I}$ represents the change of bound intracellular substrate concentration steady state for the simulated strain, and δP represents the change of the parameter being varied. If we define P^* to be the default parameter value for the current parameter being varied, we then vary the parameter in the space $[0, 10P^*]$. By using a Latin hypercube method of sampling, we choose 10000 points in the parameter space and apply these to each individual parameter, finding the relative sensitivity for each point. We choose to omit the parameters primarily involved in the spatial distribution of substrate, only varying parameters involved in the GRN, since this is the mechanism we wish to target. We also choose to omit the degradation parameters, since these are mostly universal to all of the genes. Hence varying these parameters would involve targeting all genes simultaneously which is not only an unrealistic target but will exhibit similar behaviour to preventing the whole network from being expressed.

6.4.1 Wild-type strain

We exhibit the parameter sensitivity results using the steady state for the wild-type strain with box plots in Figure 6.8. In (a) we denote the dissociation and saturation constants involved in the model, we can immediately see that the dissociation constant related to RamR (K_R) is the most sensitive. By varying this parameter we should see direct effects on the activation of *ramA* transcription. It is interesting to note that the sensitivity of this parameter is larger than that of any of the dissociations constants related to RamA (K_{A_i}). Thus in this strain, targeting *ramA* expression via a repressor to reduce the genes expression may be a more effective method than targeting the RamA binding process to the promoter regions of various other genes in the network. However, we must note that

the sensitivity of all RamA dissociation constants are still significant, with the dissociation with *ramA* and *acrAB* (K_{A_1}) showing more sensitivity than the dissociation with *acrR* (K_{A_2}) and *acrEF* (K_{A_3}). This is expected, as in this wild-type strain we have normal levels of *acrAB* expression, so we should expect lower expression of *acrEF* and hence a smaller sensitivity upon parameters related to it. We note that the other two parameters with notable significance, are related to AcrR (K_C) and substrate (K_I). The first of these is expected due to direct inhibition of expression of the efflux pump gene *acrAB*. Regarding K_I, we do not know the full mechanisms behind how the substrate interacts with the network, but this could provide insight for potential further research. We show transcription and translation rates in (b). We note that for each individual gene the transcription rates show similar sensitivity to the translation rates. Thus when targeting gene expression, both transcription and translation seem to be feasible targets. It is clear that the wild-type system is the most sensitive to the expression of four genes, namely *ramR* and *ramA*, *acrR* and *acrAB*. This gives us clear insights into the most important genes to target when inhibiting efflux in a wild-type strain. The other genes are *envR* and *acrEF*, with the strain exhibiting little sensitivity to either. This again is expected, as with no major restrictions upon *acrAB* expression we expect H-NS to be prevalent and the expression of *envR* and *acrEF* to be minimal.

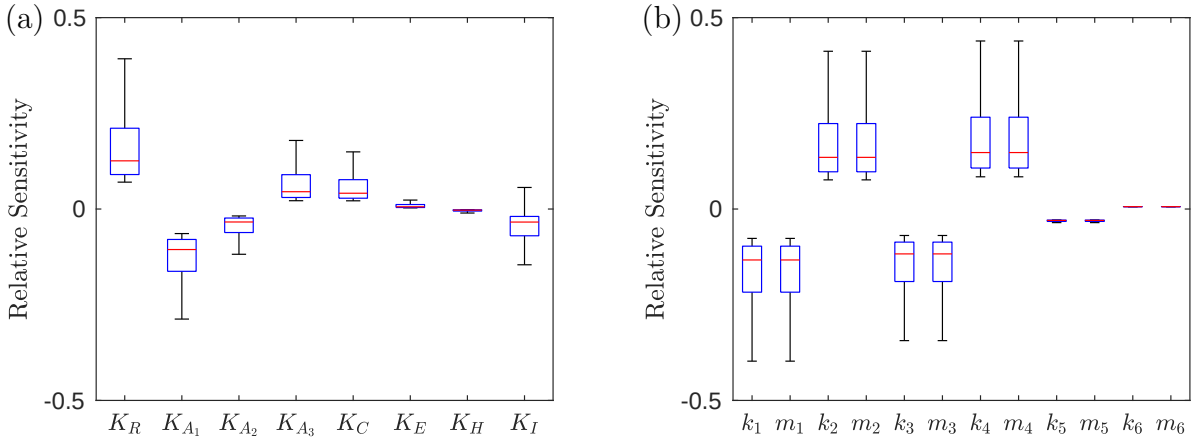

Figure 6.8: Box plots showing the relative sensitivity of parameters involved in the GRN for the wild-type strain, varying parameters in the region $[0, 10P^*]$, where P^* is the default parameter value. In (a) we depict the dissociation and saturation constants, in (b) we depict the various transcription and translation rates related to mRNAs and proteins.

6.4.2 EST strain

We exhibit the parameter sensitivity results using the steady state for the EST strain in Figure 6.9. As expected due to the gene being knocked out, we can immediately see that all parameters involved with *acrAB* have lost all sensitivity. In (a) the most sensitive parameter is the dissociation of RamA with *acrEF* (K_{A_3}). This is expected as AcrEF is the only active efflux pump in this strain. Compared to the wild-type strain (Figure 6.8), we can see decreased sensitivity to the dissociation of RamR (K_R). This could be due to RamA having a smaller activation effect on *acrEF* expression than *acrAB* expression, thus inhibition of *ramA* expression from RamR would have less of an effect. We also see increased sensitivity of the dissociation of EnvR from *acrAB* and *acrEF*. With *envR* being constitutively expressed in this case, we should expect higher sensitivity from this local repressor. In (b) we note the most sensitive parameters are related to the expression of *ramR*, *ramA*, *envR* and *acrEF*. The strain shows similar sensitivities to all of these genes and thus targeting any of their expressions should be a viable target for inhibiting efflux. Notably however, the strain is most sensitive to *envR* and *acrEF*, leading us to believe that repressing *acrEF* expression directly or via *envR* may be a more effective target than preventing activation of the gene's expression.

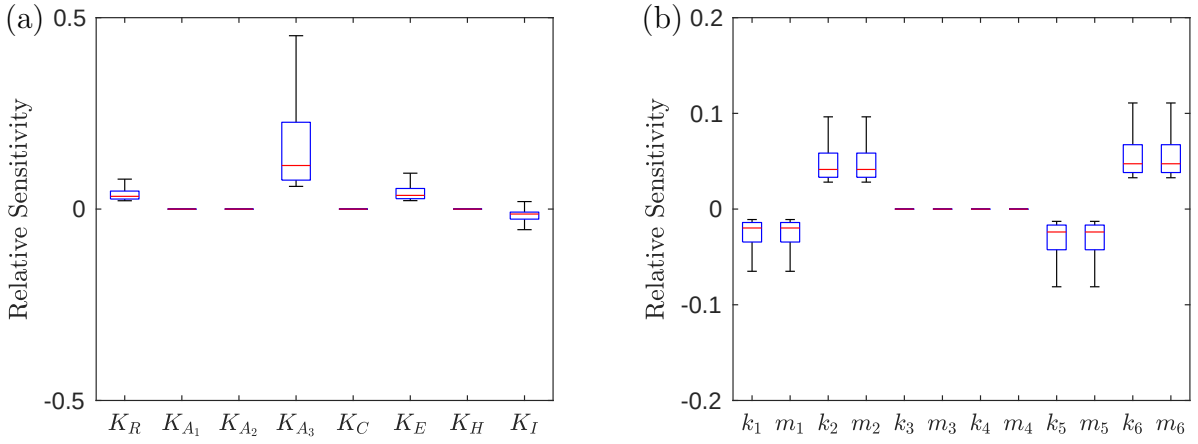

Figure 6.9: Box plots showing the relative sensitivity of parameters involved in the GRN for the EST strain, varying parameters in the region $[0, 10P^*]$, where P^* is the default parameter value. In (a) we depict the dissociation and saturation constants, in (b) we depict the various transcription and translation rates related to mRNAs and proteins.

6.4.3 RamR mutant strain

We exhibit the parameter sensitivity results using the steady state for the RamR mutant strain in Figure 6.10. Immediately, compared to the wild-type strain (Figure 6.8) we can see that all of the parameters relating to *ramR* (K_R, k_1 and m_1) all have no sensitivity due to the mutations of RamR. Additionally the sensitivity of the desaturation constant relating to substrate (K_I) is reduced, which could be due to the substrate only now having an effect on Lon Protease concentration due to the mutations of RamR. In (a) we can see that the dissociation of RamA with *acrR* (K_{A_2}) is the most sensitive, this is interesting to note as our time dependent asymptotic analysis uncovered this link as one of the key mechanisms for activating efflux in this mutant strain. The other RamA dissociation parameters range of sensitivity are both decreased compared to the wild-type strain, which could be due to the higher concentration of RamA in this strain, such that large activation will occur regardless of the dissociation constant. We note the sensitivity of dissociation related to *acrEF* (K_{A_3}) is minimal, which is expected due to high *acrAB* expression in this strain. We also see an increase in the dissociation of H-NS (K_H), which could be due to a higher concentration of RamA. If H-NS does not inhibit *acrEF* expression so strongly, we would see higher activation of *acrEF* expression through large concentrations of RamA. In (b), we can see that the most sensitive parameters are related to the expression of *ramA*, *acrR* and *acrAB*. The strain is most sensitive to *acrAB* expression, which we would expect as it is direct expression of one of the efflux pumps, which is over-expressed in this strain. Interestingly, there is increased sensitivity to changes in *envR* expression compared to the wild-type (Figure 6.8). Whilst we have hardly any expression of *envR* in this strain, the sensitivity increase here could be due to the overexpression of *acrAB*. We note that both RamR mutant and wild-type strains exhibit similar sensitivity to changes in *ramA* and *acrR* expression, even with the differences within their GRNs.

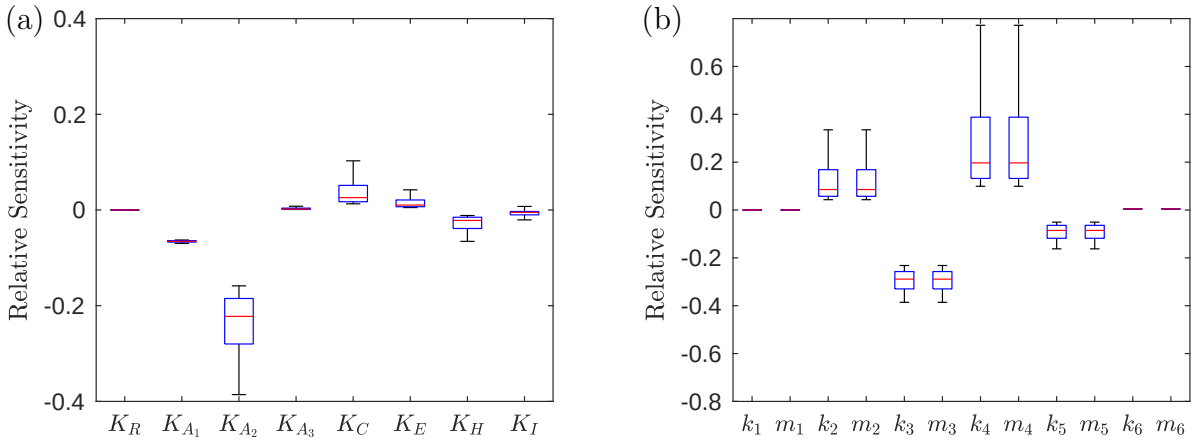

Figure 6.10: Box plots showing the relative sensitivity of parameters involved in the GRN for the RamR mutant strain, varying parameters in the region $[0, 10P^*]$, where P^* is the default parameter value. In (a) we depict the dissociation and saturation constants, in (b) we depict the various transcription and translation rates related to mRNAs and proteins.

6.4.4 EST RamR mutant strain

We exhibit the parameter sensitivity results using the steady state for the EST RamR mutant strain in Figure 6.11. As there are multiple manipulations to the genes in this network, we can see that the amount of parameters that exhibit sensitivity has decreased compared to the wild-type strain. As expected, all parameters relating to *acrAB* and *ramR* are fully insensitive. Compared to the EST strain (6.9), we can see in (a) that the most sensitive parameter is the dissociation constant of EnvR from *acrEF* and *acrAB* (K_E). This could be due to the overexpression of *acrEF* in this strain and hence the local repressor would be likely to exhibit higher sensitivity. We note that the dissociation of RamA with *acrEF* (K_{A_3}) has reduced in this strain, which could be due to a higher concentration of RamA in the system and hence large activation is likely to occur regardless of the dissociation constant. In (b) we can see that the parameters related to the expression of all genes have become much more sensitive compared to the EST strain, with the strain most sensitive to changes in *envR* and *acrEF* expression. Again, this leads us to believe that repressing *acrEF* expression may be a more effective target than preventing activation of the gene's expression.

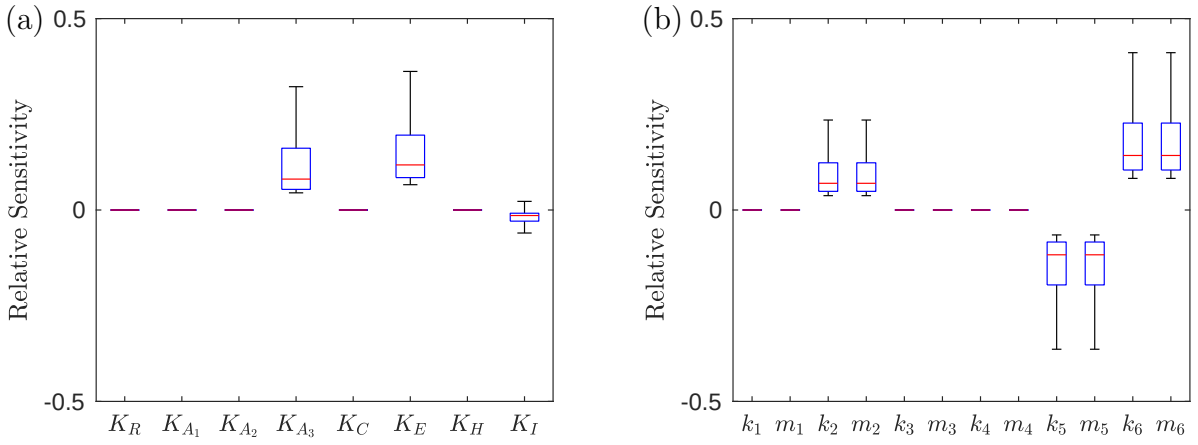

Figure 6.11: Box plots showing the relative sensitivity of parameters involved in the GRN for the EST RamR mutant strain, varying parameters in the region $[0, 10P^*]$, where P^* is the default parameter value. In (a) we depict the dissociation and saturation constants, in (b) we depict the various transcription and translation rates related to mRNAs and proteins.

6.5 Network Manipulation

While the parameter sensitivity analysis has given us insight into the sensitivity of the substrate at steady state, it is important to note that we do not know the effects caused by manipulating parameters through the rest of the timecourse. Therefore we take the parameters to which the model is most sensitive in the above analysis and plot relevant time dependent simulations. As we would like to repress efflux expression for all strains, we omit parameters relating to *ramR* expression, as RamR is not present in our mutant strains. In addition we also omit direct *acrAB* and *acrEF* expression through transcription and translation, due to them both being trivial targets to vary efflux expression. For each parameter, we either multiply or divide the original parameter by a factor of ten, in order to exhibit a proportionally sizeable manipulation from the original parameter value. To exhibit our manipulations, for each strain we plot a simulation with default parameter values against a simulation with manipulated parameter values. We find the AUC for both of these simulations using the trapezium rule (function "trapz" in MATLAB) and plot the difference between AUC for both default and manipulated simulations.

Firstly, we show the effects of varying gene expression through transcription, demonstrated by Figures 6.12-6.14. In Figure 6.12, we can see the effects of decreasing expression of *ramA*. We note that a decrease in efflux is universal between all strains i.e. the intracellular substrate increases. This is further highlighted in Figure 6.12 (e) as the change in overall substrate exposure is large for all strains. However, we note that when it comes to the EST strain (Figure 6.12 (b)), the steady state is hardly altered compared to the normal simulation. This highlights the importance of time dependent simulations as there is a sizeable difference in mid time dynamics which is missed by the parameter sensitivity analysis.

In Figure 6.13, we can see the effects of increasing expression of *acrR*. Notably we see no effects in either of the EST strains (Figure 6.13 (b), (d) and (e)). This is expected as AcrR is the local repressor of *acrAB*, which is not present in these strains. Noticeable differences to efflux dynamics is however shown in the wild-type and RamR mutant strains, with an increase in intracellular substrate concentration over all time.

In Figure 6.14, we can see the effects of increasing expression of *envR*. Similar to *ramA*, we can see notable differences to the efflux dynamics in all strains, shown by notable differences to the substrate exposure (Figure 6.14 (e)). However, barring the EST RamR mutant strain (Figure 6.14 (d)), there is very little difference to the steady states of all manipulated strains. This clearly differs from the early and mid time dynamics, with sizeable differences compared to the default simulations. Thus, this may give us insights into how *envR* expression effects the long term dynamics: the analysis leads us to believe that there are only large changes to the steady state of substrate concentration when a large concentration of AcrEF is present. In comparison between all three manipulations (Figures 6.12-6.14), *acrR* expression is only a viable target for inhibiting efflux in strains with *acrAB* expression. We can see that varying *ramA* expression has the largest effect upon the long term dynamics of substrate concentration in the majority of the strains, whereas interestingly varying *envR* expression has the largest effect on the early and mid time dynamics of substrate concentration.

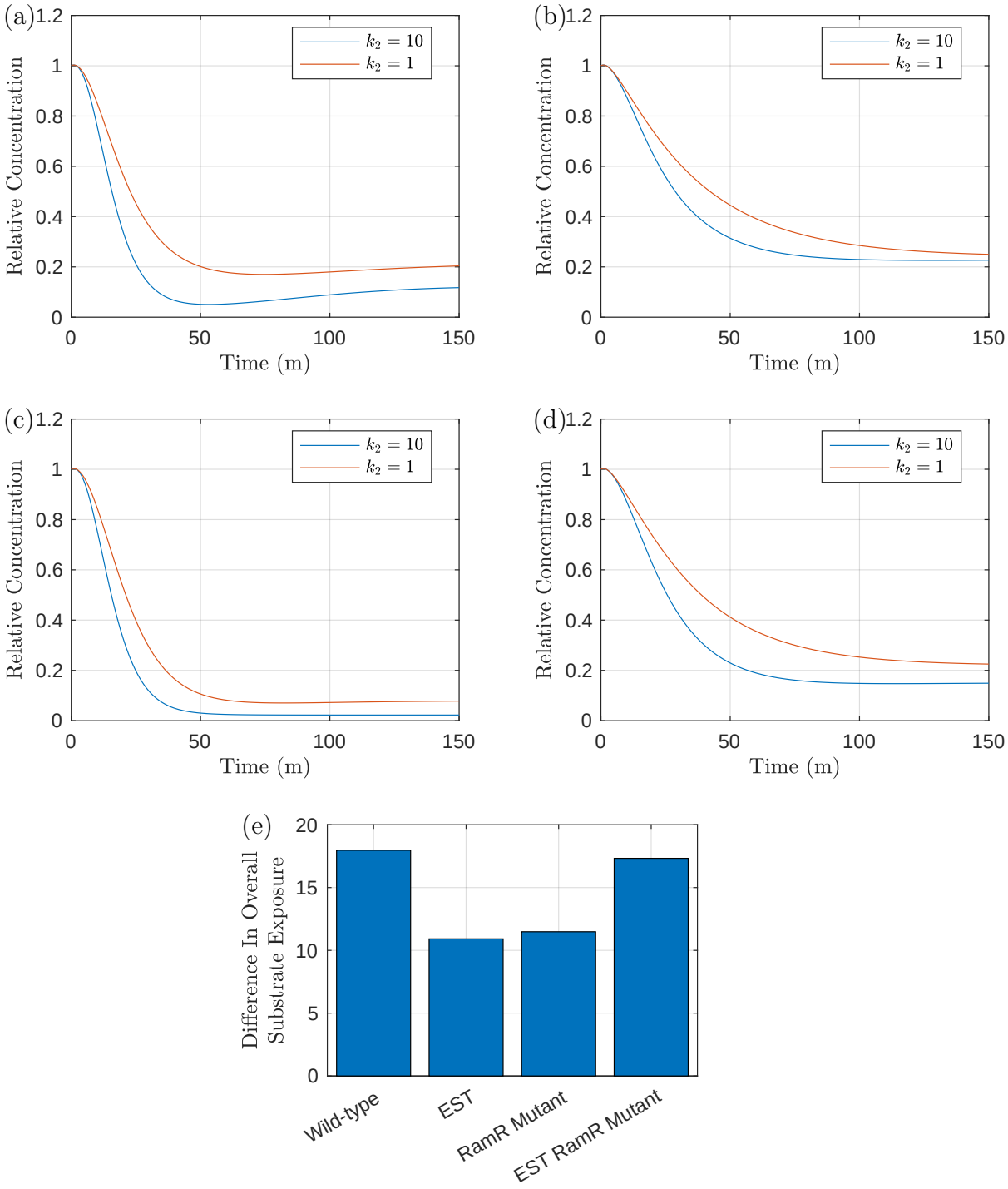

Figure 6.12: Plots exhibiting the effects of varying *ramA* expression (default parameter value $k_2 = 10$) on the intracellular bound substrate over time. In (a) we have the wild-type strain, (b) the EST strain, (c) the RamR mutant strain and (d) the EST RamR mutant strain. Finally in (e) we exhibit the difference in AUC between the manipulated parameter value simulation to the default parameter value simulation for each strain.

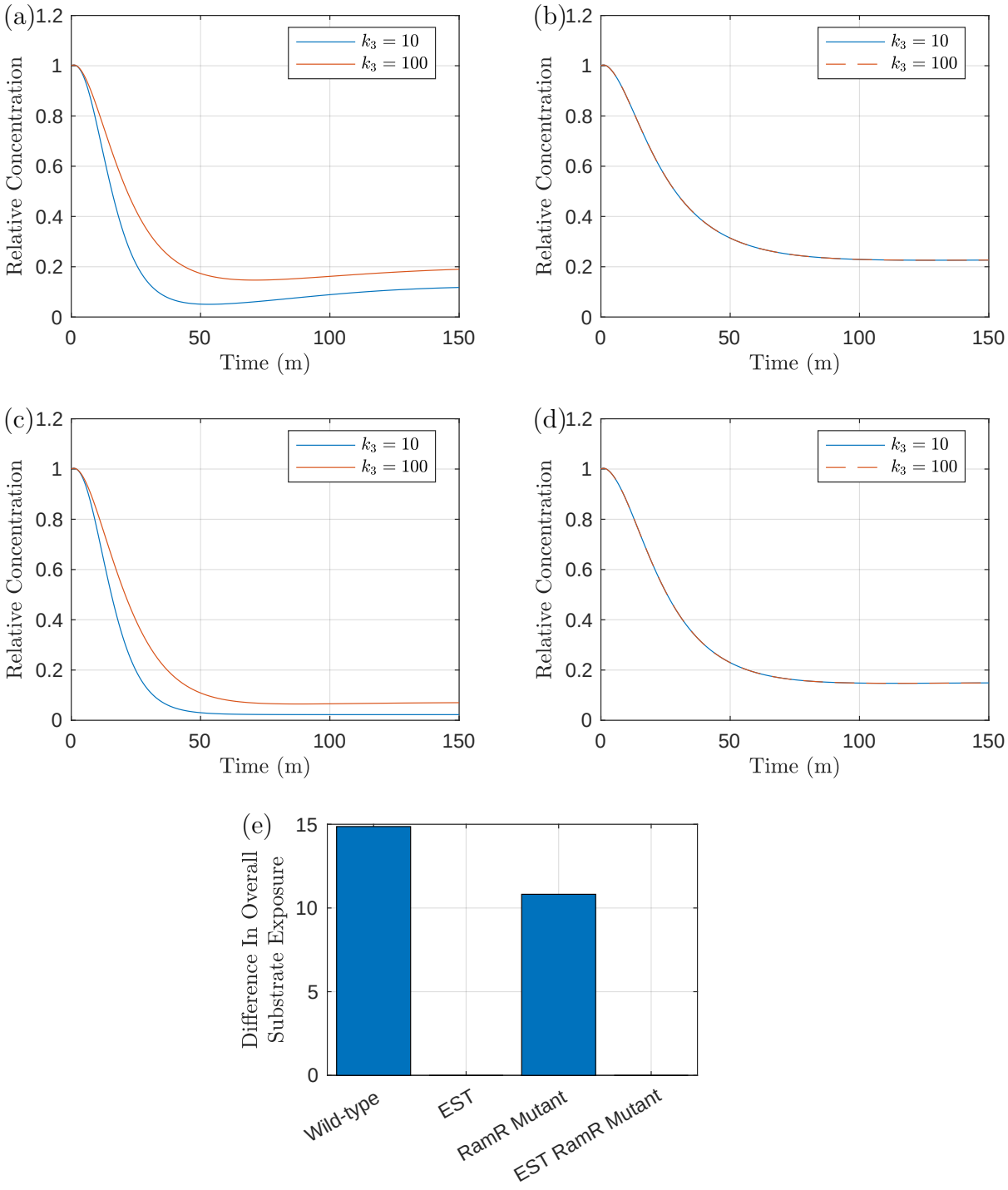

Figure 6.13: Plots exhibiting the effects of varying *acrR* expression (default parameter value $k_3 = 10$) on the intracellular bound substrate over time. In (a) we have the wild-type strain, (b) the EST strain, (c) the RamR mutant strain and (d) the EST RamR mutant strain. Finally in (e) we exhibit the difference in AUC between the manipulated parameter value simulation to the default parameter value simulation for each strain.

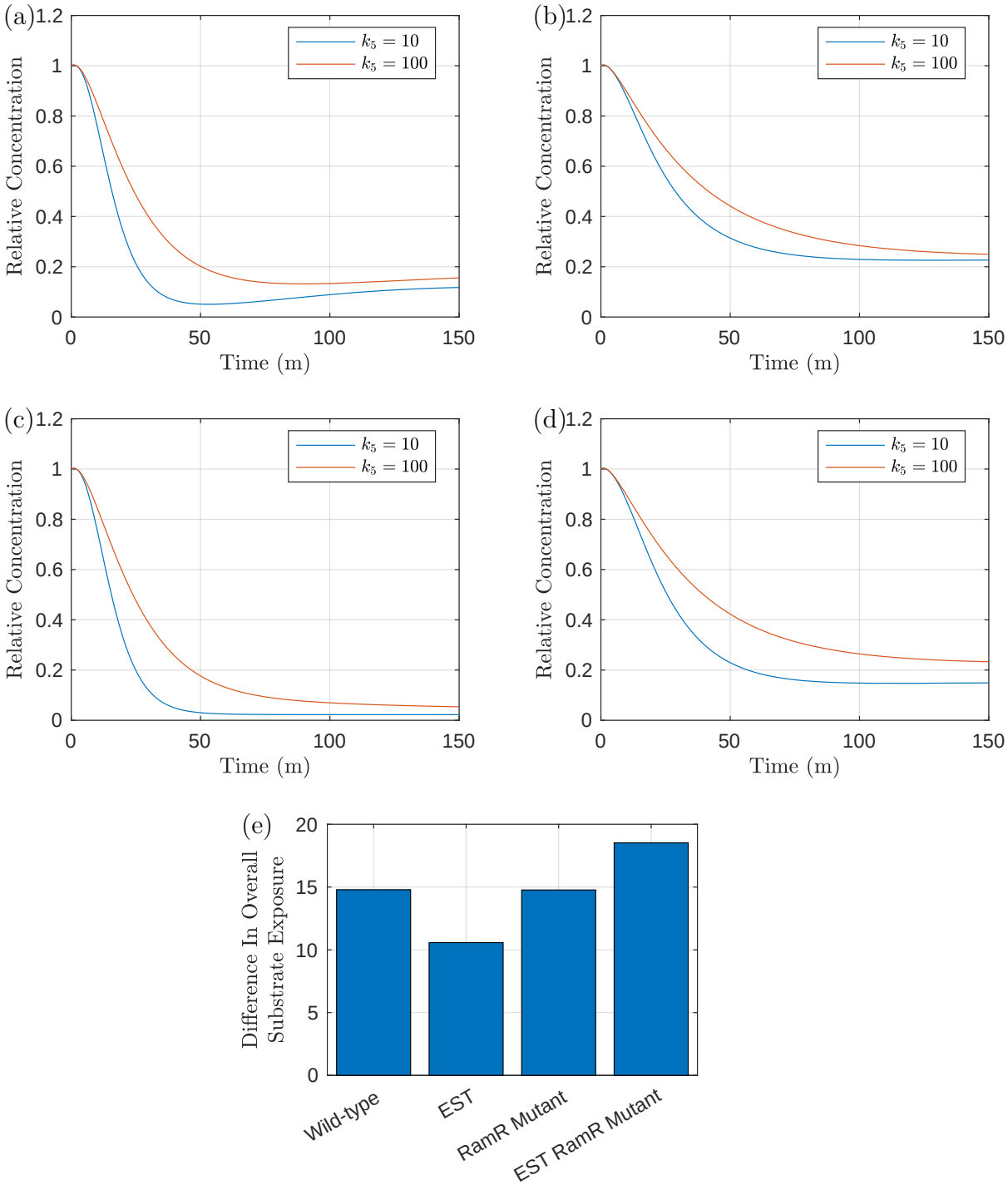

Figure 6.14: Plots exhibiting the effects of varying *envR* expression (default parameter value $k_5 = 10$) on the intracellular bound substrate over time. In (a) we have the wild-type strain, (b) the EST strain, (c) the RamR mutant strain and (d) the EST RamR mutant strain. Finally in (e) we exhibit the difference in AUC between the manipulated parameter value simulation to the default parameter value simulation for each strain.

In regards to the dissociation and saturation constants, we only vary the parameters K_{A_1}, K_E, K_H and K_I since these parameters are connected to multiple genes. With dissociation constants that are connected to singular genes, we should expect similar results to directly varying the target gene's expression as per the previous manipulations. In Figure 6.15, we can see the effects of varying RamA dissociation from *ramA* and *acrAB*. Interestingly whilst this manipulation has changed the dynamics of the wild-type strain (Figure 6.15(a)), the RamR mutant strain (Figure 6.15(b)) has only very small reductions in efflux over all time periods (further shown by total exposure in Figure 6.15(e)). This could be due to the overexpression of *ramA* in this strain meaning there is plenty of RamA to activate *acrAB* expression regardless of the dissociation constant. When it comes to the EST strains (Figure 6.15(b) and (d)), we note that there is only a minute difference in dynamics to the normal simulations. Whilst this is expected for the activation of *acrAB* expression (since the gene is not present), this gives us insight into the self activating nature of *ramA* expression. These results suggest that the effect of this is minimal and does not play a huge part in the network.

In Figure 6.16, we can see the effects of varying EnvR dissociation from *acrAB* and *acrEF*. Notably, the manipulations to all strains do not differ hugely from varying the direct expression of *envR* in Figure 6.14, again exhibiting larger effects in the early time dynamics. Thus targeting the expression of the gene and the protein produced appear to be viable targets.

In Figure 6.17, we can see the effects of varying H-NS dissociation from *envR* and *acrEF*. For the EST strains (Figure 6.17 (b) and (d)), we can clearly see no effect upon the efflux over time, further shown by the total substrate exposure (Figure 6.17 (e)). This is expected as with no AcrAB in the system we should expect fully inactive H-NS regardless of its dissociation constant. In regards to the wild-type and RamR strains (Figure 6.17 (a) and (c)), we can see a minimal effect on efflux. Since increasing the dissociation of H-NS alleviates the inhibition of *acrEF* expression, this agrees with the view that if *acrAB* is active, then the expression of *acrEF* has little effect upon the overall

efflux, matching experimental results.

In Figure 6.18, we can see the effects of varying the saturation of substrate with *ramR* and *ramA* (via Lon Protease degradation). Whilst it is clear there are differences in all strains, the effect upon efflux and substrate exposure (Figure 6.17 (e)) is minimal. Notably both RamR mutant strains (6.18 (c) and (d)) provide a smaller difference in efflux to their counterparts (Figure 6.18 (a) and (b)). This is most likely due to mutated RamR in these strains, such that there is less feedback from intracellular concentration upon the GRN. Comparatively between all manipulations, we can see that the dissociation constants relating to *ramA* and *envR* are the most sensitive for affecting substrate concentration, and thus have the most potential for inhibiting efflux.

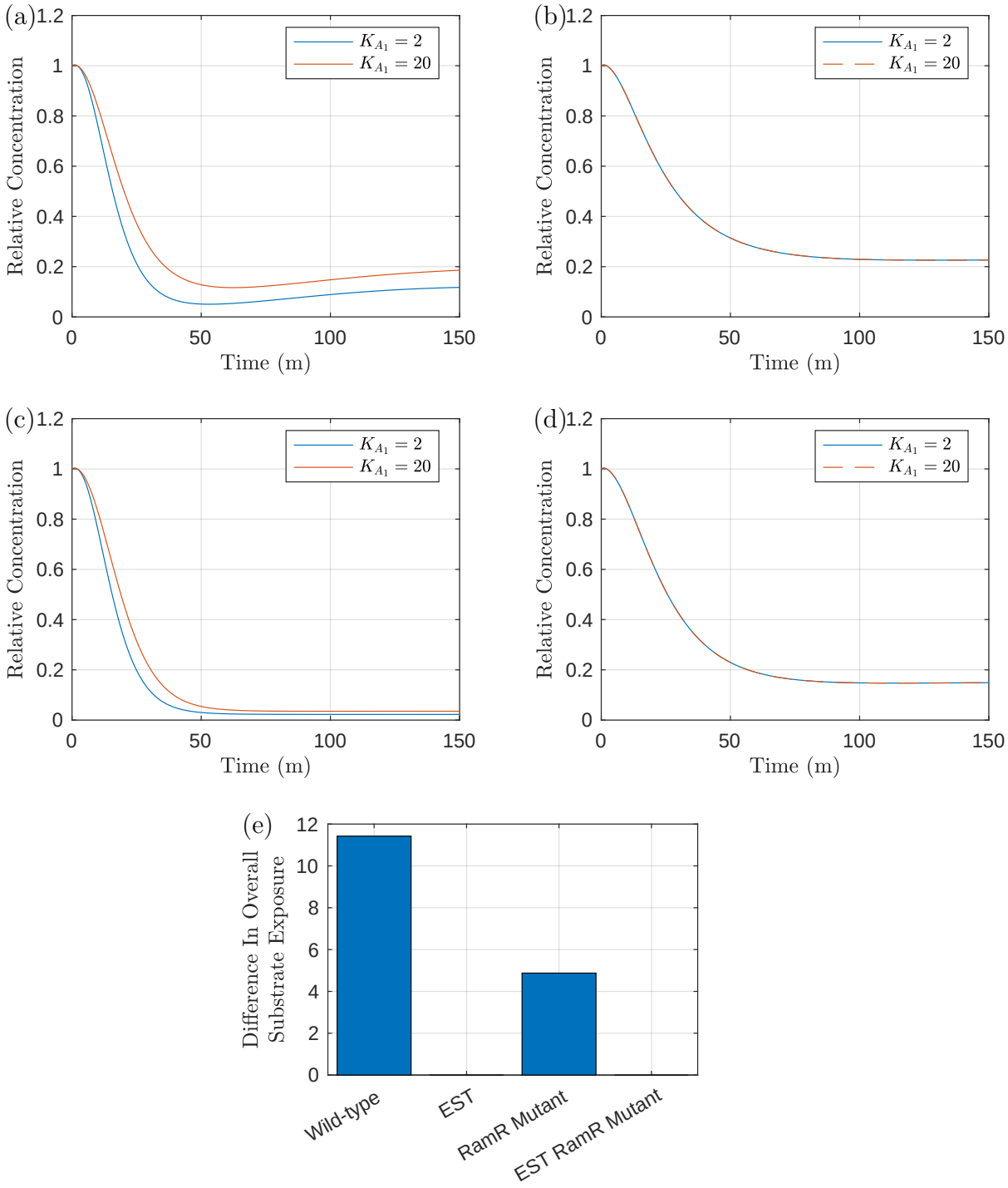

Figure 6.15: Plots exhibiting the effects of varying RamA dissociation with *ramA* and *acrAB* (default parameter value $K_{A_1} = 2$) on the intracellular bound substrate over time. In (a) we have the wild-type strain, (b) the EST strain, (c) the RamR mutant strain and (d) the EST RamR mutant strain. Finally in (e) we exhibit the difference in AUC between the manipulated parameter value simulation to the default parameter value simulation for each strain.

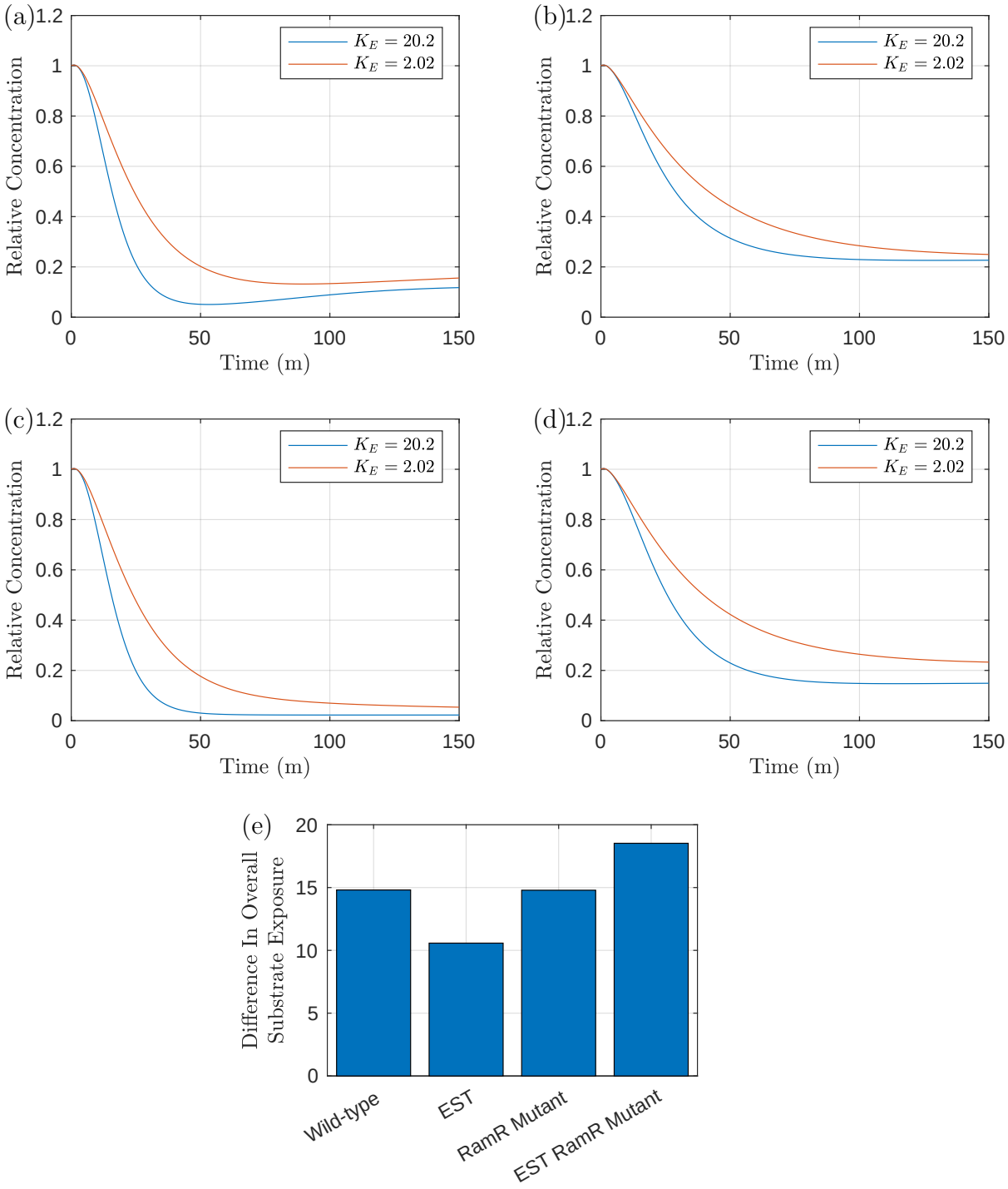

Figure 6.16: Plots exhibiting the effects of varying EnvR dissociation with *acrAB* and *acrEF* (default parameter value $K_E = 20.2$) on the substrate over time. In (a) we have the wild-type strain, (b) the EST strain, (c) the RamR mutant strain and (d) the EST RamR mutant strain. Finally in (e) we exhibit the difference in AUC between the manipulated parameter value simulation to the default parameter value simulation for each strain.

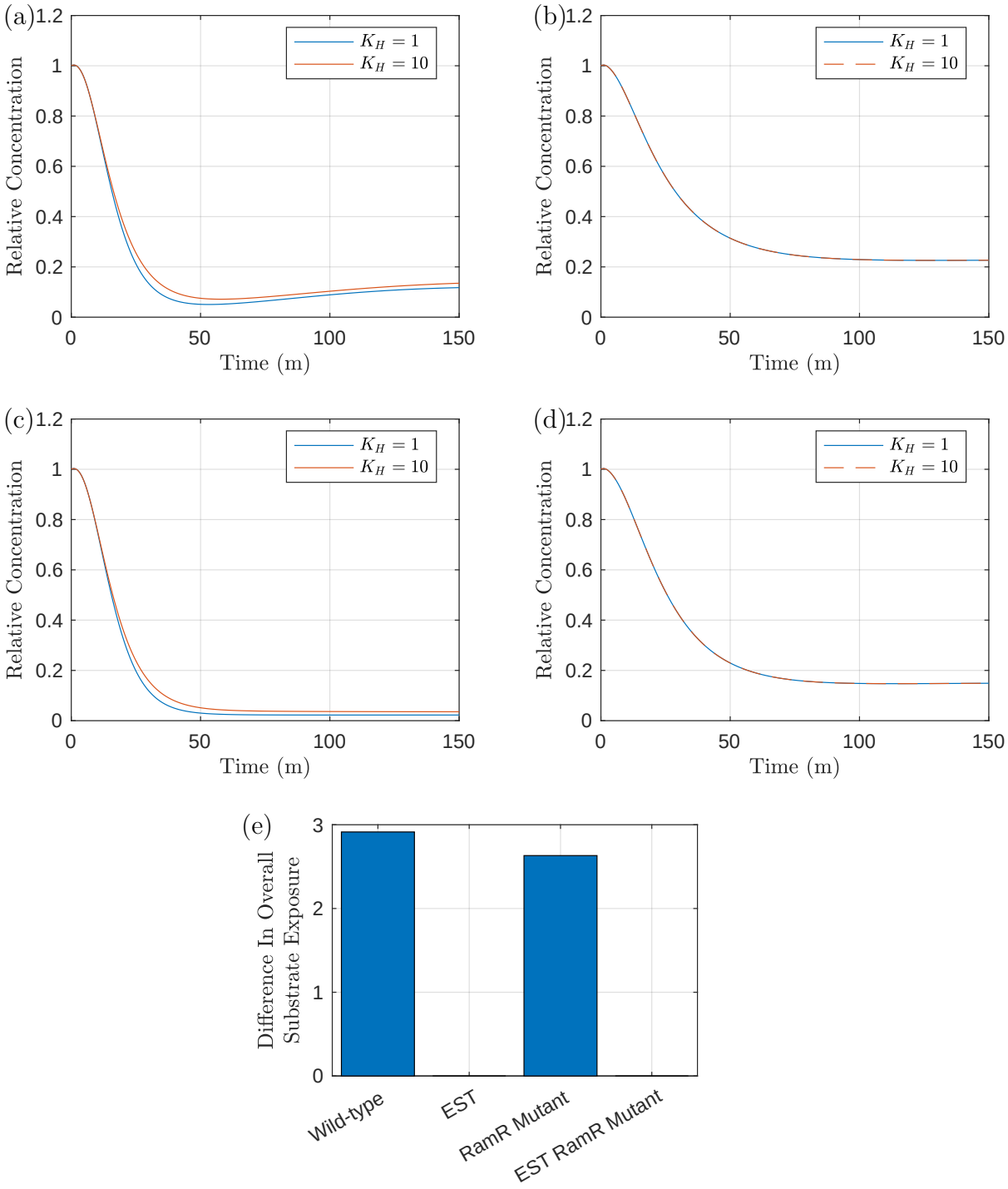

Figure 6.17: Plots exhibiting the effects of varying H-NS dissociation with *envR* and *acrEF* (default parameter value $K_H = 1$) on the substrate over time. In (a) we have the wild-type strain, (b) the EST strain, (c) the RamR mutant strain and (d) the EST RamR mutant strain. Finally in (e) we exhibit the difference in AUC between the manipulated parameter value simulation to the default parameter value simulation for each strain.

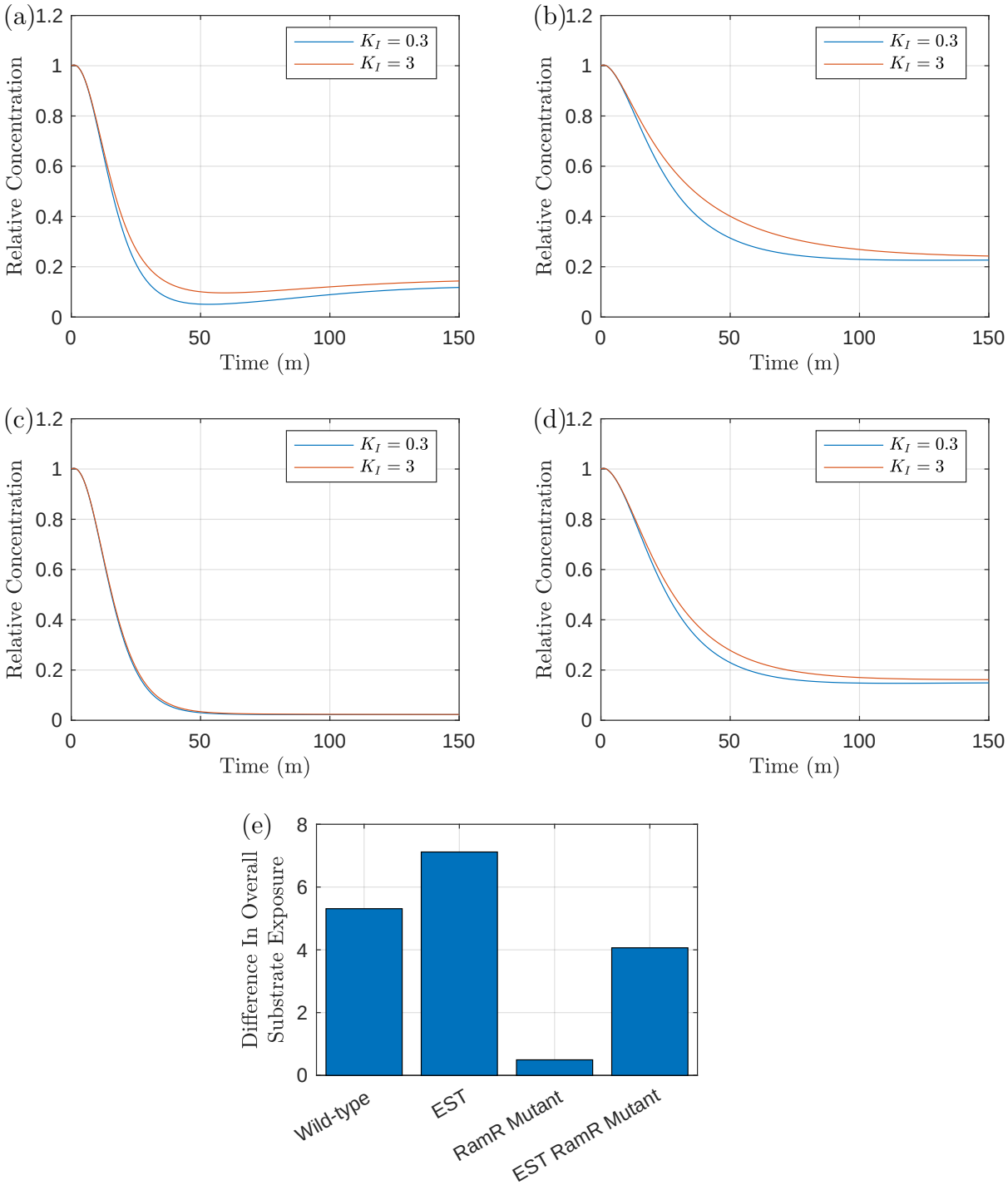

Figure 6.18: Plots exhibiting the effects of varying substrate desaturation with *ramR* and *ramA* (via Lon Protease) (default parameter value $K_I = 0.3$) on the substrate over time. In (a) we have the wild-type strain, (b) the EST strain, (c) the RamR mutant strain and (d) the EST RamR mutant strain. Finally in (e) we exhibit the difference in AUC between the manipulated parameter value simulation to the default parameter value simulation for each strain.

Whilst manipulating one parameter did provide notable changes to the efflux dynamics of the strains, our results show that in order to provide broader changes, further manipulations are needed. It was shown from varying the dissociation constants of proteins that the results did not hugely differ from varying the expression of genes that produce these proteins. In addition the only expression of genes that had notable change to all strains were the expression of *ramA* and *envR*. In Figure 6.19, we show the effects of varying both *ramA* expression and *envR* expression. The combination of manipulations has clear effects on the dynamics in all strains, although the EST strains (Figure 6.19 (b) and (d)) do show a lesser change in dynamics to the wild-type and RamR mutant strains (Figure 6.19 (a) and (c)). In addition, the total substrate exposure (6.19 (e)) has similar differences in exposure for one manipulation in all strains, however multiple manipulations have larger effects to the wild-type and RamR mutant strains than the EST and EST RamR mutant strains. These differences are likely due to there being one efflux pump already inactive in the latter strains. In both RamR mutant strains (Figure 6.19 (c) and (d)) however, we see much larger changes to the dynamics compared to their non mutant counterparts (Figure 6.19 (a) and (b)). This is a useful insight as the RamR mutation has been proven to cause MDR. We note that in all strains there is a notable difference in the mid time dynamics, with the efflux rate of substrate slowed. Thus, in regards to an antibiotic substrate, the slowing of efflux time may be crucial. If cells within the culture cannot expel enough antibiotic at a fast enough rate, the antibiotic may have already caused irreversible damage to the cells and hence the cells may die even if they are able to pump out enough antibiotic to a low enough concentration that would normally be under a killing threshold, thus preventing MDR in the strain.

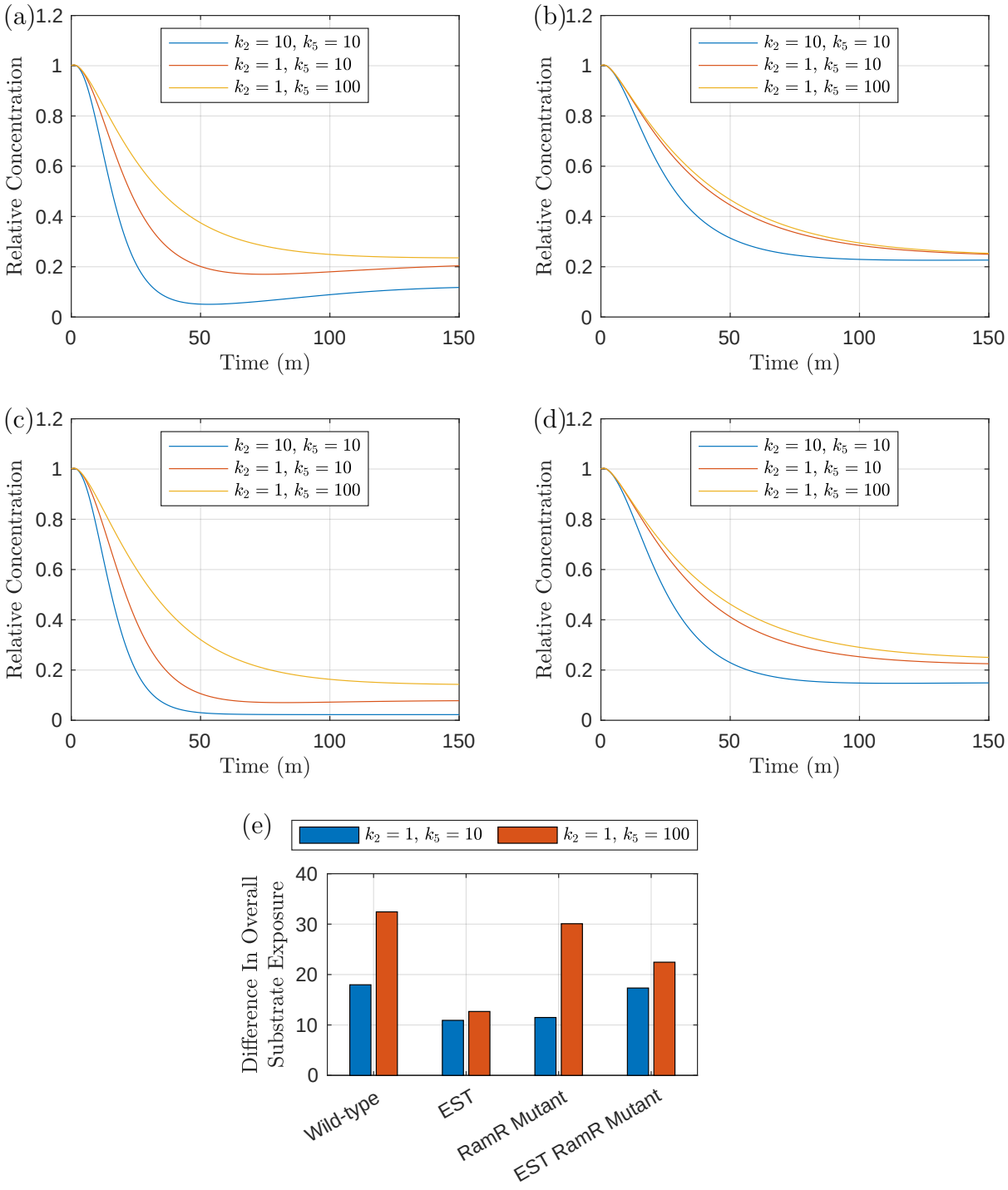

Figure 6.19: Plots exhibiting the effects of varying *ramA* and *envR* expression (default parameter values $k_2 = 10, k_5 = 10$) on the bound intracellular substrate over time. In (a) we have the wild-type strain, (b) the EST strain, (c) the RamR mutant strain and (d) the EST RamR mutant strain. Finally in (e) we exhibit the difference in AUC between the each of the manipulated parameter value simulations to the default parameter value simulation for the strains.

6.6 Discussion

By combining our two previous models of a GRN and substrate efflux, we have created a multi scale model that better encapsulates the behaviour of how a *Salmonella* culture expresses genes in order to react to a substrate stressor. Firstly, by using information from further studies into the network as well as insights from the asymptotic analysis in Chapter 3, we have adapted and simplified our GRN model from Chapter 2. Using this updated GRN model, we combine the model with our spatial model on substrate efflux from Chapter 5 to create a multi scale model. We have achieved this by linking the concentration of efflux pumps with the efflux rate in our spatial model, as well as the substrate having effects upon expression of *ramR* and degradation of RamA. By keeping our parameters as similar as possible to our previous GRN model simulations, we have recreated the efflux dynamics fitted to our spatial model for the wild-type and EST strains. This has enabled us to run simulations of the model, in order to exhibit the effect of the substrate upon the expression and behaviour of genes within the GRN. In addition to the wild-type and EST strains, we have also simulated potential RamR mutant counterparts in order to see the effect of mutations in the GRN to the spatial dynamics of substrate.

Similar to previous chapters, we have produced a parameter sensitivity analysis on parameters in the GRN using the steady state of the intracellular substrate. We have completed sensitivity analysis for all four simulated strains, in order for us to identify targets for inhibiting efflux for each strain. By taking these parameters forward, we have produced time dependent simulations in order for us to show the effect of varying these parameters on the full time course. Whilst the long term behaviour was expected from the parameter sensitivity analysis, we gained important insights with certain genes having a larger effect upon short and mid time efflux behaviour. Comparing the manipulations on all strains, we have identified the genes *ramA* and *envR* as the most viable targets for inhibiting efflux. This is due to the strains displaying the most sensitivity to the parameters linked with these genes. We have exhibited the effects of manipulating both genes across all strains, with sizeable effects shown to the efflux dynamics. Thus, by

creating this multi scale model, it has enabled us to identify the potentially most important genes in the network to inhibit efflux and combat MDR.

In summary, whilst our GRN model in Chapter 2, gave us insight into the interplay of genes that govern efflux, it did not give us insights into how the expression of these genes affect the *Salmonella* cell and population. In addition, the spatial model in 5 gave us insights into how a *Salmonella* population expels substrate, however it did not give us insights into how the cells activate mechanisms in order to react to the substrate. By combining these two models we can manipulate any part of the GRN and find the resulting larger scale effect upon substrate dynamics. Conversely, we can alter the spatial dynamics of substrate surrounding and within a population and find the smaller scale reaction of cells by gene expression. This model provides a useful tool for achieving new hypotheses on new and existing strains, enabling us to identify new biological experiments to help further our knowledge and combat MDR.

CHAPTER 7

CONCLUSIONS

With the ever growing threat of antibiotic resistance, MDR *Salmonella* strains have been listed as a high priority for where new treatment methods are required [100]. One of the main defensive mechanisms used by Salmonella is efflux pumps that can expel multiple different antibiotics from the cytoplasm of the cell. The AcrAB-TolC and the AcrEF-TolC systems have been identified as major efflux pumps that contribute to MDR [10]. Inhibition of these efflux pump systems is a potential method to combat antibiotic resistance in bacteria, preventing the bacteria from being able to expel antibiotics via active transport [68]. However, inhibition of these efflux pumps is a complex process, as the regulation of these efflux pumps are governed by complex gene regulation networks and inhibition of one efflux pump system can cause up regulation of another efflux pump system [12]. These GRNs contain multiple different genes and proteins that interact with each other's expression, ultimately leading to the expression of the genes that produce structural efflux pump proteins when the cell is under stress. The genes within these networks vary in expression between different strains, with overexpression of efflux pump genes being common in mutant MDR strains [97]. In this thesis, we have produced multiple mathematical models to investigate strains of *Salmonella*, including wild-type and MDR strains. These models have ranged from the cellular scale of gene regulation to the population scale of antibiotic distribution within bacterial strains and their environments. By modelling these strains on multiple scales, we have gained many insights into the role of efflux in

causing MDR.

Our first model in Chapter 2 models the intracellular processes of gene regulation governing the expression of the efflux pump genes *acrAB* and *acrEF*. For this model, we consider two strains: a wild-type strain and a mutant strain. Both of these strains consist of the same genes governing efflux pump expression, however the latter has non-functional RamR protein which indirectly causes overexpression of efflux pump genes. Thus in order for an inhibition adjuvant to antibiotic treatment to be developed, the GRN processes must be fully understood. For the inhibition to be effective, it must be able to repress the efflux pump systems in multiple different strains. We produce simulations of this model, starting from a down regulated state. Whilst this model gave us basic insights into how a cell reacts to a constant stressor via gene expression, the combination of a large number of parameters and multiple indistinct parameter values meant we were unable to draw firm conclusions from the model simulations.

In Chapter 3, we have applied asymptotic techniques to reduce the need for specific parameter values for the model in Chapter 2. This approach enabled us to complete a series of time dependent asymptotic analyses upon the wild-type and mutant cases, revealing nine and ten timescales respectively. We see mRNA transcription being dominant on the early timescales, with protein translation closely following for those mRNAs. As protein levels increase, inhibition of relevant transcription begins, decreasing certain mRNA concentrations. Finally, degradation comes into effect bringing all variables to steady state. By doing this process, we have broken down our nondimensional model (which does not have a full set of analytical solutions) into a step by step model of each dominant process. Thus, we are left with simplified models of our system, only taking into effect the dominant behaviours that control the GRN.

By performing this asymptotic analysis, we have also achieved asymptotic approximations to the steady states of the system, which were not analytically solvable in our full model. On most timescales we have full analytical solutions for each variable's behaviour, enabling us to see the full breakdown of how each variable acts and how step by step

the system evolves over time. By performing parameter variations upon the steady state values, we have been able to identify certain parameter groupings that have the most effect on the expression of efflux genes in both the wild-type and mutant case. For both cases, it was shown that both η and ξ relating to the binding affinity of EnvR to the two efflux pump genes and *envR* expression exhibited some of the strongest sensitivities, thus showing evidence for the gene *envR* to be a potential inhibition target. This is biologically plausible as *envR* is the local repressor of the efflux gene *acrEF* but also can repress the gene *acrAB*. As this gene affects both pumps directly, by targeting *envR* we may be able to maximise inhibition of both efflux pumps. Notably however, the processes of EnvR repression on the efflux pump genes were only dominant on the latter timescales. On early timescales these repression processes did not appear at leading order. This may show the limitations of *envR* as an inhibition target, with the gene more likely to affect the long term behaviour only.

Most other parameters exhibited a reasonable relative sensitivity, providing evidence that multiple genes could provide realistic inhibitory targets. Perhaps more importantly however, was the sensitivity of ω relating to the link between the concentration of AcrAB and the activation / repression of *acrEF*. Notably, this link appeared as a dominant process in both strains on the latter timescales. Whilst we do not currently know the full biological details of this link, the sensitivity of this parameter grouping suggests that it could provide a possible efflux inhibition target. This provides a strong case to delve into and further understand the mechanisms linking the various efflux pumps, as they could provide the key to inhibiting efflux.

Whilst exploring the steady state analysis has provided plentiful insights into efflux inhibition targets at the system's long term behaviour, it is important to note that this does not fully encompass the system's earlier behaviour. By summarising the asymptotic analysis showing the dominant behaviour on all timescales, we are able to exhibit a step by step breakdown of the system. With this summary, we were able to distinguish easier the differences of behaviour between the wild-type and mutant cases. In particular we

noted the importance of *ramA* in the mutant case, with direct and indirect activation of *acrAB* through RamA. Whilst at steady state the indirect activation (via AcrR) is still prevalent, at leading order in the mathematical analysis the direct activation is not and appears to be an important factor in early activation of *acrAB* expression. This has given us reasonable grounds to consider *ramA* as a potential inhibition target, targeting *acrAB* expression directly at early time, and indirectly at long time. Although this gene may not be one of the most sensitive targets at long term behaviour, the step by step breakdown shows that the early interactions of the gene are of huge significance. Thus by targeting *ramA*, we may provide a method for inhibiting early efflux expression enough so that an antibiotic can kill the bacteria before its efflux pumps become fully active. The analysis has therefore also revealed the possible importance of effective timing of efflux inhibition and how this may vary between targets.

Although this model gave us insight into how genes interplay starting from a down-regulated state, it did not consider how a change in antibiotic concentration could itself affect the network. In Chapters 4 and 5, we produce models of the distribution of an antibiotic concentration within and surrounding a *Salmonella* population. In these models we consider an antibiotic that is a substrate of four efflux pumps: AcrAB, AcrEF, MdsAB and MdtAB. Notably two of these efflux pumps are apparent in our GRN model in Chapter 2. We produced these models in order to replicate experimental data of ethidium bromide efflux assays. This data consists of experiments taken upon a wild-type strain of *Salmonella* and various efflux pump knockout strains. By replicating this data, we hoped to achieve insights into the dynamics of the four efflux pump systems.

We started with a simplistic model in Chapter 4, formulating a PDE model of substrate concentration of a spherical cell and surrounding extracellular space. We produced numerical simulations of the model by discretising the domain using finite difference methods. By then using parameter fitting techniques, we were able to fit the model to each of the *Salmonella* strains by varying the efflux parameter X. Initially, we proposed differing outer boundary conditions for the model (zero far field and no flux). Whilst the parameter

fitting results for this model did not show strong alignment to the data for both boundary conditions, it was shown that for the long time behaviour, having a no flux boundary condition produced fits that aligned better to the data. This gave us reason to believe that in the experiments, the extracellular space is limited enough such that expelled substrate (via either efflux or diffusion) is constantly diffusing back into the strains. In addition, it was interesting to note the disparity between the reasonable fits to the AEST knockout strain (all efflux pumps knockout) against the substandard fits to any strain with efflux active. Furthermore, in fits to all strains, the model could not replicate the early time dynamics that were shown by the data. These results made it clear that the current model was missing essential dynamics and thus needed adaptation to fully encapsulate the behaviour exhibited by the strains.

In Chapter 5, we formulated a model improving on the model in Chapter 4. As the early dynamics of the strain were not present in the previous model, we firstly introduced binding dynamics of the substrate. Ethidium bromide is a DNA-intercalating agent that fluoresces when bound to DNA and thus is found within the cell in two states (bound and unbound), by including these binding dynamics the model was expanded into a system of PDEs. Parameter fitting techniques immediately displayed the improvements to the model, with the model being able to replicate early and intermediate time behaviours, producing a near perfect fit of data of the AEST strain. The model showed improvements on the wild-type strain compared to the previous model. However it was clear that the constant efflux parameter was incapable of encapsulating the behaviour of strains that had active efflux. Therefore we adapted our efflux parameter to be variable, defined by a simple formation and deformation ODE. Parameter fitting results showed the model better replicated the dynamics of the wild-type strain with strong alignment to the experimental data on all time scales. However, the efflux variable now showed unrealistic behaviour, with the efflux depleting very quickly and only present for a short period of the experiment. By making the increase of efflux dependent on the intracellular substrate concentration, not only did we achieve more realistic efflux dynamics, we achieved fits with stronger

alignment to the data. This lead us to believe that the strains have some feedback mechanism involving the rate of efflux and the internal substrate concentration.

By using the optimal parameters for the most extreme cases: AEST (no active efflux) and wild-type (full efflux), we were able to produce fits for the efflux pump knockout strains. This enabled us to produce efflux profiles for each strain, which after making assumptions we used to estimate the efflux profile of each individual efflux pump system. We noted that these efflux profiles displayed similarities to the behaviour of our efflux pump variables in our model in Chapter 2. This gave us good reason to believe that the feedback mechanism between the internal substrate concentration and efflux could be the result of the regulation of genes within a GRN.

In Chapter 6, we produced a multiscale model, linking the models in Chapters 2 and 5 to simulate a GRN feedback mechanism. By using new knowledge from further studies into the network, we were able to adapt our GRN model from Chapter 2. In addition, by using insights gained from the asymptotic analysis in Chapter 3, we further adapted the GRN, simplifying the model by removing elements that were not influential in the dominant processes revealed by the asymptotic analysis. Lastly, by linking the intracellular substrate to certain mechanisms of the GRN (repressing *ramR* expression and Lon Protease degradation), we were able to combine our ODE and PDE models, using similar finite difference methods from Chapter 5 to produce numerical simulations. For this model, we compared wild-type, EST (AcrAB knockout) strains and respective RamR mutant counterparts. By using the final fitted parameters in Chapter 5, we compare our model to the data of the wild-type and EST strains, maintaining as many parameter values as possible from Chapter 2. We then simulated the RamR mutant counterparts strains by manipulating the GRN, enabling us to predict how these strains behave in the presence of a substrate stressor.

Similar to our asymptotic analysis in Chapter 3, we performed parameter sensitivity analysis varying GRN parameters, this time however measuring the difference to the steady state of the intracellular substrate concentration. Taking forwards the most sen-

sitive parameters for all of the strains from this analysis, we performed time dependent simulations showing the effects of manipulating these parameters. These simulations enabled us to exhibit the effects on the dynamics of substrate efflux throughout the full time course of the simulations. It was shown that the genes *ramA* and *envR* were the most viable targets for inhibiting efflux in all strains, which aligned with our results from the asymptotic analysis in Chapter 3. Therefore experimenting with an inhibition adjuvant that targets processes involving these genes could prove useful to inhibiting efflux.

We have only displayed some of the many capabilities that this multiscale model provides in Chapter 6. By creating this model we have provided a basis for understanding MDR in *Salmonella* with multiple opportunities for further research. The model provides the ability to target or manipulate any area of the GRN or cell spatial structure to achieve new hypotheses on how the culture will react to the substrate. Manipulations could be achieved by the addition of new variables into the model, such as including the dynamics of an adjuvant that targets the GRN, or a synthetic molecule that slows efflux activity or alters membrane permeability. In addition to this further research, another clear extension to this thesis would be extending the time dependent asymptotic analysis from Chapter 3 to incorporate all elements of the multiscale model. By breaking down the GRN model to multiple different timescales, we demonstrated the increased volume of information we were able to obtain from the analysis. If we were to apply this method to the multiscale model, we would be able to obtain more in depth information of the workings of the bacteria, with the ability to determine which genes are the most influential on the expulsion of substrate at various different timescales.

There are of course many other areas where we could expand this model, one of these being the inclusion of stochastic events. This could be incorporated through multiple processes in the model, for example: gene expression, degradation, binding dynamics and substrate diffusion. Specifically for gene expression, we could consider the effects caused by intrinsic (process that affect singular genes) and extrinsic noise (global processes that could affect multiple genes). As the concentration for specific genes within our GRN are

low, we therefore have a low copy number of mRNAs and proteins. These concentrations are therefore susceptible to intrinsic noise as the fluctuations in the processes affecting these molecules can not be assumed as negligible (which is the case in larger concentrations). In regards to extrinsic noise we have not considered cell growth, death and changes to the physical environment in our models, which could have effects on the gene expression of all or individual cells within the population [88]. In addition, cell growth and death could be linked to the expression of efflux pump genes. Not only through their link to the antibiotic concentration, the production of the efflux pump proteins could be costly to the population and prevent or reduce the ability for cells to produce other essential survival mechanisms.

We believe that this work has provided useful insights into the mechanisms behind MDR in *Salmonella*. In the multiscale model, we have created a basis with positive capabilities for future research, we hope that the success of this model will inspire the creation of other GRN and efflux models for different bacterial species. With the hypotheses we have generated on potential inhibitory targets and pathways, this should provide evidence for further investigation of certain areas of the network. We hope the analysis will also inspire potential therapies to be tested experimentally in order to produce new strategies against efflux related MDR bacteria.

LIST OF REFERENCES

[1] Agbaje, M., Begum, R., Oyekunle, M. et al. (2011) Evolution of *Salmonella* nomenclature: a critical note. **Folia microbiol.**, 56: 497–503

[2] Alanis, A. (2005) Resistance to antibiotics: are we in the post-antibiotic era? **Arch Med Res**, 36: 697–705

[3] Alcalde-Rico, M., Hernando-Amado, S., Blanco, P. et al. (2016) Multidrug efflux pumps at the crossroad between antibiotic resistance and bacterial virulence. **Front. Microbiol.**, 7: 1483

[4] Andino, A. and Hanning, I. (2015) Salmonella enterica: survival, colonization, and virulence differences among serovars. **The Scientific World Journal**, 2015.

[5] Bailey, A.M., Ivens, A., Kingsley, R. et al. (2010) RamA, a member of the AraC/XylS family, influences both virulence and efflux in *Salmonella enterica* serovar typhimurium. **J. Bacteriol**, 192 (6): 1607–1616

[6] Baron, C. (2010) Antivirulence drugs to target bacterial secretion systems. **Curr. Opin. Microbiol.**, 13 (1): 100–105

[7] Baron, S. (1996) **Epidemiology–Medical Microbiology**. University of Texas Medical Branch at Galveston.

[8] Baucheron, S., Coste, F., Canepa, S. et al. (2012) Binding of the ramr repressor to wild-type and mutated promoters of the *ramA* gene involved in efflux-mediated multidrug resistance in *Salmonella enterica serovar Typhimurium.* **Antimicrob. Agents Chemother.**, 56: 942–948

[9] Bernstein, J.A., Khodursky, A.B., Lin, P.H. et al. (2002) Global analysis of mRNA decay and abundance in *Escherichia coli* at single-gene resolution using two-color fluorescent DNA microarrays. **Proc. Natl. Acad. Sci. U.S.A.**, 99 (15): 9697–9702

[10] Blair, J., Richmond, G. and Piddock, L. (2014a) Multidrug efflux pumps in gram-negative bacteria and their role in antibiotic resistance. **Future Microbiol.**, 9: 1165–1177

[11] Blair, J.M. and Piddock, L.J. (2016) How to measure export via bacterial multidrug resistance efflux pumps. **MBio**, 7 (4): e00840–16

[12] Blair, J.M., Smith, H.E., Ricci, V. et al. (2014b) Expression of homologous RND efflux pump genes is dependent upon AcrB expression: implications for efflux and virulence inhibitor design. **Journal of Antimicrobial Chemotherapy**, 70 (2): 424–431

[13] Blanco, P., Sanz-García, F., Hernando-Amado, S. et al. (2018) The development of efflux pump inhibitors to treat Gram-negative infections. **Expert Opin. Drug Discov**, 13 (10): 919–931

[14] Borghans, J., De Boer, R. and Segel, L. (1996) Extending the quasi-steady state approximation by changing variables. **Bull Math Biol**, 58: 43–63

[15] Carr, E.J. and Pontrelli, G. (2018) Modelling mass diffusion for a multi-layer sphere immersed in a semi-infinite medium: application to drug delivery. **Mathematical biosciences**, 303: 1–9

[16] Casadevall, A. and Pirofski, L.a. (2003) The damage-response framework of microbial pathogenesis. **Nat. Rev. Microbiol**, 1 (1): 17–24

[17] Chai, Q., Webb, S.R., Wang, Z. et al. (2016) Study of the degradation of a multidrug transporter using a non-radioactive pulse chase method. **Anal. Bioanal. Chem.**, 408 (27): 7745–7751

[18] Charlebois, D.A., Balázsi, G. and Kærn, M. (2014) Coherent feedforward transcriptional regulatory motifs enhance drug resistance. **Phys. Rev. E**, 89 (5): 052708

[19] Corless, R.M., Gonnet, G.H., Hare, D.E. et al. (1996) On the lambertw function. **Adv Comput Math.**, 5 (1): 329–359

[20] Crank, J. (1979) **The mathematics of diffusion**. Oxford university press.

[21] Cussler, E.L. and Cussler, E.L. (2009) **Diffusion: mass transfer in fluid systems**. Cambridge university press.

[22] Davidson, F.A., Seon-Yi, C. and Stanley-Wall, N.R. (2012) Selective heterogeneity in exoprotease production by *Bacillus subtilis*. **PLoS One**, 7 (6): e38574

[23] Davies, J. and Davies, D. (2010) Origins and evolution of antibiotic resistance. **Microbiol. Mol. Biol. Rev.**, 74: 417–433

[24] de Leon, S.B.T. and Davidson, E.H. (2009) Modeling the dynamics of transcriptional gene regulatory networks for animal development. **Dev. Biol.**, 325 (2): 317–328

[25] Diao, J., Charlebois, D.A., Nevozhay, D. et al. (2016) Efflux pump control alters synthetic gene circuit function. **ACS Synth. Biol.**, 5 (7): 619–631

[26] Du, D., Wang, Z., James, N.R. et al. (2014) Structure of the AcrAB-TolC multidrug efflux pump. **Nature**, 509 (7501): 512–515

[27] Du, D., Wang-Kan, X., Neuberger, A. et al. (2018) Multidrug efflux pumps: structure, function and regulation. **Nature Reviews Microbiology**, p. 1

[28] Duhamel, J., Kanyo, J., Dinter-Gottlieb, G. et al. (1996) Fluorescence emission of ethidium bromide intercalated in defined DNA duplexes: evaluation of hydrodynamics components. **Biochemistry**, 35 (51): 16687–16697

[29] Dunster, T. (1996) Asymptotics of the generalized exponential integral, and error bounds in the uniform asymptotic smoothing of its stokes discontinuities. **Proc. R. Soc. Lond.**, 452 (1949): 1351–1367

[30] Duval, V. and Lister, I.M. (2013) MarA, SoxS and Rob of *Escherichia coli*–global regulators of multidrug resistance, virulence and stress response. **Int. J. Biotechnol. Wellness**, 2 (3): 101

[31] Engquist, B. (1989) Far field computational boundary conditions. **J. Comput. Math.**, 7 (2): 113–120

[32] Fernando, D.M. and Kumar, A. (2013) Resistance-nodulation-division multidrug efflux pumps in gram-negative bacteria: role in virulence. **Antibiotics**, 2 (1): 163–181

[33] Fick, A. (1855) V. on liquid diffusion. **Lond.Edinb.Dubl.Phil.Mag**, 10 (63): 30–39

[34] Filloux, A. (2012) **Bacterial regulatory networks**. Caister Academic Press Norfolk.

[35] Gill, E.E., Franco, O.L. and Hancock, R.E. (2015) Antibiotic adjuvants: diverse strategies for controlling drug-resistant pathogens. **Chem. Biol. Drug. Des.**, 85 (1): 56–78

[36] Glass, L. and Kauffman, S. (1973) The logical analysis of continuous, non-linear biochemical control networks. **J. Theor. Biol.**, 39: 103–129

[37] Hay, M., Li, Y.M. and Ma, Y. (2017) Deletion of AcrS results in increased expression of *acrE* and confers an increase in kanamycin resistance in *Escherichia coli* bw25113. **J Exp Microbiol Immunol Pearls**, 3: 63–69

[38] Hirakawa, H., Takumi-Kobayashi, A., Theisen, U. et al. (2008) AcrS/EnvR represses expression of the *acrAB* multidrug efflux genes in *Escherichia coli*. **J. Bacteriol.**, 190 (18): 6276–6279

[39] Holden, E.R. and Webber, M.A. (2020) MarA, RamA, and SoxS as mediators of the stress response: Survival at a cost. **Front. Microbiol.**, 11.

[40] Hooshangi, S. and Bentley, W. (2011) Lsrr quorum sensing "switch" is revealed by a bottom-up approach. **PLoS Comput Biol**, 7: e1002172

[41] Horiyama, T., Yamaguchi, A. and Nishino, K. (2010) Tolc dependency of multidrug efflux systems in salmonella enterica serovar typhimurium. **J. Antimicrob. Chemother**, 65 (7): 1372–1376

[42] Jabbari, S., King, J., Koerber, A. et al. (2010) Mathematical modelling of the *agr* operon in *Staphylococcus aureus*. **J. Math. Biol.**, 61: 17–54

[43] Kaoui, B., Lauricella, M. and Pontrelli, G. (2018) Mechanistic modelling of drug release from multi-layer capsules. **Comput. Biol. Med**, 93: 149–157

[44] Karlebach, G. and Shamir, R. (2008) Modelling and analysis of gene regulatory networks. **Nat. Rev. Mol. Cell Biol.**, 9: 770

[45] Kevorkian, J. and Cole, J. (2013) **Perturbation methods in applied mathematics**, vol. 34. Springer Science & Business Media.

[46] Koch, A.R. (1970) Transport equations and criteria for active transport. **Am. Zool**, 10 (3): 331–346

[47] Lagarias, J.C., Reeds, J.A., Wright, M.H. et al. (1998) Convergence properties of the nelder–mead simplex method in low dimensions. **SIAM Journal on optimization**, 9 (1): 112–147

[48] Langevin, A. and Dunlop, M. (2018) Stress introduction rate alters the benefit of acrab-tolc efflux pumps. **J. Bacteriol.**, 200: e00525–17

[49] LeVeque, R.J. (2007) **Finite difference methods for ordinary and partial differential equations: steady-state and time-dependent problems**. SIAM.

[50] Li, S., Brazhnik, P., Sobral, B. et al. (2008) A quantitative study of the division cycle of *Caulobacter crescentus* stalked cells. **PLOS Comput. Biol.**, 4: e9

[51] Lim, S. and Nikaido, H. (2010) Kinetic parameters of efflux of penicillins by the multidrug efflux transporter acrab-tolc of *Escherichia coli*. **Antimicrob. Agents Chemother.**, 54: 1800–1806

[52] Ma, D., Alberti, M., Lynch, C. et al. (1996) The local repressor AcrR plays a modulating role in the regulation of *acrAB* genes of *Escherichia coli* by global stress signals. **Mol. Microbiol**, 19 (1): 101–112

[53] Martínez, J.L. (2012) The antibiotic resistome: challenge and opportunity for therapeutic intervention. **Future Med. Chem**, 4 (3): 347–359

[54] Maurizi, M. (1992) Proteases and protein degradation in *Escherichia coli*. **Experientia**, 48 (2): 178–201

[55] McKay, M.D., Beckman, R.J. and Conover, W.J. (1979) Comparison of three methods for selecting values of input variables in the analysis of output from a computer code. **Technometrics**, 21 (2): 239–245

[56] McNeil, H.E., Alav, I., Torres, R.C. et al. (2019) Identification of binding residues between periplasmic adapter protein (PAP) and RND efflux pumps explains PAP-pump promiscuity and roles in antimicrobial resistance. **PLOS Pathog.**, 15 (12): e1008101

[57] Michelson, S. and Slate, D. (1992) A mathematical model of the p-glycoprotein pump as a mediator of multidrug resistance. **Bull Math Bio**, 54: 1023–1038

[58] Michelson, S. and Slate, D. (1994) A mathematical model for the inhibition of the multidrug resistance-associated p-glycoprotein pump. **Bull Math Bio**, 56: 207–223

[59] Nachman, I., Regev, A. and Friedman, N. (2004) Inferring quantitative models of regulatory networks from expression data. **Bioinformatics**, 20: i248–i256

[60] Nagano, K. and Nikaido, H. (2009) Kinetic behavior of the major multidrug efflux pump acrb of *Escherichia coli*. **Proc. Natl. Acad. Sci. U.S.A.**, 106: 5854–5858

[61] Nishino, K. (2016) "Antimicrobial drug efflux pumps in salmonella." In **Efflux-Mediated Antimicrobial Resistance in Bacteria**. Springer. pp. 261–279

[62] Nishino, K., Hayashi-Nishino, M. and Yamaguchi, A. (2009) H-NS modulates multidrug resistance of *Salmonella enterica* serovar typhimurium by repressing multidrug efflux genes *acrEF*. **Antimicrob. Agents Chemother**, 53 (8): 3541–3543

[63] O'Regan, E., Quinn, T., Pagès, J.M. et al. (2009) Multiple regulatory pathways associated with high-level ciprofloxacin and multidrug resistance in *Salmonella enterica* serovar enteritidis: involvement of RamA and other global regulators. **Antimicrob. Agents Chemother.**, 53 (3): 1080–1087

[64] Organization, W.H. et al. (2014) Antimicrobial resistance: 2014 global report on surveillance. **Antimicrobial resistance: 2014 global report on surveillance.**

[65] Organization, W.H. et al. (2015) Global action plan on antimicrobial resistance.

[66] Perez, A., Gomez, M., Kalvapalle, P. et al. (2017) Using cellular fitness to map the structure and function of a major facilitator superfamily effluxer. **Mol. Syst. Biol.**, 13: 964

[67] Peterson, J.W. (1996) "Bacterial pathogenesis." In **Medical Microbiology. 4th edition**. University of Texas Medical Branch at Galveston.

[68] Piddock, L. (2006) Multidrug-resistance efflux pumps? not just for resistance. **Nat. Rev. Microbiol.**, 4: 629–636

[69] Poole, K. (2005) Efflux-mediated antimicrobial resistance. **Journal of Antimicrobial Chemotherapy**, 56 (1): 20–51

[70] Pos, K. (2009) Trinity revealed: Stoichiometric complex assembly of a bacterial multidrug efflux pump. **Proc. Natl. Acad. Sci. U.S.A.**, 106: 6893–6894

[71] Ralston, A. (2008) Simultaneous gene transcription and translation in bacteria. **Nature Education**, 1 (1): 4

[72] Rampioni, G., Pillai, C.R., Longo, F. et al. (2017) Effect of efflux pump inhibition on *Pseudomonas aeruginosa* transcriptome and virulence. **Sci. Rep.**, 7 (1): 1–14

[73] Rasko, D.A. and Sperandio, V. (2010) Anti-virulence strategies to combat bacteria-mediated disease. **Nat. Rev. Drug Discov**, 9 (2): 117–128

[74] Reznikoff, W. and Gold, L. (2014) **Maximizing gene expression**, vol. 9. Elsevier.

[75] Ricci, V., Attah, V., Overton, T. et al. (2017) CsrA maximizes expression of the AcrAB multidrug resistance transporter. **Nucleic Acids Res.**, 45 (22): 12798–12807

[76] Ricci, V., Blair, J. and Piddock, L. (2014) Rama, which controls expression of the mdr efflux pump acrab-tolc, is regulated by the lon protease. **J. Antimicrob. Chemother.**, 69: 643–650

[77] Ricci, V., Busby, S.J. and Piddock, L.J. (2012) Regulation of RamA by RamR in *Salmonella enterica* serovar typhimurium: isolation of a RamR superrepressor. **Antimicrobial agents and chemotherapy**, 56 (11): 6037–6040

[78] Richtmyer, R.D. (1957) **Difference methods for initial-value problems**. Interscience.

[79] Rossi, N.A., Mora, T., Walczak, A.M. et al. (2018) Active degradation of MarA controls coordination of its downstream targets. **PLOS Comput. Biol.**, 14 (12): e1006634

[80] Rowe, B., Ward, L. and Threlfall, E. (1997) Multidrug-resistant *Salmonella typhi*: a worldwide epidemic. **Clin. Infect. Dis.**, 24: S106–S109

[81] Ryan, K., Ray, C. and Sherris, J. (2004) An introduction to infectious diseases. **J. Med. Microbiol.**, 4: 345–347

[82] Saier, M., Paulsen, I., Sliwinski, M. et al. (1998) Evolutionary origins of multidrug and drug-specific efflux pumps in bacteria. **FASEB J.**, 12: 265–274

[83] Senapati, M. (2006) **Advanced engineering chemistry**. Firewall Media. pp. 87–88

[84] Sharma, A., Gupta, V.K. and Pathania, R. (2019) Efflux pump inhibitors for bacterial pathogens: From bench to bedside. **Indian J. Med. Res**, 149 (2): 129

[85] Shmulevich, I., Dougherty, E., Kim, S. et al. (2002) Probabilistic boolean networks: a rule-based uncertainty model for gene regulatory networks. **Bioinformatics**, 18: 261–274

[86] Sköld, O. (2011) **Antibiotics and antibiotic resistance**. John Wiley & Sons.

[87] Spengler, G., Kincses, A., Gajdács, M. et al. (2017) New roads leading to old destinations: efflux pumps as targets to reverse multidrug resistance in bacteria. **Molecules**, 22 (3): 468

[88] Swain, P.S., Elowitz, M.B. and Siggia, E.D. (2002) Intrinsic and extrinsic contributions to stochasticity in gene expression. **Proc. Natl. Acad. Sci.**, 99 (20): 12795–12800

[89] Tian, T. and Burrage, K. (2006) Stochastic models for regulatory networks of the genetic toggle switch. **Proc. Natl. Acad. Sci. U.S.A.**, 103: 8372–8377

[90] Urso, R., Blardi, P. and Giorgi, G. (2002) A short introduction to pharmacokinetics. **European review for medical and pharmacological sciences**, 6: 33–44

[91] Van Dyke, M. (1975) Perturbation methods in fluid mechanics/annotated edition. **STIA**, 75: 46926

[92] Versypt, A.N.F. and Braatz, R.D. (2014) Analysis of finite difference discretization schemes for diffusion in spheres with variable diffusivity. **Computers & chemical engineering**, 71: 241–252

[93] Wall, M., Hlavacek, W. and Savageau, M. (2003) Design principles for regulator gene expression in a repressible gene circuit. **J. Mol. Biol.**, 332: 861–876

[94] Wang, Z., Han, Q.Q., Zhou, M.T. et al. (2016) Protein turnover analysis in *Salmonella Typhimurium* during infection by dynamic SILAC, topograph, and quantitative proteomics. **J. Basic Microbiol.**, 56 (7): 801–811

[95] Wang-Kan, X., Blair, J., Chirullo, B. et al. (2017) Lack of AcrB efflux function confers loss of virulence on *Salmonella enterica serovar Typhimurium*. **MBio**, 8: e00968–17

[96] Weaver, D., Workman, C. and Stormo, G. (1999) "Modeling regulatory networks with weight matrices." In **Biocomputing'99**. World Scientific. pp. 112–123

[97] Webber, M. and Piddock, L. (2003) The importance of efflux pumps in bacterial antibiotic resistance. **J. Antimicrob. Chemother.**, 51: 9–11

[98] Weston, N., Sharma, P., Ricci, V. et al. (2018) Regulation of the AcrAB-TolC efflux pump in enterobacteriaceae. **Res. J. Microbiol.**, 169 (7-8): 425–431

[99] Whitehead, R.N., Overton, T.W., Kemp, C.L. et al. (2011) Exposure of *Salmonella enterica serovar Typhimurium* to high level biocide challenge can select multidrug resistant mutants in a single step. **PLoS One**, 6 (7): e22833

[100] WHO et al. (2017) Global priority list of antibiotic-resistant bacteria to guide research, discovery, and development of new antibiotics. **Geneva: WHO**.

[101] Wilson, M., McNab, R. and Henderson, B. (2002) **Bacterial disease mechanisms: an introduction to cellular microbiology**. Cambridge University Press.

[102] Wright, G.D. (2016) Antibiotic adjuvants: rescuing antibiotics from resistance. **Trends Microbiol.**, 24 (11): 862–871

[103] Yi, C., Saidel, G. and Gratzl, M. (1999) Single cell model for simultaneous drug delivery and efflux. **Ann Biomed Eng**, 27: 208–218

[104] Zhang, C.Z., Chang, M.X., Yang, L. et al. (2018) Upregulation of acref in quinolone resistance development in escherichia coli when acrab-tolc function is impaired. **Microb Drug Resist**, 24 (1): 18–23